Vortex Generators for Flow Separation Control

Wind Turbine Applications

Baldacchino, Daniel

DOI
10.4233/uuid:99b15acb-e25e-4cd9-8541-1e4056c1baed

Publication date
2019

Document Version
Final published version

Citation (APA)
Baldacchino, D. (2019). *Vortex Generators for Flow Separation Control: Wind Turbine Applications*. [Dissertation (TU Delft), Delft University of Technology]. https://doi.org/10.4233/uuid:99b15acb-e25e-4cd9-8541-1e4056c1baed

Vortex Generators for Flow Separation Control

Wind Turbine Applications

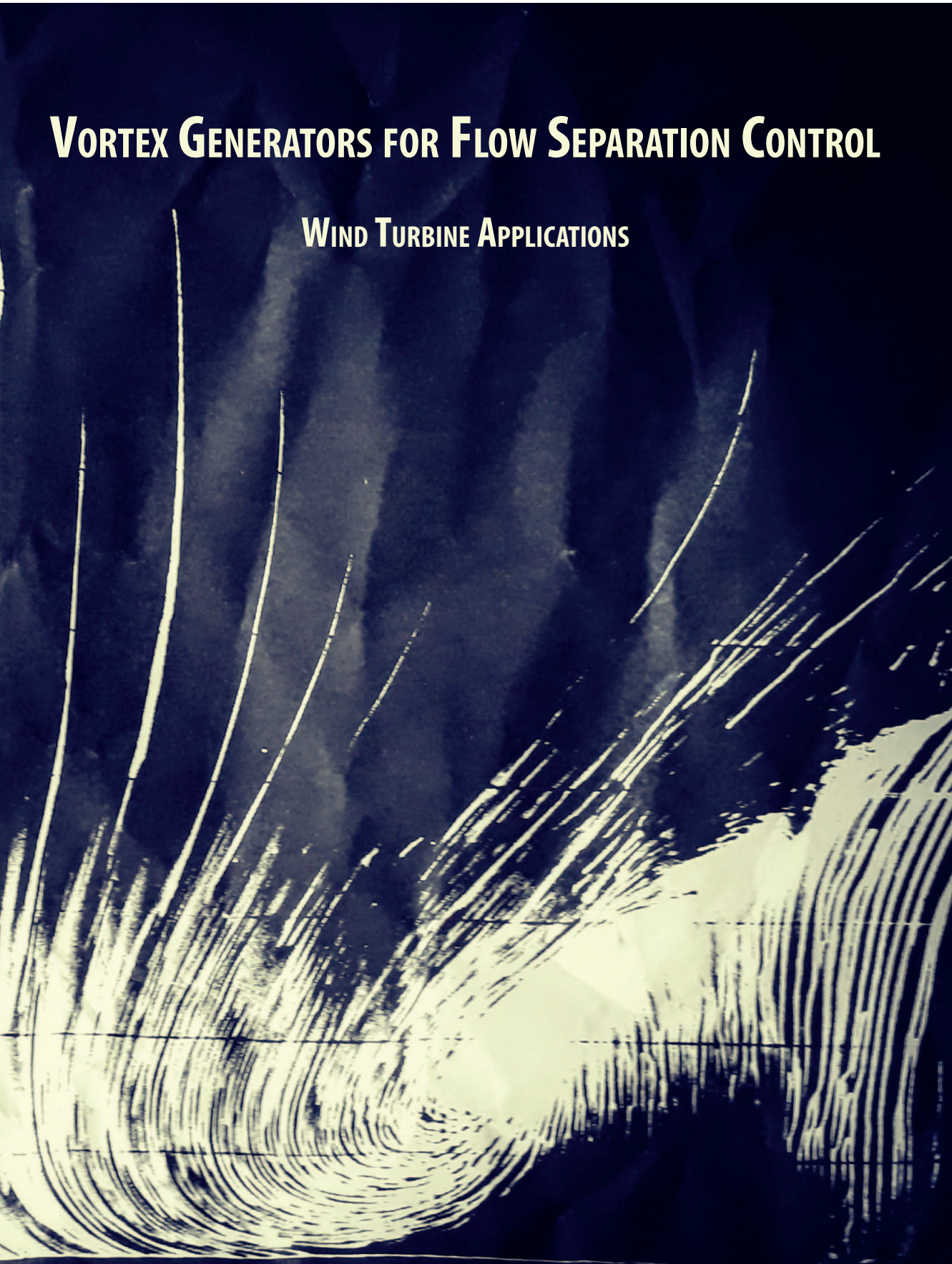

Daniel Baldacchino

Vortex Generators for Flow Separation Control

Wind Turbine Applications

DANIEL BALDACCHINO

Propositions
accompanying the thesis
Vortex Generators for Flow Separation Control: Wind Turbine Applications
by *Daniel Baldacchino*

1. Rotor blade performance characteristics are relatively more sensitive to skewed inflow when vortex generators are present.
2. Wing stall dynamics are invigorated by vortex generators.
3. 'Vortices generator' is a more accurate descriptor of the vortex generator.
4. Steady VG vortices do not exist.
5. Project-funded PhDs provide structure, but discourage scientific freedom.
6. Independence is nurtured through guidance, not by the lack of it.
7. Sustainability is an alien concept for the society removed from nature.
8. Empathy and professionalism are not mutually exclusive.
9. CFD provides the numbers but not the reasons.
10. Procrastination is essential for creativity.

These propositions are regarded as opposable and defendable, and have been approved as such by the promotors prof. dr. G. J. W. van Bussel and prof. dr. ir. C. J. Simão Ferreira.

Stellingen
behorende bij het proefschrift
Vortex Generators for Flow Separation Control: Wind Turbine Applications
door *Daniel Baldacchino*

1. De karakteristieken van rotorbladprestaties zijn gevoeliger aan asymmetrische instroming in de aanwezigheid van wervel generatoren.
2. De dynamica van vleugelovertrek wordt versterkt door wervel generatoren.
3. 'Wervels generator' is een accuratere beschrijving voor wervel generator.
4. Stabiele wervels gecreëerd door wervel generatoren bestaan niet.
5. Project gefinancierde PhDs bieden structuur, maar ontmoedigen de wetenschappelijke vrijheid.
6. Onafhankelijkheid komt tot uiting door begeleiding, niet door het ontbreken ervan.
7. Duurzaamheid is een vreemd concept voor de maatschappij die muren bouwt.
8. Empatie en professionaliteit sluiten elkaar niet uit.
9. CFD verschaft getallen maar geen redenering.
10. Uitstelgedrag is essentieel voor creativiteit.

Deze stellingen worden opponeerbaar en verdedigbaar geacht en zijn als zodanig goedgekeurd door de promotoren prof. dr. Gerard. van Bussel en prof. dr. ir. C. J. Simão Ferreira.

Vortex Generators for Flow Separation Control

Wind Turbine Applications

Proefschrift

ter verkrijging van de graad van doctor
aan de Technische Universiteit Delft,
op gezag van de Rector Magnificus prof. dr. ir. T.H.J.J. van der Hagen,
voorzitter van het College voor Promoties,
in het openbaar te verdedigen op
donderdag 19 september 2019 om 15:00 uur

door

Daniel BALDACCHINO

Master of Science in Sustainable Energy Technology
Delft University of Technology, the Netherlands
geboren te Pietà, Malta

This dissertation has been approved by the promotors.

Composition of the doctoral committee:

Rector Magnificus,	chairperson
Prof. dr. G.J.W. van Bussel	Delft University of Technology, promotor
Prof. dr. ir. C.J. Simão Ferreira	Delft University of Technology, promotor
Independent members:	
Prof. dr. F. Scarano	Delft University of Technology
Prof. dr. S.G. Voutsinas	National Technical University of Athens, Greece
Dr. ir. A. Loeven	Siemens Wind Power, Denmark
Dr. C. Bak	Technical University of Denmark, Denmark
Dr.-Ing. T. Lutz	University of Stuttgart, Germany
Prof. dr. ir. L.L.M. Veldhuis	Delft University of Technology, reserve member

Keywords flow control, vortex generator, asymmetric vortices, streamwise vortices, stall dynamics, integral boundary layer

Cover Enhanced oil flow visualisation of vortex/separation interaction on the DU97-W-300 airfoil (this thesis).

Chapter Spreads Nature-inspired snapshots by the author, with a connotation to vortex structures and flow control.

Colophon Typeset by the author with the LaTeX documentation system using a modified *classicthesis* class.

Printed by Ipskamp Drukkers, The Netherlands.

This research has received funding from: EU-FP7 AVATAR (FP7-ENERGY- 2013-1/no. 608396) and TKI Wind op Zee D4Rel (TKIW02007).

ISBN 978-94-6384-056-9

An electronic version of this dissertation is available at
http://repository.tudelft.nl/.

For Titi,
and everything we have together.

Summary

Vortex generators have become a ubiquitous sight on the modern wind turbine blade. These small, passive devices can increase the energy extraction potential of a rotor, but their subtle footprint disguises the technical difficulties associated with designing and integrating them onto wind turbine blades.

The complexity of rotor inflow and the blade-bound flow present specific challenges for the design of vortex generators. Flow three dimensionality effects along the blades have conventionally been factored into design tools using correction factors for two-dimensional airfoil performance characteristics. However, the introduction of local perturbations in the form of streamwise vortices adds an additional layer of complexity. Indeed, the interaction of the vortex generator and flow three-dimensionality is ill-understood, and thus, so are its design implications. Furthermore, the passive nature of vortex generators means that a lot of variables influence their performance, making design optimisation a costly process.

This thesis aims to improve the physical understanding of vortex generator physics in the context of wind energy applications, paving the way for more effective engineering tools. The objective is tackled by reviewing the state of the art, benchmarking existing tools and experiments, defining, measuring and simulating relevant test cases, and developing a new design tool.

A measurement campaign is conducted in a boundary layer wind tunnel using non-intrusive PIV measurements for assessing the details and dynamics of streamwise vortices. A second measurement campaign maps the performance of the DU-97-W300 airfoil section with vortex generators in a conventional closed-loop wind tunnel. Inviscid vortex theory is employed for modelling vortex dynamics. Xfoil features throughout as a design tool and itself as the subject of an improved airfoil design tool incorporating vortex generators.

The work is presented in three main parts:

Part I

- Literature review of experimental, computational and theoretical work on vortex generators, giving context to wind turbine applications.
- Benchmarking and validation of simulation tools with measurement data of airfoils controlled by passive vortex generators.

Part II

- Investigating asymmetric vortex array dynamics in a canonical setting by means of experiments and numerical vortex methods.

Part III

- A broad experimental study of vortex generator parameters and their influence on the performance of an airfoil.
- Development of an engineering model to assist with the design of airfoils considering the effects of vortex generators.

The extensive benchmarking exercise highlights that lower fidelity models require a higher degree of empiricism, whereas intermediate fidelity CFD codes such as BAY-models show a promising degree of robustness. The aerodynamic efficiency, given its importance in the rotor and blade design process, as well as an indicator of compounded inaccuracies, typically carries discrepancies exceeding 10% across all code fidelities.

Streamwise vortices are studied in an attached flat plate flow, in a boundary layer wind tunnel, and modelled using an inviscid vortex method based on the infinite vortex array. A skewed or asymmetric counter-rotating vortex array is chosen to represent a complex inflow scenario. Comparison of the measurement and model data suggest that with asymmetric arrays, vortex dynamics has a first order effect on the vortex trajectories. Namely, the vortices do not eject as rapidly from the boundary layer as in the typical symmetric scenario.

The effectiveness of a vortex generator is partly related to how localised its vortices remain over the control surface. To link the global and macroscopic effects, the overall influence of vortex generators on airfoil separation control is assessed on the DU-97-W300. The effect of array asymmetry is shown to influence the global performance, first improving lift slightly, and subsequently decreasing it, with an increasing degree of skewness. A comprehensive sweep of the vortex generator design space shows that the chordwise array placement, angle and height of the vortex generators relative to the boundary layer, are of prime importance. The influence of the vortex generator mounting strip, often neglected in modelling tools, is non-negligible, especially in transitional operating regimes. Vortex generators are also shown to exacerbate the stall dynamics of the wind tunnel model.

The work culminates in an engineering model for vortex generators in an integral boundary layer tool. The method exploits a source term technique, which introduces additional boundary layer shear stress, representing vortex-induced mixing. Using a data-mining approach, an empirical source term is found in terms of the height and geometric inflow angle. The outcome is XFOILVG, a new tool able to provide design direction of airfoils with vortex generators.

Samenvatting

Wervelgeneratoren zijn alomtegenwoordig op moderne windturbinebladen. Deze kleine, passieve hulpmiddelen kunnen de energiewinning van een rotor verhogen. Ondanks hun subtiele aanwezigheid gaan hun ontwerp en integratie op windturbinebladen gepaard met heel wat technische uitdagingen.

De complexiteit van de rotorinstroming en bladgebonden instroom zorgt voor specifieke uitdagingen bij het ontwerpen van wervel generatoren. De driedimensionale effecten rond de bladen zijn in ontwerpmodellen gewoonlijk geïntegreerd door correctiefactoren toe te passen op tweedimensionale karakteristieken van vleugelprofielen. Het introduceren van lokale verstoringen in de vorm van stroomsgewijze wervelingen voegt echter een extra complexiteit toe. De interactie van wervel generatoren en driedimensionale stroming, en dus ook hun ontwerpmoeilijkheden, zijn ondermaats begrepen. De passieve aard van wervel generatoren zorgt ervoor dat veel variabelen hun prestatie beïnvloeden, en dit maakt de ontwerpoptimalisatie een kostbaar proces.

Deze thesis streeft naar het verbeteren van het begrijpen van de fysica achter wervel generatoren in windenergie applicaties, om zo een weg te banen naar effectievere ingenieursmodellen. De doelstelling is benaderd door het bestuderen van de huidige stand van de techniek, het vergelijken van bestaande methodes en experimenten, het definiëren, meten en simuleren van relevante testgevallen en het ontwikkelen van een nieuwe ontwerp methode.

In een grenslaagwindtunnel is een meetcampagne met niet-indringende PIV metingen uitgevoerd om zo de details en dynamica van stroomsgewijze wervelingen te evalueren. Een tweede meetcampagne in de conventionele gesloten windtunnel bracht de prestatie van de DU-97-W300 vleugelprofiel met wervel generatoren in kaart. De wrijvingsloze werveltheorie is gebruikt om de wervel dynamica te modelleren. Xfoil wordt gebruikt als ontwerpmethode en tegelijk als onderwerp voor een verbeterd ontwerpmodel voor vleugelprofielen met wervel generatoren.

Dit werk is uit drie grote delen opgebouwd:

Deel I

- Een overzicht van de literatuur in verband met experimenteel, rekenkundig en theoretisch werk van wervel generatoren in de windenergie context.
- Het vergelijken en valideren van simulatiemodellen met experimentele data van vleugelprofielen gecontroleerd door passieve wervel generatoren.

Deel II

- Het onderzoeken van de dynamica van asymmetrische wervelrijen in een

canonieke omgeving door gebruik te maken van experimentele en numerieke wervelmethodes.

Deel III

- Een brede experimentele studie van de parameters van wervel generatoren en hun effect op de prestatie van een vleugelprofiel.
- Het ontwikkelen van een ingenieursmodel als hulpmiddel bij het ontwerpen van vleugelprofielen rekening houdend met het effect van wervel generatoren.

Een uitgebreide studie heeft benadrukt dat modellen met een lagere betrouwbaarheid een hoger niveau van empirische input vragen, terwijl CFD modellen met een middelmatige betrouwbaarheid zoals BAY-modellen een veelbelovende robuustheid tonen. De aerodynamische efficiëntie, gezien het belang ervan in het ontwerp proces van een rotor en windturbineblad, als ook een indicatie van samengestelde onnauwkeurigheden, wijken vaak af met meer dan 10% in alle modelbetrouwbaarheidslevels.

Stroomsgewijze wervelingen in een aanliggende stroming over een vlakke plaat zijn in een grenslaagwindtunnel bestudeerd, en zijn gemodelleerd door gebruik te maken van een wrijvingsloze werveltheorie gebaseerd op een oneindige wervelrij. Een onevenwichtig of asymmetrische tegengesteld draaiende wervelrij is gekozen als complex stromingsscenario. Een vergelijking van de gemeten en gemodelleerde data suggereert dat met een asymmetrische rij de werveldynamica een eerste-orde effect heeft op het werveltraject. Namelijk, de wervels worden niet zo snel verdreven uit de grenslaag als in een typisch symmetrisch scenario.

De effectiviteit van wervel generatoren is gedeeltelijk gerelateerd aan de mate waarin de wervels lokaal blijven over het controleoppervlak. Om de globale en macroscopische effecten te linken, is de algemene invloed van wervel generatoren op de controle van stromingsloslating van een DU-97-W300 vleugelprofiel geëvalueerd. Het is aangetoond dat de rijasymmetrie de globale prestatie beïnvloedt; voor toenemende asymmetrie neemt de lift eerst licht toe, waarna deze terug afneemt. Uit een uitgebreid onderzoek van de ontwerpruimte van wervel generatoren blijkt dat de rijpositie op de koorde, de hoek en de hoogte van de wervel generatoren ten opzichte van de grenslaag van primair belang zijn. Het effect van de bevestigingsstrip van vortex generatoren, wat vaak in modellen verwaarloosd wordt, blijkt niet verwaarloosbaar, vooral in omslagregio's. Wervel generatoren verscherpen ook de overtrekdynamica van windtunnelmodellen.

Dit werk wordt afgesloten met het voorstellen van een ingenieursmodel voor wervel generatoren dat gebruik maakt van een integrale grenslaag methode. Deze methode gebruikt een brontermtechniek dat een extra schuifspanning in de grenslaag toevoegt als voorstelling van wervel geïntroduceerde menging. Door het gebruik van een datadelvingtechniek is een empirische bronterm gevonden als functie van de hoogte en geometrische invalshoek. Dit resulteerde in XFOILVG, een nieuw model dat in staat is om een ontwerprichting aan te geven voor vleugelprofielen met wervel generatoren.

Contents

Part II Dynamics and evolution of embedded streamwise vortices

Part III Separation control with vortex generators

Part IV Concluding Discussion

Nomenclature

Acronyms

AEP	Annual Energy Production
APG	Adverse Pressure Gradient
AR	Aspect Ratio
AVATAR	AdVanced Aerodynamic Tools of lArge Rotors
BAY	Bender-Anderson-Yagle (model)
BEM	Blade Element Momentum
BL	Boundary Layer
BLT	Boundary Layer Tunnel
CD	Common Downwash
CDA	Cropped-Delta
CFD	Computational Fluid Dynamics
CoR	Co-Rotating
CtR	Counter-Rotating
CU	Common Upwash
DA	Delta
FOV	Field Of View
IBL	Integral Boundary Layer
LE	Leading Edge
LTT	Low Turbulence Tunnel
MS	Mounting Strip
ODE	Ordinary Differential Equation
OFV	Oil Flow Visualisation
PPVM	Periodic Point Vortex Model
RANS	Reynolds-Averaged Navier Stokes
SPIV	Stereo Particle Image Velocimetry
TE	Trailing Edge
TI	Turbulence Intensity
VG(s)	Vortex Generator(s)
ZPG	Zero Pressure Gradient
ZZ	Zig-zag (strip)

Coordinate Systems

ξ, η	Normalised planar coordinates (wall-normal, spanwise)
x, r, θ	Polar coordinates (streamwise, radial, azimuthal)
x, y, z	Cartesian coordinates (streamwise, wall-normal, spanwise)

Greek Symbols

α	Airfoil geometric angle of attack
β	Geometric vortex generator vane angle of attack
χ	Vortex strength constant
δ	Boundary layer thickness
$\delta^{\star\star}$	Density thickness
$\delta^{\star}$	Displacement thickness
ϵ	General error
Γ	Vortex strength
γ	Normalised vortex strength or strength ratio; vortex sheet strength
κ	von Kármán constant; wave number
λ	Source term decay rate
μ	Viscosity
ν	Kinematic viscosity
Ω	Anti-symmetric part of the velocity gradient tensor
ω	Vorticity
ψ	Streamfunction
ρ	Density
σ	Standard deviation, source term strength
τ_w	Wall shear stress
θ	Boundary layer momentum thickness
$\theta^{\star}$	Kinetic energy thickness
φ	Vortex generator pair skew angle
ζ	Complex plane

Roman Symbols

$\mathcal{A}$	Normalised peak trajectory amplitude
$\mathcal{D}$	Dissipation integral
$\mathcal{P}$	Normalised period of orbital motion
b	Cropped-Delta vane edge length
c	Airfoil chord
C_D	Dissipation coefficient
C_d	Drag coefficient
C_f	Skin-friction coefficient
C_l	Lift coefficient
C_n	Normal force coefficient
C_p	Static Pressure coefficient
C_p^T	Total Pressure coefficient
$C_0 \dots C_3$	Empirical source term integral coefficients
$C_{\tau,EQ}$	Equilibrium shear stress coefficient
C_τ	Shear stress coefficient
$C_{l,\alpha}$	Glide slope

D	Vane-pair separation; Dissipation
d	Internal vane array spacing
e	Vane profile thickness
G	Velocity influence coefficient
H	Shape factor; velocity influence coefficient; wind tunnel width
h	Vortex generator vane height
$H^{\star\star}$	Density shape factor
$H^{\star}$	Kinetic energy shape factor
$h^{\star}$	Normalised vane height
I_{ST}	Source term integral
K	Vortex trajectory constant
K_c	Shear-lag response parameter
L	Vortex generator vane chord length
l	Helical vortex pitch
$L^{\star}$	Normalised VG vane chord
M	Mach Number
N	Amplification factor (transition), sample size
Q	Q-criterion vortex identifier
Re_θ	Momentum thickness-based Reynolds number
Re_c	Chord-based Reynolds number
S	Symmetric part of the velocity gradient tensor, VG array span
S_{VG}	Source term shape function
T	Time scale
t	Airfoil thickness; time
u^+	Boundary layer velocity in inner scaling
u_0	Axial velocity at the vortex centroid
u_τ	Friction velocity
u_e	Boundary layer edge velocity
u_{VG}	Vortex generator vane tip velocity
W	Wind tunnel test section height
x_{VG}/c	Relative chordwise placement of vortex generators
y^+	Wall-normal position in inner scaling

Subsripts

∞	freestream value
0	initial value
cal	calibrated value
e	boundary layer edge
emp	empirical value
max	maximum value
tr	relating to transition

1

Thesis Outline

“

The universe is multiform and boundless,
and we continue to stumble upon new aspects of it.
The more we learn, the more we are amazed by the world's variety.
Our knowledge of the elementary grammar of the world continues to grow . . .

”

— Carlo Rovelli

This chapter lays out the motivation for the research presented in this dissertation, within the context of wind energy. The research questions are established and the objectives to answer them are defined. The chapter finishes with an overview of the approach chosen to tackle the research, in relation to the organisation of the thesis.

1.1. Introduction

It is estimated that in the timeframe 2015-2025, around 15% cost reductions in offshore wind may be expected from continuing innovation, risk mitigation, and technology upscaling - ensuring wind energy remains a competitive contributor to our increasingly sustainable energy mix (see Figure 1.1). Developments in the rotor/nacelle assembly will likely account for around 15% of these cuts (International Renewable Energy Agency, 2016). Innovations are driven by R&D investments, such as the continued improvement in the performance of rotor blades, yielding higher energy capture as well as improved overall reliability.

The AVATAR project (AdVanced Aerodynamic Tools of lArge Rotors) was one such investment, and partly sponsored the present work. Its main goal was

> *"the development and validation of advanced aerodynamic models . . . for the next generation of large scale wind turbines (up to 20MW)"* (AVATAR).

The trend towards larger rotors has been accompanied by a shift to a 'high yield - low load' design philosophy. This effectively means low-induction rotors with slender blades. 'Low-induction' refers to a turbine's operating design point which is lower than the $1/3$ optimum, trading off aerodynamic efficiency for peak load shaving. For example, the three-bladed INNWIND rotor is conventionally designed to produce a rated 10MW of power with 86m-long blades (Jensen et al., 2017). By contrast, the AVATAR rotor is designed to produce the same power but with a lower power density owing to the lower operating induction ($0.3 \rightarrow 0.24$) and longer blades (86m $\rightarrow$ 100m). To withstand the loads borne by the long blades, the inboard blade airfoil sections are designed with thicknesses up to 60% chord (Sieros, 2017), as illustrated in Figure 1.2. Additionally, flatback airfoils featuring thick trailing edges up to 15% chord, become attractive aeroelastic solutions.

However, thicker airfoil sections present relatively stronger adverse pressure gradients to the oncoming flow, making them increasingly susceptible to flow separation; flatback airfoils shed an unsteady, bluff body wake due to the blunt trailing edge. These unsteady flow regimes may manifest as higher fatigue loads, low-frequency stall noise, and a decrease in the turbine's annual energy production (AEP), directly impacting (increasing) the Levelised Cost of Energy (Oerlemans, 2011; Skrzypiński et al., 2014).

Vortex generators (VGs) are a means to control this separation, and will be studied in this thesis.

1.2. Motivation

Vortex generators for wind turbines, or any other application for that matter, are developed using simulation tools and testing. Due to the prohibitive efforts and costs of testing each and every design iteration, suitable modelling techniques are necessary. These may span a wide range in fidelity, offering general design

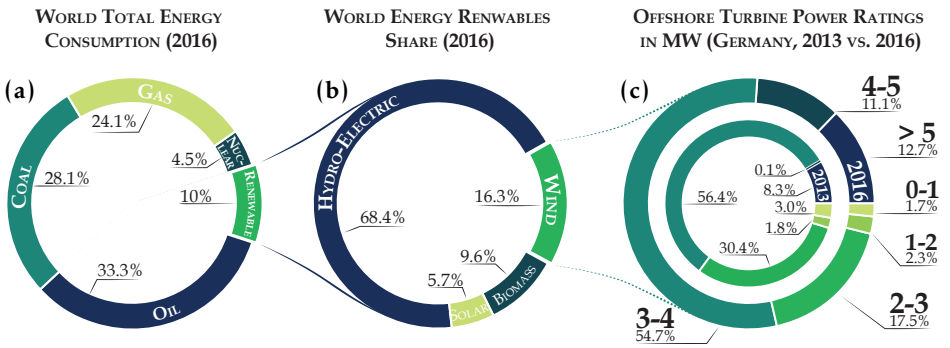

Figure 1.1: (a) World wide energy consumption by fuel type and (b) corresponding share of renewable energy supply in 2016 (International Energy Agency, 2017); (c) Cumulative installed offshore turbines in Germany by nameplate rating (Fraunhofer-IWES, 2017).

direction or detailed insights for fine tuning purposes. However, since the typical length scale of these passive devices is similar to the local boundary layer thickness, computational approaches resolving the flow details also come at a steep cost. There is thus a preferential drive for developing lower-fidelity and engineering-type models which can be used for fast iterative design evaluation. Achieving this requires a sound understanding of the relevant physical phenomena associated with vortex induced mixing.

1.3. Research Objectives

The overarching goal of this thesis is therefore

> *to improve the physical understanding of vortex generator physics, paving the way for more efficient and robust engineering tools.*

To address this, three specific research objectives are defined:

I. Establishment of the state of the art in VG modelling

Development of better VG models must commence with an understanding of the vortex evolution and dynamical properties, and how these affect the boundary layer. This must be understood in general but also in the context of wind turbine-specific applications. In light of this, the following research questions are further identified:

- *What is the current level of understanding of VG physics and extent of modelling efforts?* (Chapter 2)
- *How well do state of the art models for vortex generators fair?* (Chapter 3)

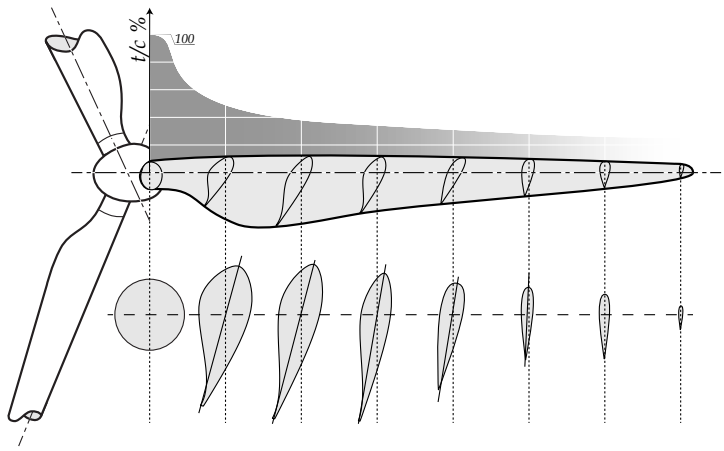

Figure 1.2: A typical wind turbine blade thickness distribution, similar to the AVATAR rotor design (not to scale).

II. Investigation of the dynamics and evolution of embedded streamwise vortices

Open questions remain as to the sensitivity of VG efficacy to the flow regimes that might be encountered on a rotating wind turbine blade. The thick airfoils and complex blade flows present specific problems with which designers must contend. Even more so, when considering integrated design with vortex generators. This necessitates a critical review and assessment of the inflow conditions presented by the wind turbine blades. Due to its complexity, addressing this can quickly become very cumbersome. Thus,

- *How can a complex inflow case be simplified and tested in a wind tunnel to assess the corresponding sensitivity of the VG control response?* (Chapter 4)

III. Separation control and modelling with vortex generators

Despite their passive nature and relatively straight forward operating principle, an embedded vortex flow is not a simple one. This has hampered the robustness and effectiveness of engineering models. An additional barrier is the lack of validation means through systematic, and applied experimental parametric studies. This is especially true for the thick airfoils which are relevant for wind energy applications. Thus, based on the outcome of prior goals, we will ultimately address

- *Which parameters are relevant for the design of passive vortex generators and to what extent?* (Chapter 5)
- *How can these be combined in an efficient engineering tool?* (Chapter 6)

1.4. Approach

These research questions will be tackled through experimental and numerical means, as summarised in Table 1.1.

Stereo Particle Image Velocimetry (SPIV) measurements of vortex generators were performed in a Boundary Layer wind Tunnel (BLT), which enabled the generation of a thick (in the order of 0.1m), attached, turbulent boundary layer. This was necessary to allow a detailed assessment of the vortices and their effect on the boundary layer. The potential flow approach by Jones (1955) is extended to account for vortex asymmetry, offering new insight on the vortex dynamics, supporting the boundary layer measurements.

Applied separation control was investigated in the Low Turbulence wind Tunnel (LTT) with an extensive measurement campaign on a thick wind turbine airfoil, the DU97-W-300. The influence of numerous vortex generator parameters was investigated at a moderately high Reynolds number by assessing the lift and drag performance of the airfoil, aided with flow visualisations.

An extension of the viscous-inviscid Xfoil code, Xfoilvg was developed enabling airfoil performance assessment with vortex generators. An extensive database of experimental and synthetic data was assembled using measurement data presented in this thesis and the AVATAR project. This database includes various VG configurations, airfoils and flow regimes, synthesized to produce an empirical relation to capture the VG effect.

Table 1.1: Overview of experimental campaigns performed in this work.

Facility	Measurement	Medium	Focus
BLT	SPIV	Flat Plate	BL/Vortex Interaction
LTT	Pressure/Oil Visualisation	Airfoil	Separation control

1.5. Thesis organisation

The remainder of the thesis is laid out as shown in Figure 1.3, and addresses the research objectives in five interrelated parts:

Part I. State of the Art

- Chapter 2 first describes the relevant literature to further develop the research objectives formulated in the previous section.
- Chapter 3 presents a one-of-a-kind benchmark of up to six VG simulation tools, the result of a collaborative effort within the AVATAR project.

Part II. Dynamics and evolution of embedded streamwise vortices

- Chapter 4 presents the experimental and numerical analysis of asymmetric vortex wakes, shedding light on the possible effect of skewed inflow.

Part III. Separation control with vortex generators

- Chapter 5 describes the separation control experiment on the DU97-W-300 airfoil.
- Chapter 6 presents the development and validation of XFOILVG.

Part IV. Concluding Discussion

- Chapter 7 presents a summary of the thesis conclusions and an outlook for relevant future investigations.

Part V. Appendices

- Appendix A provides additional setup information of the numerical aspects of the benchmark as well as the reference data.
- Appendix B details the Boundary Layer Tunnel, data processing statistics, and measurement uncertainty.
- Appendix C details the Low Turbulence Tunnel, data processing statistics, measurement uncertainty, and supplementary polars.
- Appendix D presents the database used for the calibration of the XFOILVG module.

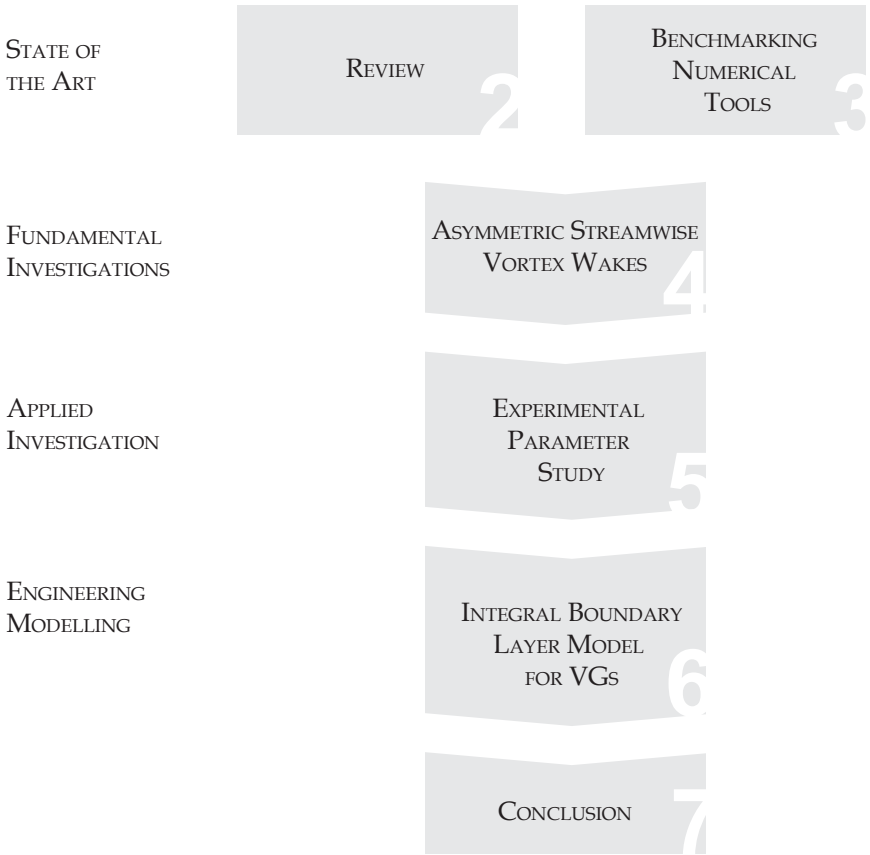

Figure 1.3: Thesis outline.

I

State of the Art

2

Vortex Generators: Reviewing the State of the Art

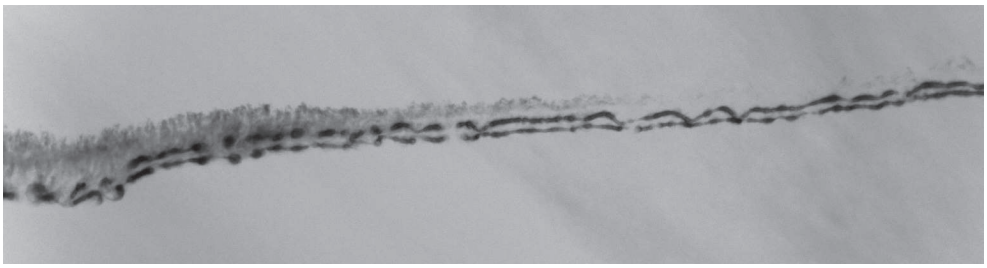

The developing Crow instability behind a cruising turbojet is visualised as condensing vapour from the exhaust is entrained by the tip vortices. Delfgauw, Netherlands.

The breadth of the flow control field is brought into focus around the application of passive vortex generators for flow separation management. This chapter first sets the context for scientific and engineering work on passive vortex generators with a brief historical account. The operating principles are discussed in terms of boundary layer manipulation, vortex structure and dynamics, and the efficacy for flow separation control. The chapter then presents efforts to model vortex generators and their effects, discussing open questions throughout. This is ultimately synthesized to highlight research gaps and opportunities, lending credence to the research questions outlined in Chapter 1.

2.1. Introduction

2.1.1. Blade add-ons

Rotating wind turbine blades are host to numerous phenomena which give rise to highly three-dimensional, unsteady and noisy flow regimes. These are often related to the mode of operation and turbine design itself, such as dynamic inflow due to delayed responses from the rotor near-wake, dynamic stall and yaw misalignment (Schreck, 2007). The latter has for example been shown to increase the outer blade-bound radial flows (Micallef et al., 2014). Furthermore, the boundary layer flow at the inboard blade regions is separation prone due to the thick airfoil sections. Such zones of separation are highly three dimensional, and the associated centrifugal-pumping effect gives rise to radial flow. Other external factors also influence the blade-bound flow regime, such as gusts, wind shear and wind veer. As turbine rotors grow, they experience stronger cyclic variations and hence become more susceptible to these flow phenomena. This presents difficulties to the wind turbine designer.

It is possible to overcome some of these challenges directly through integral design practice. For example, the traditionally blunt cylindrical profile at the blade-hub connection can be better streamlined, as seen on the Enercon E-126 machine with its iconic teardrop-shaped nacelle. In another example, rather than correcting for performance degradation due to erosion and contamination, roughness-insensitivity can, to some extent, be designed into the airfoils. Alternatively, such issues may be alleviated more robustly using *blade add-ons*. The term has found increasing use of late in the wind industry, due to the popularity of retro-fittable turbine improvement solutions. This practice has transformed the blade add-on approach into somewhat of a core competence in its own right. Indeed, a niche industry surrounding rotor design upgrades has emerged, providing wind turbine designers and operators with solutions to improve fleet performance (see e.g. the SmartBlade-3M collaboration [2017] and Power Curve Solutions [2017]). Some of the blade add-ons commonly found on wind turbine blades are described in Table 2.1 and Figure 2.1. These devices work passively to, for example, mitigate trailing edge noise using serrations, and delay flow separation using vortex generators. Other examples which have not yet found commercial application are wing-tip sails for accelerating the wake recovery process behind a rotor (Gyatt and Lissaman, 1985).

2.1.2. Biomimicry

Many of these solutions draw inspiration from nature, which holds the products of millenia of genetic optimisation. Fish and other mammals have evolved features over millions of years which help them adapt to their particular needs; needs which are partly dictated by their surroundings and physiology (see Figure 2.2). Some examples are:

Table 2.1: Overview of commonly deployed passive wind turbine blade add-ons, where they are typically found along the blades and what function they serve. Superscripts refer to the labelled diagram below and the midboard region is loosely defined as the 30% – 70% radial span.

Add-On	Where	Why
Boundary layer fence[1]	Inboard	Prevent root-prone separation pockets from contaminating outer regions of the blade
Gurney flap[2]	Inboard	Augment sectional lift by increasing effective airfoil camber
Spoilers[3]	Inboard	Increase lift and torque contribution from inboard blade section
Trailing edge serrations[4]	Midboard-Outboard	Attenuate trailing edge noise
Vortex Generators[5]	Inboard-Midboard	Prevent airfoil flow separation, reduce unsteady loads and increase AEP
Winglets[6]	Outboard (tip)	Reduce tip vortex induced drag and increase energy output

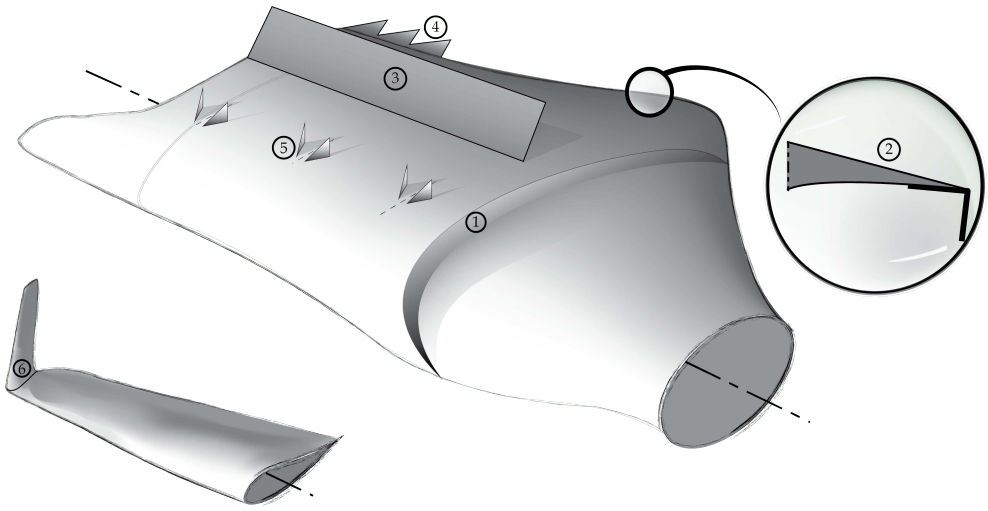

Figure 2.1: A depiction of common wind turbine blade add-ons.

- Certain extant (flying) birds are known to posess small extended leading edge feathers, which activate during landing or abrupt manoeuvres. This *alula* (Latin for *small wing*) alleviates separation through mixing by a relatively strong leading edge vortex (Lee et al., 2015).
- Silent flight is the speciality of the owl. Research has shown it is one of the few (flying) birds to incorporate trailing edge feather-strands which reduce trailing edge noise (Sarradj et al., 2011).
- The fins of large humpback whales feature ridged leading edges, or *tubercles*. Studies have shown these enable high-angle of attack manoeuvres through vortex-induced mixing over the fin surface (Fish and Lauder, 2006).
- Shark skin has evolved smart ridges which researchers found reduce profile drag by stabilising laminar boundary layers (thus preventing transition to turbulence). Recent findings have also suggested that these dermal structures also possess anti-fouling properties - features which would certainly be desirable for wind turbine blades exposed to the elements (Sullivan and Regan, 2011).

It is evident that some or all of these elements have inspired engineering solutions in various applications, including the idea to use vortex-induced mixing for flow separation control.

2.1.3. Passive vortex generators

The effectiveness of an aerodynamic surface to generate lift requires that the pressure recovers to the freestream state downstream of the body. If the flow separates, this recovery is incomplete, and the ensuing loss of lift, coupled with increased pressure drag, degrades performance. The turbulent mixing action of a streamwise vortex re-energises the boundary layer with the outer flow and delays flow reversal, effectively decreasing the effect of a strong adverse pressure gradient (Schubauer and Spangenberg, 1960; Lengani et al., 2011).

Boundary layer control can be actively achieved through suction (removing retarding flow) and blowing (adding momentum), or turbulent mixing with actively generated vortices, with say jets and longitudinal plasma actuators. In fact, the field of flow control is a wide and diverse one. This chapter will focus the discussion on passive vortex generators, and in particular on recent research efforts relevant for wind energy applications. The interested reader can consult broader reviews of the topic by Gad-el Hak and Bushnell (1991), Lin (2002) and Ashill et al. (2005).

Complementary to active techniques, passive flow separation control can be achieved with fixed vortex generator devices. One such typical device is a vane protruding above the surface to roughly the local boundary layer height and angled to the incoming flow as shown in Figure 2.3. Similar to a Delta Wing system (see e.g. Hoerner and Borst, 1985), a leading edge vortex develops along the vane and is shed near the tip, creating a wake of upwash and downwash regions. This effectively

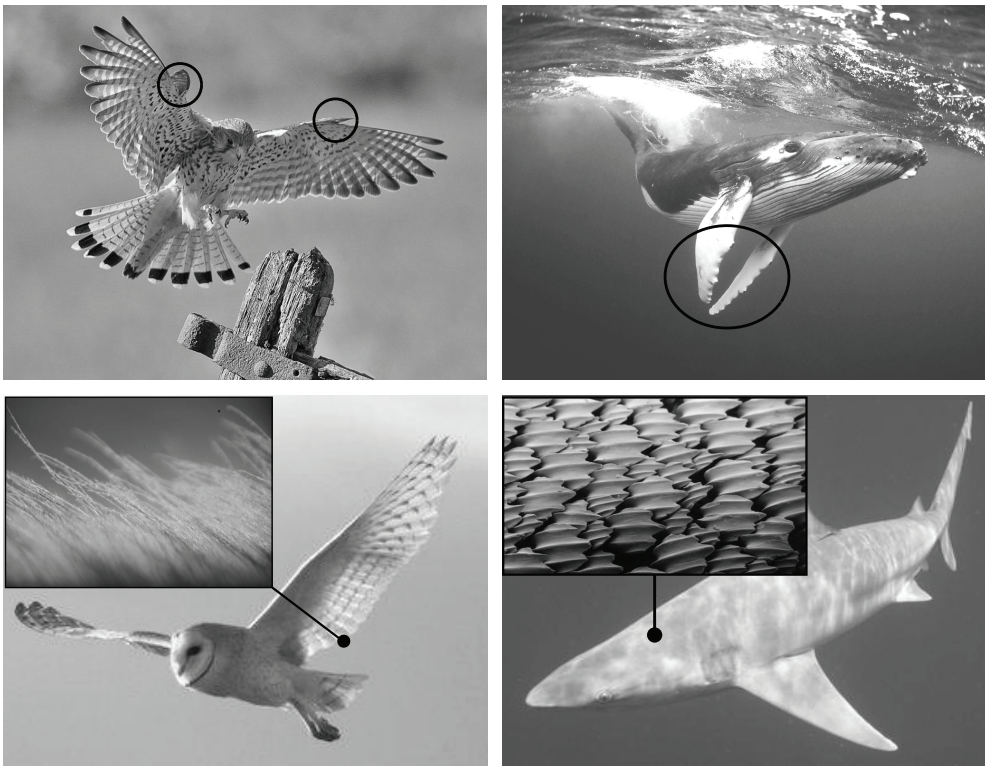

Figure 2.2: Extended alula feather of a Kestrel during landing (*top left*) (Bannister, 2012); leading edge tubercles on the fins of a manoeuvring humpback whale (*top right*) (Locke, 2015); splayed feathers at the trailing edge of a barn owl's wings (*bottom left*) (Jaworski, 2015); and dermal riblets on a Galapagos shark (*bottom right*) (Smirnoff, 2018). Alulae and tubercles are examples of hyper-boundary layer add-ons, whilst the owl feathers and shark dermal riblets reside at or within the boundary layer depth.

diverts some of the high-momentum outer flow into the boundary layer region to re-energise it. In fact, Gad-el Hak and Bushnell (1991) classify the control mechanism of passive vortex generators as "momentum addition to near-wall flow".

The simplicity and robustness of VGs have, over time, led to their widespread adoption in the aviation, automobile and energy sectors, controlling shock- and pressure-induced separation in external (e.g. wings) and internal flows (e.g. turbine ducts). Current usage on wind turbines is primarily intended for controlling the separated flows encountered at inboard blade stations. As noted previously, these sections are prone to separation due to the higher sectional thicknesses and angles of attack experienced. However, the reality of performance loss due to blade surface degradation has driven vortex generators further outboard. In other instances, though much less developed, small outboard VGs have also been explored for dynamic stall control (Mai et al., 2008; Choudhry et al., 2016).

When properly designed and integrated, the main effect of vortex generators

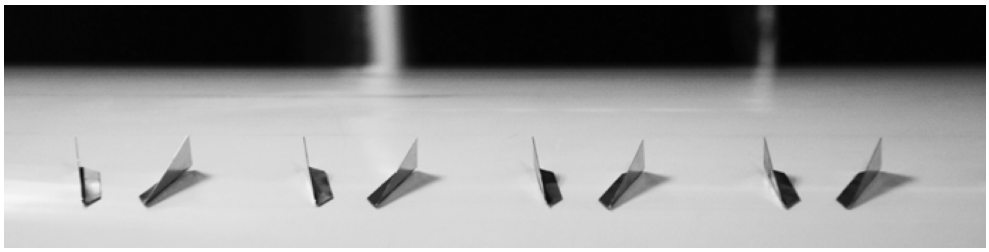

Figure 2.3: Delta-shaped passive vortex generator vane pairs mounted on an airfoil section.

on a wind turbine rotor is to increase the energy capture by a slight increase in the tangential and normal blade loads. The yield improvement will depend on the initial blade design, the condition of the blade surface, and therefore also the climate and site conditions. Studies suggest typical improvements in the order of 1 – 3% AEP, reflecting a comparable reduction in the cost of energy (Bak et al., 2016).

A word about passive-activation concepts

A subset of VGs are passively-deployable vanes. Such devices have not been extensively investigated, but offer the benefits of active systems without the burden of auxiliary power and hardware. One can think of a self-actuating (lifting) vane, that can hinge and therefore lift when sufficient flow is present. The VG could also operate on a swivel system such that the attack angle is self aligning. Both would reduce penalty drag. Another patented solution is a flow-driven oscillating vortex generator, aeroelastically tailored to oscillate at resonant frequencies. Such a device can be mounted at zero incidence to the flow or stowed away in the substrate (Quackenbush et al., 2010).

2.1.4. Chapter organisation

The remainder of this chapter will introduce and discuss salient research works and concepts relevant for the context of this thesis. The following section sets the tone with a brief historical account of vortex generator research. In section 2.3, we review the fundamental mechanisms and evidence for separation control using streamwise vortices. Section 2.4 presents an overview of VG design concepts and their efficacy in various applications. Section 2.5 delves deeper into the structure of the streamwise vortices and efforts to characterise their properties. Section 2.6 is dedicated to the subject of vortex dynamics and meandering, while section 2.7 discusses the various attempts to simulate and model a vortex generator flow and its effect on separating flows. The chapter is synthesized in section 2.8, setting the basis for the remainder of the thesis.

2.2. A brief historical account

Passive vortex generator research has a rich history, but the earliest demonstration of the vortex generator concept for separation control is widely attributed to Harlan D. Taylor (1947). In the years following, research and demonstration projects have gradually increased our understanding of vortex generator physics. In the late 50s and early 60s, some seminal research efforts by Jones (1955), Gould (1956), Schubauer and Spangenberg (1960) and Pearcey (1961) laid important conceptual foundations for understanding the VG vortex dynamics and the interactions with a boundary layer.

Fundamental and applied investigations in the decades since, have shed light on the vortical structures associated with VGs, as well as VG design methodologies. Throughout the 80s and 90s, a significant experimental effort from NASA and Stanford gradually unravelled the mean and turbulence properties of the VG vortices, and how their formation and development differed for single vortices, pairs and arrays (see e.g. Westphal et al., 1987; Pauley and Eaton, 1988; Wendt et al., 1993). The development and gradual adoption of Particle Image Velocimetry (PIV) at the turn of the century enabled instantaneous measurement of entire velocity fields. This saw a re-emerging interest in vortex generators, with studies treating the vortex structures and turbulent dynamics in greater detail (e.g. Velte et al., 2008; Cathalifaud et al., 2009; Lengani et al., 2011) as well as more exhaustive assessments of the VG geometric parameters and their influence of the flow control efficacy (e.g. Godard and Stanislas, 2006; Lögdberg et al., 2010).

2.3. Separation control

2.3.1. Mechanisms of vortex-controlled separation

As outlined in the introduction to this thesis, vortex dynamics will be treated in isolation from a separating flow case. The two will be combined in an application of separation control of an airfoil. We will eventually propose a modelling approach which implicitly combine the fundamentally three-dimensional aspects of streamwise vortices, with an inherently two-dimensional integral boundary layer (IBL) approach. It is therefore useful to consider arguments for the two 2D approach from the perspective of vortex/boundary layer interaction. This section is inspired by Drela's elegant interpretations of boundary layer theory (Drela, 2014).

Starting with the governing integral boundary layer equations, Equation 2.1 expresses the evolution of the momentum defect represented by the thickness θ, and Equation 2.2 refers to the evolution of the energy thickness $\theta^\star$:

$$\frac{d\theta}{dx} = \frac{C_f}{2} - (2+H)\frac{\theta}{u_e}\frac{du_e}{dx} \tag{2.1}$$

$$\frac{d\theta^\star}{dx} = 2C_D - 3\frac{\theta^\star}{u_e}\frac{du_e}{\partial x} \tag{2.2}$$

The complete definitions are summarised in Table 2.2. The dissipation coefficient C_D is the normalised dissipation integral $\mathcal{D}$ which is, in turn, a measure for the local rate of flow kinetic energy conversion into heat. Therefore $\mathcal{D}$ arises from the action of shear stresses on the fluid as it deforms due to the predominant gradients in the wall-normal direction. In mathematical terms,

$$\mathcal{D} = \int_0^\delta (\mu + \mu_t)\left(\frac{\partial u}{\partial y}\right) dy \tag{2.3}$$

The total shear stress can be thought of as the sum of laminar (μ) and turbulent (μ_t) contributions, here in the form of an effective viscosity. The latter may arise from turbulence and organised vortical structures in the flow. As will be discussed in a later section, an embedded streamwise vortex gives rise to strong velocity gradients in both wall-normal and spanwise directions, even more so when the vortices exhibit meandering (Angele and Muhammad-Klingmann, 2005).

From the theoretical stand point, an energy budget view of the boundary layer can be further described by combining Equation 2.1 and Equation 2.2. One can thus explicitly describe the evolution of the kinetic energy, here in terms of the shape parameter, as

$$\frac{1}{H^\star}\frac{dH^\star}{dx} = \frac{2C_D}{H^\star} - \frac{C_f}{2} + \left(H - 1 - \frac{2H^{\star\star}}{H^\star}\right)\frac{\theta}{u_e}\frac{du_e}{dx} \tag{2.4}$$

For an incompressible flow in equilibrium, this equation reduces to

$$\frac{\theta}{u_e}\frac{du_e}{dx} = \frac{1}{H-1}\left(\frac{C_f}{2} - \frac{2C_D}{H^\star}\right) \tag{2.5}$$

To reduce the risk of separation of the boundary layer is to increase the maximum tolerated pressure gradient, or conversely, to minimize the most negative streamwise velocity gradient tolerable. Thus, the left hand side of Equation 2.5 can be minimised by increasing the dissipation term, while keeping C_f safely above zero, for an attached flow. As shown in the numerous studies with vortex generators, embedded streamwise vortices do just this - by increasing the dissipation some way away from the surface, without directly affecting C_f. For instance, Lengani et al. (2011) directly showed that vortex generators transfer energy from the mean flow to the boundary layer. This was achieved by deduction of the turbulence production and dissipation terms from direct measurement of the mean and turbulent flow field of a controlled, decelerating turbulent boundary layer. The energy transfer

Table 2.2: Definition of integral boundary layer parameters relevant for incompressible flow.

Parameter	Equation	Description
$\delta^\star$	$\int_0^\delta (1 - \frac{u}{u_e})\, dy$	(Mass) Displacement thickness
θ	$\int_0^\delta \frac{u}{u_e}(1 - \frac{u}{u_e})\, dy$	Momentum thickness
$\theta^\star$	$\int_0^\delta \frac{u}{u_e}(1 - \frac{u^2}{u_e^2})\, dy$	Kinetic energy thickness
H	$\delta^\star / \theta$	Shape factor
$H^\star$	$\theta^\star / \theta$	Kinetic energy shape factor
C_f	$\frac{\tau_w}{\frac{1}{2}\rho u_e^2}$	Skin friction coefficient
C_D	$\frac{\mathcal{D}}{\rho u_e^3}$	Dissipation coefficient

from the mean flow increases the turbulent kinetic energy, represented by μ_t above, and prevents or delays separation in the boundary layer. Note that, locally, the skin friction will be affected by the physical presence of the device, but also due to local inflow or outflow regions created by the vortices which would tend to either increase or decrease the skin friction. Downstream of the devices, the flow returns to an overall healthier (lower shape factor), spanwise-homogeneous state.

This IBL interpretation of vortex-aided separation control gives a theoretical perspective to the empirically proven hypothesis of Schubauer and Spangenberg (1960), that the effect of vortex generators on a flow, is equivalent to a reduction in the streamwise pressure gradient. Other interpretations of the VG effect come in the form of the entrainment concept and added momentum. However, the dissipation perspective discussed above, in line with experimental observations, is a convenient and apparently consistent way of treating the VG effect in an integral boundary layer approach.

2.3.2. Applications

Sullivan (1984) documented pioneering wind turbine field experiments with VGs in the 1980s with the stall-regulated MOD-2 turbine, followed by the Elkraft[1] (Antoniou et al., 1996) and AWT-26 machines (Griffin, 1996). These experiments revealed AEP gains of 4 – 10%, but at the cost of moderately higher dynamic loads. A co-rotating (CoR) array with Delta-shaped (DA) vanes was chosen for the field tests, but counter-rotating (CtR) VGs performed equally well in the wind tunnel

[1] Elkraft operated the world's first offshore wind farm, Vindeby, which began producing power in 1991. Elkraft was later acquired by DONG energy, which was in turn rebranded in 2017 as Ørsted, signalling a shift towards renewable energy. Incidentally, 2017 also saw the final decommissioning of the Vindeby wind park, after 25 years of operation.

tests. Moreover, these early studies demonstrated that VGs could be used to mitigate roughness-induced performance degradation, a useful 'band-aid' for field turbines subject to weathering.

In 2D airfoil wind tunnel tests with and without flow control, Timmer and van Rooij (1993), Griffin (1996) and more recently, Manolesos and Voutsinas (2015), observed sharper stall onset with VGs, suggesting a more vigorous stall mechanism with VGs. Manolesos and Voutsinas (2015) further observed a lift bifurcation with VGs operating at maximum lift, prior to stall. These effects are likely the results of three dimensional separation. Gould (1956) identified that the junction between two surfaces could compromise the effectiveness of the flow control strategy. In their case, it was the wing/fuselage junction, but observations can be extended to wind tunnel mounted wing sections. They recommended that the primary array, together with a series of side VGs, should be configured to encourage downwash in the corner formed between the two bodies. The results and methodology of this early work appear to have gone relatively unnoticed throughout years.

In other works, direct indicators of control efficacy are the skin friction (Godard and Stanislas, 2006), boundary layer shape factor (Ashill et al., 2005; Lögdberg et al., 2009), backflow coefficient (Lögdberg et al., 2010), and global force measurements of lift and drag (Manolesos and Voutsinas, 2015; Fouatih et al., 2016). Lin (2002) and Ashill et al. (2005) demonstrated the effectiveness of submerged ($h/\delta < 1$) vortex generators which introduce lower device drag compared to conventional VGs. Godard and Stanislas (2006) optimised a submerged VG array for separation prevention in a wind tunnel test section with a tailored APG, and evaluated effectiveness in terms of the increase in skin friction. In this sense, the optimal array consisted of CtR Delta vanes, with vane angles of $\pm 18°$ and $h/\delta = 0.37$. The performance proved insensitive to the vane length for $L > 3h$. Low-profile VGs were spurred on by the potential in-flight parasitic drag reduction for aircraft. Authors have stressed the lower tolerance of submerged devices to changing flow conditions, which casts doubt over the suitability of submerged VGs for wind turbines.

Quantitative flow-visualisation is also a popular and generally straight-forward way of gaining general flow insight. Of particular application to vortex generator performance assessment are smoke, oil and tuft visualisation, examples of which are shown in Figure 2.4 for various applications. Generally speaking, these are utilised to provide quantitative information regarding the flow state. However, qualitative information can often also be synthesized from such measurements. One such example is the smoke visualisation shown in Figure 2.4(a) performed by Lögdberg et al. (2009). According to the authors, smoke is concentrated on the upwash side of the vortices, leaving dark bands in the adjacent regions. Babinsky et al. (2009) describe oil traces behind a micro-ramp in terms of expected transverse-shear distribution and the presence of primary and secondary vortical structures. A typical cross-shear signature of two counter-rotating vortex pairs is shown in Figure 2.5.

Quantitative flow visualisation has recently been demonstrated on field turbines.

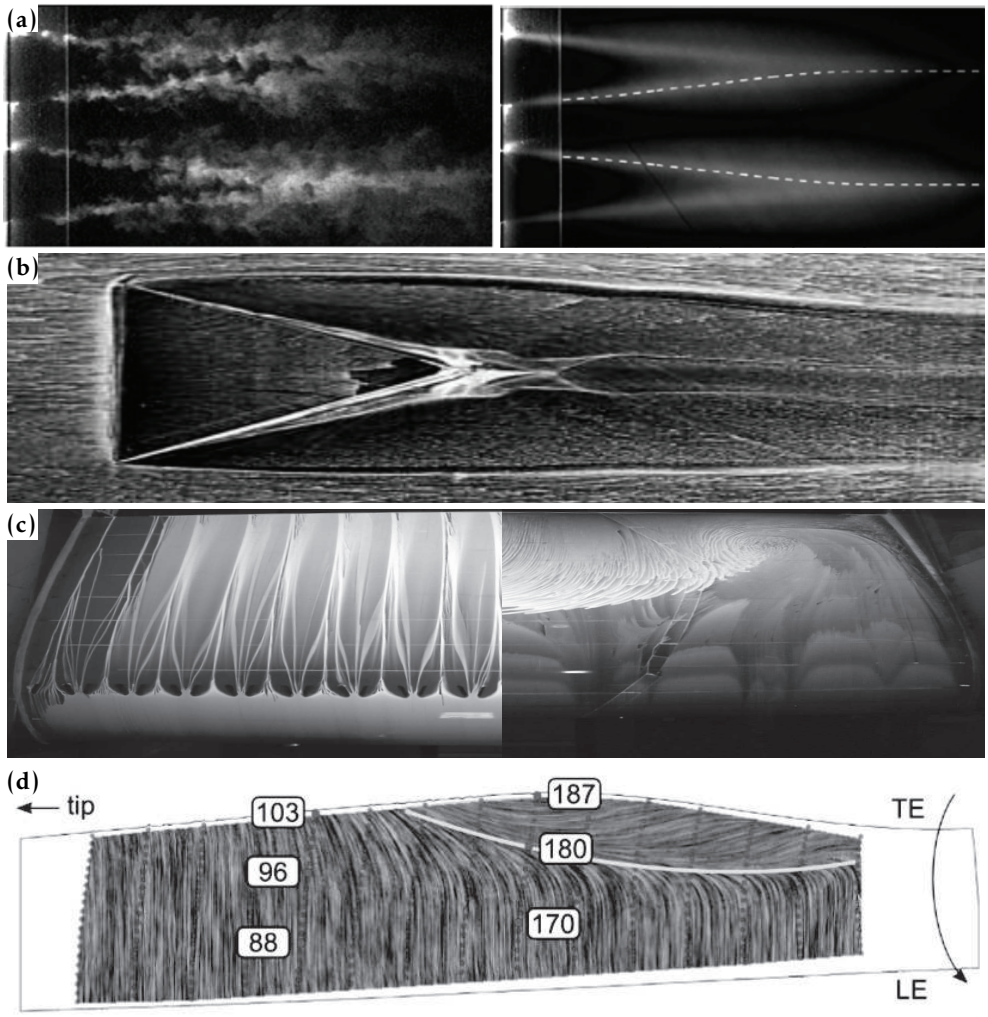

Figure 2.4: Flow visualisations: (a) smoke traces of developing streamwise vortices along a flat plate - (*left*) instantaneous snapshot and (*right*) ensemble averaged image (Lögdberg et al., 2009); (b) oil flow visualisation of a micro-ramp wake on a flat plate (Babinsky et al., 2009); (c) oil flow visualisation of airfoil flow with (*left*) VG-controlled attached flow, in contrast with (*right*) uncontrolled and partially separated flow (Chapter 5); (d) synthesized tuft visualisation of the root section of a rotating wind turbine blade (Vey et al., 2014).

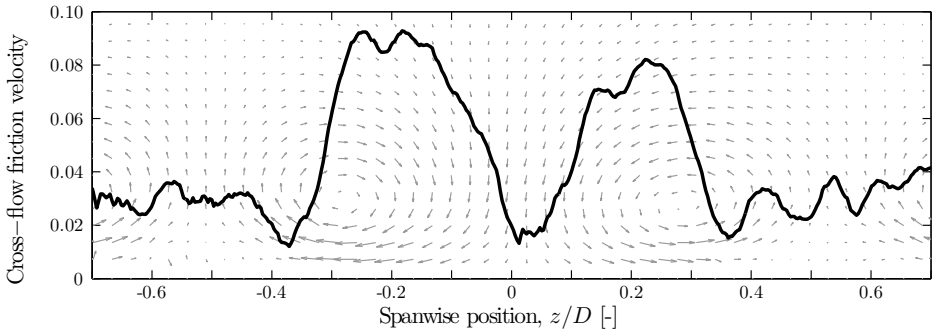

Figure 2.5: Cross-flow wall shear velocity superposed on a background vector plot of a counter-rotating vortex array (common downwash).

This can for instance assist with flow model validation, and in facilitating placement of VGs on wind turbine blades. The technique involves studying the mean separated regions using tuft visualisation, extracting the mean separation line (Vey et al., 2014). The VGs can then be located on the blades relative to this mean line.

2.4. Design concepts

Vortex generator geometry may be parametrised by a number of variables classified under (*i*) vane geometry, and (*ii*) array configuration, as shown in Figure 2.6. These are mainly the

- chordwise position of the VGs x_{VG}/c,
- the height of the VG h,
- aspect ratio (AR) h/L,
- inclination angle β, and
- the intra- and inter-spacing of the VG vanes and pairs (d, D).

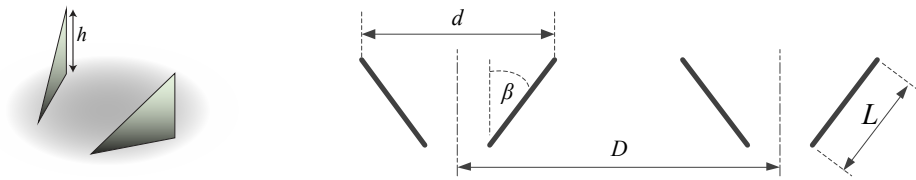

Figure 2.6: Views and nomenclature of a periodic vortex generator array arrangement.

Vortex generators smaller than the boundary layer thickness have been referred to as low-profile, embedded, submerged, sub-boundary layer and micro-VGs. Essentially, all refer to devices whose tips are smaller than the height of the impinging boundary layer. The importance of this emphasis may not be immediately apparent. However, conventionally, vortex generator heights were at least in the order of the boundary layer thickness and in fact, often much larger (Gould, 1956). Because of the initial pioneering work and limited operational know-how, a simple safety measure was to oversize the devices. This appeared to work, at least for separation and buffet control applications, and is still a common practice in wind turbine rotor blade design.

The vortex system produced by a vortex generator vane is primarily described by the vortex strength (Γ), trajectory, and decay rate - all of which have been used by some authors to indirectly assess the effectiveness of VG designs (Jones, 1955; Pearcey, 1961). Jones (1955) and Gould (1956), independently treated the VG flow from a theoretical standpoint for the first time. Jones modelled counter-rotating vortex arrays in wall-proximity using periodic point vortices, and derived a closed form solution for the vortex trajectories. Analysis showed that in-plane vortex kinematics are independent of the vortex strength, whereas the streamwise evolution varied in direct proportion to it. Experimental measurements on flat plate boundary layers have shown good agreement with Jones' model (1955), and even extended its use to account for vortex decay (Lögdberg et al., 2009). Moreover, Hoerner and Borst (1985) showed that the vortex trajectory was relatively insensitive to light compressibility effects ($M < 0.75$), but the vortex strength increased in direct proportion, and the decay rate worsened slightly, indicating possibly competing effects. Considering that modern wind turbines are only just pushing the $M = 0.3$ boundary, no significant compressibility effects are expected.

Gould (1956) also derived a metric by which to evaluate the effectiveness of different VG designs. This quantity assessed the flux of streamwise momentum in the wall-normal direction, taking into account the image vortices, array spacing, the effect of diffusion as well as the vortex trajectories. Field tests on a transonic aircraft showed qualitative agreement with theory. Design recommendations were provided, placing an optimal pair spacing at $6h$ with $D/d = 3$, with incidences in the range of $15° - 20°$. A counter-rotating (common downwash) configuration was recommended for incipient separation within $15h$ of the VGs. These design criteria come remarkably close to those proposed by Godard and Stanislas (2006) some 50 years later through experimentation.

These models inspired Pearcey's (1961) detailed discussion of a VG design methodology, proposing optimisation objectives that maximise (*i*) the vortex near-wall residence time and/or circulation per unit span, or (*ii*) the lift gain achievable. The first determines the array effectiveness, in other words, the extent of the back-flow region which can be controlled. The second pertains to the array efficiency. For example, counter-rotating VGs with common upwash (CU) proved ineffective compared to a common downwash (CD) arrangement because of premature vortex

ejection, i.e. low near-wall residence time (Pearcey, 1961). Furthermore, Pearcey (1961) noted that CtR VG arrays were more complex to optimise due to the higher degrees of freedom, compared with co-rotating arrays, but may be better suited for separation elimination. However, co-rotating and wing-type generators were better suited to environments where "the local flow direction is either not known, or subject to change." Lögdberg et al. (2010) also distinguished these two design objectives, and in a meticulous boundary layer study on VG system robustness, further demonstrated that a system optimised for efficiency is not necessarily the most robust. This was evident from the sharp response in the shape factor around separation to small changes in the vortex strength.

Lin (2002) described vane shape variants, including rectangular, triangular and trapezoidal profiles. The latter two are commonly referred to as Delta (DA) and cropped-Delta (CDA) profiles. These devices were the preferred choice in low speed applications for separation control on aircraft wings (Lin, 2002). Triangular and rectangular vanes produce vortices of similar strength, but the latter incurs unnecessary parasitic drag. Many of these concepts were foreshadowed by Schubauer and Spangenberg (1960), as shown in Figure 2.7.

Lögdberg et al. (2010) posed an important question: whether it was the local vortex strength encountered at a certain position downstream of the VGs (and presumably close to the separation point), or the initial vortex strength generated, that was more important for separation control. They concluded that for a certain range (and having satisfied a minimum strength to prevent separation), the shape factor is insensitive to the position at which the vortex is generated. That is, for the same initial vortex strength, the exact upstream generation point was not as critical. This indicates that what matters is the total VG-added flux, and not the exact magnitude of the strength and decay.

2.5. Vortex structure

As is classified in Bradshaw (1987), vortical flows may be loosely classified as isolated-, junction- and embedded-flows and all appear to some extent in a wide variety of engineering and industrial settings. Much has been done with the understanding of isolated vortices such as the wing tip and Delta wing vortex in unbounded flow. In this sense, unbounded refers to vortices which are many times their core radius from a solid boundary. Most of these are motivated by questions of vortex stability and lifetime - for instance, schedule aircraft takeoff intervals. However, embedded vortices presented new practical challenges.

With hot-wire boundary layer measurements, Westphal et al. (1987) showed that, fundamentally, the effect of an adverse pressure gradient on embedded (near the wall) vortices was to accelerate core diffusion and intensify vortex interaction. Additionally, Pauley and Eaton (1988) measured stronger decay with closer and stronger vortices for VG pairs, and Wendt et al. (1993) for VG arrays. In a later study, Wendt (2004) further characterised the vortex circulation and flow topology for

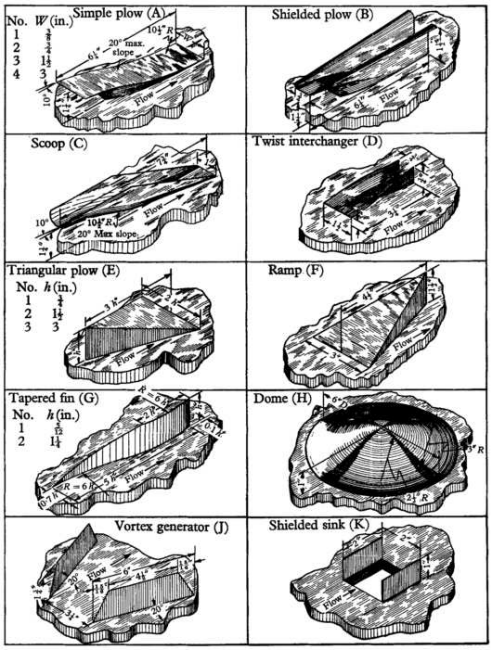

Figure 2.7: Typical passive vortex generator designs (Schubauer and Spangenberg, 1960).

different rectangular, aerodynamically profiled VGs. The vortex strength increased linearly with the vane angle for $\beta \leq 20°$. Similar trends were seen for the normalised vane height (h/δ), as well as the vane aspect ratio (L/h). Furthermore, Angele and Muhammad-Klingmann (2005) and Lögdberg et al. (2010) showed for different VG pairs and arrays that Γ, varied in proportion to hu_{VG}, where u_{VG} is the streamwise velocity at the VG tip. This relation was previously assumed from thin-airfoil theory and deployed in numerous VG models (e.g. Jones, 1955; Ashill et al., 2005; Nikolaou et al., 2005).

In certain flow configurations however, Velte et al. (2016) showed that the appearance of secondary structures (which include the horseshoe vortex), bleed vorticity from the primary vortex, modifying the characteristic variation of the strength with u_{VG}. The appearance of these structures, the organisation of which is shown in Figure 2.8, depends on the geometric vane angle, as well as the relative height of the device and the Reynolds number.

Authors throughout the years have loosely referred to the pathlines around VGs as helical. For example, Pearcey (1961) referred to "fluid particles with high momentum in the stream direction [that] are swept in along helical paths towards the surface [...]." However, helicity implies a strict relationship between the vortex tangential and axial velocity distribution. Only recently was this proven by Velte et al. (2008) in the case of rectangular, Delta and cropped-Delta vortex generators, sized to the local boundary layer thickness. A Batchelor vortex model (or q-vortex)

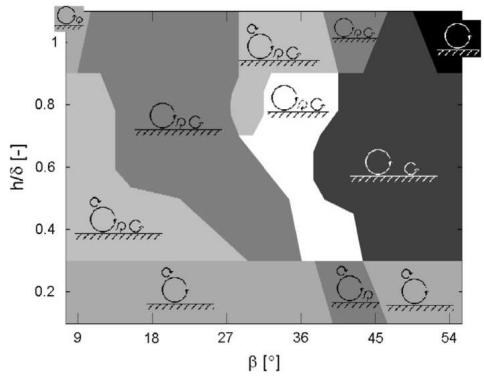

Figure 2.8: Secondary flow regimes mapped in $(h/\delta,\beta)$-space, detected behind a single rectangular vortex generator vane for $\mathrm{Re}_\delta = 1670$ (Velte et al., 2016).

was proposed and also shown to possess streamwise self-similarity up to $50h$ downstream the device trailing edges (Velte, 2013). With this model, the shed vorticity lines are described using a helical path of pitch l, providing

$$u(r,\theta,x) = u_0 - u_\theta(r,\theta,x)\frac{r}{l(\theta,x)}. \tag{2.6}$$

where the axial velocity u is given in a vortex-centred cylindrical reference frame which peaks at the centroid to u_0, and as a function of the in-plane velocity u_θ. The vortex-collocated velocity field was directly extracted from a PIV-measured flow field, after establishing a polar coordinate system over the local vortex core. The swirling centre experiences an axial flow u_0. The right-hand side of the helicity relation is fit to the measured axial profile by tuning the helical pitch l. An overview of other vortex models and their evolution is given in Table 2.3.

Note here the parallels between vortex generators and a wind turbine wake, orders of magnitude apart, expressed in Figure 2.9. Studies have demonstrated and utilised a helical vortex model for investigating the structure and instabilities of rotor wakes (Okulov and Sorensen, 2004; Okulov, 2004). In this context, wind turbines can be thought of as large passive vortex generators. Some of the concepts discussed with respect to vortex generator design may also be applied to wind turbine wakes. For instance, exploring passive wake steering: the grouping of rotors configured for counter-rotation within farms with a common upwash between the rotors, to use vortex generator terminology. This would exploit the swirl in the wakes to cause mutual wake ejection away from the rotor axes, minimising the impact on downstream turbines.

Westphal et al. (1987) investigated a single vortex developing in a non-separating turbulent boundary layer. Vortex characteristics were studied, subject to zero and adverse pressure gradients. Core growth was observed, accompanied by peak

Table 2.3: Analytical and semi-empirical models describing vortex core and evolution of properties

Model	Description	Investigator(s)
$u_\theta = \frac{\Gamma}{2\pi r}\left[1-\exp\left(-\frac{r^2}{\epsilon^2}\right)\right]$ $u_x = u_0 - \frac{r}{l}u_\theta$	Helical Batchelor vortex model	Velte et al. (2008)
$u_\theta = \frac{\Gamma}{2\pi r}\left[1-\exp\left(-\frac{r^2}{\epsilon^2}\right)\right]$	Simple Batchelor vortex model	Various
$\Gamma = 2\chi h u_{VG}$	Vortex strength	Angele and Muhammad-Klingmann (2005)
$\gamma = 2\chi\frac{hu_{VG}}{D}$	Vortex strength per unit span	Lögdberg et al. (2010)
$\frac{\Gamma(x)}{u_\tau h} = f\left(h^+, \frac{x-x_t}{h}\right)$ $\frac{\Gamma_5(x)}{u_\tau h} = f\left(h_e^+\right)$	Vortex strength functional dependency	Various [see reviews: Lin (2002) Ashill et al. (2005)]
$\frac{d\Gamma}{dx} = -KC_f\frac{\Gamma}{h}$	Decay of vortex strength	Ashill et al. (2005)

vorticity decay. An initially symmetric, circular core became increasingly elliptic, elongated in the spanwise direction. This was particularly discernible as the ratio of the core radius to wall-normal centre position plateaued at 0.5, approximately $60h$ downstream the device trailing edge. All these trends were accentuated in the presence of the APG.

Strong pressure gradients may also lead to vortex breakdown, as discussed in the extensive review by Escudier (1988). Of relevance to VG flows is the work by Velte et al. (2011), in which atypical vortex transition over a bump behind a vortex generator array was observed. Even though this was observed at a rather low Reynolds number, it has relevance for understanding the roles of vortex decay and breakdown, as well as possible limits to the operating envelope of VGs in field applications.

2.6. Unsteady vortex dynamics

Apart from the inviscid vortex dynamics that have been discussed thus far, vortex *meander* (or *wander*) is an additional phenomenon that has received quite some attention for free vortex flows. Meandering also arises behind bluff body (Gentile et al., 2016), wind turbine (España et al., 2011) and helicopter wakes (Kindler et al., 2011). In the latter, because of the self-similar spiral structure of the wake,

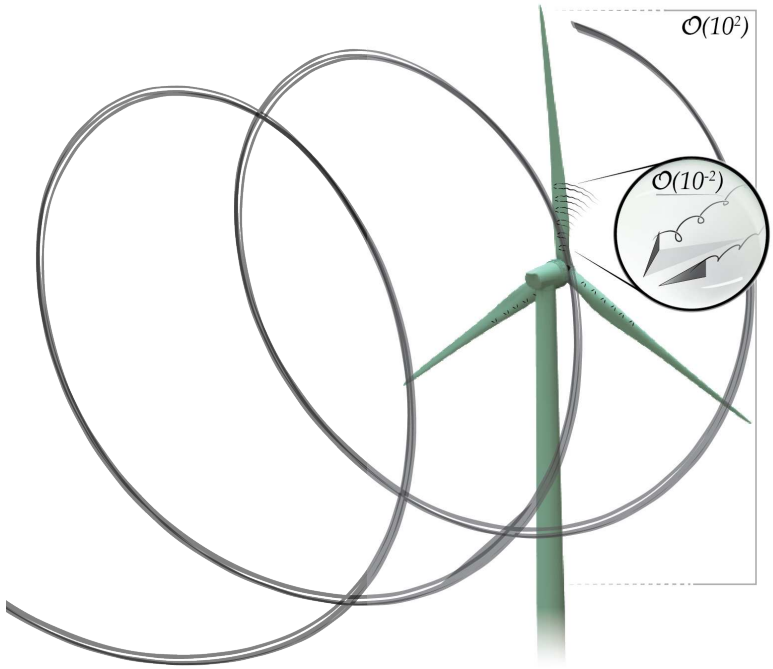

Figure 2.9: Vortex wakes: separation of scales.

meandering is often referred to as an *aperiodic* vortex motion.

2.6.1. Relevance

In 1989, Westphal and Mehta (1989) noted that *"if such a* [meandering] *motion occurs, it would also contribute to the measured Reynolds stresses and therefore confound attempts to model the turbulence in calculation methods."* This perfectly captures the necessity to understand vortex meandering, not simply from the point of physical causation, but because of implications on modelling and system design.

Jacquin et al. (2003) indicated that meandering may arise due to

- external turbulence in the freestream flow,
- wall-bounded turbulence and shear layer instabilities, and
- the vortex shedding process itself.

The first two have received considerable attention, particularly from the aeronautical engineering field. Whilst the vortices are considered quasi-stationary, there is little doubt that the vortex shedding process itself is an unsteady one, with the possibility of countless secondary flows originating at the device, as discussed in the previous section.

The implications of vortex meander on flow control efficacy are not well understood. This is partly because the numerous VG design variables can independently influence different elements of the generated vortex. Thus, it is difficult to isolate the effect of meandering on the control ability. Therefore, the majority of studies merely acknowledge its likely presence and offer some insights with regards to the vortex characteristics. A notable exception is the forced meander experiment performed by Westphal and Mehta (1989), discussed in the following section.

The cause of meandering remains an open question (Edstrand et al., 2016), and the purpose of this section is not to review the possible causes, but rather to present observations of unsteady vortex dynamics in the context of VG flows.

2.6.2. Vortex dynamics in the context of VGs

Streamwise vortices evolving in a wall-bounded flow which experience disturbances in the spanwise and wall-normal directions ought to raise levels of $\overline{v'v'}$ and $\overline{w'w'}$. However, Westphal et al. (1987) proposed evidence for a counter argument. Prior experiments on embedded streamwise vortices showed ellipticity in the vorticity contours, assembled from a series of hot-wire measurements. They tested the hypothesis that this could arise due to non-negligible vortex meandering. The authors concluded that meandering was not responsible for the observed vortex-smearing. For example, oil film measurements of skin friction displayed sharply defined peaks. Meandering would tend to smear or smoothen such a profile. Wall-normal fluctuations were later shown to be lower than the spanwise ones, although inspection of $\overline{v'v'}$ would have given a more reliable indicator of meandering. It was therefore postulated that the limited space for vortex growth within the boundary layer was a more likely cause of the elliptical distortion of the core. Pauley and Eaton (1988) corroborated this by similar observations on common downwash vortex pairs. The authors also investigated common upwash pairs and noted vertical elongation as the vortices moved away from the wall and approached each other. Therefore, horizontal elongation due to the mirror vortex was according to the authors a more likely explanation, based on their own findings with the interaction of real counter-rotating vortices.

To further examine the possible symptoms of vortex meandering, Westphal and Mehta (1989) investigated the same configuration in the same facilities, this time laterally oscillating the VG vane with a low frequency of 1Hz. Though the authors chose a low frequency to avoid shedding of smaller scale structures, the latter could not be verified in their measurements. Nonetheless, the bulk lateral range of motion of this embedded Delta vane vortex, was on the order of the vortex diameter. The results showed flatter mean vorticity contours (or conversely, elongated in the lateral direction) with 40% lower peak vorticity. Most notably, the wall-normal and streamwise normal stresses increased in the forced core region. The magnitudes of $\overline{u'v'}$ and $\overline{u'w'}$ which dominate the turbulence production process, were largely unchanged, the effect of forcing mainly being a redistribution. The authors proposed that only for values of $|\omega_x|\sigma_z/U_\infty > \mathcal{O}(0.1)$ will vortex meander

significantly affect mean and apparent turbulent quantities of the measured flow. The physical interpretation of this metric is a lateral forcing velocity arising from the meander of a coherent streamwise vortex, hence the appearance of both the vorticity and the deviation in the lateral vortex position. Although the peak vorticity did decrease downstream, the amplitude of a natural meander in a boundary layer can be expected to increase (Bushnell, 1984). Thus application of this metric to this experiment is dubious, as is the inherent assumption of negligible wall-normal meandering motions. Nevertheless, the authors conclude that, since lateral forcing only just produced perceptible changes, natural meander of a coherent vortex in a boundary layer cannot be responsible for observed flattening in vortex cores, and will not generate appreciable apparent stresses.

Mehta and Bradshaw (1988) investigated a vortex pair in a common upwash configuration. Despite observing elevated levels of $\overline{v'}$ and $\overline{w'}$ fluctuations in the vortex core, their sharp maxima were interpreted as an absence of vortex meandering. A similar deduction was made from sharp spanwise skin friction signatures, observed prior by Westphal et al. (1987) for a single vortex. Low levels of $\overline{u'}$ were also interpreted as such - higher levels would be expected from a meandering vortex with an axial velocity deficit and thus, high $\partial u/\partial z$ at the core. However, the VGs were in this case acting in the wind tunnel settling chamber, and favourable pressure gradients have a stabilising effect on streamwise vortices. Thus the observations are not particularly representative or indeed straightforward.

As indicated in the discussion of prior work thus far, point-wise measurements did not allow direct extraction of vortical structures. Hence, vortex meandering could only be postulated through circumstantial evidence, resulting in discrepancies over its interpretation in literature. This prompted Baker et al. (1974) and Devenport et al. (1996) to treat the effect of vortex meandering theoretically. In Devenport's analysis, it was shown mathematically that all vortex shapes tend to smear towards a q-vortex under the influence of Gaussian meandering. In fact it was posed that the common observation of a Gaussian vortex velocity distribution about the core might in fact be due to the omnipresence of vortex meandering. At least, in the case of Devenport et al. (1996), an otherwise laminar wingtip vortex showed strong levels of turbulence, which were largely due to the effects of meandering. These relations provided a means to correct point-wise measurements using fixed probes and have mostly been validated at later stages with more advanced flow measurements techniques (Heyes et al., 2004). The advent and continued development of PIV has enabled spatial and temporal resolution of fluid flows. It thus became possible to directly resolve and track vortices in space (and time) and has become an important tool in the fundamental study of vortices (Shah et al., 1999) and turbulence (see e.g. Elsinga et al., 2012).

Some of the first ever Stereo PIV measurements behind counter-rotating VG arrays were performed by Angele and Muhammad-Klingmann (2005). The VGs in their setup were used to control a turbulent separation bubble in a strong APG. In follow up work, the authors used local vortex identification methods to demon-

strate a clear variation of the instantaneous vortex centroids (Angele and Grewe, 2007). Spanwise motions were of the order of the vortex core size, and larger than excursions in the wall-normal direction, as shown in Figure 2.10. Instantaneously, the primary vortices were more concentrated (smaller, having higher streamwise vorticity), compared to the vortices extracted from the mean flow. Thus, the vortex movement tends to produce larger and weaker mean structures. Higher wall-normal velocity fluctuations appeared to corroborate the larger spanwise movements detected, and peaking in-plane shear stress at the average vortex position suggested the existence of apparent stresses induced by meandering contributions. The authors also hypothesized that although turbulent fluctuations of the vortex cores is largely random and isotropic, the ensuing inviscid interactions are not, giving rise to anisotropic (in the spanwise and wall-normal directions) and possibly skewed instantaneous distributions. However, evidence of the latter was not provided.

Cathalifaud et al. (2009) further analysed the configuration of Godard and Stanislas (2006) in a non-separating APG imposed with a fixed ramp. This included a comparison of passive VG vanes and active jets, in an attempt to characterise differences. They observed that the turbulent kinetic energy was concentrated in the upwash region as the primary vortices developed. As they do so, the mean primary vortex structure becomes more diffuse, weaker in intensity and mixed in with the surrounding boundary layer turbulence. After $20h$, the coherent structures become individually undetectable, even though their global effect persists. The authors statistically characterised the instantaneous distribution of streamwise vortices. For active jets, they showed that numerous smaller, more concentrated streamwise vortices lead to a mean flow field containing distinct primary vortices. A similar statement for the passive vanes could not be emphasized as strongly since the data analysed was collected at a location where the vortices were of the order of streamwise structures in the uncontrolled boundary layer.

The notion that passive vanes might in fact generate multiple like-signed streamwise vortices contrasts with the long-held idea of single, persistent primary vortices. Such a possibility may help shed light on the observed performance differences between different vane shapes, which have thus far, eluded sound physical reasoning. Recent work has hinted at the relevance of these dynamics through subtle changes to the typical right-delta VG vane design. Such modifications include streamlining the vane plates (Hansen et al., 2016) and more complex modifications such as 'vortex-nests' and rounded edges (Siemens Wind Power, 2014). Such changes are proposed with the primary goal of mitigating device drag and self-noise by discouraging secondary structures and smaller scale vortex shedding. However, secondary structures and small scale shedding may in fact be an essential part of the mechanism of streamwise vortex flow control.

Gardarin et al. (2008) investigated submerged VGs in a boundary layer tunnel, with a physical ramp to promote local separation. These authors proposed optimising VG layouts for separation control by maximising the vortex lifetime, which in turn depends on managing cooperative instabilities. Measurements of

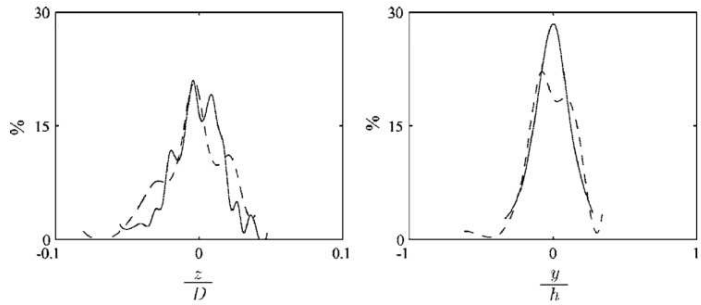

Figure 2.10: Spanwise (*left*) and wall-normal (*right*) vortex core distribution of the individual vortices (solid lines) and the pair separation (dashed) (Angele and Grewe, 2007).

$\overline{u'w'}$ were qualitatively likened to the expected fluctuations of a free vortex with bi-normal Gaussian meandering. The authors suggest this occurs due to straining by the image vortex, which, together with energetic perturbations in the turbulent boundary layer, can trigger short wave cooperative instabilities. The authors propose VG design criteria which maximise vortex lifetime, by delaying the onset of this instability. These arguments are based on an expression for the vortex lifetime of the form $X/\delta \propto U_h A/\tau$, where A is the critical amplification ratio ($A = 6$ for the onset of cooperative instabilities). The remaining parameters are indirectly linked to h/δ, the vortex strength Γ, as well as the vortex array arrangement, which determines the inviscid shear rate τ. The model appears to produce VG designs typically found in experiments and applications. However, difficulties remain due to the complexity of determining the separation location, which in turn influences the number of spanwise devices required to effectively eliminate pockets of separation. Additional factors of practical importance such as the pressure gradient are not considered, but the work demonstrates a useful approach for the optimisation of passive, vortex-driven flow control devices.

Using SPIV, Beresh et al. (2010) investigated the source of a low-frequency meander and turbulence structure (Beresh et al., 2012) of a fin-trailing vortex in a transonic boundary layer. In contrast to the cases considered thus far, the fin was 2.5 times the boundary layer thickness. Instantaneous vortices were mapped and statistical analysis of the positions showed that meander increased downstream (measured until $8h$) but decreased with vortex strength (i.e. geometric inflow angle). The typical spanwise meander amplitude was approximately $0.05h$ and only slightly lower in the wall-normal direction - the difference practically disappearing with increasing vortex strength and/or downstream position. In combination with low-profile wedge-type VGs upstream of the fin, it was shown how energising the boundary layer increased the typical meandering motions by 40%. After meandering corrections (see Figure 2.11), the mean vortex velocities did not display significant sensitivity to meandering, despite evident variations in the vortex position. In contrast, high levels of artificial turbulence were measured in the vortex

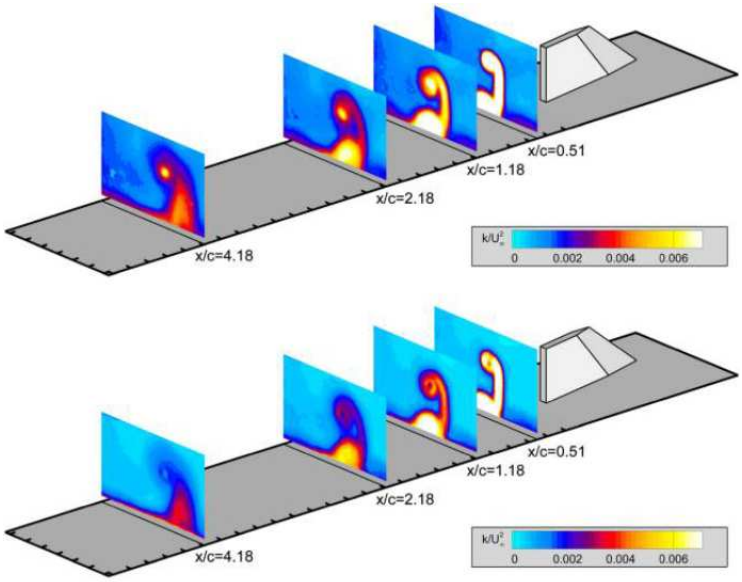

Figure 2.11: Turbulent kinetic energy behind a wall mounted fin before (*top*) and after (*bottom*) meandering correction (Beresh et al., 2012)

core. The authors deduced that fluctuations of the vortex shape and strength must therefore dominate over positional variations, which they deduced by reinterpreting the Reynolds stress distributions in cylindrical coordinates.

Unable to pinpoint a single dominant source of meandering, Beresh et al. (2010) highlight the importance of wall- and freestream turbulence as well as the shear layer of the device itself. The latter, with bound vorticity predominantly normal to the primary vorticity, is itself a source of turbulence and instability for the primary vortex. Relevant evidence is found in measurements and visualisations of a Delta wing in free flight in the early works of Sarpkaya and Henderson Jr. (1985), Miller and Williamson (1995), and for a half Delta wing at high angle of attack in Shah et al. (1999). The near-wake was evidently characterised by strong streamwise vortices rolling up over the wing edge. However, coherent spanwise rollers, referred to as 'strakes' or 'striations' were also observed shedding from the wing trailing edge at low to moderate Reynolds numbers. Visualisations showed that this detaching boundary layer is highly unstable aft of the wing. Ultimately, far-wake observations did clearly show interaction of the primary streamwise vortices and this secondary vorticity.

For the case of the wall-mounted fin, Beresh et al. (2009) showed this lateral vorticity (and hence turbulence) component originating in part at a corner separation zone (secondary vortex) at the fin/wall junction . The strength of this corner vortex was much lower than the primary fin vortex, and was presumably unrelated to the

horseshoe vortex system. This type of junction flow is more commonly observed at the end-walls on wings (Manolesos et al., 2014) and compressor cascades (Yu et al., 2013) and forms due to the interaction of the wall and body boundary layers. In these cases, the wing/blade aspect ratio is typically greater than 1.5. Therefore the observed corner vortex in the fin studies is rather surprising given an aspect ratio of 0.5, similar to that found in common VGs. This suggests that local phenomena may also be present on VG vanes. Certainly, it indicates that subtle design changes may have an important impact on the formation, turbulence structure and thus lifetime of generated vortices. Other parameters of importance are probably the vane angle β, h/δ as well as the vane profile. Overall however, for typical VG geometries, the generated streamwise vortices exist within the turbulent boundary layer for an appreciable portion of the operating envelope. Therefore, surrounding boundary layer turbulence is likely an important source of vortex meander, the vortex acting as a passive tracer subject to turbulent fluctuations.

In principle, increased vortex interaction increases diffusion and loss of control effect. On the other hand, vortex meander effectively redirects the wall-normal streamwise-momentum flux, sweeping a larger portion of the underlying surface compared to stationary vortices. This could prove beneficial for shifting separation zones. All in all, whether vortex meander is intrinsically beneficial for flow separation control remains to be seen.

2.7. Modelling

Numerous techniques for modelling vortex generators flows have been explored in literature, most of which are CFD-based. The most direct and intuitive approach is to model the effect of VGs by including them as a local geometrical protrusion in the domain. This approach requires a fully three-dimensional treatment and a dense grid due to the complexity of the flow and the small size of the devices (see e.g. Nikolaou et al., 2005; Jirasek, 2005; Stillfried et al., 2011).

2.7.1. Computational Fluid Dynamics

In 1999, Bender et al. (1999) developed a simplified technique in which the effect of VGs was modelled without including the geometry explicitly in the computational mesh. This approach is now commonly known as the BAY model. The method relies on the addition of a side force as a source term in the momentum equation. This essentially introduces swirl into the flow, giving rise to the formation of vortices produced by the VGs. Jirasek (2005) suggested further improvements to the original model. More recently, Florentie et al. (2018) and Manolesos et al. (2018) found that the direct body force representation of the jBAY approach does not necessarily result in the highest accuracy, compared to a body resolving mesh in the way the modelled VG body forces.

Besides adding a source term based on a lateral lift force, other researchers constructed source terms based on a specific circulation, or on the velocity induced

by this circulation according to the Biot-Savart law. This method is referred to as a vortex-source model. Research based on this method is found in the spanwise averaged CFD method of Nikolaou et al. (2005) and the three-dimensional approach by Zhang et al. (2011). Jirasek (2005) further noted that the key problem of these models is the *a priori* determination of the initial circulation introduced by the VGs. Later Törnblom and Johansson (2007) presented a method in which a Reynolds stress approach is used in a statistical sense. They explicitly introduced the vortex-added velocity and associated stresses to the differential Reynolds stress transport equations to mimic the increased mixing due to the VGs.

In the 1985 paper detailing the mean and turbulent structure of embedded streamwise vortices, Shabaka et al. (1985) noted that the "[...] prediction of the decay of secondary flow is a severe test of a turbulence model." The difficulties of RANS with non-equilibrium vortex flows with axial flow is also partly due to the lack of "vortex cases in their calibration base, which is [instead] dominated by homogeneous turbulence and thin shear flows" (Spalart et al., 2015). Understanding the role of meandering on the vortex structure is thus particularly important in the case of model development and calibration. However, it is also a conceptual inconsistency with linear eddy-viscosity models, which are unable to account for turbulence history effects. These are essential to the correct modelling of non-equilibrium turbulent flows. Measurements in a turbulent trailing vortex attesting to this non-equilibrium nature showed that the Reynolds stresses lagged the mean flow strain field (Chow et al., 1997). The anisotropy associated with it is particularly challenging for RANS models because of the Boussinesq approximation. Such examples as the $k-\epsilon$ and $k-\omega$ linear eddy-viscosity models tend to produce overly-diffusive vortices. Rather than full Reynolds Stress Transport (RST) models, intermediate solutions have been proposed. Rotation and streamline curvature such as those used in Spalart and Shur (1997) are empirical modifications to otherwise linear-eddy viscosity models and, whilst they can typically reproduce the mean flow reasonably well, they tend to do so at the expense of suppressed Reynolds stresses. Another intermediate solution is the lag-RST model (Churchfield and Blaisdell, 2013), which solves a two-variable linear eddy-viscosity in combination with a differential equation describing the lag between the Reynolds stress and the mean flow strain rate tensor.

Although commercial codes increasingly adopt rotation and curvature corrections to circumvent this, the topic stands to benefit from more research.

2.7.2. Reduced Order Modelling

Another class of models could be considered of reduced order, in that they rely more heavily on assumptions and simplifications of flow complexities. Smith (1994) used an asymptotic approach to model the effects of vortex generators on a turbulent boundary layer. The method demonstrates the power of the reduced order model, enabling assessments of subtle VG shape modulations, and more prominent design parameters such as the vane spacing and length. Model predictions were largely in

agreement with reported measurements, however comparisons were not directly shown.

Kerho and Kramer (2003) proposed a method of introducing VG-added mixing into the integral boundary layer code XFOIL. They "enhanced the turbulence production in the turbulent boundary layer formulation by modifying the stress transport formulation". The article suggests a modification of the dissipation coefficient through the shear stress coefficient by introducing a step input, which decreases exponentially downstream of this location. This is roughly analogous to the statistical approach of Törnblom and Johansson (2007), but applied to a two-dimensional integral boundary layer method. Thus, an obvious limitation of this approach is that, the fully three-dimensional flow field induced by an array of vortex generators, is represented in a two-dimensional formulation. Hence, the modified dissipation will not have a direct connection to the three dimensional dissipation distribution in the boundary layer, but will be a representative spanwise averaged quantity amounting to the same global effect.

2.7.3. Applications

Many modelling attempts consider canonical and simplified flows. More realistic applications of VGs on wings for instance, have also been examined using CFD techniques. However, applied parametric studies of airfoils equipped with VGs are uncommon. Some examples are reviewed here.

Fouatih et al. (2016) recently conducted a parametric study on a slender 15% thick NACA4415 airfoil with Delta vane devices at a chord-based Reynolds number $\mathrm{Re}_c = 2{\times}10^5$. The authors observed low sensitivity to the VG packing density (d and D). Optimum vane angles (in terms of maximum C_l/C_d) were in the range of $\pm 11 - 12°$ for rectangular and Delta vanes. Gao et al. (2015) performed computational fluid dynamic (CFD) simulations on the DU97-W-300 airfoil at $\mathrm{Re}_c = 3 \times 10^6$ with different VG vane lengths, spacing and height, albeit with a rather limited parameter space. The authors hint that stronger vortices do not necessarily benefit flow controllability. Furthermore, an increase in vane length from $2.8 - 3.4h$ was detrimental to performance, whilst increasing vane height from $5 - 6$mm increased lift and $C_{l|\max}$, at the cost of higher drag and reduced airfoil efficiency.

2.8. Synopsis

This chapter has reviewed vortex generator research relevant to the objectives of this thesis. The following summarises the salient points in relation to the research objectives defined in Chapter 1:

I. State of the art in VG modelling

- Models for vortex generators exist in various forms. These most often describe all or part of the flow field associated with the streamwise vortices, and its evolution together with integral vortex properties such as

the vortex strength;

- A second type of model combines the streamwise vortices with an external flow which is solved by numerical treatment of the Navier-Stokes equations in an Eulerian domain. The model in this context pertains to the vortex generation process and is typically a variation of a body-force method;
- Higher fidelity computational approaches do not model, but rather resolve the vortex generation process around the flow control devices, and thus typically requires a more refined computational grid.

High fidelity computations remain computationally expensive and feature only in very specific cases in literature. They are thus not feasible for design iteration. Hence, lower-fidelity BAY-type models have gained popularity with mixed success, although there is some consensus over the robustness of empirical tuning factors. Nonetheless, correct prediction of the vortex evolution and far-wake effect may suffer due to the lower-grid resolution.
In the application of wind turbine and airfoil design, many integrated design methods still rely on integral boundary layer methods due to their speed of computation and relative accuracy. However, there has been limited work to integrate the effect of vortex generators into the IBL approach. In general, there has been a weak transfer of empirical insight to physical models.
Chapter 3 will synthesize various modelling approaches in a benchmark of state-of-the-art methods.

II. Dynamics and evolution of embedded streamwise vortices

- Numerous works have studied the mean and turbulent vortex characteristics. A much smaller portion have dedicated attention to the unsteadiness, or meandering, of the generated vortices in an embedded boundary layer flow. More importantly, this unsteady nature of the streamwise vortices and its effect on measured properties is rarely addressed;
- In the vast majority of cases, these types of experiments consider inflow orthogonal to the device array leading edge, in what we will later term an axial inflow configuration.

The majority of fundamental works study vortices in very controlled conditions, be it on a flat plate or wing with uniform inflow in a wind tunnel, or in the computational domain. Steady vortex dynamics have received much attention for equal strength vortices, but only a few works investigate the extent and implications of mismatched vortex strengths.
Chapter 4 defines skewed inflow in the VG array reference frame, in context of flow control over rotating wind turbine blades. This flow case is considered an important complement to the conventional axial inflow simplifications for assessing VGs.

III. Separation control with vortex generators

- Various works in literature investigate a wide range of vortex generator parameters on wings, ducts or bumps for separation control;
- Limited works have investigated wind-energy specific airfoils, which are characterised by larger thicknesses and thick trailing edges. These works have also mostly been of a computational nature;
- Operational characteristics in the stall regime with VG control have received little attention in reported literature.

A clear view of the effect of VG parameters on airfoil performance is lacking. Moreover, there are signs that the flow three-dimensionality and VG interactions may lead to dynamic load situations, which are as yet, ill-understood. Chapter 5 presents a detailed parametric vortex generator study on a DU97-W-300 airfoil. Following on, Chapter 6 will present an improved IBL method which is based on a source-term modelling approach to provide a VG capable design tool using the Xfoil framework.

3

Benchmarking simulation tools for vortex generator flows

Weathered wood grain akin to co-rotating vortex array streamlines. Hydra Island, Greece.

This chapter details a benchmark and validation of computational tools for predicting the effect of vortex generators on airfoils. DU97-W-300 and NTUA-T18 airfoil measurement campaigns are used as a validation basis. The computational tools span from engineering-level integral boundary layer tools to fully-resolved grid-based computational fluid dynamics codes. The airfoil polars are compared for various vortex generator cases and boundary layer conditions, highlighting major differences and challenges. This chapter appears in (IOP) *Journal of Physics: Conference Series*, 753(2), 2016b.

3.1. Introduction

3.1.1. Background

Modelling of VGs has been an important and recurring research topic. Apart from a few isolated studies employing expensive DNS/LES type calculations (e.g. Liu et al., 1996; Spalart et al., 2015), RANS-based approaches are by far the most common. A popular method of simplifying VG modelling was pioneered by Bender et al. (1999) and extended by Jirasek (2005). Here, the VG was indirectly modelled by introducing a local flow-dependent forcing term to the momentum and energy equations. The side forces generated in this manner are approximated from thin airfoil theory and are mildly dependent on a (geometry-related) calibration coefficient (Bender et al., 1999). This effectively triggers the rollup and development of a streamwise vortex, whilst alleviating the dense grid requirements of fully resolved (FR) geometries. Statistical and analytical models have also been developed (von Stillfried et al., 2012; Velte et al., 2008). Intermediate methods based on the robust integral boundary layer (IBL) method were explored by NASA in 2003, modifying the widely used XFOIL code to incorporate the effect of VGs (Kerho and Kramer, 2003). Engineering approaches are also possible (Mueller-Vahl et al., 2012; Skrzyp-iński et al., 2014); however, since these rely on empirical data, their robustness is determined by how well different parameters are represented in the underlying knowledge base.

3.1.2. Objective and outline

From an engineering design standpoint, parametric exploration is an important aspect for design. Tools therefore must be assessed for their robustness and ability to capture the trends of equipping airfoils with VGs. For this purpose, different RANS- and IBL-based tools are benchmarked and validated against airfoil measurements with and without vortex generators (Manolesos and Prospathopoulos, 2015; Ferreira et al., 2015). The experimental databases, prediction tools, and the vortex generator cases are described in section 3.2. Results and discussion are presented in section 3.3 and section 3.4, concluding with section 3.5.

3.2. Experimental database and numerical tools

The experimental data used for this validation study concerns the Delft-designed 30% thick DU97-W-300 airfoil and an 18% NTUA T18 airfoil. All experimental and numerical data analysed in this chapter were obtained by other collaborators within the AVATAR project. The author's role was to benchmark and analyse these results.

3.2.1. Experimental airfoil data

The DU97-W-300 airfoil model was tested in the Low Turbulence Tunnel at the Delft University of Technology and detailed in Timmer and van Rooij (2003). The

tunnel is a closed-throat, single-return type circuit with a test section measuring 1.80m × 1.25m, and 2.60m long, as detailed in Appendix C. A contraction ratio of 17.8 : 1 between the settling chamber and test section results in a freestream TI below 0.1% at 80m/s. The airfoil model was fitted vertically in the test section onto mechanically actuated turntables on either side, as shown in Figure 3.1a. The model chord length was 0.65m and featured a thick trailing edge of approximately 1.7% chord. The data used for validation was obtained at a chord-based Reynolds number of 2×10^6 (Mach No. = 0.13). Polars were acquired in the freely transitional regime, as well as for forced transition using zig-zag tape on the suction side of the airfoil (11mm wide, 0.35mm thick) at 5% chord.

The NTUA T18 model was tested in the closed-loop wind tunnel at the National Technical University of Athens, at $\mathrm{Re}_c = 0.87 \times 10^6$ and Mach = 0.07 (Manolesos and Voutsinas, 2015). The tunnel has three access areas for conducting tests and in this case, the 1.8m × 1.4m and 3.75m long section was used for the measurements, as shown in Figure 3.1b. The airfoil model had a chord length of 0.60m. Polars and pressure distributions were acquired for a fully turbulent (tripped) flow. This was enforced using zig-zag tape (12mm wide, 0.40mm thick) at 2% chord over the central section of model suction side.

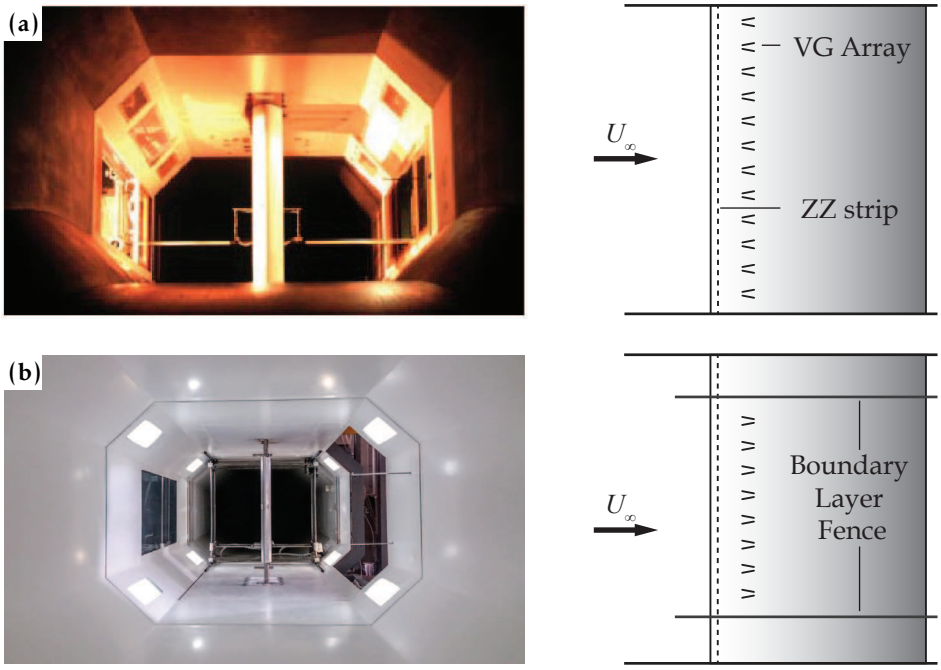

Figure 3.1: Test-section and setup schematic for the (a) DU97-W-300 airfoil (Timmer and van Rooij, 2003) and (b) NTUA T18 airfoil (adapted from Manolesos and Voutsinas (2015)).

For both experiments, the height of the roughness used is considered oversized for minimum tripping requirements at the tested Reynolds numbers (Timmer and van Rooij, 2003; Manolesos et al., 2014). Thus the zig-zag tape not only trips the oncoming laminar boundary layer, but also contributes an inherent parasitic drag by increasing the boundary layer displacement and momentum thickness. The comparison with computations which do not take the physical thickness into account will demonstrate the effect on the polars in the following section. The DU and NTUA airfoils were fitted with counter-rotating, passive vane-type VGs sized to the boundary layer height in common downwash and upwash configuration respectively. The chosen VGs were optimised to produce the highest C_l/C_d. The VG design used on the DU airfoil was based on separation control recommendations by Wentz (1975), effective at the 20% – 30% chord region, and scaled for the 0.65m model. For the NTUA T18 airfoil, a computational parametric study was conducted, results of which are used in the comparisons later on. The simulations were performed on a half-pair strip, exploiting lateral symmetry conditions to assess the impact of the vane and array configuration parameters, based on a common upflow configuration. The vortex generators in both experiments were manufactured from 0.2mm aluminium sheeting and arranged in array configuration, spanning the entire length of the models.

Details of the experimental setups and VG configurations are summarised in Table 3.1.

Experimental measurements and uncertainty

In both setups, the lift was evaluated by summation of the model surface pressures, which were obtained using surface taps located around the model chord in a staggered formation. Profile drag was determined using wake-rake measurements, located downstream of the models, or using the resolved model surface pressures in the separated regime when the wake region became too large and unsteady. The LTT pressure measurements were obtained using optical readings of a liquid tube manometer array, connected to each pressure tap. Pressure measurements of the NTUA T18 airfoil were read using a digital manometer for direct post-processing (see e.g. Manolesos and Voutsinas (2015) for further details of the setup).

In such setups, systematic errors may arise from misalignments (e.g. zero angle offset), bias in pressure measurements, signal drift due to temperature effects, and model manufacturing defects. Interference from adjacent pressure taps is minimised by staggering their spanwise distribution and keeping the orifice diameter small (< 1.0mm). These are minimised through careful design and reliable manufacturing methods.

Random errors are minimised by using high precision equipment. The DU-airfoil pressure measurements were acquired by an optical sensor coupled with a multi-tube liquid manometer. Diurnal variations of atmospheric temperature and pressure have a small influence on the density of the manometer fluid and resulting pressure level. Additionally, aerodynamic heating can raise the liquid

temperature through contact with the bleed air. This can lead to signal drift if unaccounted for, although after some initial start-up period, these factors diminish. Uncertainty in the angle of attack is below 0.01° and the smallest resolution of the manometer is 0.1mm (≈ 1Pa). The error propagation based solely on these factors results in an average uncertainty of ±0.001 for C_p, ±0.005 on C_l and ±0.0003 on C_d. This corresponds to a worst-case 1% error on lift and drag. Flow separation on the surface results in fluctuating wall and wake pressures. In this case multiple readings are taken and averaged. However, the liquid manometer and connective tubing inherently damp out pressure fluctuations, and so to some extent naturally indicate averaged readings and reduce sampling errors. NTUA pressure measurements were acquired through a Furness scanner and read through a manometer and Scanivalve pressure transducer. This set of measurements carries an uncertainty of 0.02° on the angle of attack, ±0.0002 on C_p, ±0.0007 on C_l and ±0.0004 on C_d.

Wind tunnel corrections are an additional source of uncertainty. These are applied to both models and take into account wall and model blockage, as well as streamline curvature. However, in the immediate post stall-regions, wind tunnel airfoil flows are typically characterised by corner separation and stall cell formation, leading to a highly three-dimensional flow structure along the span (Manolesos et al., 2014). Thus the model surface pressures in the post-stall region should be interpreted with caution as they are likely not indicative of the spanwise averaged flow.

The periodic placement of VGs gives rise to spanwise-periodic flow and loading. For the wake-rake drag, the periodicity is addressed by spanwise averaging values taken at different spanwise positions along a VG array wavelength. An equivalent approach is by definition applied to the 3D computations for both drag and lift (see next section). However, experimentally, the true spanwise-averaged lift is not-possible due to the staggering of the pressure taps. Only by repeating measurements with different relative VG array positions to the pressure taps, or balance measurements, can a more indicative value of for the spanwise average lift be obtained.

3.2.2. Numerical tools

All CFD codes are based on finite-volume Navier-Stokes solvers and have been run for an incompressible, steady flow. The uncontrolled cases have been computed in 2D whilst all VG cases were computed on a half-pair strip, imposing spanwise-periodic boundary conditions on the domain side walls. All codes use different, uniquely generated grids which ensure $y^+ < 2$, fully resolving the boundary layer. Except for fully-resolved CFD VG simulations, the vanes are considered zero-thickness. Grid independence is ensured and only the finest grid results are presented here. An overview of the predictive tools is given below and summarised in Table 3.2. Further details about the numerical grids is provided in Appendix A.

DTU computations were performed using the in-house EllipSys RANS solver

Table 3.1: Flow facilities, airfoil models and VG parameter details used for benchmark

Airfoil	Wind Tunnel	Test Section W×H×L	Freestream turbulence intensity	Model pressures	Wing aspect ratio	Model solid blockage
DU97-W-300	Closed loop	1.80m × 1.25m × 2.60m	< 0.1% at 50m/s	102 sensors	1.92	≈ 10% at 16°
NTUA T18	Closed loop	1.80m × 1.40m × 3.75m	0.2%	60 sensors	2.0	≈ 9% at 16°

Airfoil	Thickness t/c [%]	Exp. Data Type[a]	Chordwise position, x_{VG}/c [%]	Shape	Config.	h/δ	Vane Angle, β	Vane chord, L/h	Intra-vane spacing, d/h	Inter-vane spacing, D/h
DU97-W-300	30%	P/C_p	20%,30%	Delta	CtR[b]/CD[c]	1	±16.4°	3.5	3.9	7.0
NTUA T18	18%	P/C_p	30%,40%	Delta	CtR/CU[d]	1	±20°	3	3.7	11.7

[a]P: Polar data, C_p: Pressure data; [b]CtR: Counter-rotating; [c]CD: Common-downflow; [d]CU: Common-upflow

Table 3.2: Code contributions

Code	Developer	Type	Space	Turbulence	Transition	VG modelling	Grid Size
EllipSys	DTU	CFD	3D	k-ω SST	e^N	BAY/Fully-Resolved	$1-7\times10^6$
Q^{3}UIC	DTU	IBL	2D	Closure Relations	e^N	Shear-lag correction	140 panels
MaPFlow	NTUA	CFD	3D	k-ω SST	–	BAY	1×10^6
VGFlow	NTUA	CFD	2D	k-ω SST	–	Vortex model + RANS	0.05×10^6
OpenFOAM	TUDelft	CFD	3D	k-ω SST	–	BAY	$2-4\times10^6$

(Michelsen, 1992, 1994; Sørensen, 1995.). Convective terms are discretized using the QUICK scheme, as given by Leonard (1979). The turbulent simulations are carried out using Menter's k-ω SST model described in Menter (1993), while the transitional simulations are based on the e^N transition model as described in Michelsen (2002). Along with simplified BAY-type simulations, fully-resolved VG computations were also performed on a single VG vane with imposed spanwise periodic boundary conditions to mimic the array effect.

Q^3UIC is a Quasi-three dimensional Unsteady Interactive boundary layer Code built on a viscous-inviscid interaction technique, developed at DTU by Ramos-García et al. (2014). This code uses a strong coupling between the viscous inner and inviscid outer flow using the transpiration velocity concept. The outer inviscid part is modelled by a two-dimensional panel method, and the viscous part is modelled by solving the integral form of the laminar and turbulent boundary layer equations. Transition can be forced by employing a boundary layer trip or computed freely using the e^N envelope transition method with Mack's modification to account for the turbulent intensity (Mack, 1977). VGs are modelled based on the approach of Kerho and Kramer (2003). A source term is added to the shear-stress transport equation, effectively increasing the production of turbulence and mass entrainment starting at the VG location in a decreasing fashion, simulating the formation and eventual decay of an embedded vortex. In the implementation used for the present comparisons, the initial magnitude of the VG-induced perturbation was determined by trial and error so as to give the best prediction of $C_{l|\max}$.

NTUA calculations were performed using the in-house MaPFlow code, a multi-block compressible solver equipped with preconditioning in regions of low Mach flow (Papadakis and Voutsinas, 2014). The discretization scheme is cell centred and makes use of the Roe approximate Riemann solver for the convective fluxes. In space, the scheme is second-order accurate, defined for unstructured grids. Turbulence is also modelled using the k-ω SST model. The effect of VGs is simulated by means of the BAY model (Bender et al., 1999) and jBAY (Jirasek, 2005) refinements, in which the VG is replaced by a surface with zero thickness.

The second NTUA approach for VG modelling is based on a phenomenological model proposed by Nikolaou et al. (2005) and builds on the MaPFlow code. An explicit VG model is used which is based on the superposition of a vortex flow field on the Navier-Stokes equations. A spanwise averaging operation then simplifies the system to a two-dimensional viscous flow problem with additional source terms and fluxes representing the vortex flow field. A system of co- or counter-rotating vortex lines are released from the specified VG positions, and left to operate on the flow. These vortex filaments are assumed to follow the flow, which is mainly true except in the proximity of the VG.

TUDelft calculations were performed in OpenFOAM, an open source CFD software distributed under the General Public Licence (GPL), and detailed in Jasak (1996). OpenFOAM is a segregated finite volume code able to solve compressible and incompressible flows. For this analysis, the steady, incompressible RANS equa-

tions are solved using the SIMPLE algorithm and the governing equations are solved using first order upwind discretization schemes for the convective terms. The fully turbulent simulations use Menter's two-equation k-ω SST model (Menter, 1993) for closure. VG simulations are conducted using a newly implemented BAY model in OpenFOAM, detailed in Florentie et al. (2014).

3.3. Benchmark results

3.3.1. Key performance indicators

The following metrics were defined to better quantify the comparisons. Figure 3.8 and Figure 3.9 summarise these key performance indicators, the values of which can be found in Appendix A. The metrics were evaluated for each airfoil case with and without vortex generators at relevant angles of attack as described below. Subscripts 'num' and 'ref' refer to the numerical calculations and reference measurement values respectively such tat,

$$\delta C_l = \frac{C_{l,\text{num}} - C_{l,\text{ref}}}{C_{l,\text{ref}}} \tag{3.1}$$

$$\delta C_d = \frac{C_{d,\text{num}} - C_{d,\text{ref}}}{C_{d,\text{ref}}} \tag{3.2}$$

$$\delta C_{l,\alpha} = \left(\left.\frac{dC_l}{d\alpha}\right|_{\text{num}} - \left.\frac{dC_l}{d\alpha}\right|_{\text{ref}} \right) \Big/ \left.\frac{dC_l}{d\alpha}\right|_{\text{ref}} \tag{3.3}$$

The differences and relative errors in C_l, C_d and $C_{l,\alpha}$ are determined at two angles of attack: 0° and $\alpha_{C_{l|\max}}$. The relative error in the lift, drag and lift slope between the computations and reference measurements are then used as a basis for comparison. The maximum lift-drag ratio, or aerodynamic efficiency, and the angle of attack at which this occurs is an important property of wind turbine airfoils. This is often incorporated in the objectives of airfoil design optimisation. Therefore, the optimum aerodynamic efficiency $C_l/C_d|_{\max}$ is additionally defined for comparison. The optimum geometric angle of attack is also noted. Thus we define $\delta C_l/C_d|_{\max}$, the numerical error in the maximum aerodynamic efficiency, compared to the reference data.

This is computed at the corresponding optimum angle of attack, α^{opt}. The offset in the experimental and predicted optimum angle of attack is quantified using the metric $\delta\alpha^{\text{opt}}$. Since calculations were typically performed in discrete steps of 2°, the metrics at maximum lift and optimum aerodynamic efficiency can only be approximated.

3.3.2. DU97-W-300, 30%t/c, $\text{Re}_c = 2\times10^6$

The case without roughness is considered first in Figure 3.2. The EllipSys and Q^{3}UIC codes are equipped with transitional models, and appear to capture the

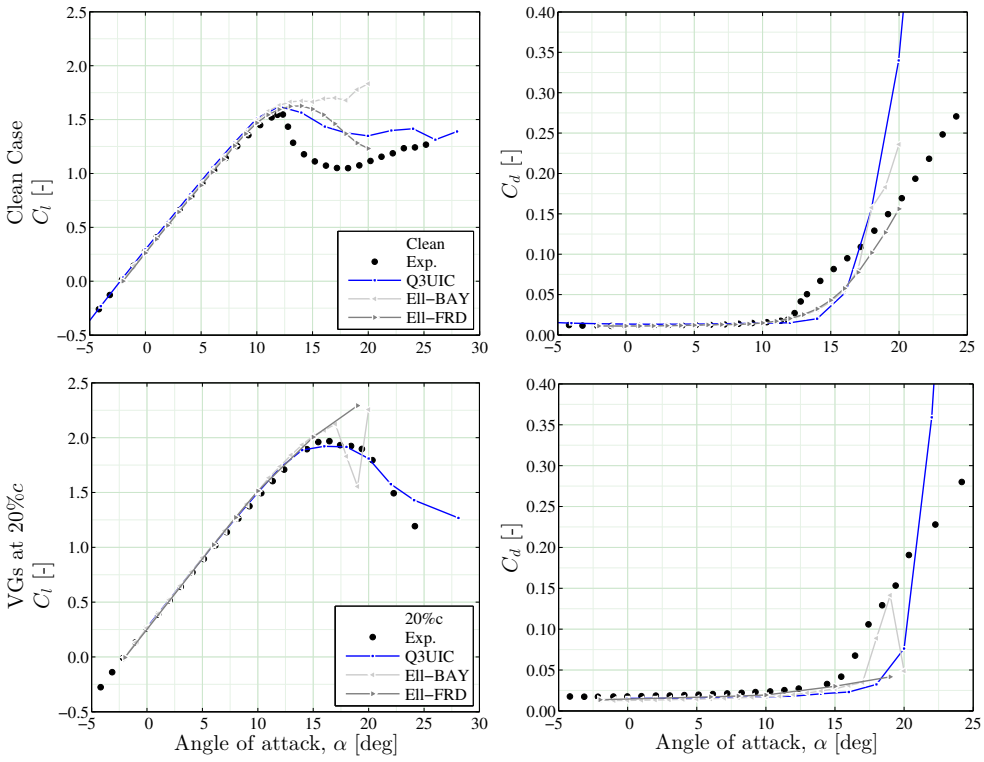

Figure 3.2: Lift and drag polars for transitional computations of the clean DU97-W-300 airfoil.

lift and drag characteristics very well without VGs. The drag prediction is very good, differences with experiments being close to the uncertainty level on the measurements. The maximum lift is within 6% of the measured value whereas the maximum lift angle is overpredicted by approximately 1° by EllipSys. Q^{3}IUC captures this peak more accurately. Both predictions overestimate the lift in the post-stall region and under-estimate the drag. Typically, prior to stall, a separated flow region starts forming from the trailing edge, and gradually grows forward as maximum lift is attained. This process is notoriously difficult for RANS and IBL codes to predict, especially considering that separation is in fact a 3D phenomenon. The pressure distributions highlight the performance in a region near $C_l|_{\max}$ and in the post-stall regime ($\alpha = 12°$ and 16°) in Figure 3.3. The slightly higher lift is explained by a higher suction peak and lower surface pressure around 30%c. In the post-stall regime, we see that the extent of separated flow (indicated by the pressure plateau on the suction side) is underestimated by the codes, thus predicting higher lift and lower drag, the latter now composed mainly of pressure drag.

With the addition of VGs at 20%c, $C_{l|\max}$ is extended from 1.55 to 1.97, until $\alpha_{C_{l|\max}} = 16.5°$. Q^{3}UIC captures this very well, albeit for a slightly lower $C_{l|\max}$.

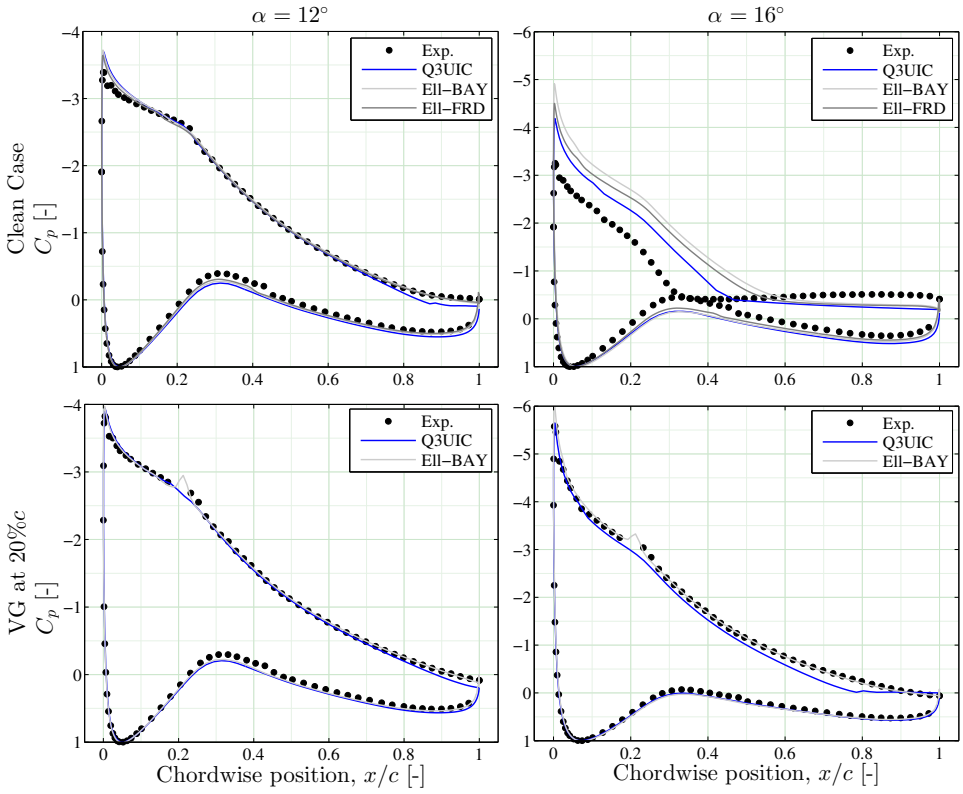

Figure 3.3: Pressure distributions for the DU97-W-300 airfoil in free transition; $C_p(x)$ for (*Left column*) $\alpha = 12°$ and (*right column*) $\alpha = 16°$ (Note different graph scale).

EllipSys appears to overpredict the effect of the VGs, and both BAY and fully-resolved simulations perform similarly. The experimental drag in the linear region is slightly higher than computations, likely because of the parasitic drag from the VG base plate on the model. Apart from increasing the boundary layer thickness slightly, this is also has the effect of forcing transition at the leading edge of the plate, something which is not modelled in the computations. This also accounts for the slightly overestimated lift slope. The pressure distributions shown in Figure 3.3 support these observations. Interesting to note is that Q^{3}UIC predicts the onset of trailing edge separation over the aft 20%c at $\alpha = 16°$. This effectively de-cambers the airfoil, resulting in the lower suction peak and an overall shift in the pressure distribution on the upper side, resulting in lower lift. Note that after application of wind tunnel corrections, the effective measured angle of attack may differ by up to $\pm 0.3°$ from the rounded geometric angle. However, computations were conducted at round integer values. Therefore, differences in the measured and predicted pressures are partly attributed to this small discrepancy.

A roughness case is also considered in Figure 3.4. For this case, computations were run with fully turbulent conditions. All codes over-predict the performance of the DU97-W-300 (without VGs). Van Rooij and Timmer (2003) remarked that zig-zag tape has a lower critical Reynolds number compared to other trip devices, making it an efficient tripping device. However, its presence still increases the boundary layer thickness and appears to cause early turbulent separation, which the computations do not capture. The pressure distributions illustrate this further in Figure 3.5.

The presence of VGs counteracts the earlier turbulent separation by re-energising the flow downstream. For these reasons, the comparisons are more favourable with VGs since the issue of early turbulent separation is circumvented. With VGs at 20%c, $C_l|_{\max}$ and its corresponding angle of attack are captured rather well by the BAY-type EllipSys computations, albeit with sharper stalling behaviour compared with measurements. The remaining predictions overshoot $C_l|_{\max}$ and its location. VGFlow and MaPFlow perform similarly, and do not predict separation until higher angles of attack. The same can be said of fully-resolved EllipSys calculations. A BAY model has been implemented in MaPFlow and EllipSys, yet both predictions

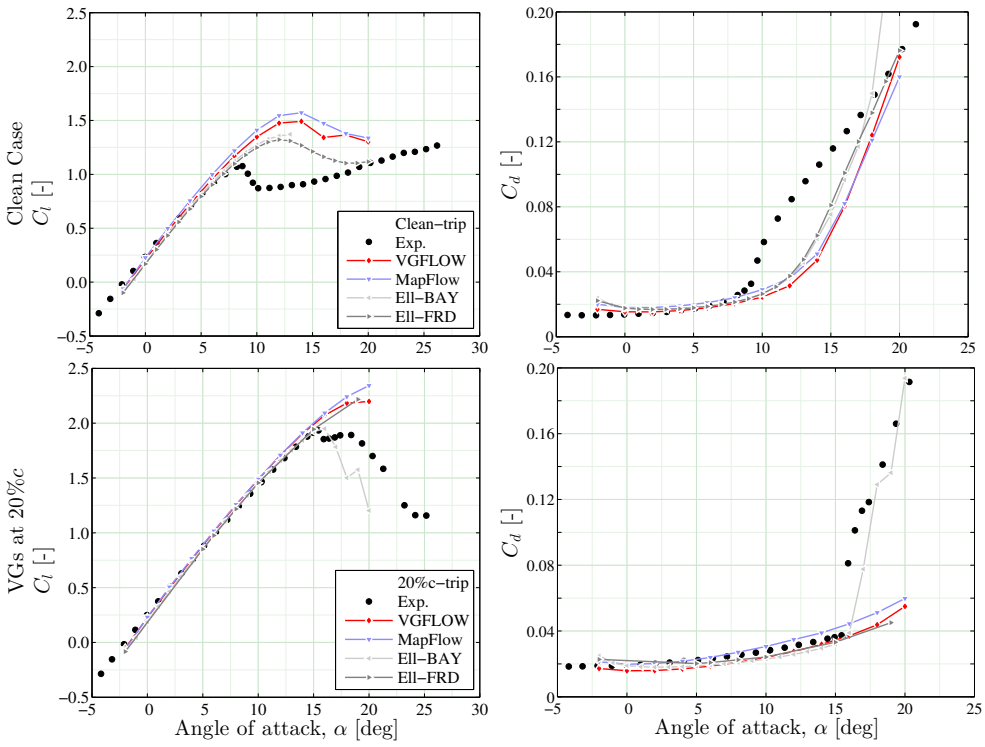

Figure 3.4: Lift and drag polars for turbulent computations of the tripped DU97-W-300 airfoil.

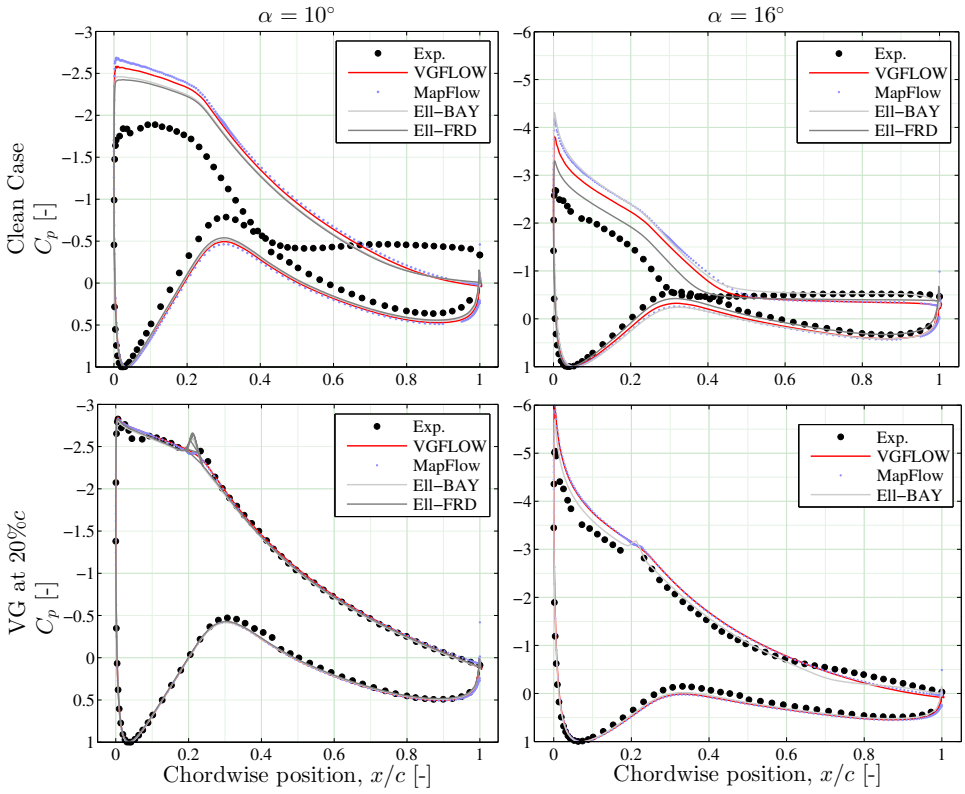

Figure 3.5: Pressure distributions for the turbulent (tripped) DU97-W-300 airfoil; $C_p(x)$ for (*Left column*) $\alpha = 10°$ and (*right column*) $\alpha = 16°$ (Note different graph scale).

differ. The pressure distributions in Figure 3.5 show that MaPFlow predicts a higher suction peak and upper side pressure, even without VGs. The stepped post-stall characteristic in the measured lift polar is typical of 3D separation effects and is probably related to an intermittent interaction of separated flow regions with the streamwise vortices. However, the latter cannot be verified from the presented data without supporting flow field investigations. Drag predictions improve slightly in the VG case with respect to the clean case due to the significant reduction in pressure drag from the zig-zag strip. Pre-stall drag is predicted fairly well by all codes.

3.3.3. NTUA T18, 18%t/c, $\mathrm{Re}_c = 0.87 \times 10^6$

A comparison of the lift and drag polars for the NTUA T18 airfoil is shown in Figure 3.6 for controlled and uncontrolled cases (all with roughness trips). The predictions capture the soft stalling characteristics in the clean case rather well, but this occurs at a higher $C_l|_{\max}$ level than in the computations. Results from all CFD codes are

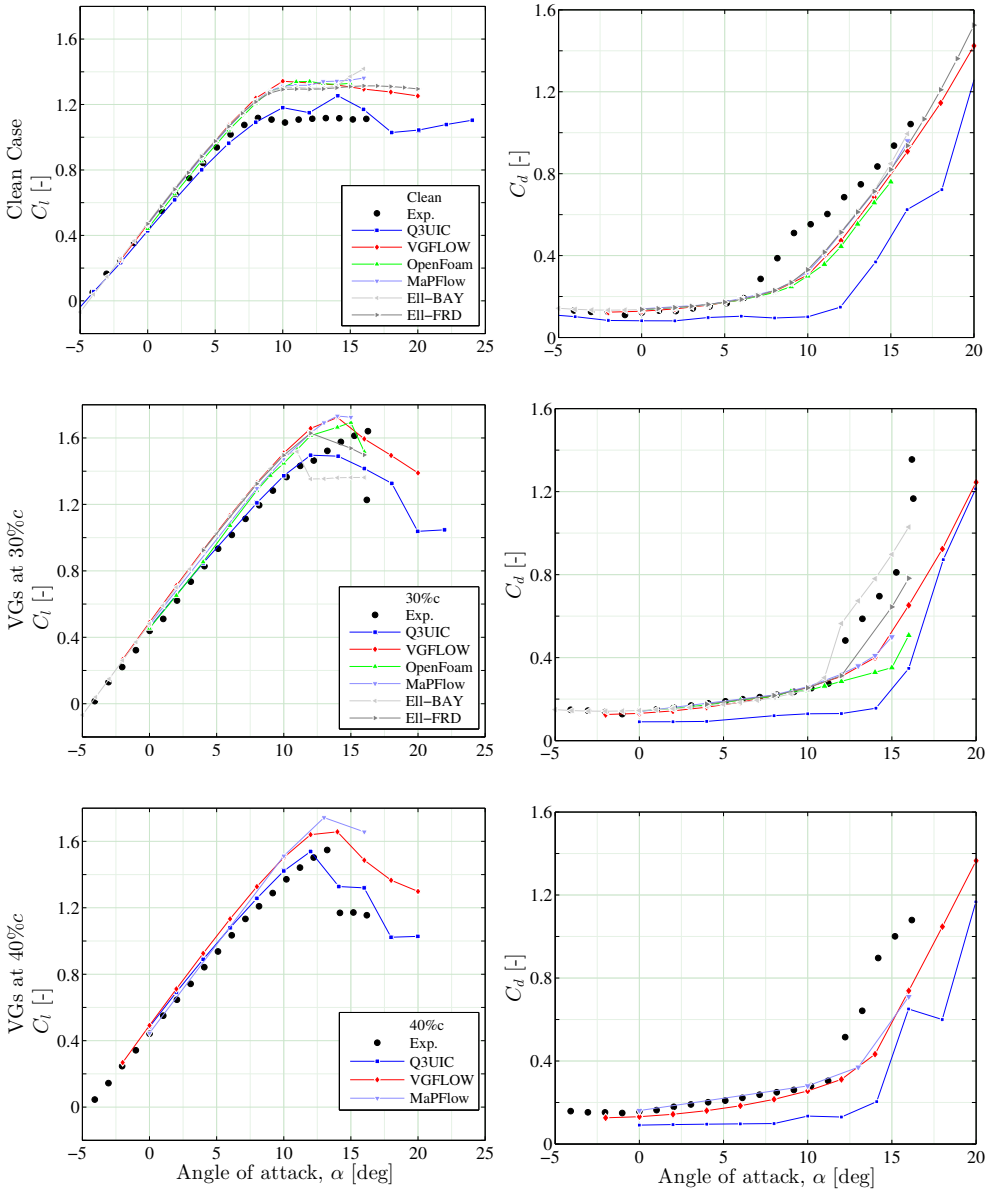

Figure 3.6: Lift and drag polars for computations of the NTUA T18 airfoil. Rows represent the Clean Case and VGs at 30%c and 40%c respectively (fully turbulent experiment and simulations).

quite comparable until stall. The pressure distribution for the uncontrolled case for $\alpha = 12°$ and $16°$ in Figure 3.7 shows that the issue is related to the prediction of the separated region. MaPFlow again appears to overestimate the suction pressure distribution whereas Q^{3}UIC underestimates it over the aft 40%c.

In general, the results show higher spread with VGs, around $C_l|_{\max}$, but also with respect to the lift slope, again indicating possible effects of the roughness strip. Both BAY-type and fully-resolved simulations show an increased performance with VGs, as do the lower-complexity VGFlow and Q^{3}UIC, but over predict the VG effect compared to the experimental results. The EllipSys-BAY results appear to signal the abrupt stalling behaviour, albeit some degrees earlier than the steep drop in the measured lift. For $\alpha = 12°$, the experimental pressures do not indicate separation with VGs (no visible pressure plateau in the aft region). In contrast, Q^{3}UIC and EllipSys-BAY predict trailing edge separation over the aft $20-30\%$ chord. The computational meshes used in the EllipSys and OpenFOAM simulations were generated on a noisy surface measurement of the actual wing model, which explains the fluctuating pressure values close to the LE (Figure 3.7). This is possibly the reason for the earlier stall in the EllipSys results.

With VGs at 40%c, MaPFlow again overestimates the performance whilst OpenFOAM underpredicts lift. Q^{3}UIC and VGFlow fair reasonably well in predicting the lift polar, but $C_{l|\max}$ is over- and underestimated, respectively. Interestingly, Q^{3}UIC also appears to capture the stepwise lift drop after $C_{l|\max}$. Comparing the pressure distributions for $\alpha = 16°$ for the measured and predicted separated zones confirms the different maximum lift characteristics for this airfoil. This again highlights the difficulties in the prediction of separated flow and its consequence for practical purposes.

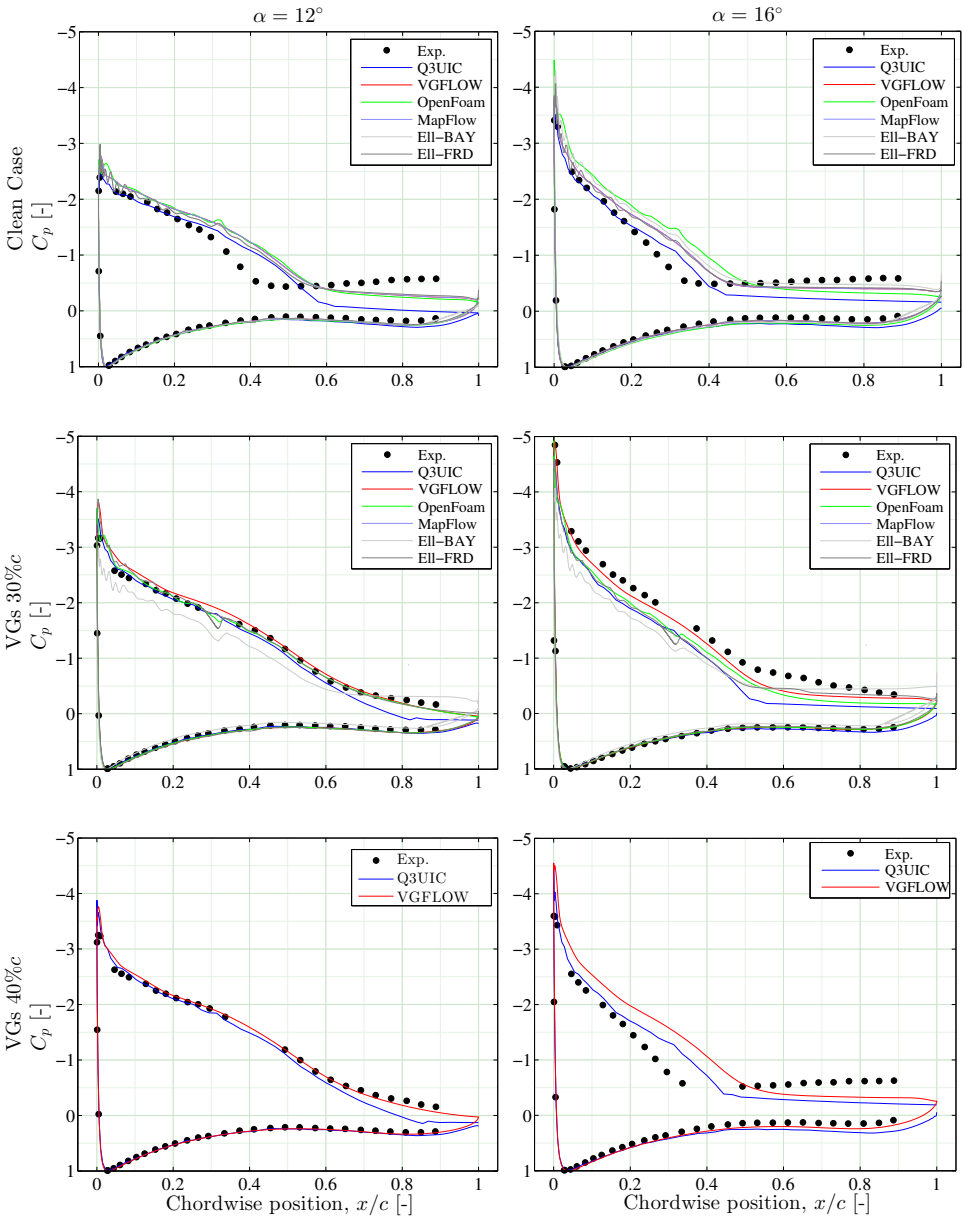

Figure 3.7: Pressure distributions for the NTUA T18 airfoil; $C_p(x)$ for (*Left column*) $\alpha = 12°$ and (*right column*) $\alpha = 16°$. Rows represent the Clean Case, VGs at 30%c and 40%c respectively. (Note different graph scale).

3.4. Discussion

Some effects of the VGs on airfoil performance are captured well, limited by classical issues with the prediction of separated flows (Spalart and Venkatakrishnan, 2016). The experimental loads were indirectly obtained through model and wake pressure measurements. The immediate post-stall region presents issues with data interpretation due to the 3D flow nature and both experimental and computational (2D, low aspect-ratio 3D) results should be interpreted with caution. Balance measurements would offer a better indication of the average flow over the wing in this regime. The same can be said of the periodic VG flow; the provision of reliable and representative polar data with these devices is not as trivial as the simplicity of the devices would suggest.

The tools show some discrepancies in the prediction of the magnitude and position of $C_{l|\max}$, and hence, the extent of the linear range, which is a vital property for design and optimisation. The prediction of $C_{l|\max}$ is even more complicated with VGs because it represents a critical balance between the decaying vortex system and the incipient separation. As suggested in Spalart et al. (2015), investigations into the cause of this will likely require consideration of dedicated turbulence modelling, considering the complex turbulent structure of the vortices.

3.5. Conclusion

Measurements from two wind energy type airfoils equipped with passive vortex generators have been used to benchmark the performance of computational codes. Predictions for transitional flow on the DU97-W-300 compare quite well without control devices. However, artificially roughened surfaces pose modelling problems, particularly predicting the onset of early turbulent separation. Unless models account for the presence of a physical roughness element, this issue will likely persist when assessing airfoil flows in the fully-turbulent regime.

In conclusion, the added complexity and computational cost of fully resolved CFD for vortex generator flows appears to offer only marginal improvements over well calibrated, simplified codes such as Q^3UIC and VGFlow. However, at present, experimental data for estimating robust tuning parameters covering a wide range of airfoils, device configurations and flow conditions are limited. Therefore, as an intermediary approach, BAY-type models are a promising solution which can potentially capture the effects of vortex generators on airfoils.

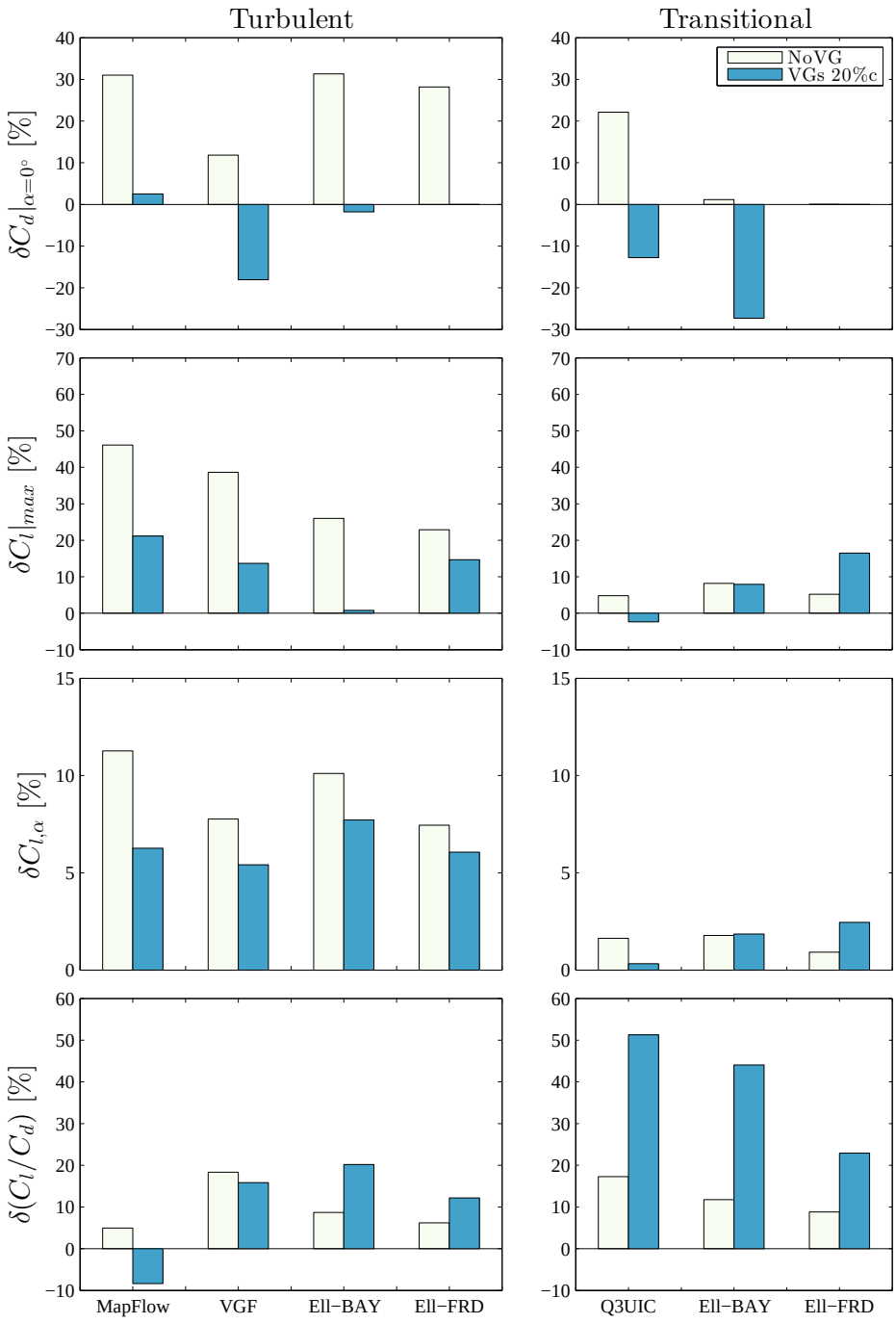

Figure 3.8: Comparison of key performance indices for the DU97-W-300 airfoil. Note the different scales of the graphs.

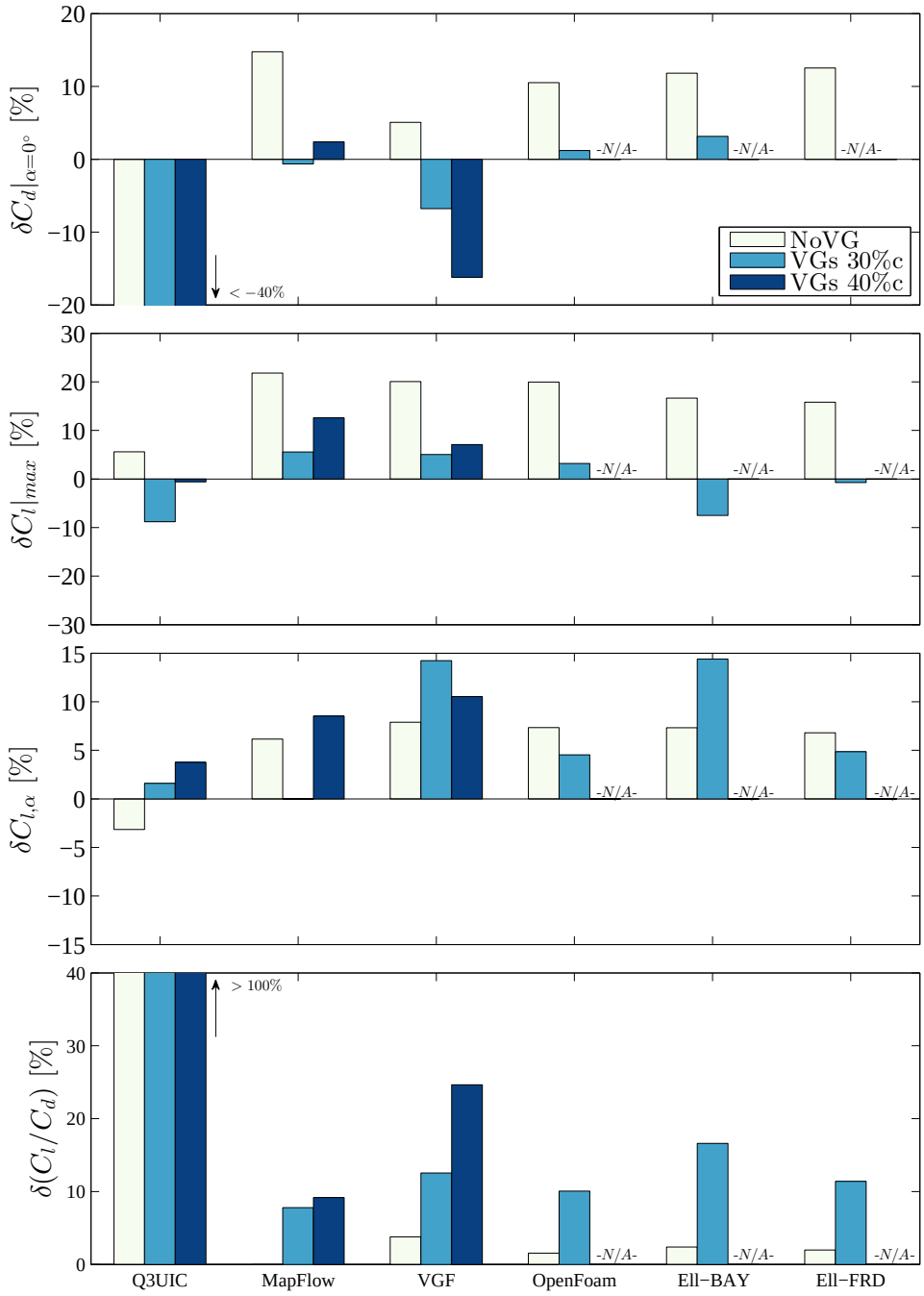

Figure 3.9: Comparison of key performance indices for the NTUA T18 airfoil. Note the different scales of the graphs.

II

Dynamics and evolution of embedded streamwise vortices

4

Dynamics and evolution of asymmetric vortex wakes

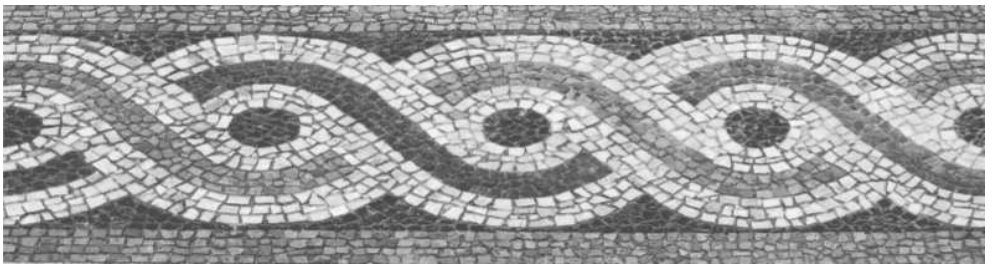

Mosaic pattern reminiscent of the flow field around an infinite, co-rotating vortex array; Agios Eleftherios, Athens, Greece.

The chapter introduces the asymmetric vortex array as a simplification of skewness inflow effects. Particle image velocimetry measurements are conducted to understand vortex development and the associated boundary layer modulations. A point vortex model is developed to study the influence of unequal vortex strengths on the array dynamics. The model is then validated and used to support experimental observations of suppressed vortex ejection. This chapter has been adapted from (IOP) *Journal of Physics: Conference Series*, 753(2), 2016a.

4.1. Introduction

4.1.1. Background

Vortex generators are applied on wind turbine blades following significant design iterations, involving VG integration studies using computations, and wind tunnel testing of airfoil sections with and without VGs. This is complemented by an assessment of blade-bound flow for positioning of the VGs. Literature investigations in Chapter 2 revealed how VGs in the general community are assessed with the incoming flow aligned with the streamwise or axial dimension, orthogonal to the leading edge of an array. Whilst this is likely an artefact from the early interest in using VGs in aircraft and diffusers, it is dubious that the same applies to the rotating blade of large wind turbines. Blade root flows pose different inflow conditions to the VG arrays than the simplified scenarios on fixed wing sections. Evidence of this complex inflow is for instance found in Micallef et al. (2014) and Herráez et al. (2016), through observations of appreciable spanwise flows in blade root regions. A schematic representation of the skew angle arising due to spanwise flow is shown in Figure 4.1 and Figure 4.2. This demonstrates that for a spanwise flow roughly 20%c of the normal flow magnitude, the skew angle can exceed 10°.

4.1.2. Objective and outline

Aside from the external flow, the installation process of the VGs itself involves a deal of uncertainty. Compounded by effects of rotor yaw misalignment, wind shear and gusting which can lead to excursions from design conditions, it is conceivable that VG arrays experience a degree of skewed inflow during operation. Assessing the impact of such inflow conditions for VG arrays is of prime importance for understanding flow control performance in more practical conditions and for improving the robustness of VG designs.

This chapter will address this topic from a fundamental perspective. The following section presents a more focused review of relevant experiments and modelling approaches to deal with the dynamics of unequal streamwise vortices. In section 4.3, an experimental boundary layer campaign will detail the vortex dynamics and their sensitivity to skewness. The final section complements with the development and validation of the point vortex model.

4.2. Asymmetric streamwise vortices

4.2.1. Empirical observations

A VG array designed to produce equal counter-rotating (CtR) vortices, and which is subjected to a skewed inflow, will instead result in an unequal or asymmetric vortex array, as shown in Figures 4.2. However, the behaviour and dynamics of asymmetric vortex arrays have scarcely been addressed in literature. On the other hand, single trailing edge vortices and vortex pairs in ground effect have received much more

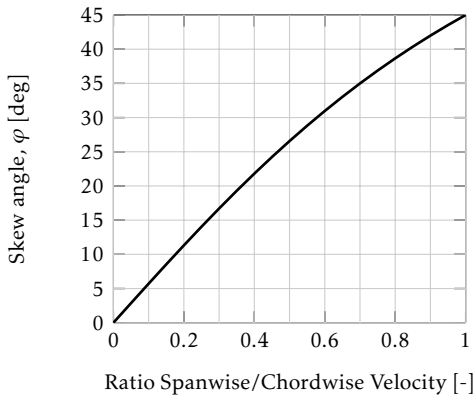

Figure 4.1: Skewing sensitivity to crossflow on a rotating blade.

attention, often motivated by understanding the behaviour of aircraft wakes during take-off and landing, close to the ground. The appearance of weaker secondary structures as a result of this interaction is also a well-known phenomenon and is relevant to the present study. Harvey and Perry (1971) demonstrated that primary vortex rebound in ground effect was due to the separation of the crossflow boundary layer, giving rise to a secondary vortex, which in turn influenced the path of the primary. In this case, the strength of the secondary became comparable to that of the primary. In other cases, as reported in Dee and Nicholas (1968), the secondary strength was weaker, resulting in a spiralling trajectory about the primary vortex. Harris et al. (2010) and Harris and Williamson (2012) studied a counter-rotating pair in ground effect and also observed weaker secondary structures which in turn exhibit secondary instabilities. Secondary vortices have also recently been observed behind vortex generator vanes within turbulent boundary layers, as in Velte et al. (2008) for a single vane and Lögdberg et al. (2009) for a VG pair. In the latter, the relative strength of the secondary and primary structures was seen to increase in the direction of the freestream. More recently, Velte et al. (2016) observed the formation of multiple secondary structures behind a single VG vane. Different vortex systems emerged as a function of the vane angle and relative boundary height. The formation of particular vortex wakes was found to correlate with the strength and ground proximity of the primary vortex. A strong interaction of all structures is expected; however, such complex wakes are not observed in symmetric vortex array configurations (Velte et al., 2011).

In other instances, unequal vortices arise as a result of direct generation. Pauley and Eaton (1988) analysed an asymmetric vortex pair in a turbulent boundary layer produced with vanes of different height. In this case, they achieved a vortex pair strength ratio, denoted hereafter as γ, of 0.5. They observed accelerated diffusion and distortion of the weaker vortex as well as rapid convection about the stronger vortex structure. This also resulted in a faster decay of the weak vortex. For a pair

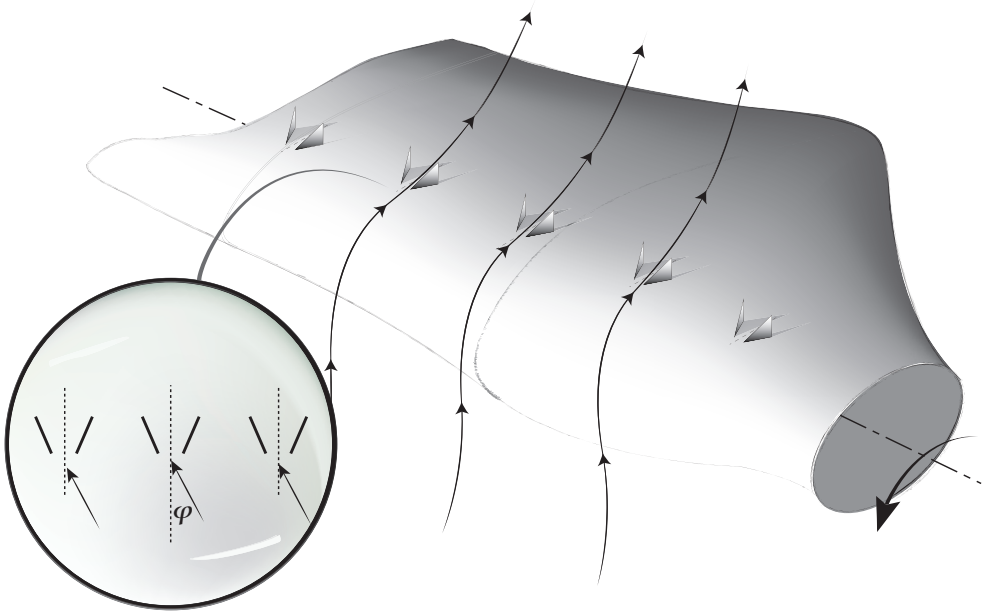

Figure 4.2: Schematised skewed inflow (φ) relative to a counter-rotating vortex generator array mounted near the blade root of a horizontal axis wind turbine.

of adjacent vortices A and B, their strength ratio can generally be defined as

$$\gamma = \frac{\Gamma_B}{\Gamma_A}, \quad \text{such that} \quad |\gamma| \leq 1 \tag{4.1}$$

and is an important parameter governing the interaction of the vortex pair. Lögdberg et al. (2009) investigated asymmetric vortex arrays in the context of separation control on bluff-body vehicles. In this case, the authors produced unequal strength vortices by skewing (or rotating) the vane pair as a whole (explained in more details in Figure 4.3.3). This causes the effective geometric angle of each vane to increase/decrease, producing different strength vortices. Despite the substantial effect on the vortex paths, skewed inflow was found to affect the boundary layer shape factor only minimally.

4.2.2. Point vortex models

Early vortex generator designs were based on optimisations of the vortex trajectories. An important objective was to maximise the vortex residence time in the vicinity of the wall where its effect is most required. Using a potential flow model, Jones (1955) provided the framework for this purpose. An analytical function was found describing the paths of equal counter-rotating vortices in an infinite array. Following these developments, Pearcey (1961) derived optimal VG designs, based purely on the kinematic properties derived from Jones' model. Despite the assumption of

potential flow, measured near-wake vortex trajectories compared well with theory. However, vorticity diffusion and circulation decay posed modelling limitations. Vortex re-organisation in the boundary layer far downstream appears to explain lateral deviations from inviscid theory. Lögdberg et al. (2009) modified Jones' model to account for these limitations and the resulting model captured better the actual symmetric vortex dynamics in the far wake (> 200h downstream). Other computational efforts based on CFD have shown reasonable success in predicting vortex paths and the effect on the boundary layer (e.g. Fernández-Gámiz et al., 2014; Spalart et al., 2015).

Point vortex models have been used extensively throughout literature. Aref (2007) details the potential of these simple models in modelling physical vortex systems. Von Kármán devised the $N = 2$ vortex model to describe the behaviour of the vortex-street and further derived stability criteria for this system (Pozrikidis, 2009). More recently, Harris and Williamson (2012) used a periodic point vortex model (PPVM) to study the dynamics of secondary vortices arising from the wall-interaction of a counter-rotating vortex pair. Their model revealed different flow modes and showed consistent qualitative agreement with observations. Asymmetric trailing wakes from periodically oscillating bodies have also been tackled using point vortex models (Stremler et al., 2011; Xuzhao and Gursul, 2016). Stremler et al. (2011) for instance found that translating or orbiting regimes can be expected depending on the initial spatial conditions and impulse of the system. Laminar, staggered and symmetrical bluff-body wakes were investigated in great detail by Basu (2014) and Basu and Stremler (2015). These wakes were analysed using a Hamiltonian dynamics approach and a detailed picture of the complex types of motion emerges. Agreement with experimental data is generally quite fair in these references, but more importantly, considering the significant model assumptions and limitations, is the ability of these simple point vortex models to unravel governing dynamic mechanisms in wakes and other vortex dominated flows.

4.2.3. Experiment design rationale

In this thesis, particular attention is given to the role inviscid vortex dynamics plays on skewed VG effectiveness within a boundary layer. The effect of skewness is to create an series of streamwise vortices of periodically unequal strength. The only known instances this has been considered prior are documented in Table 4.1. To serve as a benchmark with the work of Lögdberg et al. (2009), a similar choice of $h/\delta = 0.25$ is chosen, and in-line with the recommendations of Godard and Stanislas (2006) to produce effective, clearly distinguishable vortices.

Realistically, the manner in which a skewed inflow presents itself to a VG array of spacing D on a rotating blade would give rise to three main effects relative to a counter-rotating, symmetric array:

(i) vortices of alternately unequal strength due to relative changes to the effective vane angles,

(ii) a shorter effective vortex period, proportional to a factor $\cos\varphi$, and

Table 4.1: Overview of experimental details for controlled investigations of asymmetric vortices.

	Parameter	Pauley and Eaton (1988)	Lögdberg et al. (2009)	Present Study
Vortex Generators	Shape	Delta	Rectangular	
	Configuration	Pair	Array	Array
	Organisation	CtR common upwash	CtR common downwash	
	Vane angle, β [deg]	±18°	±15°	±18°
	Relative height, h/δ	1.53/0.77[1]	0.36	0.25
	Relative chord, L/h	2.5/5	3	2.5
	Intra-spacing, d/h	2.8/5.6	2.1	2.5h
	Inter-spacing, D/h	-	8.3	6
	Asymmetry mechanism	Unequal vane heights	Individually skewed pairs	
	Skew angle, φ [deg]	-	0:5:20°	0:10:20°
Flow Conditions/ Measurements	Boundary layer, [2]Re_θ	Zero-pressure gradient, turbulent boundary layer, tripped		
		1700	6000	3000
	Measurement locations, $(x-x_{VG})/h$ [-]	6.5, 22, 44.5, 67.5/ 13, 44, 89, 135	6,17:25:67, 67:50:267	1:1:10,15 25,50
	Measurement technique[3]	5-hole pressure probe, 1D-3C	HWA 1D-3C	SPIV 2D-3C

[1] Vanes of unequal height $h = 2/1$ cm, altering the geometric similarity for the smaller vane
[2] Momentum thickness-based Reynolds number
[3] D - Dimension, C - component, HWA - Hot Wire Anemometry

(iii) adjacent vortices of increasing age, proportional to an incremental travel of $D \sin\varphi$.

In this experiment, vortex asymmetry was created simply by skewing individual vane pairs about their centroid, giving rise to differently angled vanes. Thus we only reproduce the first effect of unequal strength vortices.

4.3. Experimental Approach

SPIV measurements were conducted behind an array of rectangular vortex generators. These are immersed within an non-separating turbulent boundary layer. The reason for this choice was to focus on the vortex structures and boundary layer response.

4.3.1. Wind tunnel facility

The experiments were conducted in the boundary layer wind tunnel of Delft University of Technology. The test section is a high-aspect-ratio rectangular channel of 0.25m (width) × 2.5m (height), and 6m long, enabling development of boundary layers on the order of centimetres. This was important for characterising the embedded vortices and improving measurement accuracy. The high cross-sectional aspect ratio of the test section ensured minimal disturbances from parasitic corner flows and side-wall boundary layers. The incoming flow developed along a transparent Plexiglass plate mounted vertically and spanning the height of the test section, bounding the flow between the test section floor and ceiling. The back-wall is composed of a series of tightly linked, adjustable aluminium panels which allow the pressure gradient to be modified. Figure 4.3 is a simplified illustration of the test-section and shows the orientation of the Cartesian reference frame (see also Figure B.1 for wind tunnel schematic). The origin is located at the mid-span of the flat plate leading edge, with the (x, y, z) coordinate axes aligned with the streamwise, wall-normal and spanwise directions, respectively. Due to excessive flow disturbances and structural vibrations induced by the wind tunnel suction system, the boundary layer developing over the rear wall was not removed. However, the attached flow regime on the back wall was verified using tuft visualisation.

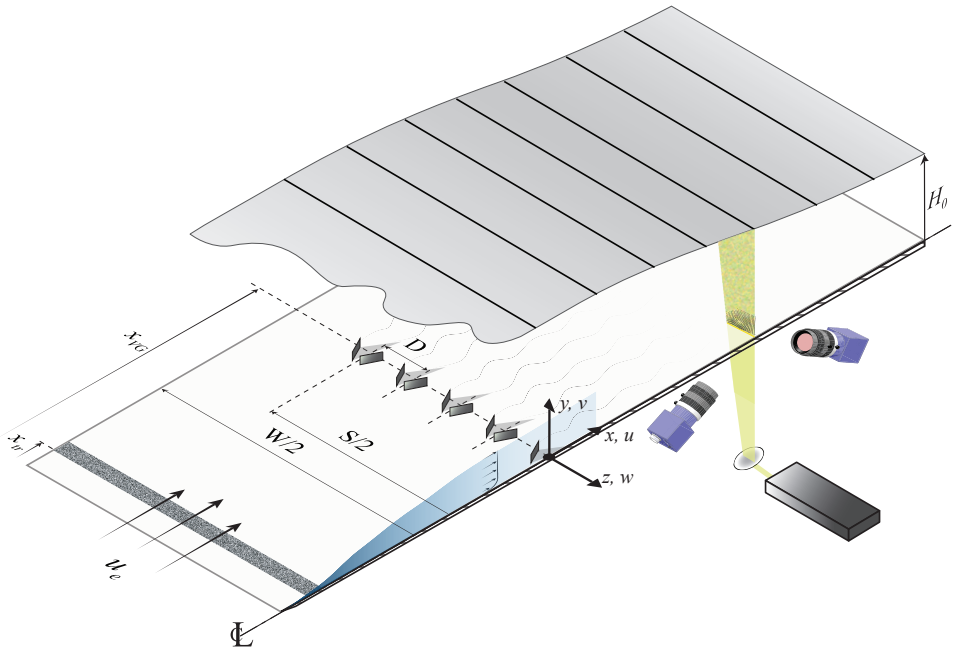

Figure 4.3: Boundary layer wind tunnel test-section illustration. The vertically-oriented Plexiglass test plate is here depicted horizontally in isometric projection for clarity.

4.3.2. Flow conditions and boundary layer characterisation

The freestream pressure distribution was estimated from pressure taps along the test plate at 100mm intervals. These wall-pressure readings were logged with a multi-port, differential pressure gauge. Monitoring this distribution also allowed for corrections of freestream acceleration, due to blockage from the developing boundary layer on the back wall.

Boundary layer transition was fixed at 150mm from the leading edge of the flat plate using a carborundum roughness strip laden with 0.8mm particles. The freestream velocity was measured using a wall mounted pitot probe, the intake of which was aligned with the leading edge of the flat plate. Experiments were conducted at a freestream streamwise velocity of 15m/s, measured at the fixed location, $x = 0$. Hot-wire measurements established a freestream turbulence intensity below 1% at the operating speed of 15m/s, for all test cases.

As a means of quantifying the state of the turbulent boundary layer, the integral properties, namely the displacement and momentum thicknesses, are defined as

$$\delta^\star = \int_0^\delta (1 - \frac{u}{u_e})\, dy \qquad (4.2) \qquad\qquad \theta = \int_0^\delta \frac{u}{u_e}(1 - \frac{u}{u_e})\, dy \qquad (4.3)$$

where the ratio of these two quantities is defined as the boundary layer shape factor H:

$$H = \frac{\delta^\star}{\theta} = \frac{\int_0^\delta (1 - u/u_e)\, dy}{\int_0^\delta u/u_e \cdot (1 - u/u_e)\, dy} \qquad (4.4)$$

The boundary layer edge was determined at the region when the streamwise vorticity dropped to below 1% of the maximum. These properties vary strongly with the direction of flow, and must thus be defined at a certain location. With the conditions and definitions given above, the fundamental boundary layer properties are summarised in Table 4.2 at the eventual location of the VG array leading edge, where the momentum thickness Reynolds number is defined as

$$Re_\theta = \frac{u_e \theta}{\nu} \qquad (4.5)$$

ν being the standard kinematic viscosity of air.

In all cases, the integrals were evaluated using the trapezium-based integral method. Note that in the presence of streamwise vortices, the integral properties must also be considered in spanwise-averaged form (averaged over one spatial period) to facilitate comparison of test cases.

The mean baseflow streamwise velocity, the normal turbulent stresses and the primary shearing stress are illustrated in Figure 4.4. These are given shown in inner boundary layer quantities, that is, normalised by the friction velocity u_τ. The latter was determined using a least-squares fit with a model for the logarithmic region of the boundary layer according to

Table 4.2: Operating conditions and boundary layer properties at the location of the vortex generator array, unless stated otherwise.

Parameter		Value	Parameter		Value
δ	[mm]	21	$\delta^\star$	[mm]	5.4
H	[−]	1.5	Re_θ	[−]	3000
Re_h	[−]	5000	u_τ	[m/s]	0.650
$\frac{dC_p}{dx}$	[Pa/m]	~ 0	TI	[%]	$< 1\%$

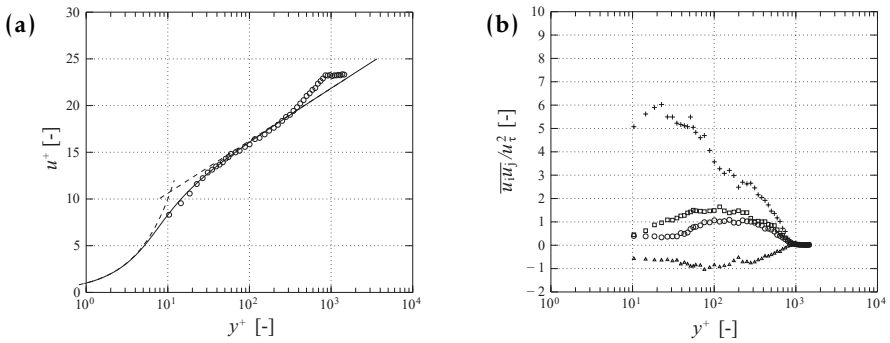

Figure 4.4: (a) Mean streamwise velocity measured at $x = 0, z = 0$: (−−) inner layer $u^+ = y^+$, log-layer $u^+ = 1/\kappa \ln(y^+) + B$, and (−) Spalding velocity profile; (b) Baseflow normal and shearing stresses: $\overline{u^2}$ (+); $\overline{v^2}$ (∘); $\overline{w^2}$ (□); $\overline{uv}$ (△).

$$u^+ = \frac{1}{\kappa} \ln(y^+) + B \tag{4.6}$$

where $u^+ = u/u_\tau$ and $y^+ = y u_\tau / \nu$; the von Kármán constant $\kappa = 0.41$ and $B = 5.0$. Superposed on the streamwise velocity profile is a best fit Spalding profile (Kendall and Koochesfahani, 2008), which also models quite well the transition between the inner and logarithmic regions.

4.3.3. Vortex Generators

The height of the vortex generators h, was sized at 5mm, according to the expected boundary layer thickness at the VG location. The overall device dimensions were designed according to the recommendations of Godard and Stanislas (2006), and are summarised in Table 4.3 and Figure 4.5. The VG vanes were 3D printed in pairs, with a matt black finish and a surface precision of 0.05mm. To avoid artificial thickening of the boundary layer, the VG pairs were printed with a final material thickness of 0.5mm, the smallest possible whilst ensuring sufficient structural integrity.

A total of 15 VG pairs were assembled in an array and located at $x_{VG} = 985$ mm,

Table 4.3: Vane, array and wind tunnel dimensions. See Figure 4.3 for nomenclature.

Parameter	Value		Parameter	Value [mm]
h	5mm	$1h$	x_{VG}	985
d	12.5mm	$2.5h$	x_{tr}	150
L	12.5mm	$2.5h$	S	750
D	30mm	$6h$	W	1500
β	18°	–	H_0	250
e	0.5mm	$0.04L$		

downstream from the flat plate leading edge. This was chosen to allow sufficient boundary layer growth whilst keeping the device array within the zero pressure gradient region of the test section. At this location, the relative height of the vortex generator was approximately $h/\delta = 0.25$. The array span S was 420mm in order to minimise edge effects at the region of measurement, and was centred around the meridian of the test section, as was the field of view of the imaging cameras.

An asymmetric streamwise vortex system was created by skewing vane pairs as a whole about their midpoint. Thus for $\varphi = 10°$, individual vane angles become respectively 28° and −8°; for $\varphi = 20°$, vane angles are 38° and 2°, according to the convention defined in Figure 4.6. This data is summarised in Table 4.4.

4.3.4. Stereo-PIV setup

The imaging components of the stereoscopic PIV system consisted of two LaVision Imager Pro LX 16Mpix cameras. The field of view was calibrated using a 50×50mm high precision plate, mounted flush and orthogonally to the test wall, over a VG pair and spanning at least one array wavelength. The cameras were equipped with Micro Nikor 105mm lenses mounted on adjustable Scheimpflug adapters to allow for an oblique focal plane relative to the laser sheet. The cameras viewed the laser sheet from opposite sides angled at 30° and observed the flow field through the Plexiglass test plate. A Quantel Evergreen Nd:Yag laser system with 200mJ/pulse of output was used to illuminate these particles in the boundary layer. To minimise reflections,

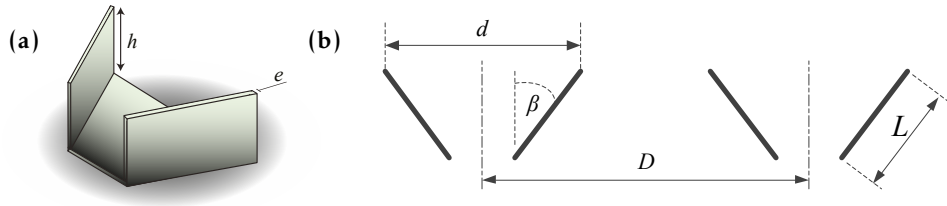

Figure 4.5: Vortex generator array configuration and terminology.

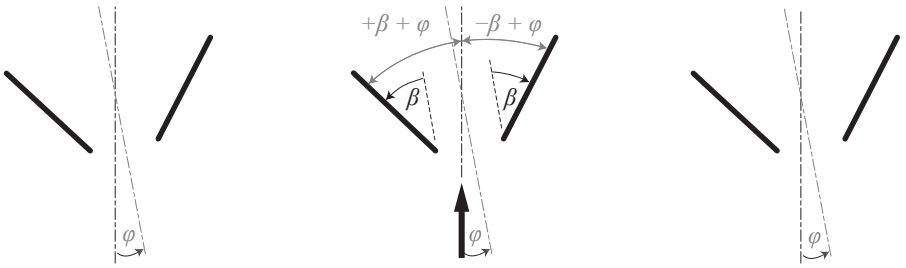

Figure 4.6: Expected influence of skewed inflow relative to an aligned VG array.

Table 4.4: Vane-pair skew arrangement.

Skew Angle, φ [deg.]	Effective angle [deg.]	
	Left Vane	Right Vane
0	18	−18
10	28	−8
20	38	2

the back wall was blackened with a matt finish, as were the VG pairs. A SAFEX smoke generator seeded the flow with diethylene glycol-water based particles on the order of 1µm diameter. The setup design is shown in Figure 4.3 and Figure 4.7., and Table 4.5 summarizes the setup properties. The entire imaging and illumination setup was mounted on a traverse system which allowed fine-tuning of the field of view relative to the test plate wall. In addition, it was necessary to traverse to a number of downstream stations to acquire flow field image-pairs in the VG wake. A total of 15 spanwise-oriented planes were scanned, corresponding to the $[1-10, 15, 25, 50h]$ streamwise positions. Note that the wind tunnel reference frame is centred at the test section meridian, at the trailing edge of the vortex generator array (when $\varphi = 0°$).

Ensembles of 500 unconditioned image pairs were obtained and post-processed using LaVision Davis 8.1.4. A final interrogation window of 16 px × 16 px with 50% overlap yielded a measurement resolution of approximately 8 velocity vectors per millimetre. Images were recording at approximately 1Hz whilst a compromise for the light pulse separation was found at 15µs. This ensured a suitable dynamic range for resolving the in-plane vortical structures whilst keeping the out-of-plane velocity components within acceptable levels of accuracy.

4.3.5. Measurement uncertainty

Various error sources can contribute to the uncertainty of the flow metrics analysed. These are related to the traverse system, wind tunnel velocity, VG angular misalignment and PIV measurements.

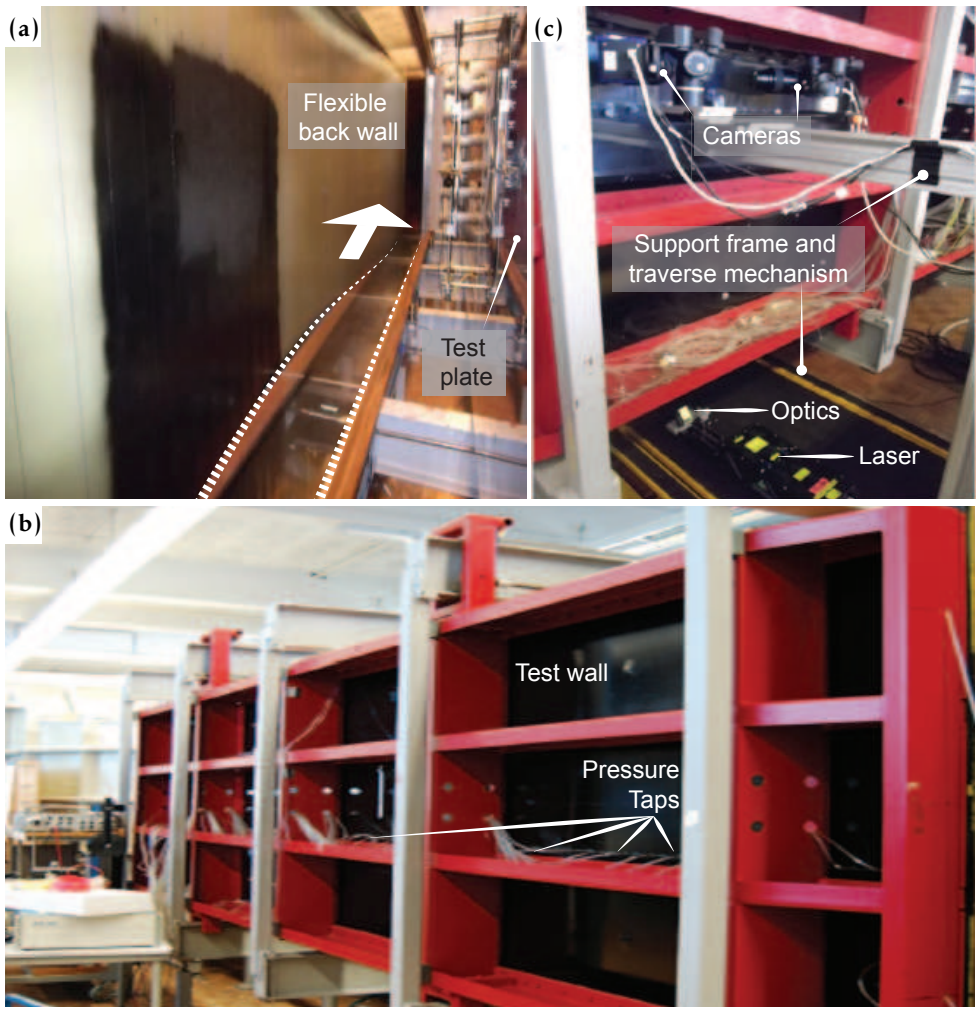

Figure 4.7: (a) Internal test section view displaying the curved back wall with blackened section and illustrating the general flow direction; (b) external view of the test section and (c) PIV setup.

Table 4.5: PIV system setup parameters.

Parameter	Setting	
Field of view, *FOV*	4872×3248 px	55×45 mm
Digital image resolution	80 px	
Interrogation window	16×16	0.2×0.2
Vector grid	570×385	
Vector spacing	7.6 px	0.095 mm
Objective focal length, f	105 mm	
f-number	2×2.8	
Laser pulse separation	$20 - 30$ µs	

The precision of the traverse system in the streamwise direction is approximately 10µm, which is in fact two orders of magnitude smaller than the laser sheet thickness for any measurement plane. The nominal tunnel velocity was measured using a Pitot-Static tube mounted at the flat plate leading edge. The digital MENSOR manometer used to acquire this signal gives an estimated accuracy of ±0.1Pa.

Errors in the flow quantities derive from uncertainties in the processed raw images which give the velocity field at each measured instance. These error sources are namely associated with the PIV processing algorithm, but also due to the limited sample size, which are treated in more detail in Appendix B.

4.3.6. Vortex characterisation

The second invariant of the velocity gradient tensor can be used as means of identifying swirling flow topologies in turbulent boundary layers (Jeong and Hussain, 1995). This metric, also known as the Q-criterion, is given as

$$Q = \frac{1}{2}\left(\|\boldsymbol{\Omega}\|^2 - \|\boldsymbol{S}\|^2\right) \tag{4.7}$$

where $\boldsymbol{\Omega}$ represents rotation and $\boldsymbol{S}$ the strain rate of a vector field. These are also respectively the anti-symmetric and symmetric parts of the velocity gradient tensor $\boldsymbol{\nabla u}$. Thus, the signed Q-criterion can be written explicitly as

$$Q_x = -\frac{1}{2}\frac{\partial w}{\partial y}\frac{\partial v}{\partial z} \cdot \mathtt{sign}\left(\omega_x\right) \tag{4.8}$$

This expression for Q is the residual between the vorticity and the strain rate. A positive Q value therefore means that regions of higher relative vorticity than the background flow are caused by the presence of vortices rather than a shear layer. Used in conjunction with the vorticity ω_x, the signed Q-criterion (4.8) can also indicate the sense of rotation of the vortical structure in order to differentiate vortices.

The streamwise vorticity is given by

$$\omega_x = \frac{\partial w}{\partial x} - \frac{\partial u}{\partial y} \tag{4.9}$$

and represents the major vorticity component of the coherent vortex. Spatial central differences have been used to estimate the derivatives appearing in (4.8) and (4.9).

To further characterise the vortex strength Γ, the area integral of the vorticity ω_x was defined as

$$\Gamma = \int \omega_x \, d\boldsymbol{A} \tag{4.10}$$

The region of integration $d\boldsymbol{A}$ was the area enclosed by a connected contour around the vortex centroid. This contour was set as the boundary defined by $5\% \cdot |Q_x^{max}|$. Trials with lower Q_x^{max} cut-off levels yielded inconsistent results.

The centroids of the ensemble-averaged vortices were identified as the centre of swirl, i.e. where the in-plane (yz) velocity $\sqrt{(v^2 + w^2)}$ is a minimum within the core region. This yielded a more robust identification scheme than gradient-based identifiers such as Q_x or ω_x maxima, which are more susceptible to local variations in the velocity gradients. The benefit of this method and other non-gradient based approaches for vortex identification become particularly useful when analysing instantaneous vector fields (e.g. Scarano et al., 1999; Kindler et al., 2011). The resolution of the cores was not compromised by particle ejection, likely because of turbulent mixing, and carried an uncertainty of approximately ±0.05mm. Note that this is the error solely due to resolution of the flow field.

4.4. Measurement results

In this section we will assess the overall evolution of the measured vortex pair using the metrics defined in the previous section.

4.4.1. Vortex evolution

The evolution of the vortices is depicted in Figure 4.8. The vorticity is illustrated here which shows not only the primary cores, but also the region below. This oppositely signed vorticity is however not a vortex, but a region of strong spanwise shear. In contrast, measurements of single and vortex pairs have shown that this shear region can roll up to form secondary vortices of opposite sign relative to the corresponding primary (Dee and Nicholas, 1968; Harris and Williamson, 2012).

Asymmetry gives rise to a strong/weak vortex pair, clearly visible from Figure 4.8. Note that in the $\varphi = 20°$ case, one vane is barely inclined relative to the inflow and only a weak vortex appears initially, which decays rapidly in the far-wake. The effect of this asymmetry has a pronounced influence on the vortex dynamics. This is shown in Figure 4.9. As the strong (clockwise) vortex strengthens, it also grows more rapidly. This results in a strong outward motion which is also a

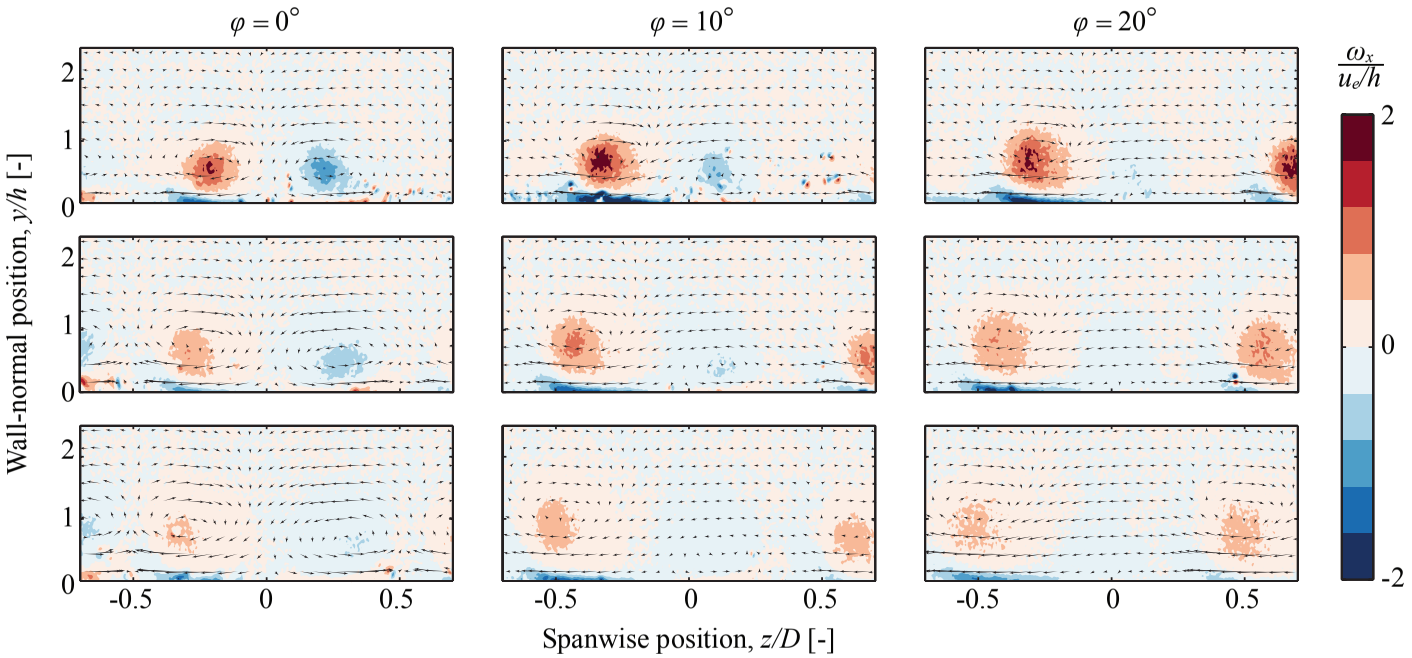

Figure 4.8: Time-averaged streamwise vorticity contours for increasing skew angle φ (columns) and evolving streamwise position (rows, top-bottom: $5h$, $10h$, $25h$). Vectors indicate the in-plane velocity.

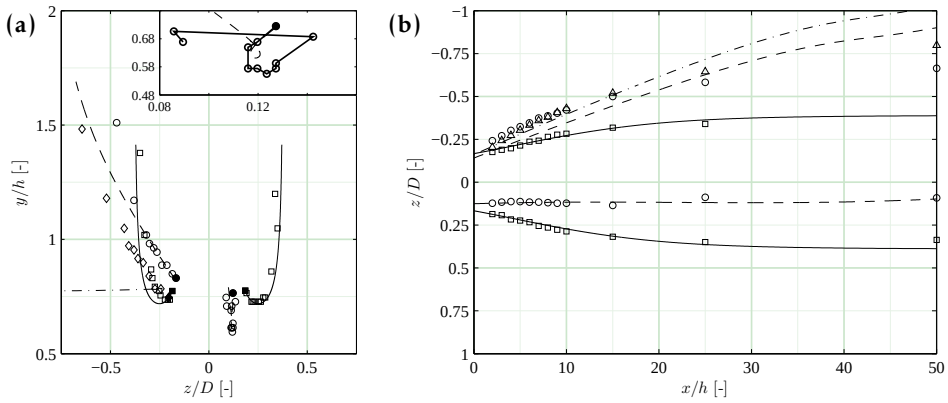

Figure 4.9: Measured (symbols) and predicted (lines) mean vortex trajectories for different skew angles: $\varphi = 0°$ (▫,–), 10° (○,––), 20° (◇,–.). Projections in the (a) yz-plane (with an inlay showing the detailed motion of the weak vortex for $\varphi = 10°$) and the (b) xz-plane.

result of the inviscid vortex interactions. A curious spiralling behaviour is noted for the $\varphi = 10°$ case. In contrast to the baseline, in which vortices from a single pair are equal and opposite, this spiralling motion causes one of the vortices (the weak vortex) to remain close to the wall. The vortex strength is shown to decay exponentially, as shown in Figure 4.10a for the positive (left) vortex arbitrarily for $\varphi = 0°$. The vortex strength is normalised with first reliable measurement station, in this case $3h$. For $\varphi = 10°$, the strong and weak vortices in the measured pair are evaluated separately in Figure 4.10b and shown to decay initially at a similar rate, but start to diverge after $25h$. This also means that the strength ratio of $\gamma = 0.35$ is roughly maintained until $25h$.

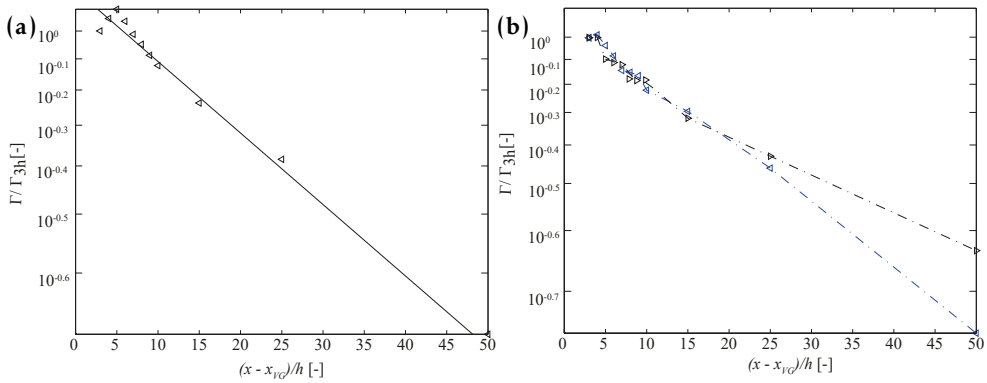

Figure 4.10: (a) Normalised strength decay for vortices for $\varphi = 0°$; (b) Normalised strength decay for the vortices of the skewed pair with $\varphi = 10°$: strong (◃), and weak vortex (▹).

4.4.2. Boundary layer development

Monitoring the spanwise distribution and streamwise evolution of the boundary layer shape factor offers a direct assessment of the impact of the vortex dynamics.

As seen from Figure 4.11, modulations due to asymmetry gradually smear out, and the weak vortex signatures become overshadowed by the strong vortex. Notice that the vortex array increasingly behaves like a co-rotating system, and thus results in a spanwise shifting of the shape factor distribution. Note also that due to the configuration of the measurement setup, flow field images of planes up to $10h$ were partly obstructed with projections of the vortex generators. It was therefore not possible to obtain spanwise averaged values for all streamwise positions.

The streamwise shape factor evolution is shown in Figure 4.12. It is evident that the spanwise-averaged shape factor is not very sensitive to vortex asymmetry. This corroborates the hot-wire measurements of Lögdberg et al. (2009). One noticeable difference is the improvement in the shape factor for $\varphi = 10°$, at least until $15h$ downstream the devices. This is also the case for which suppressed vortex ejection was observed in Figure 4.9. Although this causality cannot be ascertained, the concurrent occurrence of suppressed vortex ejection and lower persisting shape factor prompts further investigation into the vortex dynamics.

4.5. Vortex Modelling

As discussed prior, aside from the added computational effort of CFD, a vortex modelling approach follows naturally for our skewed inflow scenario with embedded streamwise vortices. To this end we will next develop and validate a periodic point vortex model.

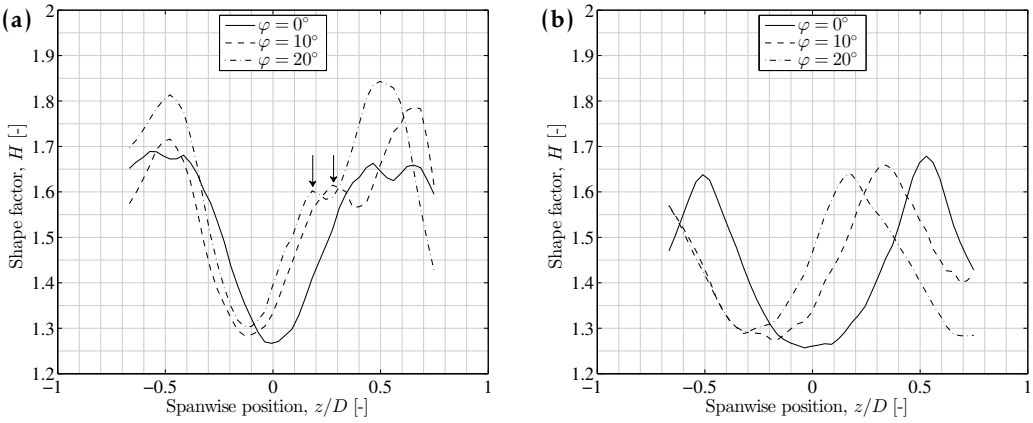

Figure 4.11: Spanwise shape factor distribution for the axial and skew cases: (a) $10h$ and (b) $25h$ streamwise positions.

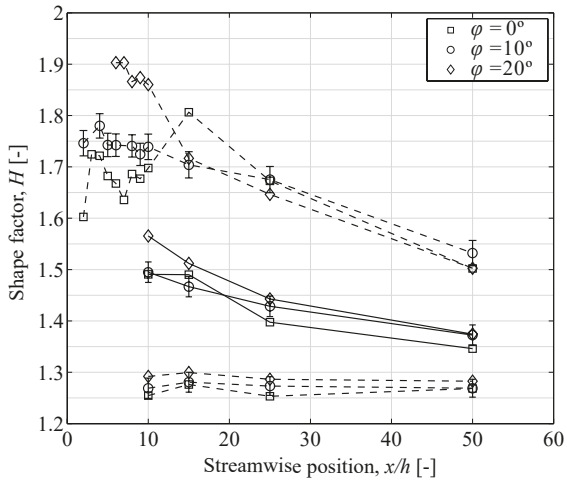

Figure 4.12: Streamwise evolution of the boundary layer shape factor. Solid lines represent the spanwise-averaged value and dashed lines indicate the upper and lower bounds (corresponding to the peaks and troughs of Figure 4.11).

4.5.1. Vortex model

To offer insight into the dynamics observed in the boundary layer measurements, the wake flow induced by the array visualised in Figure 4.6 is numerically modelled by a system of asymmetric vortices using a periodic four-vortex system. This system contains the primary vortices (A,B) and their images (a,b), as depicted in Figure 4.13. The streamfunction $\psi(z,y)$ for a single periodic point vortex array as given in Saffman (1992) is

$$\psi(z,y) = -\frac{\Gamma}{4\pi}\ln\left[\cosh\kappa(y-y_0) - \cos\kappa(z-z_0)\right] \tag{4.11}$$

where Γ is the vortex strength or circulation, (z,y) are the planar coordinates and $\kappa = 2\pi/D$ defines a spatial frequency, or wave-number, of the infinite vortex array. The partial derivatives of (4.11) yield the velocities induced by a single point vortex array. Summing the contributions from all base vortices according to the system depicted in Figure 4.13, the dynamics of the i^{th} vortex (A or B) are given by

$$\begin{aligned} w_i(z,y) &= \frac{dz_i}{dt} = -\sum_{n=1}^{N}{}' \frac{\Gamma_n}{2D}\cdot G_i^n(z,y) \\ v_i(z,y) &= \frac{dy_i}{dt} = \sum_{n=1}^{N}{}' \frac{\Gamma_n}{2D}\cdot H_i^n(z,y) \end{aligned} \tag{4.12}$$

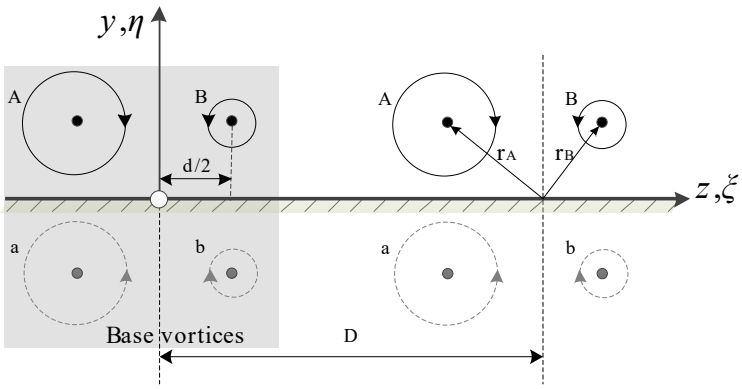

Figure 4.13: Conceptual vortex model with base vortices in shaded region and a periodic image shown with spacing D. Wall images are by definition constrained as $(x_a, y_a) = (x_A, -y_A)$ and $(x_b, y_b) = (x_B, -y_B)$, $\mathbf{r}_A$ and $\mathbf{r}_B$ being independently defined.

in which the velocity influence coefficients

$$G_i^n(z,y) = \left[\frac{\sinh\kappa(y_i - y_n)}{\cosh\kappa(y_i - y_n) - \cos\kappa(z_i - z_n)}\right]$$
$$H_i^n(z,y) = \left[\frac{\sin\kappa(z_i - z_n)}{\cosh\kappa(y_i - y_n) - \cos\kappa(z_i - z_n)}\right] \tag{4.13}$$

where the singular term for which $n = i$ is omitted, as indicated by the primed sum. Practically, these equations describe the dynamics of N infinite vortex arrays, each with an internal spacing D. This is a well known general result (see e.g. Pozrikidis, 2009), and as seen in the opening section, has been applied to study different problems in fluid mechanics. Furthermore, to address the specifics of the problem, the vortex strength is retained in the sum as we wish to obtain a system parametrised by the relative strengths. Following the convention introduced in this chapter, γ will represent vortex strength ratio Γ_B/Γ_A, where we consider that $|\Gamma_B| \leq |\Gamma_A|$, without loss of generality. Here we draw a parallel to the work by Basu (2014). In the latter, the symmetrical, periodic, four-base vortex system chosen to represent the laminar bluff-body wake is mathematically equivalent to the present vortex model (see Figure 4.13). The bluff-body wake centreline in the referenced work corresponds to the ground plane in the present context and the implied symmetry reduces both systems to an identical $N = 2$ system. One notable difference is that the majority of the literature on point vortex models considers primary vorticity normal to the mean convective flow. In the present context, the primary streamwise vorticity and mean convective flow are of course aligned.

We continue to non-dimensionalise the kinematic equations by defining simple scaling quantities. Normalising the spatial coordinates (z, y) by the length scale $1/\kappa$,

we obtain $\xi = \kappa z$, $\eta = \kappa y$. A time scale $\tau = D^2/(\pi\Gamma_A)$ is also established, such that $T = t/\tau$. Substituting these definitions in (4.12), we obtain the form

$$\left.\begin{aligned} \frac{d\xi_i}{dT} &= -\sum_{n=1}^{N}{}' \frac{\Gamma_n}{\Gamma_A} \cdot G_i^n(\xi,\eta) \\ \frac{d\eta_i}{dT} &= \sum_{n=1}^{N}{}' \frac{\Gamma_n}{\Gamma_A} \cdot H_i^n(\xi,\eta) \end{aligned}\right\} \quad \text{where} \quad \frac{\Gamma_n}{\Gamma_A} = \begin{cases} \pm\gamma & \text{for } n = B,b \\ -1 & \text{for } n = a \end{cases} \tag{4.14}$$

where we note that, by definition, the mirror vortex strengths are simply $\Gamma_a = -\Gamma_A$ and $\Gamma_b = -\Gamma_B$. Trajectories are obtained through the time-integration of the velocity induced at each base-vortex location, which is determined through equation (4.14). The system of ordinary differential equations is integrated in time using a fourth-order Runge Kutta scheme. Using a sufficiently small time step, a solution is obtained within a few seconds of computational time.

Note that since we assume a decoupling of the 2D flow field from the out-of-plane flow, we can equivalently integrate spatially (in the out-of-plane coordinate, x) by considering a representative convective velocity. This velocity can then be a prescribed constant, or more appropriately, a boundary layer velocity distribution superposed with a Batchelor-vortex axial velocity profile (Velte et al., 2008).

4.5.2. Numerical Results

Model Verification

A simple verification step is presented to demonstrate correct implementation of the model. Recall that for the trivial case of equal strength and oppositely signed vortices ($\gamma = -1$), Jones (1955) found that the system dynamics reduce to an integrable (exact) ODE. Implementation of the present PPVM is therefore verified with this analytical result. The vortex paths projected in the z-y plane are given by the exact expression

$$\operatorname{cosec}^2\xi + \operatorname{cosech}^2\eta = C \tag{4.15}$$

where C is a conserved quantity determined by the initial vortex positions (Jones, 1955). The numerical (4.14) and analytical (4.15) results are shown in agreement in Figure 4.14. From these graphs it is clear that for this configuration, vortices experience an initial wall-ward motion, followed by lateral displacement and ejection under the influence of the wall and adjacent pairs. The final approach is an asymptotic path away from the wall.

Influence of vortex row separation, for $\gamma = -1$

The relative starting position of the vortex arrays essentially determines the ensuing motion. Thus for this part of the analysis, vortex trajectories were obtained through

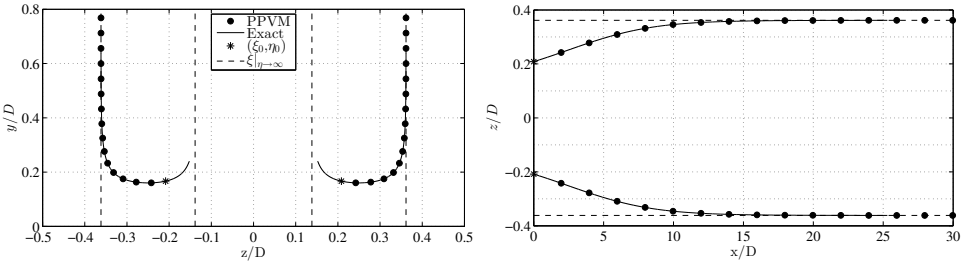

Figure 4.14: Verification of frontal (*left*) and planar (*right*) projected trajectories of the present PPVM with the analytical results (equation 4.15). Single trajectory shown for $K = 1.71$, for $(\xi_0, \eta_0) = (\pm 5\pi/12, \pm\pi/3)$.

numerical integration of Equation 4.14 for a total duration $\mathcal{T}$. Cases treated in this section pertain to $\gamma = -1$. With a sufficiently discretised phase space, a regime diagram as shown in Figure 4.15 can be produced. Every point in this map is the result of a simulation conducted for a particular combination of $(\Delta z, \Delta y \mid \gamma = -1)$. A contour is fitted to the discrete simulation values to produce this map after binning for the different classes of motion.

For oppositely signed and equal strength vortices, two regimes of motion emerge, each of which describes trajectories of qualitatively similar behaviour. These regimes are displayed in Figure 4.15. For intermediate spanwise spacings $\Delta z/D$, with small and large wall-normal separation $\Delta y/h$, vortex rows follow characteristically orbital motions. The initial positions giving rise to this motion are identified with Regime I. Sample trajectories for this motion are shown in Figures 4.16(a) and 4.16(d). The vortices trace cyclic paths, the properties of which are determined by the initial conditions. In these graphs, the base vortices are illustrated along with the mirror counterparts located on either side at $\pm D$ for illustrative purposes. Later on we will see that for all $-1 < \gamma < 0$, the vortex rows describe orbital motion for all $(\Delta z, \Delta y)$. In the ideal scenario we consider vortex generators to be identically sized and perfectly spaced. In practice, the trailing edges may be misaligned and vane height differences might exist. These differences are the physical interpretation of the different $(\Delta z, \Delta y)$-combinations in discussion.

The hatched area, Regime II, exists for intermediate values of $\Delta y/h$, for all $\Delta z/D$. This second regime represents a different type of motion in which vortex trajectories all follow a translating path, oriented according to the value of vertical displacement Δy. The resulting planar trajectories corresponding to operating points within this regime are illustrated in Figures 4.16(b) and 4.16(c). For the simple case of $\Delta y/h = 0$ (along the dashed grey line in Figure 4.15), the vortex rows essentially drive each other away from the wall, normally, such that the row separation is bounded and becomes gradually constant. This essentially corresponds to the verification plots from Figure 4.14.

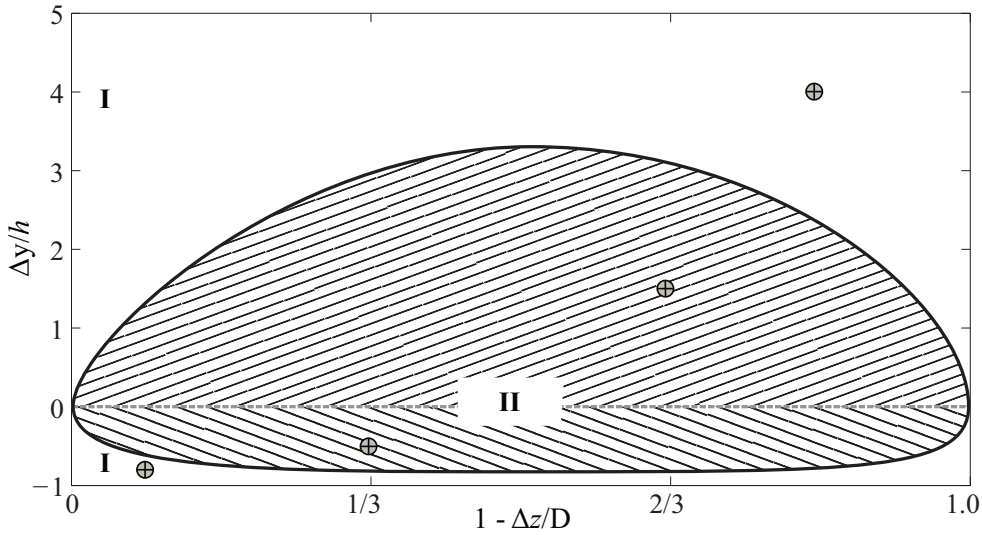

Figure 4.15: Regime diagram in $(\Delta z/D, \Delta y/h)$ space for $\gamma = -1$. Area enclosed by heavy black contour indicates translating trajectories (Regime II). The orientation of hatched lines are only for indication of the general skew direction, which reverses on either side of the dashed grey line; the latter represents a vertical trajectory. Regime (I) outside the hatched area represents orbital trajectories. Example trajectories are sampled at the four indicated cross-hairs.

Influence of vortex strength ratio, γ

In the previous section it was mentioned that any excursions from $\gamma = -1$ result in an orbital type motion. Two combinations of $(\Delta z_0/D, \Delta y_0/h)$ previously sampled in the translating regime ((b) and (c) in Figure 4.16) are chosen to illustrate this fact. Trajectories for these initial conditions are shown for two values of γ in Figure 4.17. All paths are now clearly cyclic in nature. As seen from Figures 4.16 and 4.17, we can expect a wide range of orbital behaviour. However, thus far, all orbiting trajectories have been treated as one category. It is clear that further classification is possible by analysing the peak amplitude $\Delta y_{max}/2$ and cyclic frequency of the motion $\widetilde{t}$. Note that in contrast to the large majority of works in literature studying planar wakes evolving along the same plane (e.g. Stremler et al., 2011; Harris and Williamson, 2012; Basu and Stremler, 2015), the present flow is an idealisation of a three-dimensional evolving flow. As a simplifying assumption, the in-plane vortex motions and the out-of-plane flow have been decoupled. Thus it may be useful to consider the 'orbiting' in this context as a general term encompassing helical or spiralling motions.

Two additional properties of the orbital trajectories are therefore established: (*i*) the normalised peak trajectory amplitude, $\mathcal{A} = \Delta y_{max}/2h$ and (*ii*) the normalised period of the orbital motion, $\mathcal{P} = \widetilde{t}/(L/U)$. These are illustrated in Figure 4.18 for the weak vortex with varying γ. The plots in this figure were again obtained by a set of simulations for each $(\Delta z, \Delta y \mid \gamma)$.

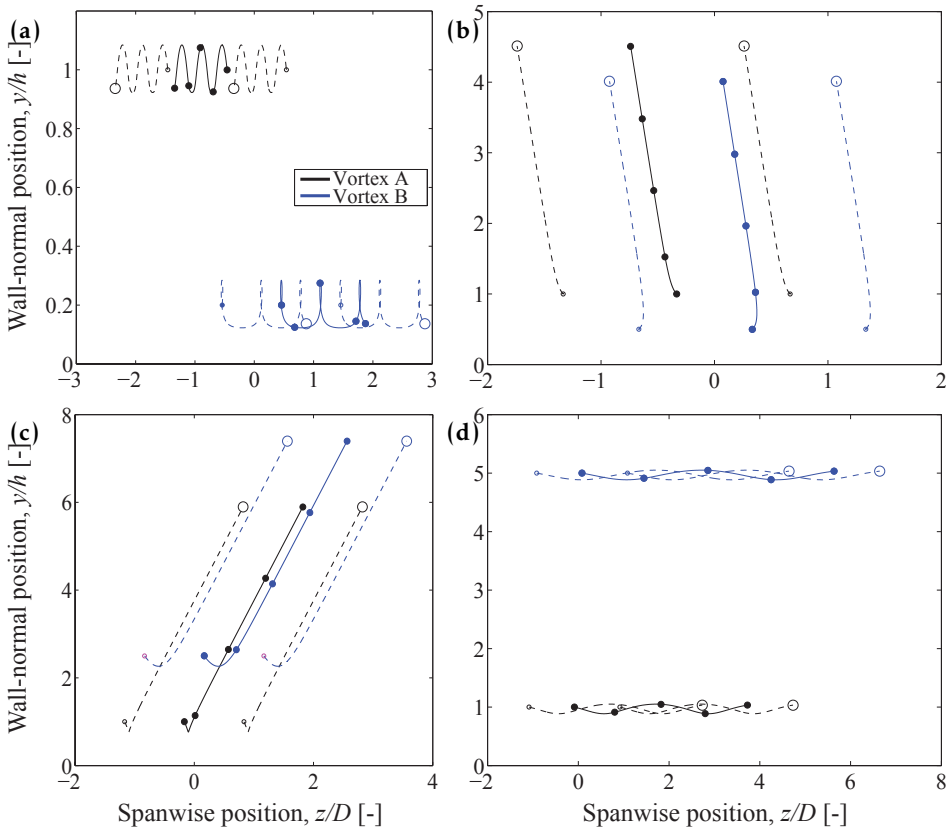

Figure 4.16: Trajectories for $\gamma = -1$, for different initial conditions $(\Delta z_0/D, \Delta y_0/h)$: (a) 11/12,–0.8; (b) 2/3,–0.5; (c) 1/3,1.5 and (d) 1/6, 4.0. Filled markers and solid lines represent the base vortices; empty markers and dashed lines represent their adjacent periodic counterparts. Markers are spaced at $0.25\mathcal{T}$. Trajectories (a) and (b) are shown for a total time 1L/U, (c) for 5L/U and (d) 10L/U.

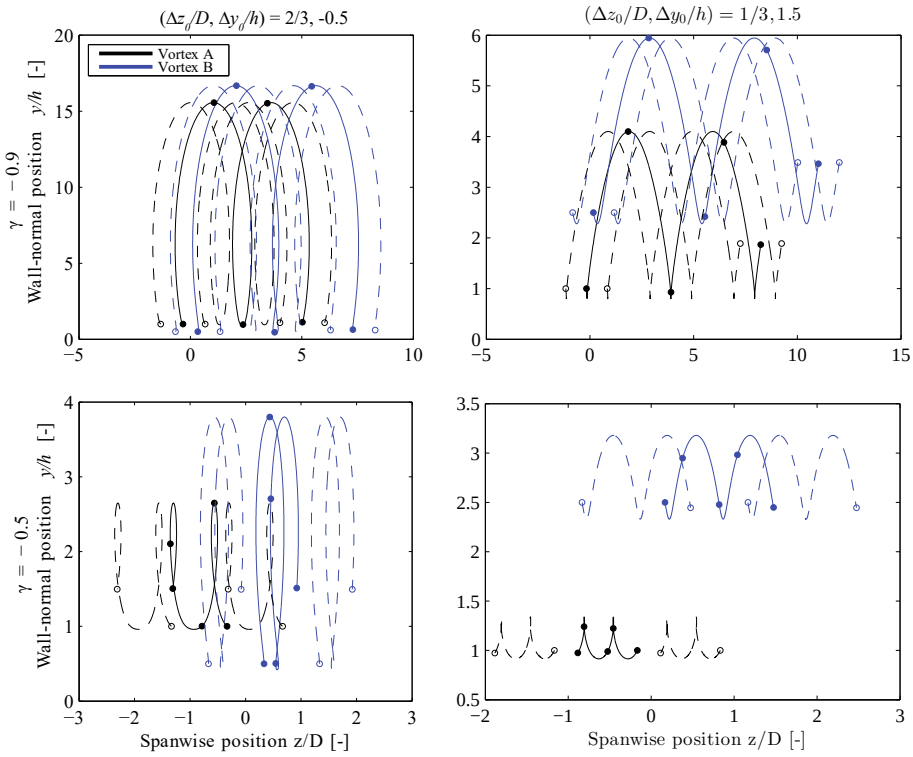

Figure 4.17: Trajectories for $\gamma = -0.9$ (*top*) and $\gamma = -0.5$ (*bottom*). Different initial conditions $(\Delta z_0/D, \Delta y_0/h)$ are prescribed: $2/3$,-0.5 (*left*) and $1/3$,1.5 (*right*). Filled markers and solid lines represent the base vortices; empty markers and dashed lines represent their adjacent periodic counterparts. Markers are spaced at $0.25T$. Trajectories for $\gamma = -0.9$ and -0.5 are shown for a total time 20L/U and 5L/U.

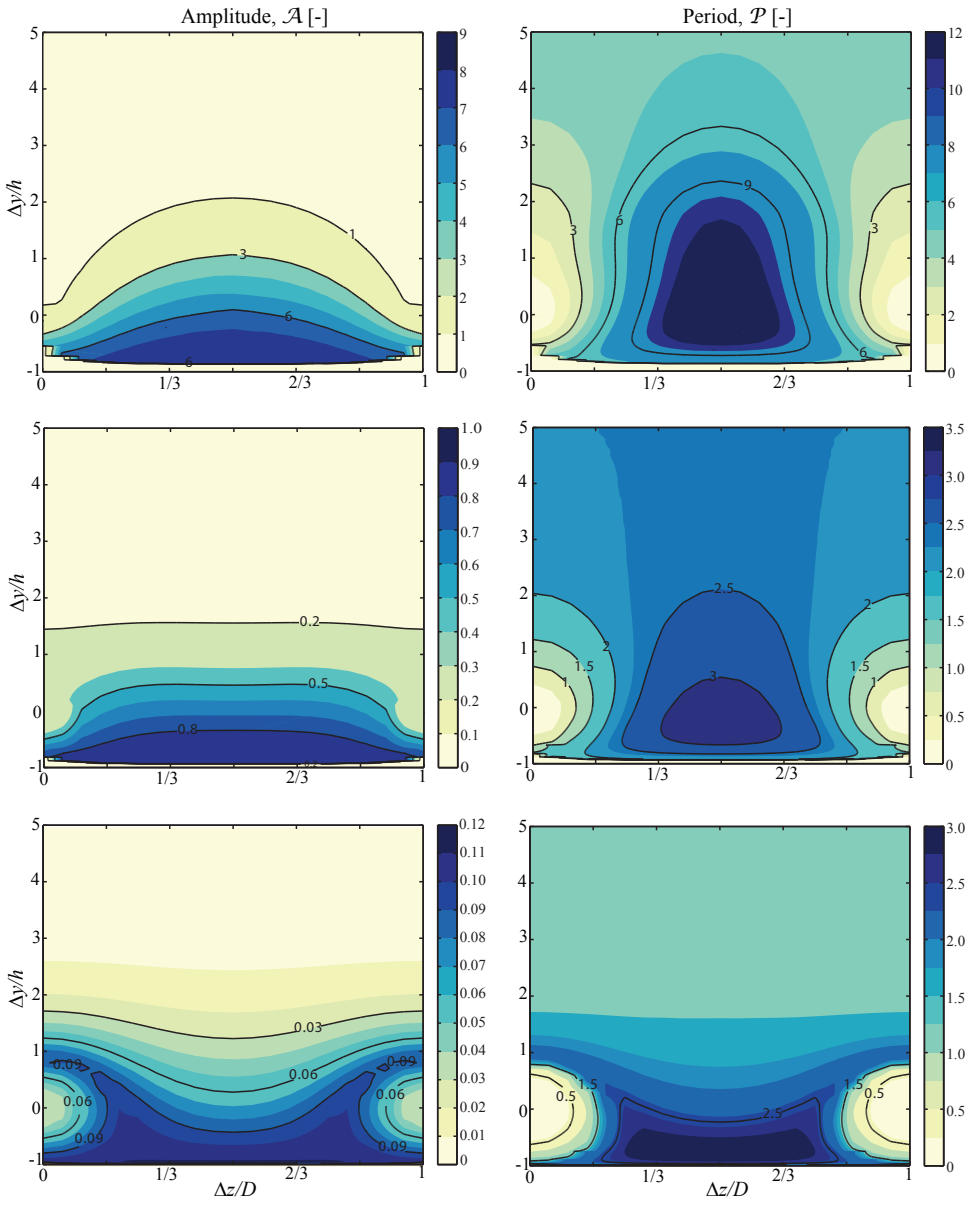

Figure 4.18: Amplitude (*left*) and period (*right*) of orbiting trajectories of the weak vortex for different values of γ: (*top*) −0.9; (*mid*) −0.5; (*bottom*) −0.1.

Thus far we have noted that any slight departure from exactly equal and opposite vortices, will also result in orbital motion. However from Figures 4.19, we notice how the maximum magnitudes of the amplitude and period decrease as $\gamma \to 0$. The first case, $\gamma = -0.9$ is chosen as a value close to -1, as might for instance occur in VG experiments due to small unintended vane misalignments. Despite classification into an orbital trajectory, we notice how the amplitude is the largest of the three presented cases, and at least around 5 times the typical VG height, for intermediate $\Delta z/D$ and small $\Delta y/h$, the latter being representative of typical VG geometries. In the measurements of Lögdberg et al. (2009), a wall-normal displacement of less than $1h$ at $400h$ downstream was observed. This slow ejection rate signifies that the amplitude scale predicted by the model, is far larger than that permitted in the real flow due to viscous effects. In any case, it would occur on much longer length and time scales than observed in practice. For intermediate values of γ, at -0.5 (middle panels, Figure 4.18), the amplitude scale decreases to the order of the initial vortex core radius (or vane height), and further still for $\gamma = -0.1$. For $\gamma = -1$ in Figure 4.15, orbital motion would only occur for impractically low or high values of $\Delta y/h$. However, results shown in Figure 4.18 imply that with moderate γ, orbital motion on the scale of the initial vortex wall-normal position becomes possible, and therefore, potentially relevant for practical applications.

In Figure 4.17, the effect of γ is elucidated for two different initial positions, $(\Delta z_0/D,\ \Delta y_0/h) = (1/3,1.5)$ and $(1/6,4.0)$. These initial conditions respectively produced translating and orbiting trajectories for $\gamma = -1$. This is noted in the trends as the amplitude and period become degenerate (shown here as null) at $\gamma = -1$ for the translating case, whereas the second sampled initial condition shows orbital behaviour (non-zero, finite $\mathcal{A}$ and $\mathcal{P}$). The characteristics of the strong and weak vortices are shown separately in Figure 4.19 and are clearly distinguishable. The weaker vortex row experiences a larger amplitude under the influence of the stronger vortex row for the initial condition $(1/3,1.5)$. The second initial condition $(1/6,4.0)$ shows a more complex behaviour as the relative amplitudes depend on γ. Note also that as $\gamma \to 0$, one vortex row becomes infinitely weaker than the other. This system would exhibit characteristics of a single co-rotating vortex row and is considered degenerate for the present study. It is therefore consistent that differences between the two vortices grow with decreasing $|\gamma|$, in the absence of viscous dissipation. The trajectory period is identical for both vortices but is determined by the initial conditions and strength ratio. These general observations are a direct consequence of the conservation of linear impulse for the vortex system.

4.5.3. Comparison with measurements

The model will next be used to analyse the skew case $\varphi = 10°$. Recall that vanes in each VG pair are nominally oriented at $\beta = \pm 18°$; therefore skewing the pair increases the angle on one vane, and reduces it on the other. The vortex strength and core positions evaluated at the $3h$ station were used to initialise the simulations with the following boundary conditions: $(\Delta z_0/D, \Delta y_0/h \,|\, \gamma) = (1/3, -1/10 \,|\, -1/3)$

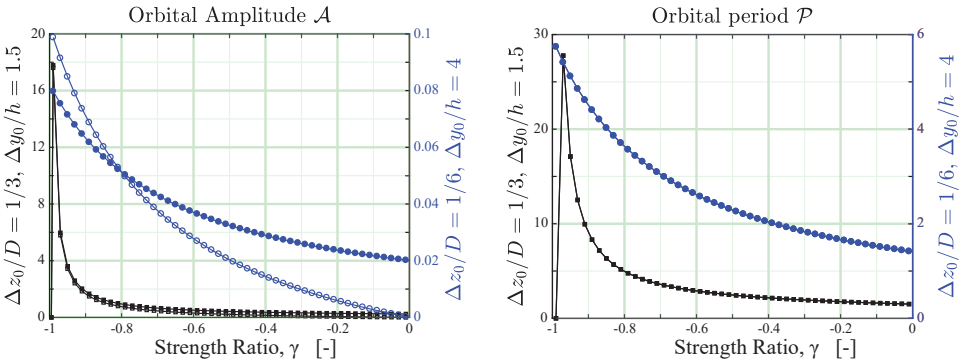

Figure 4.19: Influence of the vortex strength ratio on the orbital amplitude (*left*) and period (*right*) for the initial positions indicated on the ordinates. Solid and open symbols represent the weak and strong vortices respectively.

for $\varphi = 10°$.

Results are first shown for $\varphi = 10°$ in Figure 4.20. The analytical streamfunction (4.11) is evaluated at the measured vortex positions at $10h$ downstream and compared with the experimental flow field in the form of in-plane streamlines. Note that streamline spacing is the same for computations and measurements. Differences are immediately visible, most notably due to experimental limitations, such as near wall data availability, a slight background cross-flow, and the fact that small misalignments in the VG placement result in slightly different initial vortex positions. This is also evident from differences at the side boundaries in Figure 4.20. Nonetheless, there is a good degree of qualitative similarities between the measured and modelled flow.

For the present case, path asymmetry arises not only due to the unequal strength of the vortices. The centre of the weak vortex lies consistently below the stronger vortex in the measurements. As we have seen, the array dynamics are highly sensitive to offsets in wall-normal separation, in addition to the strength ratio γ. Referring to the orbital characteristics of Figures 4.18 and 4.19, we confirm that these starting conditions predict an orbital amplitude of around $0.5h$. The period appears higher than the actual length scale of the experiment and occurs due to the fact that we disregard the boundary layer velocity profile and axial velocity associated with the vortex. Both these would impose a smaller convective speed and thus the time scale would be higher. However, the measured and predicted orbiting regime of motion are similar. The trend in the strong vortex path shows good overall agreement but the model predicts a slower ejection rate, as shown in Figure 4.20. This is likely due to the diffusion and growth of the vortex core, which is effectively manifested as a weak wall-normal motion.

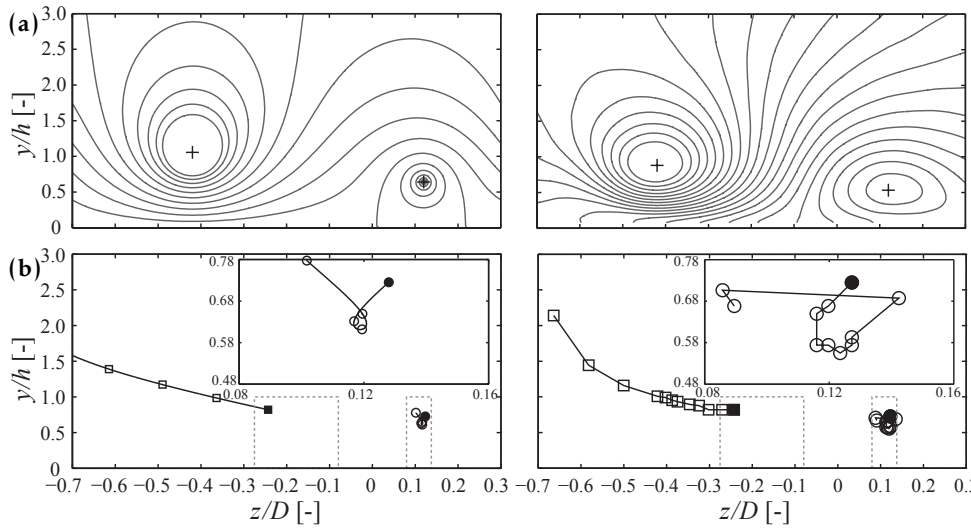

Figure 4.20: Case $\varphi = 10°$: (a) Streamfunction due to an unequal periodic array of point vortices; computed streamfunction (*left*) and measured 2D streamlines $10h$ downstream VG trailing edge (*right*) with crosses representing vortex centres; (b) primary base-vortex trajectories according to computations (*left*) and measurements (*right*); inserts show details of the weak vortex path, filled markers indicate initial vortex positions and dashed-grey contours represent the projected VG surface.

4.6. Discussion

Despite the qualitative flow agreement between the inviscid vortex model and the measured core trajectories, the observations should be interpreted with prudence. We therefore contrast these observations with the measurements of embedded *symmetric* streamwise vortices of Lögdberg et al. (2009) and offer some interpretations on a possible connection. In the latter study, measurements indicated a lateral rebound, or "hook-like" motion of symmetric vortices in the far region, becoming noticeable only after $50h$ for a symmetric VG array. The authors attributed this lateral inversion to the growth of the vortices in the boundary layer, which forces the vortices away from their inviscid trajectories to accommodate within the boundary layer. In the present case, the weak vortex undergoes a complete orbit within the $50h$ measurement region, comparable with model predictions, and much earlier than that reported in Lögdberg et al. (2009), suggesting a different mechanism. A key difference is of course the asymmetry in the present case, which we know from the inviscid model to cause orbiting regimes of motion. It is therefore conceivable that the inviscid vortex dynamics and viscous-driven lateral drifts constructively combine to give the orbital trajectory that has been observed.

Of course, the PPVM carries a number of simplifications which will limit practical applicability. Vortices are represented as singularities whose strengths implicitly remain constant in time in the absence of viscous dissipation. Spatial periodicity

is imposed through the use of the infinite array solution (4.11), thus preventing intra-row interaction. Cross-flows have also been disregarded in this study. It has so far been presumed that asymmetric vortices result from off-design conditions and other non-idealities originating from the external flow. However, vortex breakdown can also lead to complex interactions. In practice, adverse streamwise pressure gradients can cause atypical transitional behaviour of the vortex core, a form of vortex breakdown (Escudier, 1988). In fact, this was recently evidenced as an intermediate core growth stage in Velte et al. (2011). The associated peak vorticity would also change, as would the vortex dynamics. Such transitional behaviour cannot be accounted for in the present model, and would likely invalidate predictions. The appearance of additional secondary structures is expected to influence the array dynamics but unless explicitly introduced, are outside the capabilities of the PPVM because viscous effects have not been considered.

4.7. Conclusion

As a first step towards understanding the implications of off-design conditions on VG arrays, the complex blade flow has been simplified to a case of an asymmetric vortex array.

Spanwise planes up to 50 device heights downstream of a VG array were measured using PIV on a zero-pressure gradient, flat plate turbulent boundary layer. Vortex asymmetry was created by rotating each individual VG pair of height $h = 5$mm ($h/\delta = 0.25$) in an attempt to mimic the effects of skewed inflow. For a particular skew angle $\varphi = 10°$, suppressed vortex ejection was observed for the weaker vortex of the pair. Specifically, this vortex undergoes an orbiting (or spiralling) motion, thus maintaining its position closer to the wall. This appears to correspond with the slightly lower (and hence superior) shape factor which was measured for the same flow.

In support of the measurements, the flow was modelled using a periodic point vortex model with considerations of skewed inflow. The results have yielded useful insights into the dynamics of asymmetric vortex arrays. An exploration of $(\Delta z, \Delta y, \gamma)$-space exposed translating and orbital regimes. The latter ensues for all unequal strength vortices. However, the predicted length and time scales for large $|\gamma|$ are far greater than the initial vortex positions. Thus, experimentally measured wakes, even in the absence of viscous effects (or high Reynolds numbers) are unlikely to reveal these cyclic motions. For intermediate values of γ though, these scales rapidly decrease to the order of the initial vortex positions. This was validated with the experimental observations.

From the perspective of VG design robustness, the uncertainty in vane misalignment is probably in the order of a few degrees, which means that a realistic range of γ is probably much closer to unity. Thus some of the cases considered here are more likely worst case scenarios. Furthermore, the model requires further validation and the role of viscous diffusion explored for its impact on the apparent

motion of the vortices. Nonetheless, through this analysis we have demonstrated that more complex vortex interactions may arise when considering asymmetry or similar effects, and may need to be considered for effective VG design.

III

Separation control with vortex generators

5

Experimental parameter study of vortex generators on the DU97-W-300 airfoil

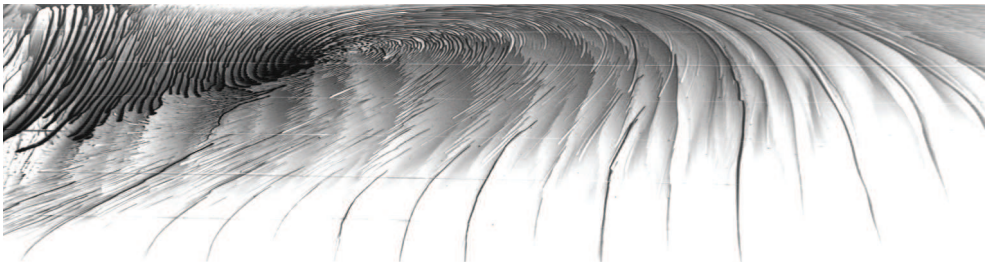

Interaction of corner vortex and streamwise vortices on the suction side of the DU97-W-300 airfoil.

This chapter presents an applied study of flow separation control using vortex generators on the DU97-W-300 airfoil. The airfoil performance is evaluated in the Low Turbulence Tunnel using model and wake pressure measurements and surface oil flow visualisations. Performance sensitivity to different VG configurations is analysed, including vane angle and height, vane-pair skewness and array spacing. The effects of a VG mounting strip and airfoil surface roughness are also assessed. Furthermore, a method to estimate the vortex strength from oil streak analyses and vortex theory is demonstrated. The statistical analysis of the airfoil lift during stall provides additional insight into stall dynamics to complement the static performance analysis. This chapter has been adapted from (Wiley) *Wind Energy*, 21(9), 745-765, 2018.

5.1. Introduction

5.1.1. Background

Various fidelity models have been developed to model VGs, such as (in increasing fidelity) integral boundary layer approaches (Kerho and Kramer, 2003), simplified and fully-resolved CFD methods (Bender et al., 1999), and scale-resolving numerical computations (Spalart et al., 2015). After mostly general and proof-of-concept type VG studies in the 1980s and 90s, advancing flow measurement techniques explained the stall delay mechanism in terms of the flow physics. Surprisingly, this more recent empirical evidence has hardly produced better informed flow models for the VGs. One barrier is the lack of validation means through systematic, applied experimental parametric studies, especially on thick airfoils, relevant for wind energy applications.

5.1.2. Objective and outline

The complex flow phenomena associated with VGs have hampered the robustness and effectiveness of engineering models. Numerical tools will therefore play an important role in the continued development of VGs for flow separation control, but better means of validation for thick wind energy airfoils are necessary. This chapter bridges this gap by addressing the following:

1. What is the performance sensitivity of a thick airfoil section to different vortex generator designs?
2. What is the relative importance of the VG design parameters?
3. How are loading dynamics altered in the presence of VGs?

To this end, the present work studies the effect of various passive vane-type VGs on the performance of the DU97-W-300 airfoil at $\mathrm{Re}_c = 2{\times}10^6$ (note that the goal is not to find an optimum VG geometry). This airfoil, shown in Figure 5.1a, was designed and tested by Timmer and van Rooij (2003) for inboard wind turbine blade sections. The approach, including VG design and experimental procedure are discussed in section 5.2. Oil flow visualisations (OFV) and polars are presented in section 5.3 and Appendix C of this thesis. Section 5.4 presents a discussion of the unsteady loading characteristics and conclusions follow in section 5.5.

5.2. Approach

5.2.1. Airfoil model and wind tunnel facility

The DU97-W-300 airfoil was tested in the closed loop, Low Turbulence Tunnel at Delft University of Technology. The test section is octagonal, measuring 1.80m × 1.25m, and 2.60m long. The model had a chord $c = 0.65$m, a thick trailing edge of 1.7% chord and spanned the height of the test section, giving an aspect ratio

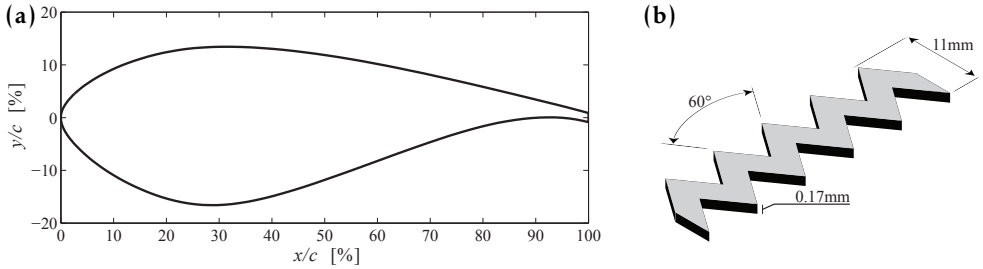

Figure 5.1: (a) DU97-W-300 model profile; (b) zig-zag tape geometry.

of approximately 1.92. A traversable wake rake for assessing the total drag was positioned approximately 60%c downstream the airfoil trailing edge. All polars were acquired at $\mathrm{Re}_c = 2\times10^6$ (Mach number 0.13), for which the tunnel turbulence levels were below 0.1%. Model blockage in the test section was around 10% near $C_{l|\max}$ for the uncontrolled airfoil. Polars were acquired in the freely transitional regime, as well as in forced transition. The latter was enforced using zig-zag tape on the airfoil upper surface along the entire wing span. As illustrated in Figure 5.1b, the thickness of this strip was 0.17mm, with a width of 11mm, its leading edge fixed at 5% chord from the airfoil leading edge. The uncontrolled airfoil polars are given in Figure 5.2 and compared with viscous-inviscid simulations performed in RFOIL (van Rooij, 1996). Transitional simulations with the e^N method (van Ingen, 1956) were produced using a critical amplification factor $N = 11$. Rough calculations initiate a turbulent boundary layer on the suction side at the location of the ZZ tape. Note also the consistency between the present clean performance and the original liquid manometer measurements of Timmer and van Rooij (2003). In keeping with prior terminology, 'clean' and 'tripped/rough' pertain to the state of the boundary layer. The presence of the VGs is described as a 'controlled' case; 'NoVG' refers to the uncontrolled airfoil.

5.2.2. Instrumentation and data acquisition

The normal and tangential airfoil loads (C_n and C_t) were determined through the model and wake rake pressure measurements, acquired through a DTC INITIUM data acquisition system. A total of 102 surface pressure taps surrounded the airfoil model, including one in the mid-section of the blunt trailing edge. The wake rake was fitted with 67 total pressure and 16 static pressure tubes. The lift was evaluated as in Figure C.6 according to

$$C_l = C_n / \cos\alpha - C_d \tan\alpha \tag{5.1}$$

where C_d was determined from the wake rake or model pressure drag. The final lift and drag coefficients were obtained after modification through wind tunnel corrections for model and wake blockage, and streamline curvature (Allen and Vincenti, 1944; Acum et al., 1966). The cross-over point is typically taken just prior

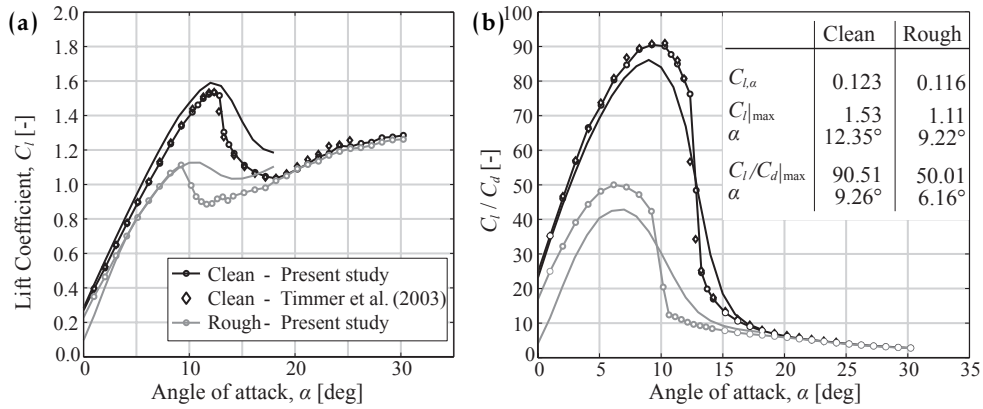

Figure 5.2: (a) Lift polar and (b) aerodynamic efficiency for clean and rough conditions. Symbols and tabulated data represent measurements, plain lines represent RFOIL predictions.

to $C_{l|\max}$. The spanwise uniformity of the uncontrolled flow was assessed with wake rake traverses at different angles of attack. One such pass is shown in Figure 5.3a for $\alpha = 6.2°$. In the attached regime, the flow is sufficiently uniform. On the other hand, vortex generators induce a three-dimensional flow, but arranged in a uniform array, the flow becomes spanwise-periodic. To assess the airfoil drag with VGs from the wake rake, a spanwise traverse was conducted for each angle of attack at 1.2mm/s and spanning a range of three VG pair spacings ($3 \times D$). The resulting spanwise averaged value, C_d, was then considered as the representative sectional drag. A typical wake scan is shown in Figure 5.3a at three angles of attack. At higher angles of attack, and thus stronger adverse pressure gradients, the vortices tend to diffuse more and thus leave a weaker signature (Westphal et al., 1987). The peaks in the drag signal correspond to the upwash regions. Here, adjacent common upwash vortices eject low momentum boundary layer fluid which manifests downstream as a stronger wake deficit. This is further illustrated by wake profiles of total pressure C_p^T in Figure 5.3b, sampled at an outflow and inflow position (peaks and troughs of Figure 5.3a). Notice how the wake profile variations largely materialise from the suction side, where the VGs are located.

For uncontrolled cases, pressures for each angle of attack were sampled for 10s before $C_{l|\max}$, and 30s in the stall regime. With VGs, the total sampling time ranged from 45-90s (determined by the duration of the wake rake traverse). Beyond $C_{l|\max}$, the wake rake was not operated due to the extent and unsteadiness of the separating wake. The drag in this operating regime, dominated by pressure drag, was instead assessed from the model surface pressures, giving only the pressure drag component. For this measurement, the sampling time was fixed at 30s. In all cases, the pressures were sampled at approximately 337Hz. The airfoil boundary layer was measured for the uncontrolled flow using the same data acquisition system and using a small traversable total pressure probe with a nozzle of 0.5mm. The complete setup is

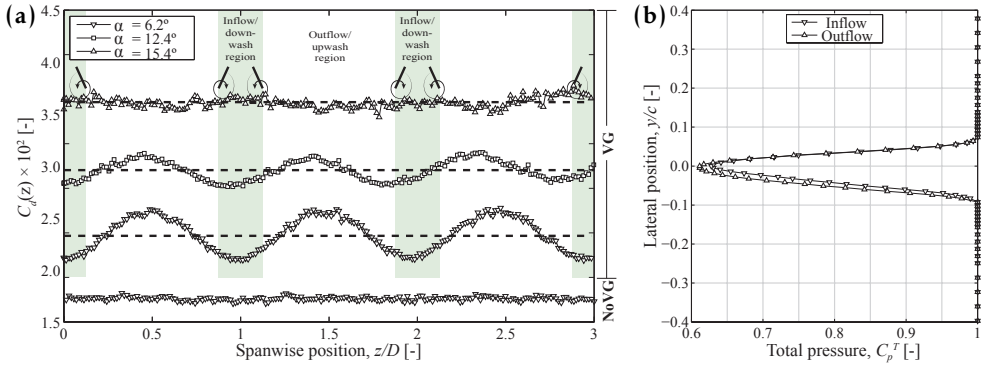

Figure 5.3: (a) A typical drag signal along a wake rake traverse; dashed lines indicate the spanwise averaged value; Case: uncontrolled and VG base design in free transition; (b) Total pressure profile in the airfoil wake sampled at $\alpha = 12.4°$ at an inflow and outflow position along the wing span; The region $y/c < 0$ corresponds roughly to the wake emanating from the suction side of the airfoil. Case: VG base design in free transition.

shown in Figure 5.4b showing the telescopic aid for positioning the probe.

The transition location was assessed using a handheld stethoscope and shown for two Reynolds numbers in Figure 5.5a. Graduations spaced at 5%c intervals on the model increased the precision of the measurements. The results compare fairly well with the expectations, particularly in the linear $C_l - \alpha$ range. The stethoscope was also used to ensure transition behind the ZZ strip; in all cases, transition to turbulence was roughly complete within one strip's width downstream of its trailing edge. Note also that measured transition locations indicate an approximate spanwise-average, as the location of the laminar separation bubble shifts somewhat along the span.

Oil flow visualisations were conducted by first coating the model with a solution of liquid paraffin and fluorescent dye. Pressure orifices were covered to prevent oil seepage during such tests. The model was then illuminated with ultra-violet light and a Nikon DSLR camera used to acquire the images. Spanwise rules equispaced 10% chord were marked to facilitate image analysis. The images are presented in their grayscale format with slightly enhanced contrast.

Experimental error sources and uncertainty

Signal drift occurs due to variations of atmospheric temperature and pressure, as well as heating up of electronic components. This is accounted for by re-biasing the pressure levels before every new run. The resolution of the electronic pressure scanners ranged from 0.2-2.0Pa; the uncertainty in the angle of attack was below 0.01°. Sampling errors were at least an order of magnitude lower due to the large sample size for each data point. The final uncertainty propagation results in a worst case error of 1% for C_p, 0.1% on C_l and 2% on C_d (see Appendix C for a detailed presentation of the uncertainty analysis). The boundary layer probe

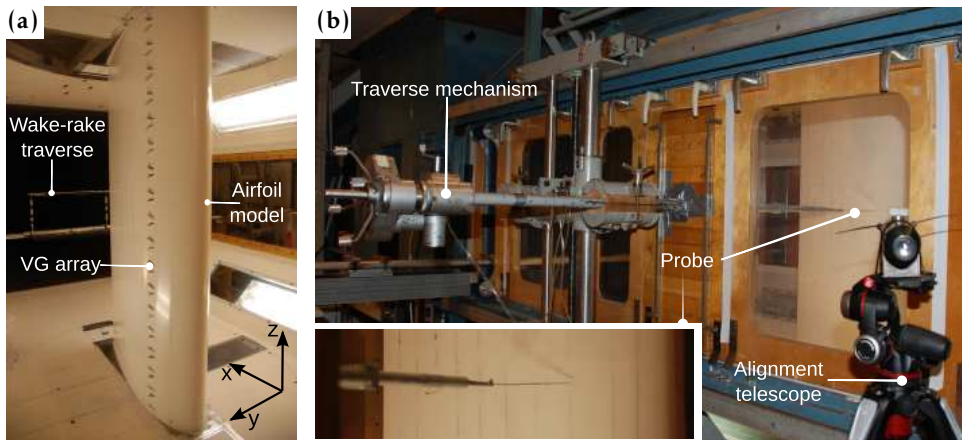

Figure 5.4: (a) Typical test-section setup showing the wake rake aft of the wing section; (b) boundary layer measurement setup.

traverse could resolve 0.01mm, but the uncertainty of the absolute wall position was approximately ±0.25mm. The absolute lift and drag quantities in the stalled regime are less reliable because of unsteady, three-dimensional flow separation.

The periodic placement of VGs gives rise to spanwise-periodic flow and loading. For the wake rake drag, the periodicity was addressed by spanwise-averaging the wake traverses along the VG array. In contrast, the true spanwise-averaged lift is not possible from the measurements due to the staggering of the pressure taps; however, computations showed that vortex-induced disturbances are localised around the vanes and the net effect on the measurements is negligible (Baldacchino et al.,

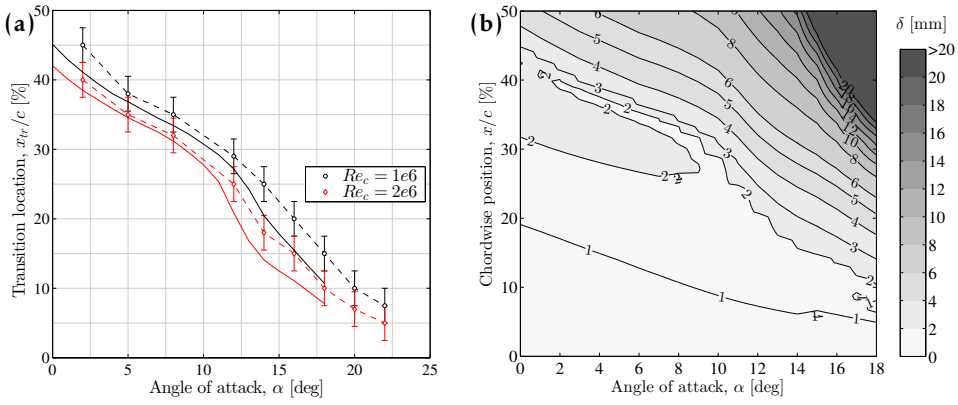

Figure 5.5: (a) Transition location on the airfoil suction side at two Reynolds numbers. Symbols/dashed lines indicate measurements and solid lines represent RFOIL predictions; (b) Boundary layer thickness estimates in $(\alpha, x/c)$ space at $\mathrm{Re}_c = 2\times10^6$ for natural transition.

2016b). Pressure signals disrupted by the VG strips and ZZ tape were replaced by interpolated estimates from adjacent undisturbed signals, whilst the small size (< 0.4mm) and staggered formation of the pressure taps minimized their mutual interference.

5.2.3. Vortex Generators

This section first presents the VG base design and its variants. Dimensions are initially defined parametrically in terms of the vane height h. A final design is then presented in Table 5.1, where the physical dimensions of h are determined based on operational considerations.

Base design and test configurations

The salient VG parameters, summarised in Figure 5.6, pertain to the (*i*) vane geometry, (*ii*) array configuration and (*iii*) skewness (as a simulated external condition). Based on the reviewed literature, the following robust base design for separation control was defined:

(i) $h/c \approx 1\%$, $L = 3h$, $\beta = \pm 15°$, Delta Wing planform (referred henceforth as simply Delta) at $x/c = 20\%$, measured between the airfoil and VG strip leading edges

(ii) $d = 3.5h$, $D = 7h$, counter-rotating, common downwash

(iii) $\varphi = 0°$, axially aligned flow.

This design reflects a commonly employed VG geometry on wind turbine blades. Design variants were then obtained by modifying these parameters relative to the

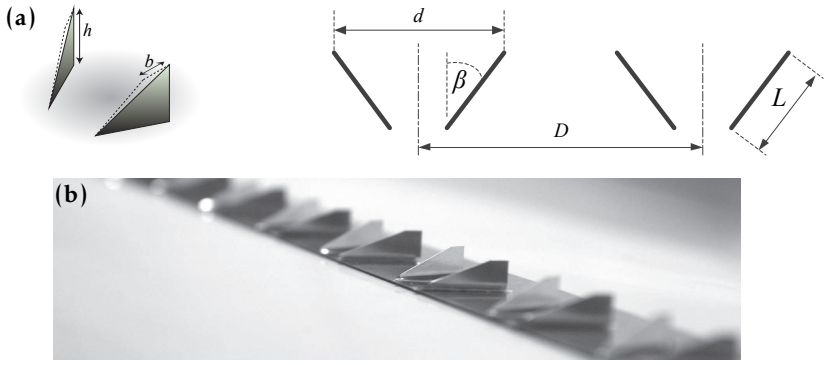

Figure 5.6: (a) Isometric view (*left*) and planar (*right*) schematic of the periodic VG-array arrangement. Nomenclature: h - vane height, b - cropped edge length, d - intra-vane spacing, D - inter-vane spacing, β - geometric vane inflow angle, L - vane length; (b) Mounted cropped-Delta vortex generators.

base design. Three vane heights were investigated, with an additional smaller ($h/c < 1\%$) and larger ($h/c > 1\%$) variant. These were in-turn tested at different chordwise positions, $10\% < x/c < 50\%$, within clean and rough conditions. The remaining variants were only measured in a clean boundary layer at $x/c = 20\%$, with vane angles: $10° < \beta < 25°$, pair angles (or skew): $0° < \varphi < 15°$ and vane lengths: $2h < L < 5h$. A cropped-Delta variation was designed such that $b = 0.2L$ (see Figure 5.6a), resulting in a 20% increase of the vane planform. The configuration was also varied with a larger spacing $D = 10h$, and ensuing CoR and CtR common upwash variants. The complete parameter space is summarised in Table 5.1.

Sizing the vane heights

The independent parameter h was required to dimension the self-similar designs. To determine a range of sensible values for the VG vane heights, it was first necessary to understand the uncontrolled flow. For a given operating point in the post-stall region, the VGs would only work if mounted in front of the mean separation line. At this position, h/δ must be large enough to generate sufficient streamwise vorticity to prevent separation. However, placing the VGs too far forward would incur increasing parasitic drag at lower angles of attack. This is especially true if the array is ahead of the natural laminar-turbulent transition location x_{tr}. Thus, both the boundary layer thickness as well as x_{tr} were required for sizing the VGs.

Measured and predicted transition locations are compared in Figure 5.5a. Increasing the Reynolds number moves x_{tr} forward for a given pressure gradient (i.e. the angle of attack, α). The trend also implies that the more forward the VG mounting location, the larger the additional drag due to the forced turbulent boundary layer. RFOIL is formulated in terms of integral parameters such as the displacement and momentum thickness ($\delta^\star$ and θ). Therefore, the boundary layer thickness may be estimated as

$$\delta = \begin{cases} 2.9\delta^\star & \text{for } x < x_{tr} \quad \text{(laminar)} \\ \theta\left(3.15 + \frac{1.72}{H-1}\right) + \delta^\star & \text{for } x > x_{tr} \quad \text{(turbulent)} \end{cases} \tag{5.2}$$

where the shape factor $H = \delta^\star/\theta$. Blasius' flat plate relation was used for laminar flow (White, 2006) whereas the incompressible entrainment coefficient is used in the case of turbulent flow (Drela and Giles, 1987). For a range of chordwise positions and angles of attack, δ is shown in Figure 5.5b. The predicted variation mirrors that of transition, since at the location of turbulent transition, the size of the boundary layer experiences a faster growth rate. Based on these calculations, the original design specification and manufacturing constraints, VG heights of 2.5, 5 and 10mm were chosen, corresponding to $h/c \approx 0.4\%, 0.8\%$ and 1.6%.

The boundary layer measurements provided some design verification for the actual h/δ. Using the total pressure measured in the boundary layer and the model static pressure at $x/c = 20\%$, the velocity profile $u(y)$ was estimated as

Table 5.1: Overall dimensions of the VG sets in the parameter study. The base design is described in first row (bold).

Shape/Config.	Transition	x_{VG}/c [%]	h [mm]	β [deg]	φ [deg]	d/h [-]	D/h [-]	L/h [-]	d [mm]	D [mm]	L [mm]
Delta/CtR-CD	**Free**	**20**	**5**	**±15**	0	**3.5**	**7**	**3**	**17.5**	**35**	**15**
Delta/CtR-CD	Free/Forced	10:10:40	2.5	±15	0	3.5	7	3	8.75	17.5	7.5
	Free/Forced	10:10:50	5	±15	0	3.5	7	3	17.5	35	15
	Free/Forced	20:10:50	10	±15	0	3.5	7	3	35	70	30
	Free	20	5	±10,12,18, 20,25	0	3.5	7	3	17.5	35	15
	Free	20	5	±15	0:5:15	3.5	7	3	17.5	35	15
	Free	20	5	±15	0	3.5	7	2,4, 5	17.5	35	10,20,25
	Free	20	5	±15	0	3.5	10	3	17.5	50	15
Cropped-Delta/ CtR-CD	Free	20	5	±15	0	3.5	7	3	17.5	35	15 ($b = 3$mm)
Delta/CtR-CU	Free	20	5	∓15	0	3.5	7	3	17.5	35	15
Delta/CoR	Free	20	5	15	0	–	7	3	–	35	15

shown in Figure 5.7a. The boundary layer edge was identified when the spanwise vorticity ($\approx |-\partial u/\partial y|$) dropped below 1% of its maximum and shown in Figure 5.7b. The rapid evolution of δ after $\alpha = 12°$ indicates a decambering effect due to flow separation, and at $\alpha = 16°$, $\delta \approx 4.5$mm. Therefore, the reference boundary layer thickness was arbitrarily defined for $(\alpha, x/c) = (12°, 20\%)$, where $\delta \approx 2$mm. This reference condition represents the maximum lift angle for the clean uncontrolled airfoil, at a position residing ahead of the small trailing edge separation zone. This gives $h/\delta \approx 1.25 \pm 0.03, 2.50 \pm 0.06$ and 5.00 ± 0.12. Note that VG cases operating in rough conditions will experience a slightly thicker boundary layer, lowering these reference values slightly. Note also that at $\alpha = 16°$, the airfoil is stalled and δ will vary more along the span due to three-dimensional separation, compared to pre-stall angles of attack.

VG construction

The vortex generator profiles were individually formed and attached to mounting strips (MS), spanning the length of the wing. This eased the interchanging of arrays during the tests. The vanes and mounting strips were manufactured from 0.2mm spring steel and the material thickness was accounted for when designing the VG heights. The strips were attached with double-sided adhesive tape according to pre-designed templates corresponding to the specific array design. The VG arrays were mounted in such a way to direct fluid into (downwash) the wing-wall junction where possible to alleviate the influence of corner separation.

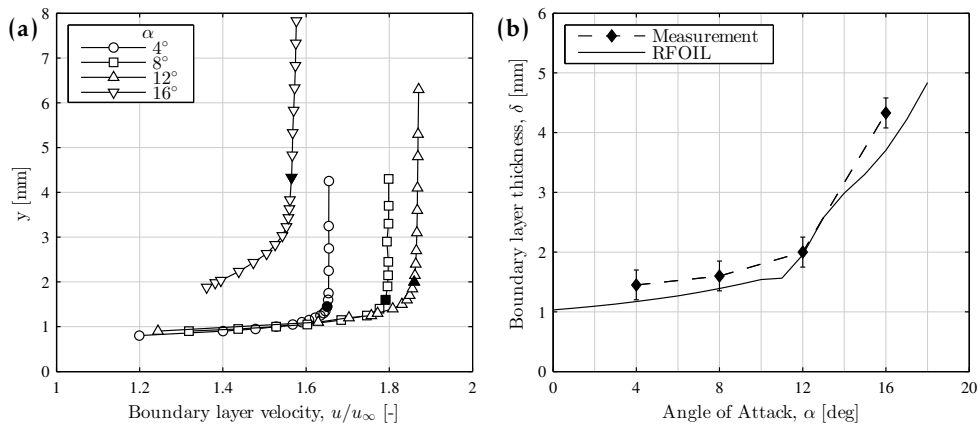

Figure 5.7: (a) Measured boundary layer profiles at $x/c = 20\%$. Filled black symbols indicate boundary layer edge; (b) Boundary layer thickness evolution with angle of attack. Case: clean, uncontrolled airfoil.

5.3. Results

5.3.1. Oil Flow Visualisation

General diagnostics

The effect of the VGs is qualitatively assessed through the response of an oil film on the airfoil surface. In Figure 5.8, the suction side of the airfoil is visualised at three increasing angles of attack. The flow direction in these images is from right to left. Before $\alpha = 15°$, the flow is attached in the uncontrolled case. The bright band running along the span around the $30 - 40\%c$ location is the laminar separation bubble. It is evident that this moves forward with increasing α. Comparing the location of the separation bubbles and the strip leading edge at $\alpha = 0°$ and $8°$, the VGs evidently induce additional drag by forcing earlier transition at low angles of attack. However, the separated suction side flow is completely reattached with VGs at $\alpha = 15°$. The structure of the separated flow is typical of mounted wings in wind tunnels, consisting of stall cells over the planform and corner cells at the wing-wall junction (Manolesos and Voutsinas, 2015).

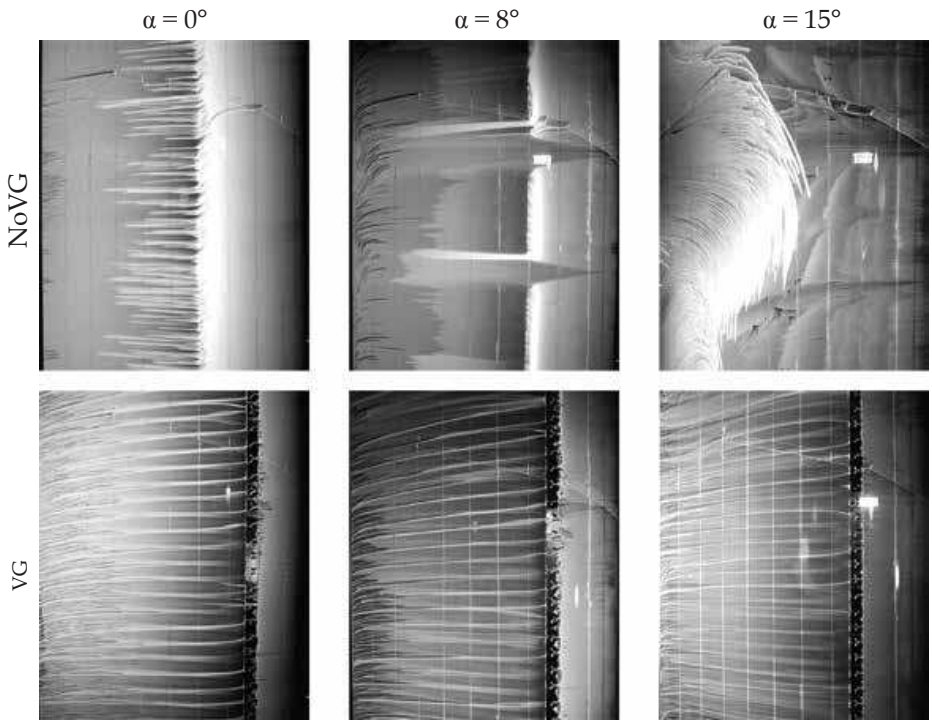

Figure 5.8: Oil flow visualisation of the clean airfoil suction side for increasing angle of attack. Case: without and with (Base Design) vortex generators. Flow direction: right to left.

Quantitative analysis

Quantitative oil film techniques are not a novelty, the majority relying on some-form of interferometry for estimating the local flow direction and skin-friction. Applications have evolved from simple two-dimensional boundary layers (Tanner and Blows, 2001), to vortex-boundary layer interaction (Peterson and Plesniak, 2004) and three-dimensional blade-bounded flows (Schülein, 2014). For the present case, distinctly aligned oil streaks are observed behind the VGs, indicative of the vortex passages. However, some considerations of the vortex flow field offer a more detailed interpretation.

The region directly between the vortex and the surface is highly sheared (recall Figure 2.5), and should result in a local oil deficiency. Further away from the vortex, as the induced secondary flow field diminishes, the oil film gradually adheres better to the surface. The passage of the vortex should therefore be characterised by a dark band flanked by brighter regions where oil has been redeposited. This is evidenced in Figure 5.9a, where the dark band lies between the two sets of dotted lines. The image intensity is sampled along two lines 'PQ' and 'RS' over a spanwise period $-0.5 < z/D < 0.5$. The vortex signature can be deduced from the preceding arguments, indicated by corresponding rectangular contours. This interpretation is aligned with the observations of Holden and Babinsky (2007) for surface flow characterisation behind wedge and vane type vortex generators. These authors also noted that secondary vortices would further complicate the flow pattern and hence, the interpretation of such visualisations. For single streamwise structures, secondary structures are indeed more prevalent and can also be deduced to some extent from oil flow visualisations behind a single vane, as illustrated in Figure 5.10. The vortex positions and rotations depicted here have not been measured and are only for indicative purposes, based on previous interpretations and measurements

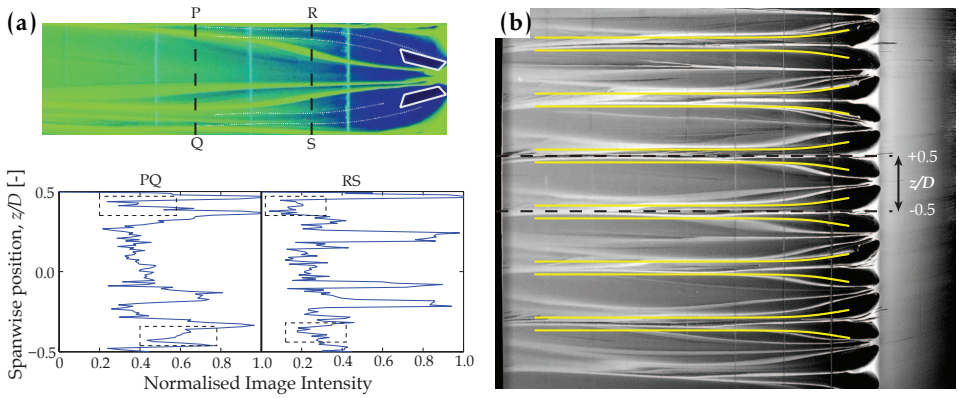

Figure 5.9: (a) Detailed oil flow visualisation over a spanwise period (*top*) with complimentary image analysis for vortex signature detection (*bottom*); (b) Visualisation overlayed with predicted vortex paths (yellow dashed lines) in the streamwise-spanwise plane (Eqs. 5.3-5.4). Case: $h = 10$mm, $x_{VG}/c = 20\%$, airfoil suction side, $\alpha = 0°$ in free transition.

Figure 5.10: Flow visualisation of a singular embedded primary vortex, with expected associated secondary structures, depicted as bright streaks. Case: $h = 10$mm, $x_{VG} = 20\%c$, airfoil suction side, $\alpha = 0°$ in free transition.

by Velte et al. (2016).

In a different yet complimentary approach, Lögdberg et al. (2010) also provide insights of wall-bounded vortex interactions simply using smoke visualisations. In that case, smoke injected near the wall was ingested by streamwise vortices and redistributed according to the swirling sense of the vortices. Smoke was concentrated at the upwash side of the vortices which, when illuminated with a thin laser sheet, left distinct traces of reflected light. The authors argued that the vortices were then *adjacent* to these bright bands. Using smoke as a seeding agent, multiple images are required to average out the turbulent smoke patterns due to the velocity fluctuations in the boundary layer. Conversely, the high relative viscosity of an oil film dampens its response to high frequency surface shear stress fluctuations. Therefore, once initial transients decay, the response captured in a single OFV image can be considered quasi-steady.

With the preceding argumentation, quantitative information may be obtained by considering the inviscid vortex trajectories predicted from Jones' vortex model (1955). The equations for these trajectories (in x, y, z coordinates) are given as

$$\operatorname{cosec}^2(\kappa z) + \operatorname{cosech}^2(\kappa y) = C \tag{5.3}$$

$$x = \frac{1}{\kappa\gamma} \int_{(\kappa z)_1}^{(\kappa z)_2} \left[1 + \frac{\tanh^2(\kappa y)}{\tan^2(\kappa z)}\right] \sinh(2\kappa y)\, d(\kappa z) \tag{5.4}$$

where κ is $\frac{2\pi}{D}$, the wavenumber of the array, C is an integration constant and γ is a non-dimensional vortex strength. The model is initialised with vortex positions corresponding to the tips of the VG vanes. Focussing on the near wake region (up

to 10h behind the VGs) in which the trajectory displays the highest curvature, the vortex strength parameter was tuned to give the best match with observations considering the centre dark band as the true vortex passage. The resulting trajectories were superposed on the oil film image in Figure 5.9b.

Incidentally, this procedure demonstrates an inverse method for estimating the initial vortex strength. This was explored further by analysing the near wake images from the VG base design in Figure 5.11. As before, the vortex strength parameter was manually tuned to obtain a best overlay with the dark band, thus obtaining $\Gamma = f(\alpha)$. We next consider $\Gamma = \chi \cdot h u_{VG}$ to be the generalised functional form of the vortex strength, where χ is a function of the device geometry and configuration (Angele and Muhammad-Klingmann, 2005; Lögdberg et al., 2010). This relation will be used to benchmark the method, after establishing a suitable estimate for the velocity.

Airfoil surface pressure measurements were then used to deduce the local velocity u_e outside the boundary layer, whose sensitivity to α is shown at the

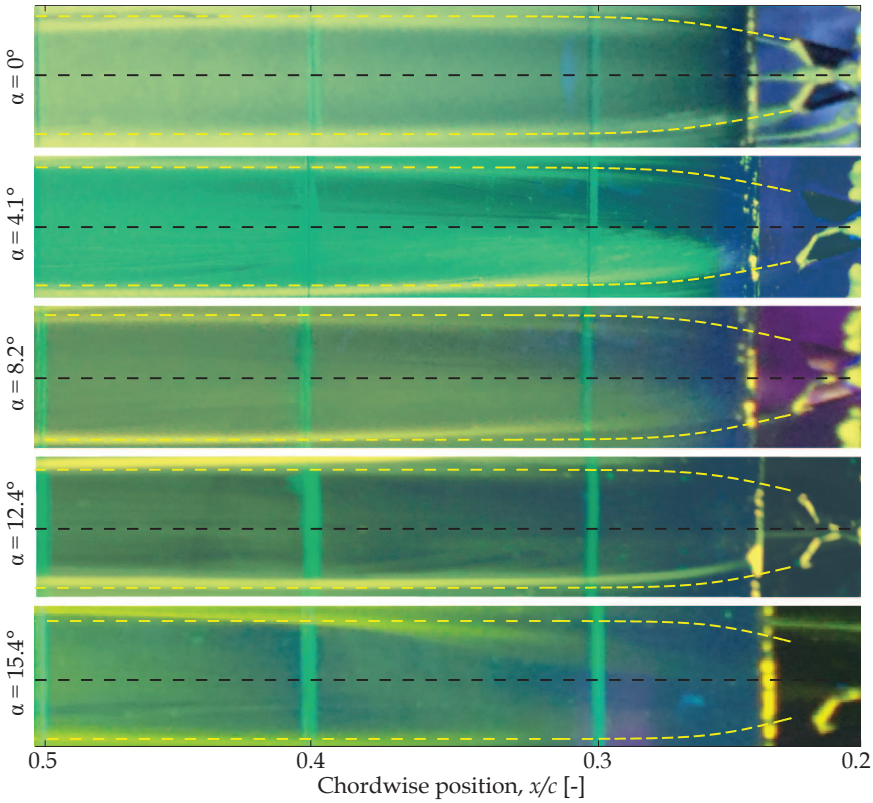

Figure 5.11: Near wake oil flow visualisation for increasing angles of attack (base design). Flow direction: right to left.

chordwise position of the VG tip ($\approx 23\%c$) in Figure 5.12a. Since the base design vanes exceed the boundary layer thickness at $\alpha = 16°$, it is reasonable to use u_e as an approximation for the VG tip speed, u_{VG}. The resulting trend between Γ and hu_e is linear, as shown in Figure 5.12b, with $\chi = 1.8$. For a similar VG arrangement in a flat plate boundary layer, Lögdberg et al. (2010) directly measured the vortex strength and reported $1.2 < \chi < 2.0$, depending on the definition of the total circulation. The estimated strength Γ is therefore not only in the correct order of magnitude, but also appears to be a reasonable approximation.[1]

The success of such a method depends on the quality of the estimated trajectory. For the present method, near-wake observations until $\approx 30h$ have been considered. It is shown in this work that inviscid theory holds fairly well until approximately $50h$ downstream the devices, after which viscous effects begin distorting the actual paths (Lögdberg et al., 2010). Limiting the analysis to the near wake region further reduces the method uncertainty in two respects. The high trajectory curvature in the near wake is most sensitive to changes in Γ, and thus best suited for the calibration procedure. Additionally, for this setup, the oil traces dip downwards under the influence of gravity. Particularly at higher angles of attack, this effect may skew the observations, as reflected in the growing error bars in Figure 5.12b. These uncertainty bounds indicate the edge-to-edge extremes of the fitted paths across the dark band in the near wake.

5.3.2. Performance polars

The airfoil performance will next be assessed by analysing the polar characteristics. In the following sections, reference is made to two types of figures. Lift and drag polars for the different VG cases have been compiled in this section and Appendix C.

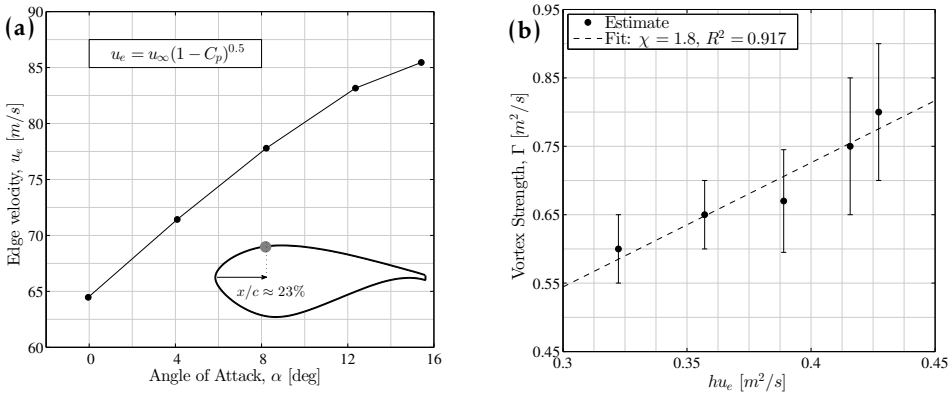

Figure 5.12: (a) Deduced edge velocity; (b) Circulation estimates for the VG base design (R - coefficient of determination). $u_\infty \approx 45$m/s.

[1] It is interesting to note a parallel between this technique, and the so-called inverse technique proposed by Haans et al. (2008) for estimating rotor blade loads using near wake velocity measurements.

Secondly, airfoil performance metrics are synthesized and compared, namely,

- the maximum lift coefficient and its corresponding angle of attack ($C_{l|\max}$, $\alpha_{C_{l|\max}}$),
- the drag at $\alpha = 0$ ($C_d|_{\alpha=0^\circ}$),
- the lift slope ($C_{l,\alpha}$), and
- the peak aerodynamic efficiency ($C_l/C_d|_{\max}$) at its corresponding angle of attack.

Note that the first local maximum C_l attained is considered the maximum lift, and $C_{l,\alpha}$ is evaluated over $\alpha = [0^\circ, 4^\circ]$.

Influence of the mounting strip

The mounting strip method used in this experiment is commonly used in practice to facilitate the attachment process. Recall that in this case, the strip height is the thickness of the 0.2mm sheet steel, giving a Reynolds number based on the strip height and freestream corrected tunnel speed of $\mathrm{Re}_h = 600$. If the mounting strip height exceeds the critical boundary layer roughness height, transition is forced at its leading edge, degrading performance. Propositions to recess the mounting strip into the blade surface would require a manufacturing overhaul, and would likely lead to undesirable localised blade stresses (Jensen et al., 2012). In addition, failure to account for the strip in numerical models may cause discrepancies with measurements (Sørensen et al., 2014; Baldacchino et al., 2016b). To investigate this, the 10mm VGs were separately tested by mounting the vanes directly to the model at $x/c = 20\%$. In Figure 5.13, the sharp transition at the strip is clearly distinguished from the oncoming laminar layer - the higher shearing of the turbulent boundary layer behind the strip tends to tear oil away from the surface and thus does not appear as bright when illuminated. Without the strip (Figure 5.13b), small regions in between the vanes have a higher concentration of oil followed by

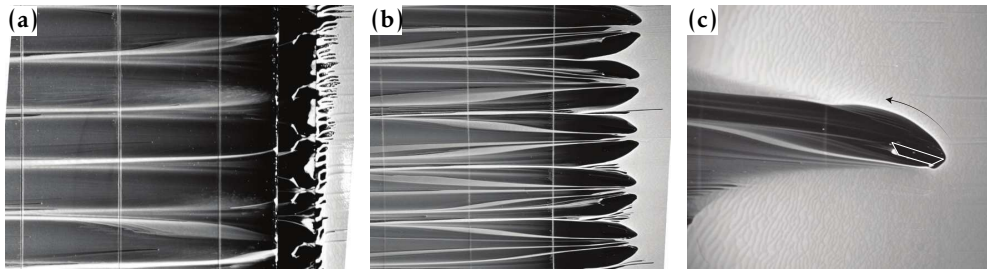

Figure 5.13: Flow visualisation of a VG array, (a) with and (b) without a mounting strip; (c) The flow past a single vane (white outline), detailing the passage of the horseshoe vortex. Case: $h = 10$mm, $x_{VG} = 20\%c$, airfoil suction side, $\alpha = 0^\circ$ in free transition. Flow direction: right to left.

a sharp transition. This indicates the persistence of a laminar boundary layer in between the vanes and thus results in slightly lower skin frictional drag. The sharp boundary between the laminar inflow wedges and the VG wake region is likely due to the horseshoe vortex emanating from the vane-wall junction, as detailed in the visualisation of a single vane in Figure 5.13c. This is known to occur in this type of flow and has been observed in measurements behind single wedges and vane-pairs (Holden and Babinsky, 2007; Velte et al., 2016).

Additionally, the mounting strip forces a local stepwise increase in the boundary layer thickness. This gradually grows downstream and effectively de-cambers the airfoil, reducing lift and causing earlier turbulent separation, as shown from the polars of Figure 5.14. A steady increase of 1 drag count ($\approx 5-6\%$) with the mounting strip is noted in the linear $C_l - \alpha$ range, accompanied by a reduction in $C_l|_{\max}$ and the glide slope. The decambering effect is highlighted by the pressure distribution shown in Figure 5.15.

Influence of VG vane geometry and chordwise placement

In subsection 5.2.3 we showed how the choice of the vane height and array chordwise position are coupled through the evolving boundary layer thickness δ. The result of these variations are shown in Figure 5.16. The trends shown in Figure 5.17 indicate an increasing $C_{l|\max}$ until $x_{VG}/c = 30\%$, with a decrease in the corresponding angle of attack, for all VG heights. The lift polars also show that the more rearward the mounting position, the more abrupt the stall characteristic. The largest VG ($h = 10$mm) only attains higher lift after the 30%c position. In general it may also be noted that the larger the VG, the more abrupt the stalling characteristics. Higher drag is observed at $\alpha = 0°$ and tends to reduce the further aft the mounting position. This is to be expected of larger VGs because of the larger frontal area and 'spoiler' type drag. The maximum efficiency is attained with the smallest VGs after the 20%c location. Meanwhile, the 10mm VGs are consistently less

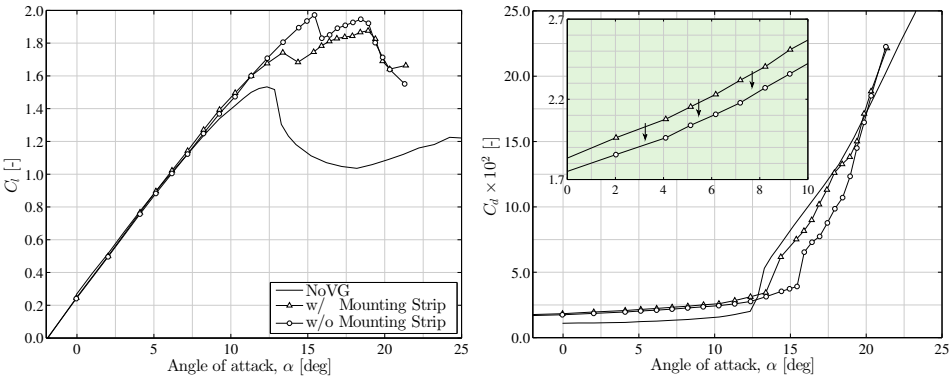

Figure 5.14: Lift and drag polar showing the influence of the VG mounting strip.

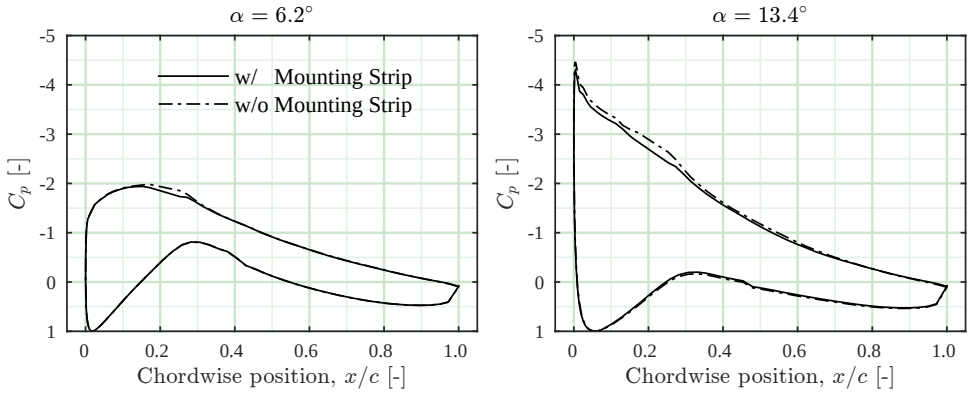

Figure 5.15: Pressure drop due to boundary layer displacement effect of the mounting strip at two (non-stalled) angles of attack.

efficient than the 5mm, over the whole chordwise range tested. The angle of attack at $C_l/C_d|_{\max}$ gradually increases downstream for the 2.5mm, but remains mostly constant for the 5 and 10mm. The 2.5mm VGs reduce $C_{l,\alpha}$ relative to the uncontrolled airfoil when mounted before the 30%c location. This also occurred for the 5mm VGs at $x/c = 10\%$. In all cases, $C_l/C_d|_{\max}$ is consistently lower compared to the uncontrolled, clean airfoil.

For the 2.5mm VGs mounted at the 10%c and 20%c locations, we notice two distinctive regions in the lift polars particularly, characterised by different slopes (both for the clean and roughened cases). This is evident from Figure 5.16 where significant slope changes occur at an angle of attack of approximately $\alpha = 12°$ and 8.5° for the 10%c and 20%c cases respectively. The distinction is also evident from the drag polar for these cases. At the forward position of 10%, it is conceivable that the small VGs behave similar to the simulated roughness since the relative VG size compared to the boundary layer thickness is large. This, in addition to the losses due to the disruption of laminar flow, explains the two-step slope behaviour of this configuration. To further support this view, we compare the clean and rough uncontrolled airfoil performance with that of the 2.5mm VGs at $x/c = 10\%$ in the clean condition. The VG and rough cases share a very similar slope in the attached regime. A sudden slope change occurs in both the controlled and (clean) uncontrolled cases at the location of maximum lift ($\alpha = 12.35°$); the slope of the controlled characteristic experiences a sudden drop, which appears to be explained by the encroachment of trailing edge separation. This progression is shown in Figure 5.18. Generating the vortices at 10% also allows more range for their development, which means they remain somewhat effective at the higher attitudes. Thus, the initial performance detriment owing to the too-forward mounting of the VGs is compensated at higher attitudes.

These design variations were also investigated with an artificially roughened boundary layer using the ZZ tape. The plots are shown in Figure C.13 with corre-

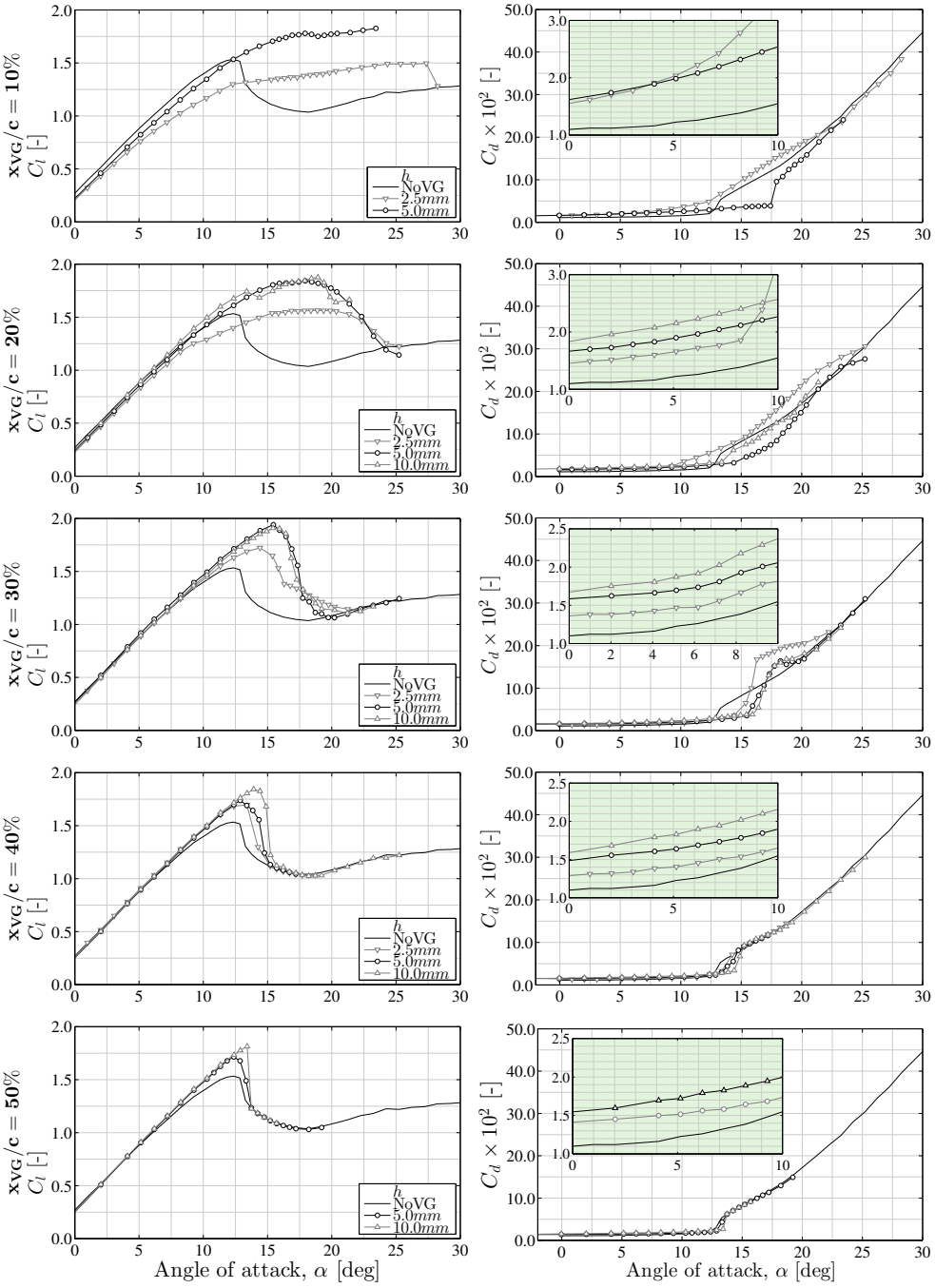

Figure 5.16: Sensitivity to array chordwise placement and VG vane height. Graphs are grouped into rows according to the array chordwise placement (top-bottom): $x_{VG} = 10\%c - 50\%c$.

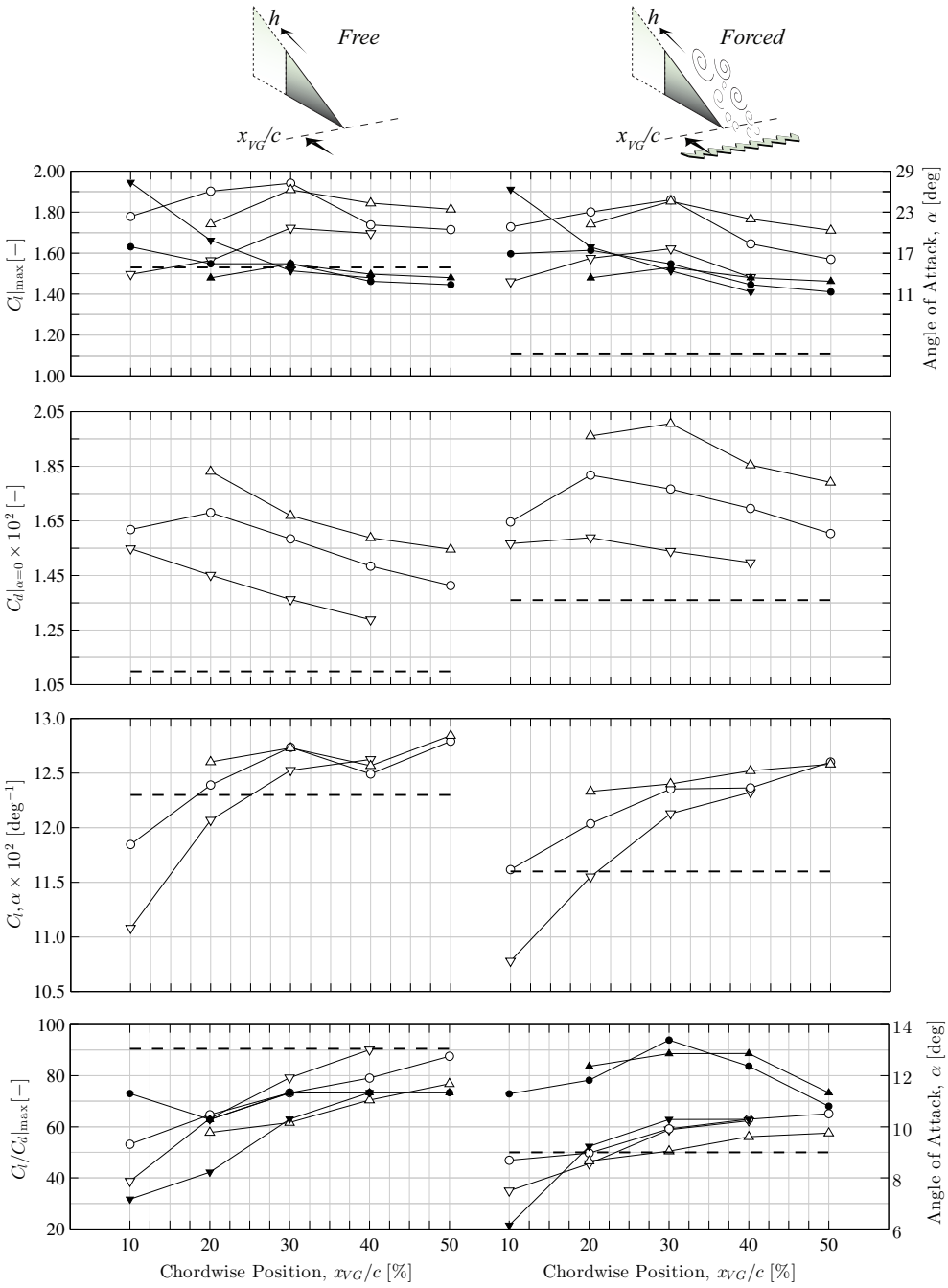

Figure 5.17: Metrics summarising the effect of chordwise array placement, vane height and boundary layer state. Symbols: $h = 2.5$mm (▽); $h = 5$mm (○); $h = 10$mm (△). Filled white symbols represent the metric (left ordinate), and filled black symbols show the corresponding angle of attack, when applicable (right ordinate). Dashed lines indicate metrics (left ordinate) for the uncontrolled case. The top-most schematics illustrate the varied parameters relevant in each column.

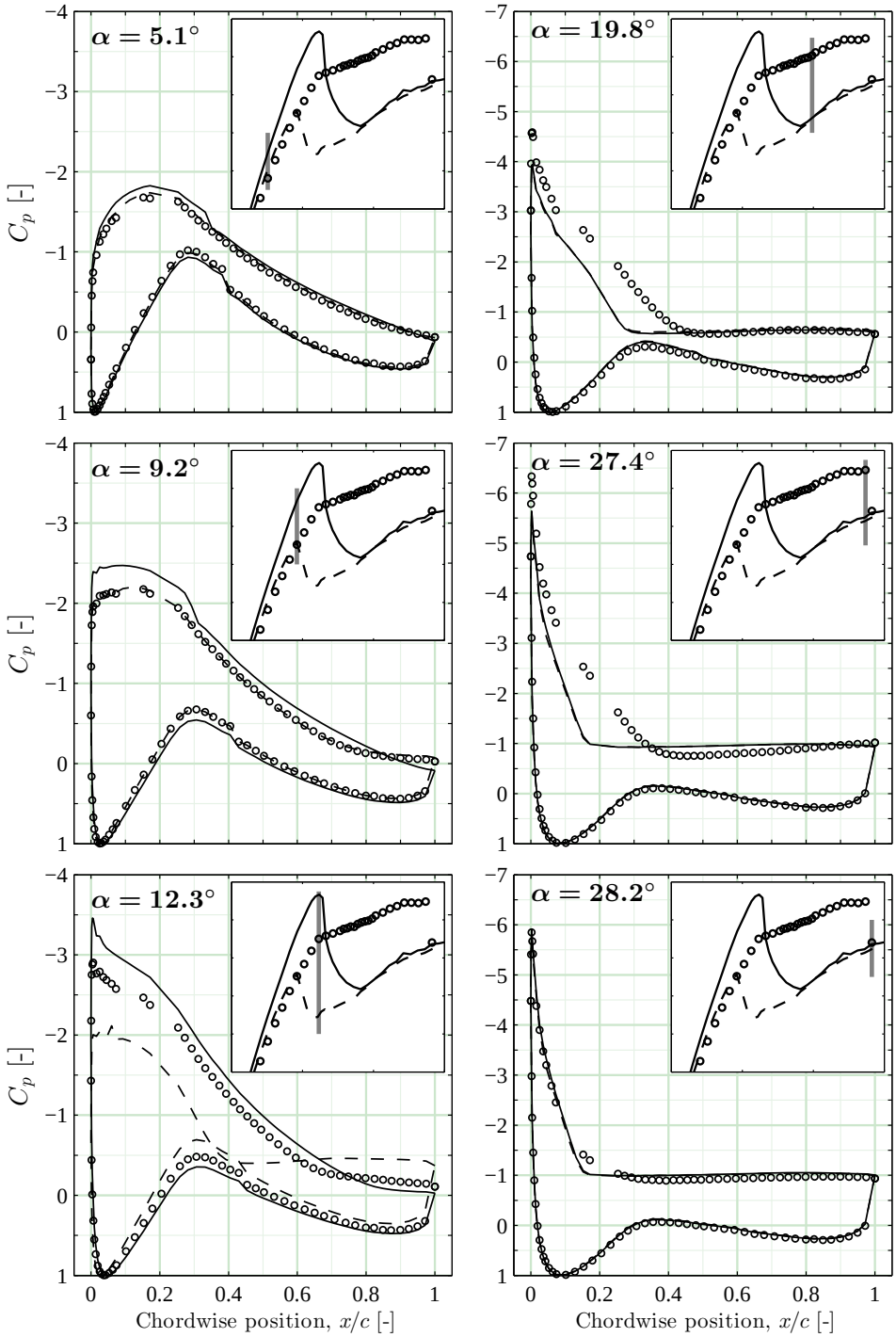

Figure 5.18: Pressure distributions for increasing angles of attack as indicated in the lift polar included in the inserts; Clean (-) and rough (- -) uncontrolled cases; 2.5mm VGs at $x/c = 10\%$ in clean condition (○).

sponding metrics in the right panel of Figure 5.17. Relative to the uncontrolled, rough conditions, the performance with VGs is generally improved and only the 2.5mm VGs at $x/c = 10\%$ result in a noticeable slope reduction. The improvement in maximum lift relative to the uncontrolled condition is noticeably higher in the rough cases and $C_l/C_d|_{\max}$ is also improved for all $x_{VG}/c > 20\%$. In the attached regime, the presence of roughness increases (offsets) the airfoil drag in a similar manner as observed for the mounting strip. For the 10mm VGs, this roughness-induced drag offset is approximately 10 – 20%. Thus, boundary layer thickening due to leading edge roughness is expected to reduce the relative impact of the mounting strip. The presence of roughness on the controlled airfoil then effectively results in a slight loss of performance, compared to the clean controlled scenarios.

The effect of the vane angle is illustrated in Figure 5.19a. The trends, shown in Figure 5.20, show a clear optimum for $\beta = \pm 12°$, yielding a $C_{l|\max}$ of 2.03 at $\alpha = 18°$. A subsequent increase in vane angle yielded lower maximum lift, largely occurring around $\alpha = 15.5°$. The drag steadily rises as $|\beta|$ increases, as seen from the drag polar, and summarised in the metric chart. The lift slope remains rather constant for all variations, but $C_l/C_d|_{\max}$ decreases steadily with increasing $|\beta|$. The results show that small changes in the vane angle have a noticeable impact on the performance; a small 2° increment from $|\beta| = 10°$ to 12°, reduces $C_l/C_d|_{\max}$ by 5% but increases $C_l|_{\max}$ by 10%. Experimental evidence has previously revealed a linear relation between the vortex strength Γ and vane angles up to 20° (Lögdberg et al., 2009; Pauley and Eaton, 1988; Wendt, 2004), but the relationship between Γ and airfoil lift does not follow the same trend. In fact, the metric chart shows an overall inverse relationship between $C_{l|\max}$ (and $C_{l,\alpha}$) and β. Notice that determining the slope includes some inherent variation due to slightly shifting set points between different cases. Notice further how $C_{l|\max}$ follows an almost similar trend with β, but clearly peaking at $\beta = \pm 12°$. The higher device angles pose larger spoiler drag, and the stronger vortex also induces more drag (in the form of rotational losses and higher skin friction). Additionally, the quality of the vortex may degrade at higher angles because of local separation on the vane itself (Pearcey, 1961). However, this would require localised flow field measurements for further verification. These observations are of particular relevance for engineering models. For example, Skrzypiński et al. (2014) investigated the effect of VGs on turbine energy production by devising an engineering model in which the effect of different VGs is assumed to affect the lift curve only by extending it. This result shows that the situation is rather more complex and requires consideration on a case by case basis.

With β fixed at ±15°, the vane length was varied from $2-5h$, the effect of which is shown in Figure 5.19b. The $L = 4h$ design delivers the highest lift. Higher drag is induced as the vanes are lengthened and hence $C_l/C_d|_{\max}$ also decreases. As with the vane angle, $C_{l|\max}$ displays a complex relationship with L/h.

The cropped-Delta variation is additionally benchmarked against the baseline Delta vanes in Figure 5.19c. $C_{l|\max}$ increased by approximately 10%, with only a marginal decrease in $C_l/C_d|_{\max}$. This occurs with only a slight reduction in the lift

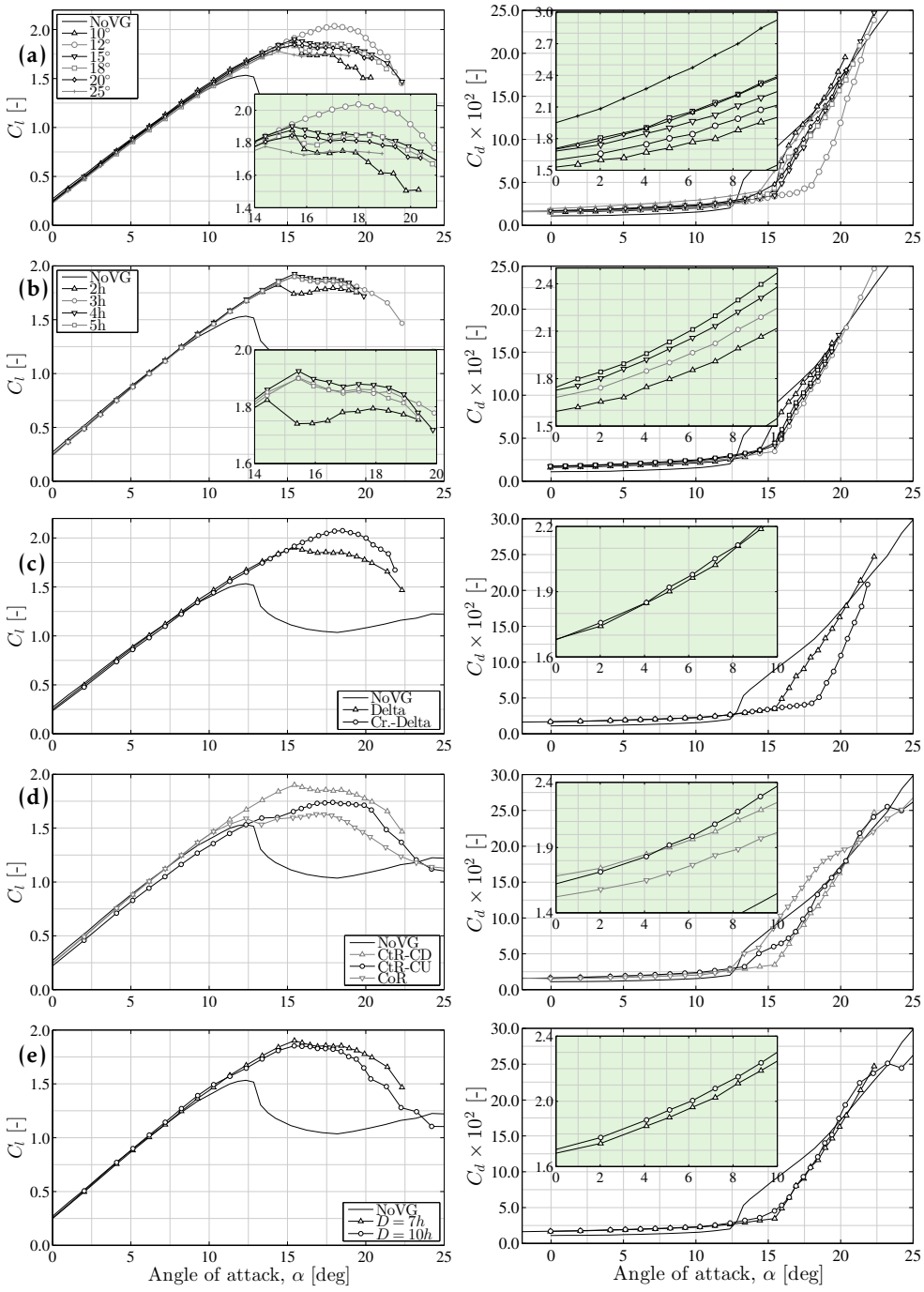

Figure 5.19: Airfoil performance sensitivity arranged in rows according to: vane angle, vane length, vane shape, array configuration and pair spacing.

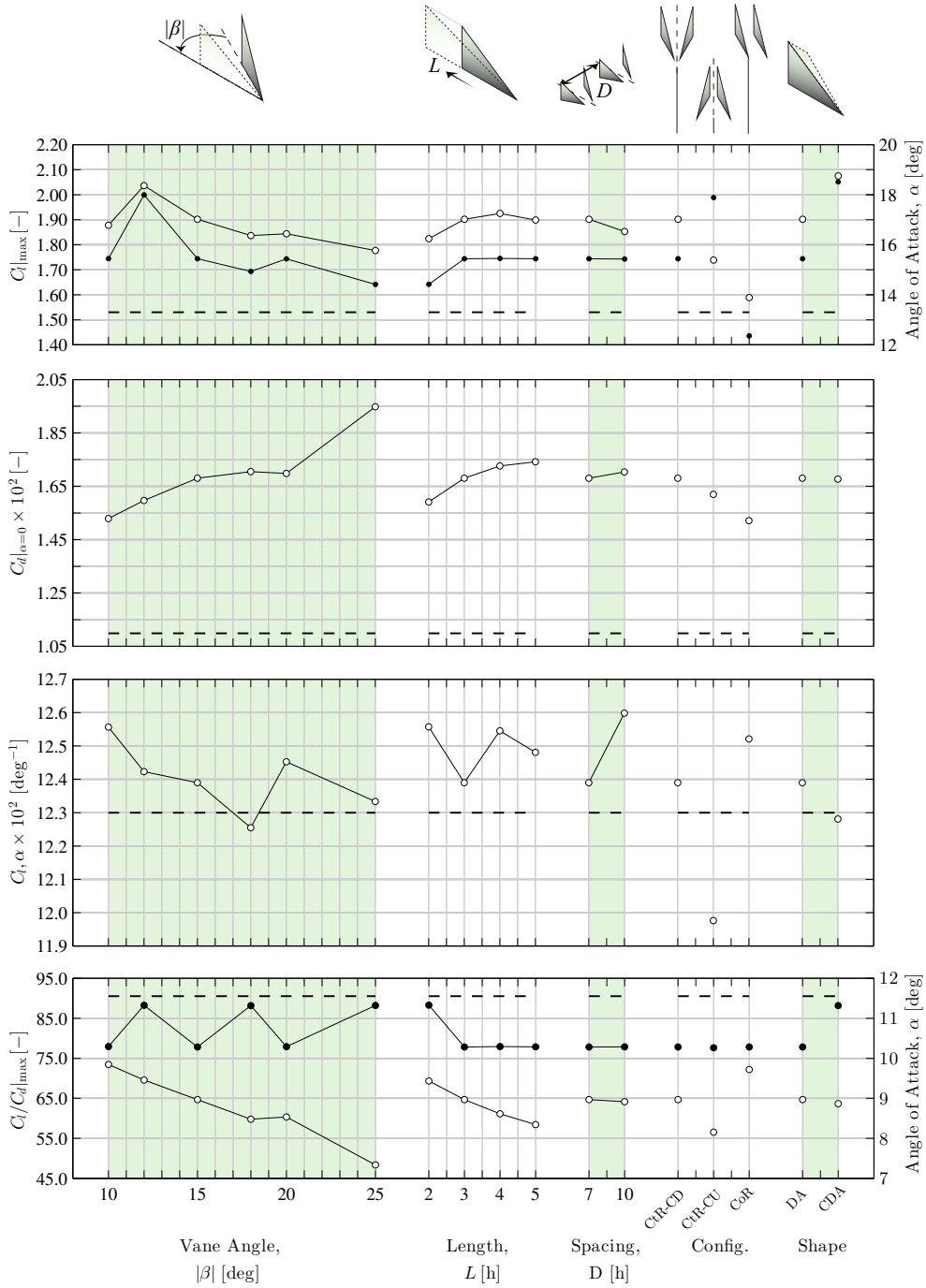

Figure 5.20: Same as Figure 5.17 for the vane angle and length, array spacing and configuration, and vane shape.

slope, meaning that the CDA variation performs better, essentially extending the lift polar.

In this section we have seen some examples of linear parametric behaviour, such as the monotonic variation of $C_{l|\max}$ and $\alpha_{C_{l|\max}}$ in $(h, x_{VG}/c)$ space. In other words, a change in the vane height or array position results in a modulation of lift along some representative polar. However, in the majority of cases, the results actually suggest non-linear relationships, in contrast to the first order estimates of engineering models (Skrzypiński et al., 2014; Pearcey, 1961), and more so, contrary to predictions from high fidelity simulations (Aparicio et al., 2016).

Influence of VG array configuration

The relative orientation of the vanes is investigated with two typical variations: a counter-rotating common upwash and co-rotating configuration. These sensitivities are shown in Figure 5.19d. Both variations result in a deterioration of maximum lift. The common upwash configuration is outperformed by the base design, in terms of both $C_l|_{\max}$ and $C_l/C_d|_{\max}$, as vortices are immediately convected away from the surface. The co-rotating array is obtained by removing like-signed vanes from the base design, thus producing half the circulation per unit span compared to the baseline. The drag is therefore lower for this configuration at low α, but the control efficacy of this design variation is severely reduced. According to Pearcey (1961), co-rotating arrays ought to be effective as long as their initial spacing exceeds $3h$. However, Godard and Stanislas (2006) observed half the increase in skin friction from a co-rotating array, compared to a counter-rotating array with the same geometry, indicating a lower efficiency of the CoR array. Additionally, an infinite system of CoR wall-bounded vortices of equal strength will drift laterally by up to 15° relative to the streamwise direction (Pearcey, 1961). Therefore, a rough estimate indicates that up to 3% of the airfoil planform behind the VGs may become devoid of vortex action. Further, the effectiveness of an entire (finite) CoR array may be dictated by reduced control authority at the edges because of vortex ejection; and it is precisely the wing-wall junction, near the array edge, that is most likely to separate first. The result therefore demonstrates that failure to control pockets of separated flow will affect global wing performance. Thus, given the complex flow separation behaviour on a turbine blade, the observations are equally relevant for practical applications.

The effect of increasing the inter-pair spacing is shown in the polars of Figure 5.19e. A slight reduction in maximum lift is observed for $D = 10h$ which is preceded by a decreased lift slope, as might be expected due to the lower circulation per unit span of approximately 30%. The drag at low angles of attack is approximately 2.9%−2.2% higher in the range $\alpha = 0°$-$10°$ for the larger spacing, despite the reduction of Γ/D. However, the larger spacing means that vortices originating from a common downwash pair commence farther from adjacent pairs. The vortex traces in Figure 5.9b support Jones' (1955) and Pearcey's (1961) theoretical demonstrations that counter-rotating (equal strength) vortex arrays gradually reorganise to form

common upwash pairs. The larger spanwise spacing thus delays the formation of counter-rotating upwash pairs and attenuates the vortex ejection rate from the wall. The near-wall residence time increases, as does the downwash-added skin-frictional drag. Moreover, the larger spacing of the CtR-CD pairs increases the ratio of the upwash/downwash region, incurring a larger low-momentum wake, and hence drag. This result is corroborated by direct skin frictional measurements behind similar arrays in the controlled study of Godard and Stanislas (2006). Notwithstanding, the observed influence of spacing is relatively low compared to other parameters, in agreement with previous observations on co-rotating (Pearcey, 1961) and counter-rotating arrays (Griffin, 1996; Fouatih et al., 2016).

Influence of VG vane skew

An additional set of tests investigated the effect of vortex asymmetry on the airfoil performance. As discussed in prior chapters, an alternative method to skewing the inflow is to skew the VG vanes relative to a uniform inflow. Whilst this does not perfectly represent the desired phenomenon, it gives an idea of the performance sensitivity. Results for different degrees of skew for the base design configuration are presented in Figure 5.21. The $\varphi = 15°$ case resembles a co-rotating configuration since one vane in each pair is effectively aligned with the inflow. Its performance is slightly worse than the base design. Only the $\varphi = 5°$ case results in a marginally better performance, with a delayed stalling angle, slightly higher maximum lift and no discernible drag penalty relative to the base design.

5.4. Loading Dynamics

During the course of a typical angle of attack ramp-up sequence, the separation mode became increasingly intermittent in the post-stall region with VGs. For the uncontrolled airfoil, stall is preceded by a growing region of trailing edge separation.

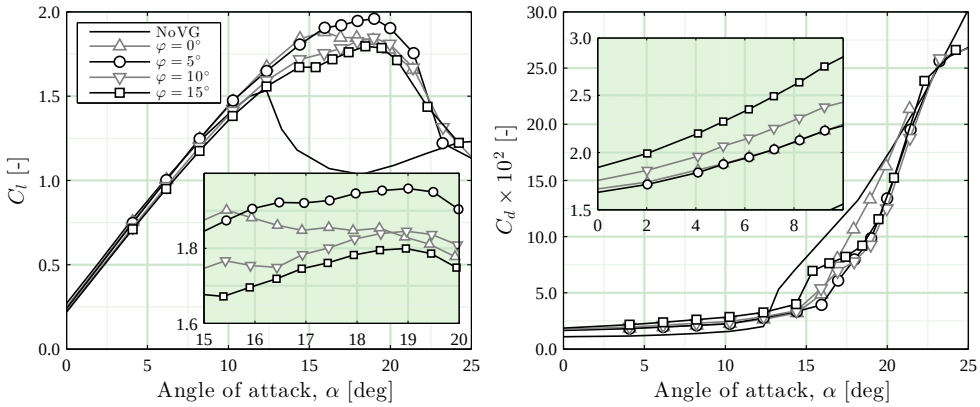

Figure 5.21: Lift and drag polar showing the influence of skewness of the base design configuration.

This is illustrated in the pressure distributions of Figure 5.22a. Note the reduction in C_p and gradual elongation of the pressure plateau as the flow separates. In contrast, for the 5mm and 10mm VGs, trailing edge separation does not appear before $C_{l|\max}$. However, beyond this critical point, the flow entered a state of vigorous separation/reattachment, observed with intermittently fully-separated and attached flow pressure distributions. This behaviour was also clearly audible as the wing section was intensely buffeted by large scale separation. Figure 5.22b illustrates the temporal average of this phenomenon for the base VG design case. It is immediately notable that the aft pressure plateau is somewhat inclined, owing to the fluctuations between the stalled and attached conditions.

The pressure samples were large enough to provide higher order lift statistics. Figure 5.23 compares lift polars of the clean airfoil with and without VGs, including the standard deviation σ. It is evident that separation dynamics intensify in the stalled regime of the controlled cases. Moreover, bimodal behaviour was occasionally observed for all VG heights aft of the 20% chordwise position. This occurred here just after $C_{l|\max}$, in contrast to Manolesos and Voutsinas (2015), who observed a bifurcation (bimodal behaviour) at $C_{l|\max}$ of an 18% thick airfoil with VGs at 30% chord. Typical lift signatures displaying bimodality are illustrated in Figure 5.24, with stepwise amplitudes of approximately 20 – 30% of the low lift levels. Note that the angle at which this was observed varies with the inverse of the VG mounting position, similar to $\alpha_{C_{l|\max}}$. Additionally, since bimodality preferentially occurs for sharp stalling configurations, it is highly sensitive to the angle of attack. Therefore, experimentally, its detection depends on the precise settings of the model angle of attack. Manolesos and Voutsinas (2015) postulated that this behaviour is linked to the motion of stall cells around the instrumented wing station. Thus, balance measurements would likely be insensitive to such local phenomena.

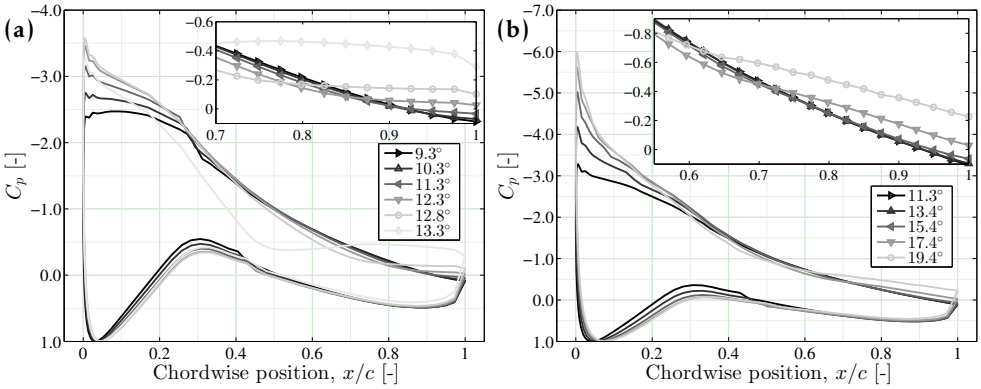

Figure 5.22: Pressure distribution for the airfoil in free transition (a) without [$\alpha_{C_{l|\max}} = 12.3°$] and (b) with VGs [$\alpha_{C_{l|\max}} = 15.4°$]. Complete distributions for angles of attack around maximum lift are illustrated together with suction side pressure details for the aft portions. Note differences in figure scales.

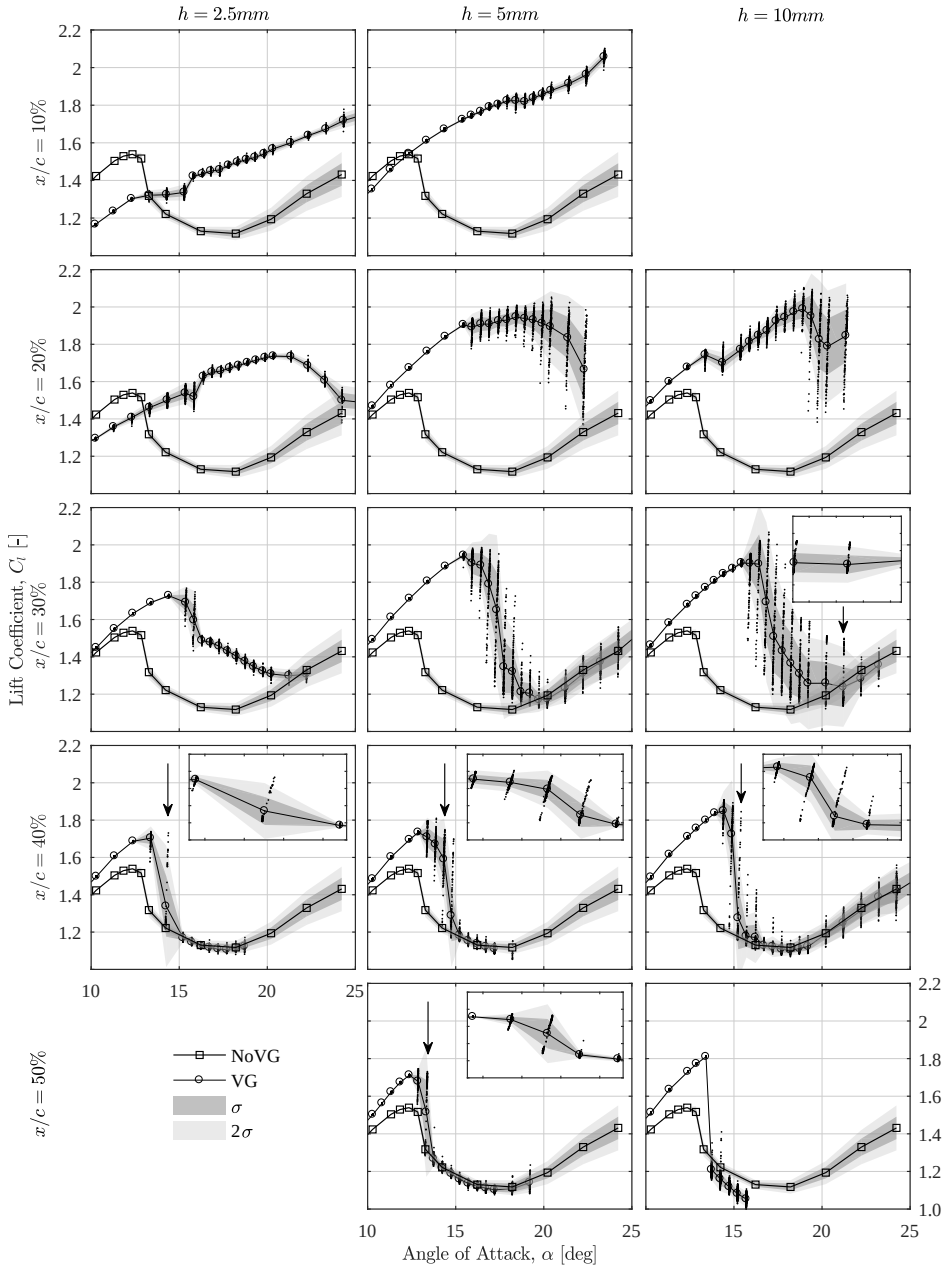

Figure 5.23: Lift fluctuations for the uncontrolled and controlled cases. The solid lines and symbols are time-averaged measurements, scattered data points show all sample observations and the shaded bounds indicate deviations from the mean. Inserts centred about (indicated) selected positions detail bimodal behaviour.

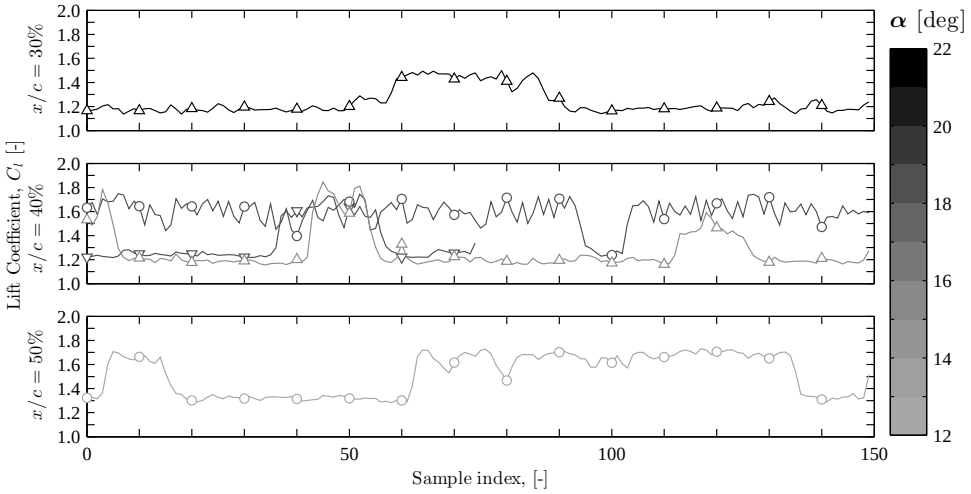

Figure 5.24: Bimodal behaviour for different VG heights and chordwise positions, observed at different angles of attack. Symbols: $h = 2.5$mm ($\triangledown$); $h = 5$mm ($\circ$); $h = 10$mm ($\triangle$).

Furthermore, lift fluctuations for all VG height/chordwise combinations are shown in Figure 5.25. Fluctuations with VGs (σ_{VG}) are normalised by fluctuations in uncontrolled conditions (σ) for a given angle of attack; stronger load variations with VGs, i.e. $\frac{\sigma_{VG}}{\sigma} > 1$, lie outside the shaded region. Note that the same fluctuation measure (σ_{VG}) has also been used for cases of bimodality, simply to illustrate the degree of the overall fluctuations. Broadly speaking, the fluctuations are stronger for larger VGs at more forward mounting positions. This also appears to hold in the pre-stall region for the 10mm VGs. Practically, this implies that oversizing VGs to compensate for design uncertainties may aggravate turbine loading dynamics and fatigue damage.

These results corroborate the early field test campaigns which already hinted that VGs may alter the dynamic load behaviour of wind turbines (Griffin, 1996). Whilst the underlying mechanisms require deeper investigation, we offer a possible explanation based on the current findings. For sufficiently large VGs, incipient separation aft of the VGs will be postponed. With increasing angle of attack, the adverse pressure gradient will gradually shorten the effective range of the vortices. When the flow is eventually retarded close to the VGs, a highly unsteady process of separation and reattachment commences: the vortices are attenuated prematurely, too soon to prevent separation, or are momentarily strong enough to enhance mixing over the airfoil and postpone it. This occurs until the separation point is sufficiently upstream of the VGs, such that they are rendered completely ineffective within the already separated boundary layer. At this point, the dynamics are less intermittent and the flow becomes 'steadily' separated.

Drawing conclusions about airfoil separation regimes is a challenging task in

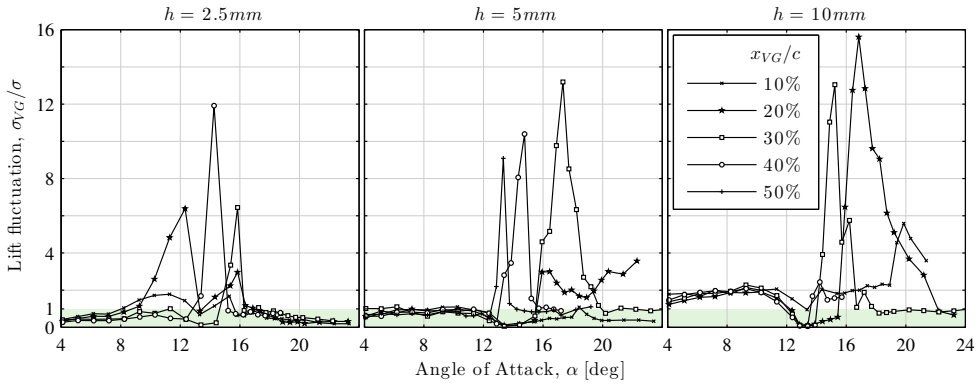

Figure 5.25: Lift fluctuation for controlled cases relative to the uncontrolled case. Data falling outside the shaded region indicates stronger fluctuations with VGs.

wind tunnel testing, due to the limited wing aspect ratio and wall-proximity effects. However, it is conceivable that rotating wind turbine blades also experience complex zonal separation regimes. For instance, boundary layer fences, which are often also used on blades, would impose a similar end-effect constraint to VG arrays also present on the blades, as that of a wind tunnel wall. In general it can be said that, vortex generators operating too close to their design envelope on a rotating blade could certainly risk pockets of separation and thus a potential impact on global performance.

5.5. Conclusion

In this chapter we have studied the sensitivity of the DU97-W-300 airfoil to various vortex generator designs. The goal was to map these sensitivities to understand the relative importance of the design variables, rather than optimising the VG geometry for this specific case.

Qualitative oil flow visualisations were performed to gauge the overall influence of the VGs on the flow regime. A detailed analysis of the oil streaks in the presence of the wall-bounded vortices has shown good correspondence with theory and prior empirical knowledge. The indirect determination of the vortex strength using this simple experimental technique, coupled with inviscid vortex theory also demonstrated a quantitative application of this experimental method.

The major VG parameters were then investigated using salient metrics such as the maximum lift coefficient and aerodynamic efficiency. The influence of the VG vane angle and length, displayed clear optima within the ranges tested ($\beta = \pm 12°$, $L = 4h$), in general agreement with past experimental studies, but contrary to the linear relations often assumed or predicted by different fidelity models. A counter-rotating, common downflow VG system with a cropped-Delta planform was superior to design variations such as a co-rotating array with Delta vanes.

On the other hand, the spanwise packing density displayed minimal influence on the metrics studied. The chordwise position of the VG array determines the control range of the streamwise vortices, and therefore had the largest effect on the performance. The airfoil performance was also sensitive to variations in the vane height, which was considered in conjunction with the chordwise placement. However, larger VG heights (> 1% chord) proved detrimental relative to smaller design variants

The presence of a VG mounting strip increased the base drag (+6%) and reduced the lift of the clean airfoil. The result cannot be generalised easily, as the severity of the effect depends on the specific airfoil's sensitivity to roughness. However, the higher this sensitivity, the larger the expected influence from the mounting strip. Thus, in field operation, where roughened conditions prevail due to weathering, the effect of the mounting strip will likely be smaller. In this regard, the leading edge roughness sensitivity was also explored using zig-zag tape. The VGs were able to offset the detrimental roughness effects, but the airfoil performance was still inferior to the clean-controlled case.

A consideration of the lift signal fluctuations revealed that the presence of VGs increased the dynamic loads in the stalled regime, albeit effectively delayed. This was pronounced for the larger VGs and forward mounting positions, reaching up to 16 times the fluctuations in the uncontrolled case. For larger VGs, higher fluctuations were induced throughout the operating envelope, not only in the stall regime.

The results presented concern the performance of the DU97-W-300 airfoil and the numerous but limited set of VG design variables explored here. However, we expect that the observed relative importance of VG parameters can be generalised to other airfoils as well.

6

An integral boundary layer engineering model for assessing airfoil performance with vortex generators

Layered terracotta roof tiles reminiscent of the microscopic structure of shark skin. Bran Castle, Bran, Romania.

An integral boundary layer engineering model XFOILVG is developed for simulation of airfoil flows with vortex generators. The method builds on previous work to establish a suitable source term expression, and uses data acquired in this thesis and the wider project framework to calibrate an empirical correction factor. The model is validated for a number of airfoil cases hosting different vortex generator configurations. This chapter appears in (Wiley) *Wind Energy*, 21(10), 906-921, 2018.

6.1. Introduction

6.1.1. Background

The work presented thus far has shown how the physics associated with vortex generator mixing is non-trivial, posing a number of modelling challenges. To achieve a cost-effective scale up of current wind turbines and wind farms, a multi-disciplinary design approach is necessary. In the present context this means considering *a priori* the effect of vortex generators on blade and rotor performance. Therefore, to assess and optimise their use, cost and time efficient VG modelling is necessary.

Despite considerable advances using CFD-based methods, such techniques are generally more time and resource expensive than the industry workhorses that are integral boundary layer tools and blade element momentum methods, making them impractical for use in iterative design processes. Therefore, extending the capabilities of integral boundary layer codes to handle mixing devices would be invaluable for airfoil and rotor design. Limited research is done in such a modelling approach incorporating VGs, and it is useful to consider the physics involved from an integral boundary layer perspective. Drela (2014) argues that VGs promote increased dissipation by introducing streamwise vortices into the boundary layer, which consequently increases the sustainable adverse pressure gradient. Lengani et al. (2011) demonstrated this by analysing the dissipation mechanisms in a separating duct controlled by vane-type vortex generators. Dissipation in this sense refers to the drain of mean flow kinetic energy through the action of the shear stress with the mean strain rate - effectively, enhanced mixing.

6.1.2. Objective and outline

Kerho and Kramer's (2003) source term approach was proposed for a specific case with a single row of co-rotating VGs. Their focus was on natural-laminar-flow airfoils with vortex generators installed far downstream for trailing edge separation control. We have also seen the potential of the approach in Chapter 3 with the Q^{3}UICK code on a single use case. Therefore, the objective of this chapter is to model the effect of VGs in an IBL code (i.e. Xfoil) by extending the source term implementation and overall code robustness for thicker airfoils over a wider operational envelope. This chapter will therefore address,

- modification of the closure relations using a source term approach;
- setting up a relation between the source term, VG geometry and boundary layer properties, using CFD and experimental airfoil reference data;
- code verification and validation whilst assessing its performance robustness.

The chapter proceeds in section 6.2 with a description of the methodology, modelling rationale and boundary layer modifications in the context of vortex generators. Validation results are presented in section 6.3 through comparisons with

flat plate experiments and airfoil measurements. Further discussion is presented in section 6.4 and concluding remarks in section 6.5.

6.2. Approach & Methods

6.2.1. Workings of the IBL code

The integral boundary layer code XFOIL is a viscous-inviscid interaction method designed for predicting airfoil flows and performance (Drela, 1989). In this framework, the flow is decomposed into two regions: the inviscid outer flow where viscosity can be neglected, and the thin-viscous shear layer that is the inner flow, where the boundary layer plays an important role.

The outer flow is solved using a linear-vorticity streamfunction panel method. A two-dimensional inviscid airfoil flow field is composed of a freestream flow, a vortex sheet of strength γ on the airfoil surface, and a source sheet of strength σ on the airfoil surface and wake (Drela, 1989). The system is closed with the Kutta condition applied at the trailing edge.

The viscous boundary layer solution is obtained using the so-called numerical integral method. The partial differential equations for continuity, momentum and energy can be reworked and transformed into the familiar ordinary differential equations in terms of integral quantities, as discussed prior in Chapter 2, and reproduced again here for completeness:

$$\frac{\tau_w}{\rho u_e^2} = \frac{C_f}{2} = \frac{d\theta}{dx} + (2+H)\frac{\theta}{u_e}\frac{du_e}{dx} \tag{6.1}$$

$$\frac{2D}{\rho u_e^3} = 2C_D = \frac{d\theta^\star}{dx} + \left(3 + \frac{2H^{\star\star}}{H^\star}\right)\frac{\theta^\star}{u_e}\frac{du_e}{\partial x} \tag{6.2}$$

The solution to these equations describes the evolution of the integral thickness and key shear quantities, namely displacement thickness $\delta^\star$, momentum thickness θ, friction coefficient C_f and the dissipation coefficient C_D (Drela, 2014). The integral momentum equation and the integral kinetic energy equation are consequently combined with a chain of laminar and turbulent closure relations in order to make the problem determinate (Garrel, 2003). Finally both solutions are coupled using a fully-simultaneous coupling scheme described by Drela et al. (1985). The entire non-linear equation set is solved simultaneously as a fully coupled system by a global Newton-Raphson method.

6.2.2. Boundary layer formulation modification

The effect of VGs can be introduced in a number of ways. In this case, the boundary layer formulation is modified through the dissipation term. To do so, a source term approach is used, in which an additional production term is added to the turbulence closure relations. The choice of closure relation should be physically

consistent, but also facilitate implementation, without compromising the code convergence behaviour. Thus, two sub-goals were to determine (1) in which equation to incorporate the source term and (2) to explore the behaviour of this source term over the streamwise domain.

Source term implementation

The source term is implemented into the rate equation (or shear-lag equation), an ordinary differential equation for the shear stress level inside the boundary layer. The equation models turbulence history effects that dominate turbulence intensity (see e.g. Drela and Giles, 1987). Additionally, the rate equation depends on an empirical constant K_c, controlling the reactivity of the boundary layer, and on the equilibrium shear stress coefficient $C_{\tau_{EQ}}$. The latter represents the shear stress level that would exist if the local boundary layer would be in equilibrium, in this sense meaning that the boundary layer profile for a turbulent flow exhibits a behaviour analogous to the similar flows of laminar boundary layers (White, 2006). In slowly changing flows, the flow is almost in equilibrium and thus C_τ closely follows $C_{\tau_{EQ}}$. However, this does not hold for rapidly changing flows, and thus the rate equation plays an important role in modelling the lag effect. A case in point are vortical flows, in which the Reynolds stresses are known to lag the mean strain field (Chow et al., 1997).

A simple expression for $C_{\tau_{EQ}}$ can be obtained from the well-known G-β locus of equilibrium boundary layers proposed by Clauser (Drela and Giles, 1987). The source term implementation is presented in Equation 6.3 where S_{VG} represents the source term itself:

$$\frac{\delta}{C_\tau}\frac{dC_\tau}{dx} = K_c\left(\left(C_{\tau_{EQ}}^{1/2} + S_{VG}\right) - C_\tau^{1/2}\right) \tag{6.3}$$

Because $C_{\tau_{EQ}}$ is seen as the fundamental parameter of the rate equation, the VG source term is added explicitly to the equilibrium shear stress coefficient $C_{\tau_{EQ}}$, effectively enhancing the production term of the turbulent kinetic energy budget. In this sense, the non-equilibrium nature of VG flow increases the tendency of the boundary layer to depart from its equilibrium state (attained in the absence of pressure gradients or streamwise vortices). This implementation was also favourable considering the convergence speed and numerical stability of XFOIL. Qualitatively speaking, these modifications promote an increased momentum thickness but reduce the displacement thickness. The shape factor decreases and the skin friction coefficient will increase (Drela, 2014; Lengani et al., 2011). It is important to note that these trends may be skewed by the physical presence of the devices, which according to Schubauer and Spangenberg (1960), cause local jumps in $\delta^\star$ and θ which are amplified with the developing boundary layer. This will become evident in the following section.

Source term shape function

The source term shape function is selected so as to mimic the streamwise vortex strength decay from mixing devices. As shown in Chapter 4, vortex strength decay is roughly exponential, arising due to the presence of wall shear, boundary layer turbulence, and mutual interference between adjacent vortices. On the other hand, vortices shed by VGs do not appear abruptly, and generally require around one vane chord length to develop before reaching their full rolled-up intensity. Therefore, the selected source term shape is given by Equation 6.4 where the source term develops gradually before decaying exponentially.

As shown in Figure 6.1, the shape function differs from the expression used by Kerho and Kramer (2003), who proposed instead a simple step function. The new source term expression consists of three variables, namely the source term strength σ_0, decay rate λ and the location of the VG with respect to the leading edge:

$$S_{VG} = \begin{cases} 0 & \text{for } x < x_{VG} \\ \sigma_0 \cdot (x - x_{VG}) \cdot \exp\left(-\lambda\left(x - x_{VG}\right)\right) & \text{for } x \geq x_{VG} \end{cases} \tag{6.4}$$

Assuming that the source term is related to the strength of the shed circulation, it is expected that the source term strength σ_0 and decay rate λ will be a function of the vortex generator configuration and the local boundary layer properties.

6.2.3. Laminar-turbulent transition

Xfoil uses the e^N method for predicting natural transition (van Ingen, 1956). This method assumes that transition occurs when the most unstable Tollmien-Schlichting wave in the boundary layer has grown by a given factor e^N, where $N = 9$ for natural transition (Drela, 1989).

Vortex generators which are typically sized on the order of the boundary layer thickness will likely lead to bypass-type transition within a short region. Research has shown that small VGs can actually delay transition, by attenuating critical perturbations in the boundary layer (Shahinfar et al., 2012). However, this is out of scope of the applications envisaged in this work. A simplified transition definition is used which assumes that VGs promote flow transition at their leading edge, independent of their configuration:

$$x_{tr} = x_{tr,free} \qquad \text{if } x_{tr,free} < x_{VG} \tag{6.5}$$

$$x_{tr} = x_{VG} \qquad \text{if } x_{tr,free} > x_{VG} \tag{6.6}$$

where x_{tr} represents the transition location with respect to the airfoil leading edge. The validity of this assumption will depend somewhat on the VG configuration and the local pressure gradient. However in many practical applications, VGs are mounted on a strip which itself can enforce transition, as illustrated in Figure 6.2.

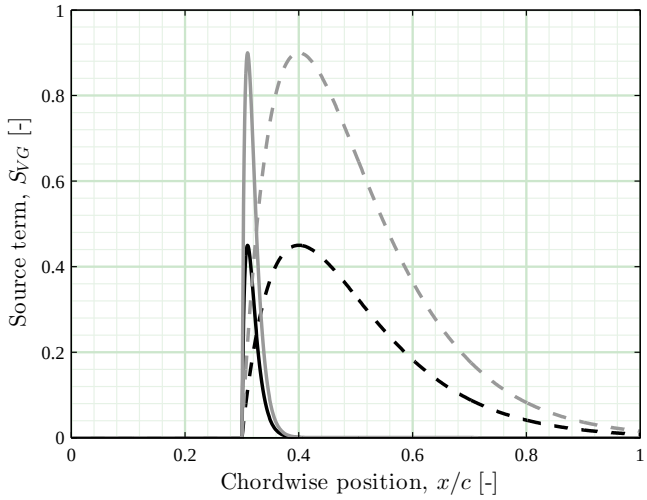

Figure 6.1: Source term chordwise distribution for a vortex generator at 30%c, for $\sigma_0 = 0.4$ (*black*) and $\sigma_0 = 0.8$ (*grey*). Decay rate $\lambda = 10$ (–), $\lambda = 100$ (––).

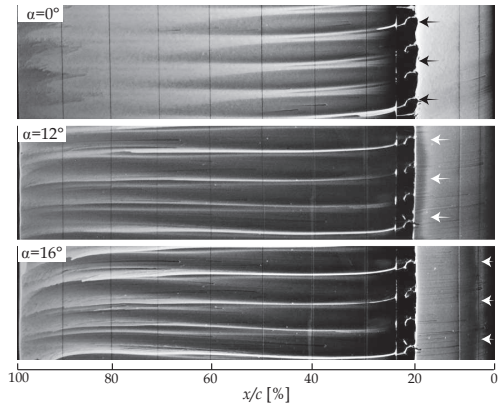

Figure 6.2: Oil flow visualisations of the DU97-W-300 airfoil depicting the (suction side) advance of the transition region ahead of the VG array with angle of attack.

6.2.4. Source term calibration

Of the three source term shape function variables, the source strength σ_0 and the decay rate λ are unknown and expected to depend on the airfoil/VG configuration. The required value of both parameters is determined here based on a calibration process using reference data (from high-fidelity numerical simulations and measurements). Measurement data on the DU97-W-300 presented in Chapter 5 are used, along with contributions from Timmer and van Rooij (2003), Manolesos and Voutsinas (2015) and the public database provided by the AVATAR project (Manolesos and Prospathopoulos, 2015; Ferreira et al., 2015). These cover a variety of VG configurations, airfoil families and inflow conditions. A summary of the data sets is given in Appendix D. For different VG configurations in various flow conditions, the source term is determined in three steps:

1. Analyse the effect of the source term parameters on lift and drag;
2. Define the target aerodynamic properties;
3. Determine the required source term parameters.

This procedure is summarized in Figure 6.3. Throughout the remainder of this chapter, cases without and with vortex generators are referred to as the *uncontrolled/NoVG* and *controlled/VG* case, respectively.

Part 1 - Source term effect

The effect of different source terms with different strength and decay parameters is presented in Figure 6.4 for two angles of attack. Increasing the source term strength and decay at low angles of attack (i.e. below stall) results in a decreasing lift coefficient and increasing drag. However, at low angles the sensitivity is small because the boundary layer is less receptive to the added dissipation. At high angles of attack the opposite is true and the increased mixing gradually takes effect with increasing angle of attack.

One may ascertain that multiple combinations of source term strength and decay predict the same lift and drag coefficient. It has been established that all these combinations of strength σ_0 and decay λ constants share the same value of the source term integral, as shown in Figure 6.5. This source term integral I_{ST}, is the area enclosed by the source term function:

$$I_{ST} = \int_0^1 S_{VG}\, d(x/c) \tag{6.7}$$

The integral is numerically determined based on the airfoil panelling using the trapezoidal rule. In keeping with the IBL modelling ethos, the definition of I_{ST} reduces the number of unknowns (originally the strength σ_0 and decay λ) to a single variable.

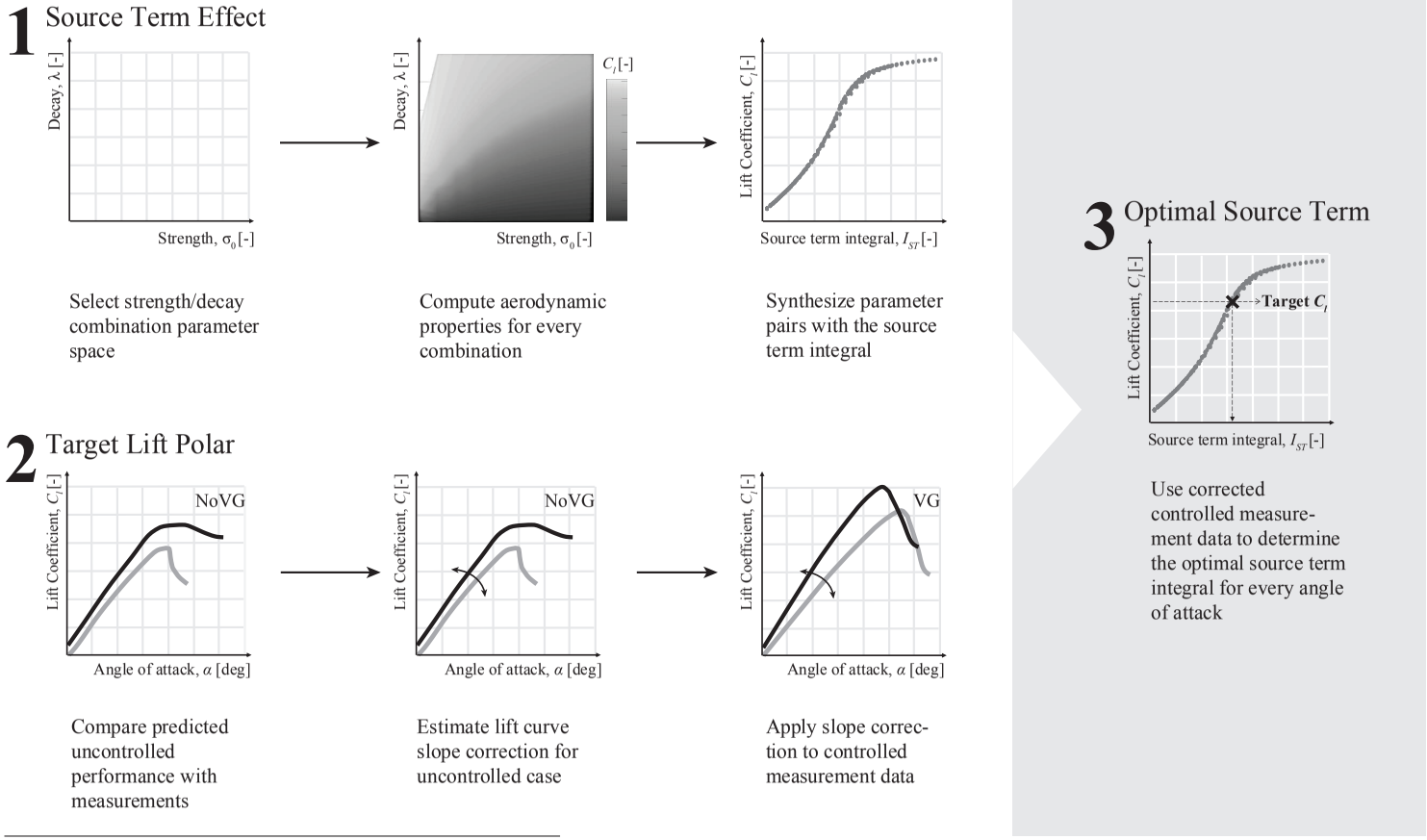

Figure 6.3: Overview of the source term calibration process.

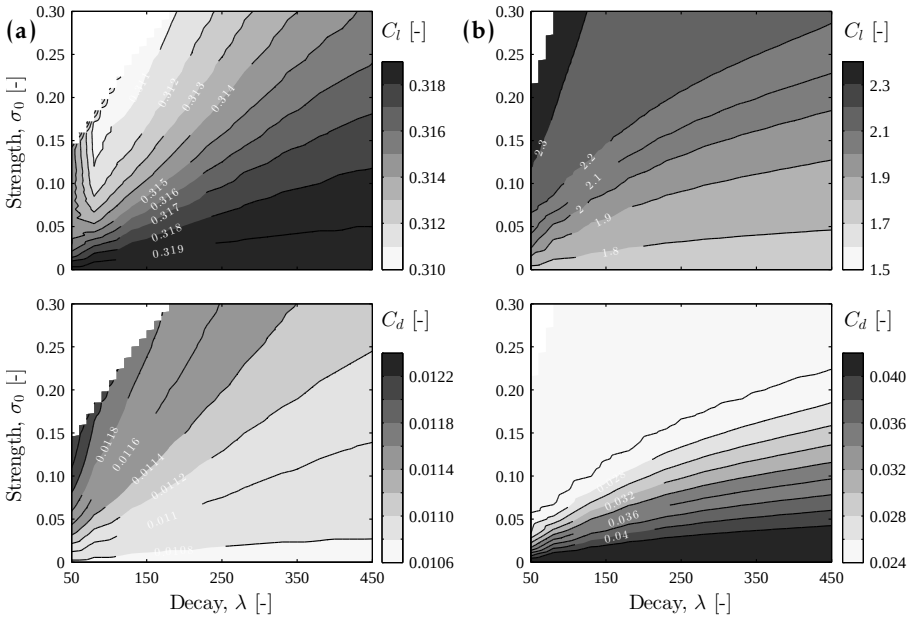

Figure 6.4: Effect of the source term strength and decay parameters on the performance of the DU97-W-300 airfoil ($\mathrm{Re}_c = 2 \times 10^6$) for (a) $\alpha = 0°$ and (b) $\alpha = 15°$.

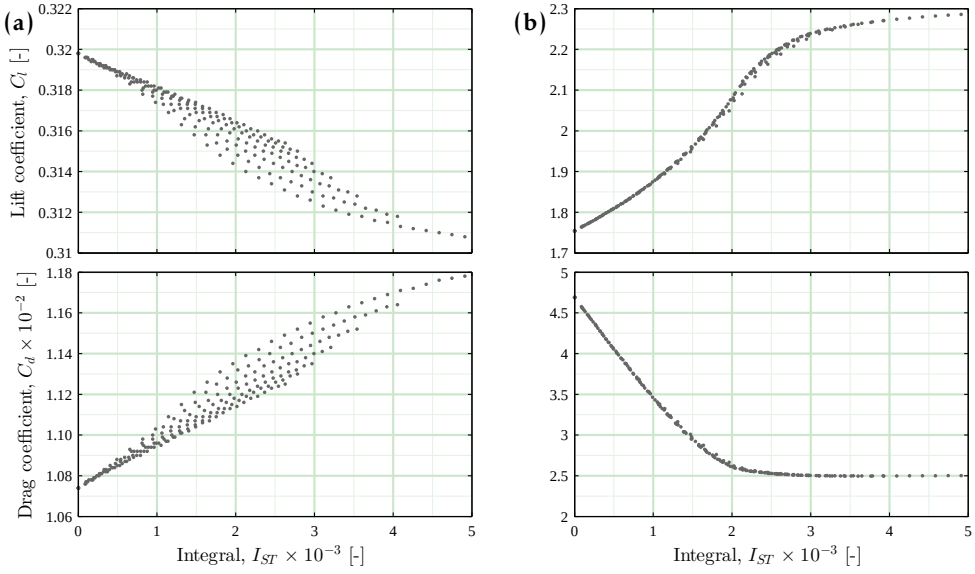

Figure 6.5: Effect of the source term integral on the performance of the DU97-W-300 airfoil ($\mathrm{Re}_c = 2{\times}10^6$) for (a) $\alpha = 0°$ and (b) $\alpha = 15°$.

A physical interpretation of the source term integral is a VG-induced kinetic-energy drain of the mean flow, increasing the turbulent kinetic energy in the boundary layer. Reducing variables in this manner is in line with the empirical observation by Lögdberg et al. (2010) that it is the total momentum flux that determines whether or not flow separation can be prevented.

Part 2 - Target lift polar

To account for discrepancies in the prediction of the uncontrolled airfoil performance, corrected (target) polars expected to be found by the airfoil code are introduced. With reference to Steps 1 and 2 in Figure 6.3, the lift slope discrepancy between baseline XFOIL predictions and reference data is first calculated. The slopes were evaluated in the interval $\alpha = [0°, 4°]$. Finally, in Step 3, the slope correction factor is applied to the reference lift polar for the VG case. This procedure avoids the source term accounting for inherent inaccuracies of the integral boundary layer code. The corrected lift polar is referred to as the target lift curve and is thus thought to be a more representative reference with which to calibrate the empirical function.

Part 3 - Source term selection

The determination of the optimal source term is based primarily on the lift coefficient. The drag coefficient is not found suitable because integral boundary layer codes significantly underestimate drag even in the uncontrolled case, and because the source term approach does not account for the additional profile drag of the VG itself. Boundary layer measurements with vortex generators providing reliable integral properties are sparsely available and thus also unsuitable for the present purpose.

6.2.5. Source term semi-empirical relation

To relate the source term magnitude to airfoil/VG parameters, a semi-empirical relation is set up. The source term magnitude should depend on the effectiveness of the VG, defined here as the strength of the shed vortex. The independent variables are subsequently selected following thin airfoil theory. Accordingly, the amount of circulation generated by a flat plate in ideal conditions depends on the chord length, the angle of attack and the incoming flow velocity. Analogously, here we consider (1) the VG length L, (2) the angle between the VG chord line and the incoming flow β, (3) the flow velocity at the VG tip, u_{VG}, and (4) the VG height, h/L, scaled as the vane aspect ratio. These variables, schematically presented in Figure 6.6, have been previously identified as being directly correlated to the strength of the shed vortex (see e.g. Wendt and Reichert, 1996; Angele and Muhammad-Klingmann, 2005; Ashill et al., 2001).

Equation 6.8 is used as a basis for setting up the semi-empirical relation. Using a weighted least-squares regression of the calibrated source terms, $C_0 - C_3$ are determined. The reliability of such a calibration depends of course on the quality

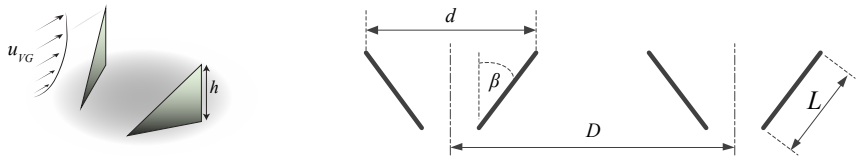

Figure 6.6: Schematic representation of the vortex generator geometry and nomenclature.

of the predictions in uncontrolled conditions. To account for this, the calibration procedure uses a weighting function taking into account the error in predicting the lift slope, maximum lift coefficient and stall angle compared to the reference data. Additionally, focus is placed on higher angles of attack since at lower angles, the effect of the source term on lift and drag is smaller than the expected accuracy of the code. This process is also shown in Figure 6.3, and yields the following empirical equation:

$$I_{ST} = C_0 \cdot \left(\frac{h^\star}{L^\star}\right)^{C_1} \cdot \left(L^\star \cdot \sin\beta\right)^{C_2} \cdot \left(u_{VG}\right)^{C_3} \tag{6.8}$$

where $C_0 = 0.0240$, $C_1 = 0.2754$, $C_2 = 0.4507$, $C_3 = 0.2987$.

The VG parameters $h^\star$ and $L^\star$ represent the non-dimensional vortex generator height and length with respect to the airfoil chord. To retrieve the flow velocity at the VG tip (u_{VG}), the Swafford boundary layer velocity profile as used in Xfoil is reconstructed using the momentum thickness Reynolds number Re_θ, the kinematic shape parameter H, the edge velocity u_e and the boundary layer thickness δ (Drela, 1989; Swafford, 1983). Figure 6.7 provides the error distribution between the calibrated source term integral, $I_{ST}|_{cal}$ and the empirical fit, $I_{ST}|_{emp}$. The residuals are approximately normally distributed.

The source term expression (Equation 6.8) is implemented in Xfoil in such a way as to minimise the required user interaction. Therefore, the only inputs required are the VG geometry: the VG height, length, inflow angle and position with respect to the airfoil leading edge. The inflow velocity u_{VG} is calculated internally using an iterative process which is consequently used to update the value of the source term according to the empirical relation.

6.3. Results

The VG modelling capabilities are assessed in this section. Results are presented for a canonical case of a flat plate with and without vortex generators, and subsequently for three airfoil sets controlled using vortex generators. The former allows a more straight-forward assessment of integral boundary layer properties whereas the latter

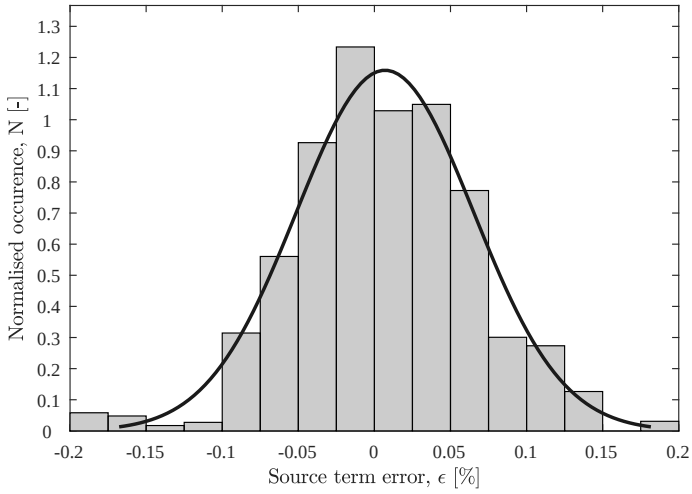

Figure 6.7: The validity of the source term equation, comparing the error between the calibrated and the calculated source term.

provides basis for global comparison.

6.3.1. Boundary layer properties

The control effect of a vortex generator is indirectly assessed by analysis of the integral boundary layer properties. The measurements presented in Chapter 4 for the turbulent flat plate boundary layer (ZPG) are used to this end. The scaled rectangular vortex generator properties for the present implementation are then $h^\star/L^\star = 0.4$ and $h/\delta = 0.25$.

The flat plate geometry, consisting of a leading-edge region, a flat (uniform) centre piece and a trailing edge was defined and panelled in Xfoil. The nose portion (the leading 1% chord) was modelled using a Hermite polynomial which was merged with the middle section using a square-root blending function. The trailing 20% chord was modelled as the aft 70% of a NACA0010 symmetric airfoil (further details of this method are found in Sanders (2014)). A uniform pressure distribution was obtained at $\alpha = 0°$.

The predicted evolution of the boundary layer properties is shown in Figure 6.8 for the uncontrolled and VG-cases. The relatively short range of the measurements downstream limits the extent of the comparisons. The predictions are comparable to the measurements to within an order of magnitude estimate. After the local perturbation of the devices, the shape factor gradually drops to approximately 1.37 at the $50h$ as a result of the vortex-induced mixing, meaning the boundary layer is further from separation. The gradual reduction in the computed shape factor is comparable to the trend measured and shown Figure 6.8c.

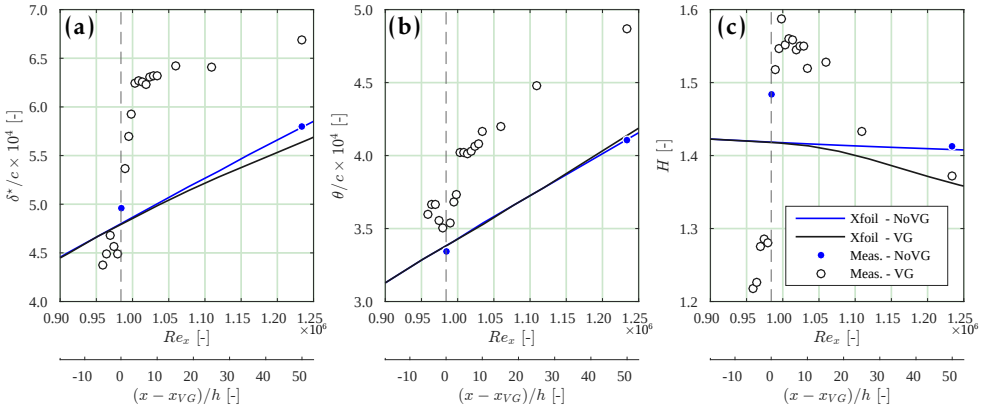

Figure 6.8: Comparison of measured (symbols) and predicted (lines) integral boundary layer properties: (a) Displacement thickness, (b) momentum thickness, and (c) boundary layer shape factor.

Notable discrepancies exist at the location of the VG itself: the measurements demonstrate somewhat of a step increase in $\delta^\star$ and θ. However, a passive device is itself a source of drag which manifests as a momentum deficit in the developing boundary layer, over and above the effect of the developing vortex. Schubauer and Spangenberg (1960) originally demonstrated this aft of passive devices in a boundary layer wind tunnel. They observed that the evolution of the relative momentum deficit remained rather constant. This implies that the device drag could potentially be modelled as a stepwise perturbation which would subsequently be convected and modulated with the developing boundary layer. Since the present model implementation does not account for this penalty drag, this additional deficit cannot be captured.

6.3.2. Global performance assessment

This part of the validation aims to (1) validate the source term expression, and (2) demonstrate the code robustness. This will be achieved by validating the source term sensitivity with VG location, height and inflow angle by comparison with data sets outside the reference data base.

Source term expression

In Figure 6.9a and Figure 6.9b, reference polars and Xfoil calculations for various VG positions are presented. The same reference DU97-W-300 data presented in the previous chapter has been used for this purpose. The present test case considers the model in free transition and equipped with counter-rotating Delta-shaped VGs with a height of 10mm and length of $3h$, set under an inflow angle of 15°. The model was subjected to a flow with a Reynolds number of 2×10^6. The vortex generators were positioned at 30, 40 and 50% chord. Placing the VGs further upstream increases maximum lift and postpones the stalling angle. At low angles of attack, the closer

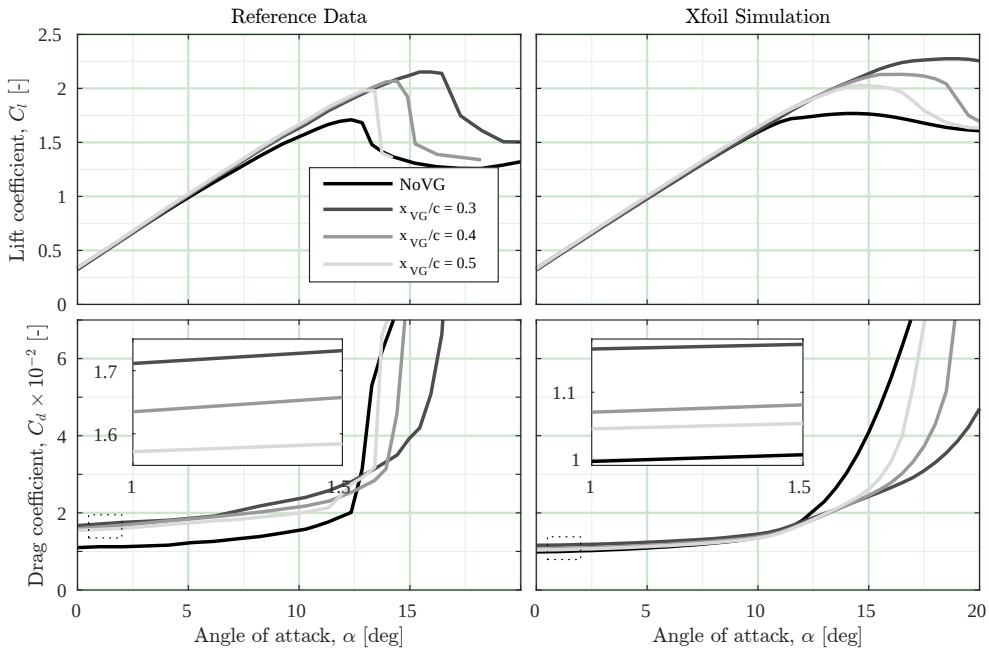

Figure 6.9: Effect of the VG location on the performance of the DU97-W-300 airfoil at $\mathrm{Re}_c = 2 \times 10^6$ with $h^\star = 0.015$.

the VGs are to the leading edge, the higher the drag. Within the current modelling framework, this occurs primarily due to the earlier forced transition to turbulence, minimising the lower-drag laminar flow region over the airfoil. These observations are evident in the experimental data, which are reasonably predicted by Xfoil.

Figure 6.10 shows a similar comparison using the same reference dataset, comparing the effect of the VG height. The Delta-shaped VGs are located at 40% chord from the airfoil leading edge and have a height of 5mm and 10mm, all other parameters dictated through geometric similarity. Increasing the VG height at this location improves their effectiveness in separation delay, but also introduces more drag at pre-stall angles of attack.

The effect of the inflow angle is presented in Figure 6.11. The reference data originates from a numerical parametric study performed within the AVATAR project (Manolesos and Prospathopoulos, 2015). The synthetic data was generated using fully turbulent, geometry-resolving CFD computations on a 33% thick FFAW3333 airfoil with a chord length of 5.84m. The use of synthetic data permitted a comparison for a high Reynolds number (in this case 14×10^6) for which experimental data with VGs is not readily available. The airfoil was equipped with 30mm high and 90mm long counter-rotating Delta-shaped VGs, mounted at 40% chord. Evidently, increasing the vane inflow angle from ±15° to ±25° increases the maximum lift. The drag at low angles of attack increases for higher vane angles, and decreases at

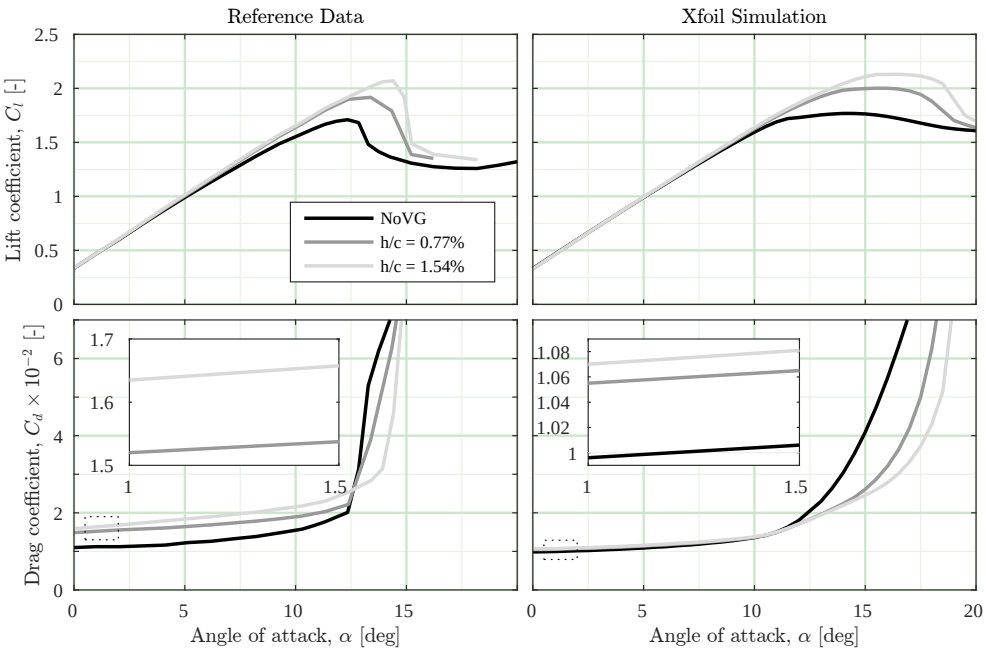

Figure 6.10: Effect of the VG height on the performance of the DU97-W-300 airfoil at $\mathrm{Re}_c = 2 \times 10^6$ with $x_{VG}/c = 0.4$.

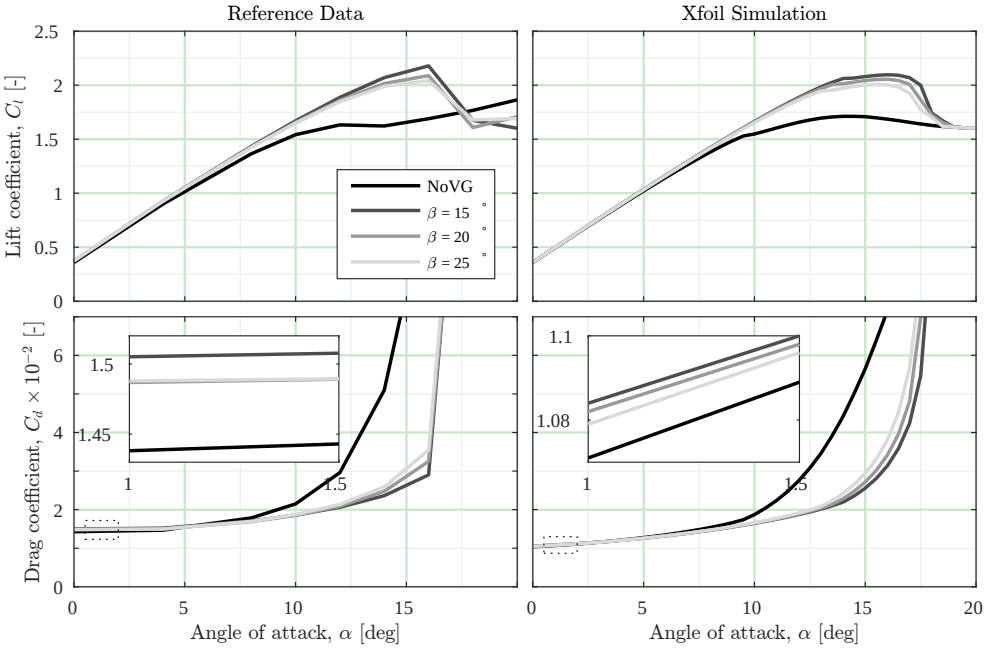

Figure 6.11: Effect of the VG inflow angle on the performance of the FFAW3333 airfoil at $\mathrm{Re}_c = 14 \times 10^6$.

high angles of attack as separation is delayed. Note that whilst the drag increases at a similar rate after maximum lift is attained, the numerical computations predict an earlier merging point than XFOIL. This is the angle at which the VGs, in all cases considered, are rendered completely ineffective because of large scale separation, resulting in a collapse of all polars.

Code robustness

Additional comparisons are made with the measurements reported in Fouatih et al. (2016). These authors presented an experimental parametric study on different VG geometrical parameters for optimising flow separation control of a transitional NACA4415 airfoil. The experiments were carried out in a subsonic wind tunnel at a Reynolds number of 2×10^5.

Figure 6.12a-6.12c present the relative change in maximum lift ($\Delta C_{l|\max}$) sensitivity to the VG height h/c, VG location x_{VG}/c and the inflow angle β on the maximum lift coefficient. Except for the VG location, the trends are generally captured well, along with the order of magnitude.

6.4. Discussion

6.4.1. Source term expression

The regression coefficients of the expression (Equation 6.8) reveal that the source term integral increases with increasing VG vane length, height, inflow angle, as well as the external flow velocity. The capability of the airfoil code to model VGs significantly depends on the quality of the source term expression. This in-turn is limited by the quality of the calibration database, and how well represented the key variables are in those datasets. These limitations can be summarised as follows:

- **Discrepancies uncontrolled airfoil prediction:** For the uncontrolled performance (without VGs), XFOIL mostly overestimates the lift slope as well as the maximum lift coefficient, and underestimates the drag. Despite efforts to anticipate for this using correct target polars, the calibrated source term will, to some extent, also account for the discrepancies in uncontrolled airfoil predictions.
- **Reference data:** The performance of the code is limited by the availability, consistency, and quality of the reference data. Not all VG parameters (e.g. pair spacing, VG shape) were sufficiently represented in the data base. Improving this representation is seen as a potential improvement of the presented method.
- **Boundary layer properties:** The velocity at the VG is calculated using the edge velocity, integral boundary layer properties and expressions for the boundary layer thickness and velocity profile. This includes additional uncertainties and affects the quality of the source term expression.

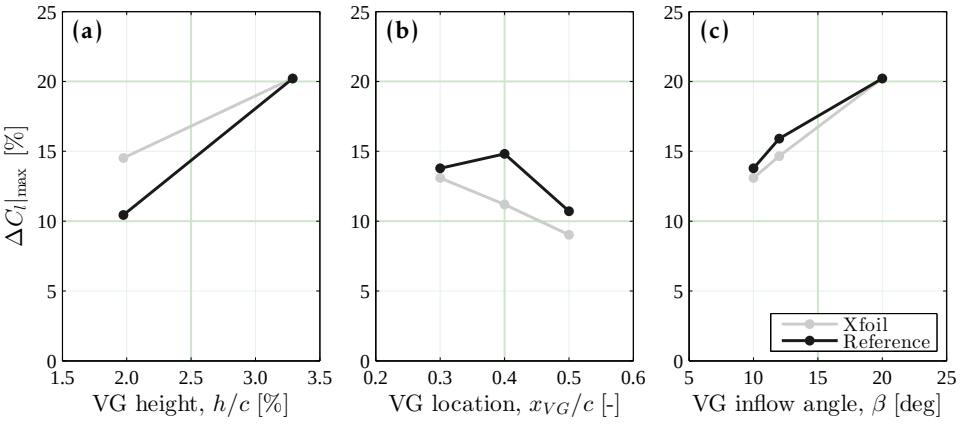

Figure 6.12: NACA4415 performance sensitivity on the VG (a) height, (b) location and (c) inflow angle at $\mathrm{Re}_c = 2 \times 10^5$.

6.4.2. Validation

Comparing all available reference cases with the Xfoil predictions, we can establish measures for the goodness of fit, as shown in Figures 6.13a-6.13c. These show the error distribution for the maximum lift coefficient, the stall angle, and the drag coefficient at zero angle of attack. The error is defined as the difference between the reference and predicted Xfoil values, normalised with respect to the reference value. The following observations can be made:

- **Maximum lift coefficient:** The error for the maximum lift coefficient is normally distributed with a mean value near zero. This result was expected since the composition of the source term expression was based on the maximum lift coefficient. With a 90% confidence interval the error of the predicted maximum lift coefficient with respect to the reference value is expected to be within ±12% accuracy.
- **Stall angle:** Whilst the modal value is roughly zero-centred, the mean error is approximately -10%, meaning that Xfoil mostly over-predicts the stall angle. However, this is a tendency of the present code for predictions even without VGs.
- **Drag coefficient:** The drag coefficient is consistently under-predicted. The drag at zero angle of attack found by Xfoil is more than 25% lower than the reference value. The net increment in drag by adding VGs is lower than given by the reference data since the parasitic VG drag has not been accounted for in the present model.

The methodology presented demonstrates a potentially useful engineering approach for modelling vortex generators in integral boundary layer codes. Reason-

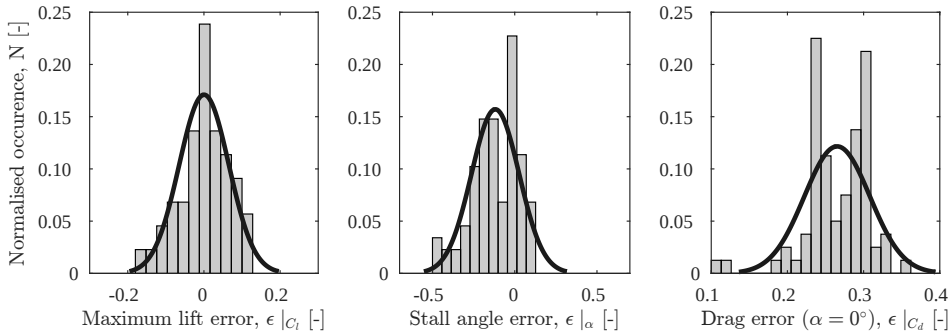

Figure 6.13: Error distribution between the reference data and the XFOIL calculations.

able predictions have been demonstrated. Some of the limitations and assumptions discussed prior can be better managed with the following suggestions:

1. **Reference data:** An expanded reference database to improve the representation of important variables within the calibration process.

2. **VG profile drag:** The model currently does not account for the additional drag introduced by the VGs. One possibility is to introduce a deficit term in the momentum equation correlated to the device geometry. Additionally, the closure relations deployed by XFOIL, such as that for skin friction, have been traditionally obtained for 2D naturally developing boundary layers. Studying the influence of vortex-induced perturbations on turbulent closure relations could pave the way for new relations accounting for embedded streamwise vortices.

3. **Laminar-turbulent transition:** Transition criteria based on the critical Reynolds number can be implemented which determines whether the VGs are capable of promoting bypass type transition.

4. **2D vs. 3D:** The fully three-dimensional flow field induced by an array of VGs is represented and modelled by a two-dimensional integral boundary layer formulation. In the close proximity of the VG, the shed vortices create a fully three-dimensional flow field. The modified XFOIL code is validated to model the global effect on lift and drag of airfoils equipped with VGs, meaning the spanwise averaged behaviour of the periodic behaviour of an array. Validating the physical correctness of this assumption could allow for better physical modelling of the VG effect.

6.5. Conclusion

This chapter demonstrates a method for modelling the effect of VGs using the integral boundary layer code Xfoil. The methodology builds on the source term approach introduced by Kerho and Kramer (2003). This was realised by adding an additional term to the equilibrium shear stress coefficient of the shear-lag equation, accounting for the increased dissipation due to streamwise vortex action in the boundary layer. A gradual step input followed by exponential decay was introduced at the VG location, mimicking the inception and evolution of an embedded streamwise vortex. This perturbation was described using three variables: the source term strength, the decay rate and the location of the VGs.

An expression was defined relating the value of the source term integral to the VG geometry and inflow conditions. This was set up using a least-square regression to calibrate the expression parameters with an extensive reference database. The resulting expression gives the required value of the source term integral as a function of the VG height, length, inflow angle and flow velocity at the tip of the VG.

The modified Xfoil code can predict the aerodynamic behaviour of an airfoil equipped with VGs. The new code is capable of addressing the effect of the VG height, length, inflow angle and chordwise position, but is not expected to capture subtle differences in VG geometry.

The error on the maximum lift coefficient is normally distributed with a mean value near zero. The stall angle is mostly over-predicted, but this is in line with the baseline airfoil predictions. The drag at zero angle of attack found by Xfoil is more than 25% lower than the reference value, which can be explained due to the lack in modelling the parasitic drag of the VGs itself.

Overall, the predicted lift polars for airfoils with VGs showed a good agreement with the reference data, and the code is demonstrated to be robust and able to model different airfoil families at a wide range of Reynolds numbers. The source term approach is proven to be promising and can be elaborated further considering some of the suggested improvements.

IV

Concluding Discussion

7

Conclusions and Recommendations

> *... but the more we discover,*
> *the more we understand that what*
> *we don't yet know is greater than what we know.*
> *The more powerful our telescopes,*
> *the stranger and more unexpected are the heavens we see.*
> *The closer we look at the minute detail of matter,*
> *the more we discover of its profound structure.*
>
> — Carlo Rovelli

The major thesis conclusions are summarised in this chapter in relation to the research questions defined at the outset. Reflections and recommendations on further research gaps, remaining or exposed by the present work, are presented in final section of this chapter.

7.1. Conclusion

The work presented in this thesis has aimed to better explain the macro and global effects of vortex generator in a wind turbine specific context. This has been organised in three main parts dealing respectively with benchmarking the state of the art, investigating macroscopic phenomena, followed by studying them on the global scale. This final chapter summarizes the main conclusions of this thesis in accordance with the research questions defined in Chapter 1, with a view towards recommended future research.

7.1.1. On the state of the art in VG modelling

The rotating blades of a wind turbine present specific challenges for designing airfoils such as a three-dimensional inflow and strong pressure gradients. Despite there being a broad level of consistent vortex generator research in recent years, rarely has this been considered in the context of rotating blades. An opportunity to define and bridge this gap thus became apparent. A consideration of radial flows present in and around rotating blade-bound flows from literature led to the definition in this thesis of the asymmetric counter-rotating vortex array. This configuration was later on chosen to represent skewing of the relative wind vector from the perspective of the vortex generators.

There have been various attempts at modelling the effects of streamwise vortices. Some are primarily concerned with the details of the vortex core itself, broadening to scaling laws for vortex evolution in a boundary layer. Modelling the streamwise vortex interaction with a separating boundary layer is many times more complex, but has been attempted in an integral boundary layer approach. Direct computation has been a much more commonly employed approach, but only for studying isolated cases. One challenge for RANS type simulations is the treatment of swirl in the turbulence models, but also in the subtleties of generating the vortex artificially in BAY-type simplifications.

To consolidate these initial findings, a benchmark and validation exercise of models and computational tools for vortex generators was performed. The test cases were two airfoils of 18% and 30% thickness featuring vortex generators for flow separation control. An integral boundary layer formulation showed promise in the efficiency of computation, although good agreement could only be obtained by matching a calibration coefficient case-by-case. .

Assessing simulation tools by comparing the final outcomes such as lift and drag is a useful gauge for performance. However, detailed investigations of the embedded vortex flows are necessary in order to explain global effects.

7.1.2. On the dynamics and evolution of embedded streamwise vortices

How can a complex inflow case be simplified and tested in a wind tunnel to assess the corresponding sensitivity of the control response?

We introduce the idea that VGs mounted on turbine blades may experience a skewed inflow relative to the array axis, in contrast to the easily and more commonly assumed axial uniform inflow. A simplified scenario of skewed inflow led to the asymmetric vortex array. This was set up by individually skewing vane pairs. Assessment of the flow field in cross-planes of the VG wakes showed that the shape factor of the underlying attached boundary layer was not very sensitive to the skew angle, or vortex asymmetry. However, the vortex trajectories were largely modulated, with respect to the conventional symmetric case. An orbiting motion in the weaker vortex for $\varphi = 10°$ resulted in it persisting closer to the wall, compared to the expected path of an ideal symmetric array, up to a height of $50h$. This corresponded with a slight improvement in the shape factor. A periodic point vortex model was developed to explain this behaviour and showed that the inviscid dynamics could dictate such a motion. Discrepancies between the measured and expected paths are particularly apparent in the wall normal position, since viscous diffusion, not considered in the vortex model, causes vortex core growth. Nonetheless, the vortex model proved effective at explaining near wake behaviour of the vortex paths.

7.1.3. On separation control and modelling with vortex generators

What parameters are relevant for the design of passive vortex generators?

The parametric investigations of the VG-equipped DU97-W-300 airfoil elucidated the most relevant vortex generator design parameters. The airfoil performance was primarily sensitive to the array configuration and chordwise position, as well as the vane height. We also showed how the presence of a VG mounting plate can exacerbate the growth of the boundary layer and promote early turbulent separation. This was manifested as a loss of lift and drag increase. Using a similar approach to recreate vortex asymmetry, vane pair skewing had a measurable effect on the airfoil performance, with a $\Delta C_{l|\max}$of 10% for skew angles up to 15°. The drag at low angles of attack consistently increased with skew angle, with up to 30% difference compared to aligned case. In the course of the experiment, we also demonstrated a quantitative application of the oil flow technique, which when used in conjunction with an inverse vortex model, yielded an estimate of the vortex strength.

Attention to the separation dynamics showed that, for a stalled airfoil in the presence of VGs, stronger lift fluctuations suggest a more intermittent mode of separation, compared to the uncontrolled case, with larger VGs in more upstream positions causing stronger fluctuations.

Optimisation of flow control devices ultimately requires knowledge of the environmental conditions of the specific application. For instance, the presence of spanwise wind turbine blade flows could make co-rotating arrays more attractive because of a lower sensitivity to inflow direction variations. Additionally, other

performance metrics such as VG self-noise may be of importance when evaluating different designs.

How can these be combined in an efficient engineering tool?

An engineering model was built on the work of Drela and Giles (1987) and Kerho and Kramer (2003), taking into account vortex-added mixing. A dissipation source-term was introduced at the chordwise vortex generator position which mimics the effect of transition. The magnitude and decay rate, mirroring the vortex formation and evolution process, were synthesised into a single integral quantity - the source term integral. The magnitude of this new term was calibrated against a large database of airfoil and flat plate measurements, yielding an empirical relation in terms of the boundary layer properties and the device geometry, namely, the normalised VG height, as well as the inflow angle. The validation highlighted drag discrepancies at lower angles of attack, mainly down to the lack of a physical model for the parasitic device drag.

7.2. Outlook

Outstanding work and remarks about follow up investigations are discussed briefly below.

Vortex asymmetry on the flow control effect

In this thesis we have explored the effect of asymmetric vortices on an attached turbulent boundary layer, as well as on an airfoil for separation control. Both indicated measurable differences compared with the symmetric counter-rotating scenario, but these experiments used slightly different vortex generator designs. To further elucidate the implications of skewness, a similar flat-plate experiment could be designed with a separating boundary layer, preferably with a controlled separation bubble. The influence of skewness can then be better quantified by assessing the response of this separation zone to the degree of asymmetry. Moreover, it would be of practical use to understand the skewness sensitivity of other vortex generator designs, particularly with respect to the vane shape and relative vane height, array spacing, and array configuration.

Rotor blade design sensitivity to asymmetry

In a separation control application, we showed that inflow skewness for counter-rotating vane arrays has a measurable effect on maximum lift and base drag. Future studies would do well to investigate skewed inflow relative to the blade leading edge with higher fidelity simulations resolving boundary layer flows. This can map the envelope of expected skewness over the blade exposed to various rotor operating conditions. With this information, combined with the variational load observations made in this thesis, blade design sensitivity can be assessed using a probabilistic approach to model the airfoil polars, similar to what has been demonstrated in Pereira et al. (2018) considering different sources of perturbation.

For wind turbine rotors, the importance of understanding yawed aerodynamics grew out of the realisation that rotors most often operate with some degree of yaw misalignment; turbines and wind farms are now designed and assessed with this flow regime in mind. Analogously, the complex bound blade flow will present, in the least, a flow which is offset from the design case, and if disregarded, could result in less favourable design solutions and compromised turbine performance. Considering the effectiveness of vortex generators in a probabilistic manner essentially adds another variable to the design space and may even indicate that other, would-be discarded designs such as co-rotating arrays, are more robust when considered from a more realistic probabilistic design point of view.

Vortex formation physics

The process of vortex formation along the vane itself has received little to no attention in literature. Research has focused on the near and far-wake, on the premise that these are the areas of interest, and that the generation process itself is largely inviscid, well understood, and not the bottleneck for computational tools. However, subtle differences in the vortical structures generated by different device shapes remain unexplained. It is conceivable that certain streamlined shapes are better at concentrating vorticity in a single coherent structure, whereas rectangular vanes have already been shown to give rise to many secondary structures. The way these secondary structures form and their influence on the lifetime of the primary vortex are important considerations for tailoring VG shapes and assessing the predictive capabilities of simulation tools.

Blade boundary layer flows

This work has largely dealt with idealised boundary layer flows for fundamental investigations. A next step would be to assess in closer detail the inner flow on a rotating blade. Field methods using tufts have been demonstrated, but model turbines provide controlled conditions ideal for research. For proper matching of the Reynolds number and scaling of the boundary layer flow, lab-scale models must revolve at high rotational speeds. This, in combination with the relatively thin blade-bound boundary layer at the laboratory scale, makes measurement very difficult. A promising line of work involves oil film interferometry, an existing measurement technique which has recently been adapted for studying skin-friction and transition on propeller blades (Schülein, 2014). Such a capability would yield valuable insights on the blade bound flow with or without flow devices, for the benefit of code validation and also to understand the interaction of a three-dimensional boundary layer with streamwise vortices.

Stall dynamics

The stall-characteristic of an airfoil strongly influences aeroelastic and vortex-induced instabilities in blades. The higher load variability introduced by the VGs which was observed in Chapter 5 might be relevant for these operating states, which present higher angles of attack (such as idling and stand-still), as well as dynamic

stall, which may occur during normal operation. Therefore the presence of VGs should be considered when evaluating these load cases.

IBL methods and closure relations

At the core of both IBL methods and RANS modelling are the turbulence models, or closure relations as is more commonly known in IBL terminology. Neither of these explicitly consider the effect of a vortex on a boundary layer. Discrepancies are thus likely to appear in the closure relations for the skin friction as well as the modelling of turbulence history effects.

In this work, the added turbulent viscosity generated by vortex-induced velocity gradients has been modelled by directly modulating the turbulent dissipation. Adding another level of detail would be to consider from first principles the velocity profiles associated with embedded vortices. These profiles would then be used for generating closure relations in a similar manner as has been successfully demonstrated for many years in traditional IBL methods (Swafford, 1983; Drela, 1989). A continuation along this approach considering boundary layer flow with streamwise vortices, particularly in flows closer to separation, can yield better suited scaling laws and closure relations. Skin-friction measurements using the oil film techniques discussed previously, even on a simple flat-plate with vortex generators, would be invaluable for this purpose.

7.3. Final remarks

This thesis has challenged established concepts and introduced some new ones for the design of better vortex generators. The research questions have addressed skewed inflow, unsteady vortex dynamics, and flow separation sensitivity and dynamics. These have ultimately been motivated from a consideration of the vortex generator operating environment - the rotating wind turbine blade. This integral line of thinking, considering the bigger picture, is key to not only improving physical understanding and modelling capabilities, but also to identify which improvements and ideas are worth pursuing.

Ultimately, the benefit of VGs is measured in AEP and cost of energy. Unless rotor designs evolve to render VGs redundant, these passive devices will remain a common feature of the modern wind turbine blade.

V

Appendices

A

Benchmark supplement

A.1. Numerical grid setups

All the grids used for the benchmark comparisons were uniquely generated by the contributing partners and detailed in a flow control report in Ferreira et al. (2015).

Fully resolved EllipSys computations were performed on grids generated using a special-purpose grid generation tool developed during the AVATAR project. The meshing algorithm first addresses the vortex generator, starting with a surface grid which wraps around the device (see e.g. Figure A.1). This process can be executed independently of the airfoil meshing process and thus many VG configurations can be pre-meshed very efficiently. The VG mesh can then be combined with an arbitrary airfoil profile in the desired configuration by careful distribution and matching of grid points around the VG and airfoil surface. The surface grid is then layered outward from the airfoil to create the 3D domain. This method results in effective block structured topologies, but typically requires closer far-field conditions ($< 30c$) to avoid excessive cell aspect ratios in the far wake. Resulting meshes used in this benchmark typically contained 64 and 128 cells in the spanwise and normal direction, and between 384-512 cells around the airfoil profile. The advantage of this approach is that the resolution and structure of the mesh can be very explicitly controlled around the VG and in its wake. The mesh for BAY-type simulations was composed of a spanwise-extruded 2D grid without local refinement around the VG, but incorporating a system of four VG vanes with symmetry conditions. All other 3D numerical tools used in the benchmark computed on a half-pair strip.

MapFlow BAY-type simulations were performed on a C-type grid with a chordwise resolution of 468 cells, 135 in the normal, and 20 in the spanwise direction.

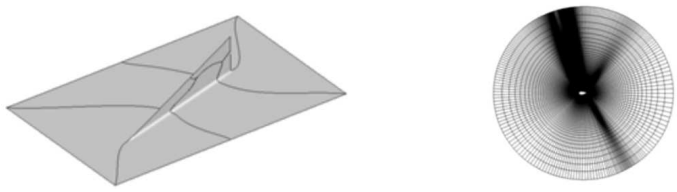

Figure A.1: Example of the (*left*) VG mesh allocation outline and (*right*) its implementation to an airfoil profile onto a typical O-grid (Ferreira et al., 2015).

The mesh was built on a 2D structured grid with local refinement in the chordwise and wall-normal directions around the VG area. The complete domain is obtained by extruding the planar mesh in the spanwise direction.

VGFlow benefits from the simplified 3D Navier Stokes formulation and computes airfoil flow with VGs in a two dimensional domain. The grids are composed as planar, structured O-grids, resulting in grids of up to two orders of magnitude smaller than the equivalent required for 3D simulations.

The OpenFOAM computations were performed on a structured O-type mesh composed of 512 circumferential cells with the far field boundary located 100 chord lengths around the airfoil. The 3D mesh was obtained by extruding a planar mesh in the spanwise direction by 36 cells, spaced by approximately 1.5mm ($\approx 11\%$ of the vane length). Either end of the domain was assigned symmetry conditions. The mesh was not refined around the VG vane, nor in its wake.

A.2. Reference metrics

Table A.1: Experimental references values for benchmarking the DU97W300 airfoil.

Case	Parameter	Unit	Clean	Clean,tr.[a]	VGs 20%c	VGs 20%c,tr.[a]
General	$C_{l,\alpha}$	[deg^{-1}]	0.114	0.121	0.122	0.123
$\alpha = 0°$	C_l	[-]	0.234	0.277	0.249	0.261
	C_d	[-]	0.014	0.011	0.019	0.018
$\alpha = \alpha_{C_l,max}$	$\alpha = \alpha_{C_l,max}$	[deg]	8.71	12.35	15.44	16.46
	C_l	[-]	1.076	1.547	1.937	1.968
	C_d	[-]	0.0284	0.0271	0.0374	0.068
$\alpha = \alpha^{opt}$	α^{opt}	[deg]	6.2	10.3	13.4	11.3
	$C_{l,d}^{opt}$	[-]	48	92	54	63

[a] tr. - free, transitional regime

Table A.2: Experimental references values for benchmarking the NTUA T18 airfoil.

Case	Parameter	Unit	Clean	VGs 30%c	VGs 40%c
General	$C_{l,\alpha}$	[deg^{-1}]	0.093	0.094	0.097
$\alpha = 0°$	C_l	[-]	0.450	0.439	0.442
	C_d	[-]	0.012	0.014	0.016
$\alpha = \alpha_{C_l,max}$	$\alpha = \alpha_{C_l,max}$	[deg]	8.17	16.27	13.24
	C_l	[-]	1.118	1.641	1.548
	C_d	[-]	0.039	0.117	0.064
$\alpha = \alpha^{opt}$	α^{opt}	[deg]	5.1	9.2	9.2
	$C_{l,d}^{opt}$	[-]	56	55	49

[a] tr. - free, transitional regime

B

PIV Experiments

B.1. Boundary Layer Tunnel Schematic

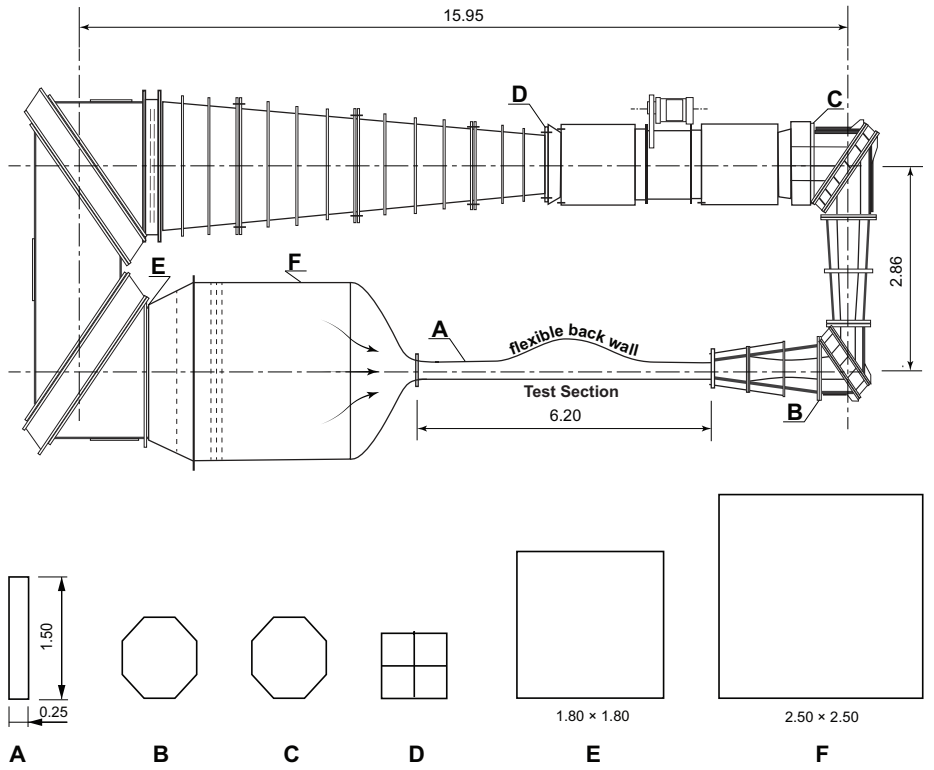

Figure B.1: Schematic of the Boundary Layer Wind Tunnel (BLT), showing a plan view of the circuit, and sectional views of the main tunnel sections.

B.2. Error analysis

In the PIV experiment, the raw measurement of velocity is used to derive the boundary layer integral properties. Errors will arise from non-idealities in the measurement setup, uncertainty in the correlation of the velocity components, as well as due to the finite sample size. The latter are the main focus in this section.

B.2.1. Spanwise inflow uniformity

Aside from fundamental sources of error, unwanted inflow three dimensionality can skew the interpretation of the results. To ensure a suitable baseflow, the uncontrolled boundary layer velocity profiles are assessed for spanwise uniformity in Figure B.2. These measurements were obtained at the location where the VG trailing edges would lie, 985mm downstream the flat plate leading edge.

B.2.2. Convergence analysis

Figures B.3-B.5 show monitors of the important velocity statistics as a function of the sample size.

B.2.3. Fundamental quantities

Due to the limited number of snapshots, a sampling error will be associated with the velocity field measurements. The following expressions represent the uncertainties associated with the 68% confidence intervals.

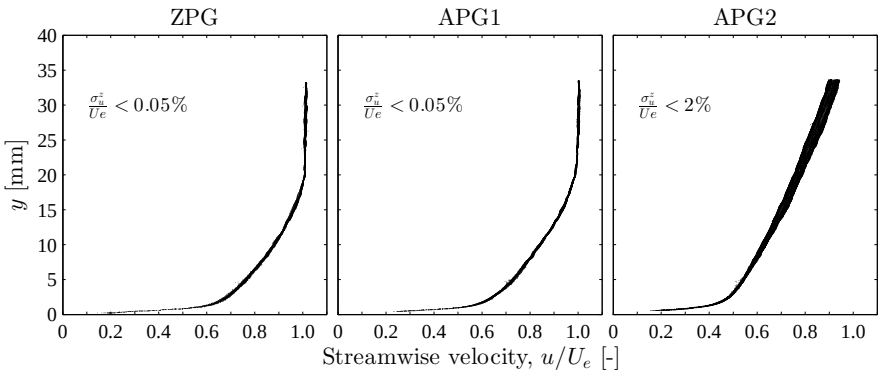

Figure B.2: Spanwise uniformity assessment for the baseflow in three pressure gradients at the location of the VG trailing edge. σ_u^z signifies the spanwise deviation of the mean velocity u at a given wall-normal position.

$$\epsilon_u = \frac{\langle u' \rangle}{\sqrt{M}} \tag{B.1}$$

$$\epsilon_{\langle u' \rangle} = \frac{\langle u' \rangle}{\sqrt{2M}} \tag{B.2}$$

$$\epsilon_{\overline{u_i u_i}} = \overline{u_i u_i} \frac{2}{M} \tag{B.3}$$

$$\tag{B.4}$$

where $M = 500$ is the sample size, or the number of realisations for a given plane.

B.2.4. Derived quantities

The error propagation to the derived quantities is discussed below.

Boundary layer integral parameters

The uncertainty propagation in the boundary layer shape factor is assessed in terms of the sampling error in the streamwise velocity, generally given by $\epsilon_u = \frac{\sigma_u}{\sqrt{N}} = \frac{\langle u' \rangle}{\sqrt{N}}$.

From the expression of the shape factor $H = \delta^\star / \theta$, we can express its compound error as

$$\frac{\epsilon_{H_j}}{H_j} = \left[\left(\frac{\epsilon_{\delta_j^\star}}{\delta_j^\star} \right)^2 + \left(\frac{\epsilon_{\theta_j}}{\theta_j} \right)^2 \right]^{\frac{1}{2}} \tag{B.5}$$

in terms of the uncertainty on the boundary layer displacement and momentum thickness $\delta_j^\star$ and θ_j. Subscript 'j' pertains to local quantities, at a particular spanwise station.

In general, for the functional relationship $y = f(x_1, x_2, ..., x_N)$ with the uncorrelated set $(x_1, x_2, \ldots, x_N)$, the error propagation is estimated as

$$\epsilon_y = \left[\left(\frac{\partial}{\partial x_1} y \right)^2 \cdot \epsilon_{x_1}^2 + \left(\frac{\partial}{\partial x_2} y \right)^2 \cdot \epsilon_{x_2}^2 + \cdots + \left(\frac{\partial}{\partial x_N} y \right)^2 \cdot \epsilon_{x_N}^2 \right]^{\frac{1}{2}} \tag{B.6}$$

Generalising $\delta_j^\star = f(u_j, u_\infty)$ and $\theta_j = g(u_j, u_\infty)$,

$$\epsilon_{\delta_j^\star} = \left[\left(\frac{\partial}{\partial u_j} f \right)^2 \cdot \epsilon_{u_j}^2 + \left(\frac{\partial}{\partial u_\infty} f \right)^2 \cdot \epsilon_{u_\infty}^2 \right]^{\frac{1}{2}} \tag{B.7}$$

Since fluctuations are much lower in the freestream compared to the boundary layer, $\epsilon_{u_\infty} \ll \epsilon_{u_j}$ and thus the contribution from the second term in Equation B.7 is neglected. The same can be said for ϵ_{θ_j}. The functional relations f and g are determined by the integration scheme, in this case, the first-order Trapezium rule. The sampling error is thus evaluated with respect to this choice of scheme. Following

through for the displacement thickness $\delta_j^\star$ and applying the integral approximation, we obtain

$$\delta_j^\star = \int_0^\delta \left(1 - \frac{u_j}{u_\infty}\right) dy \approx \sum_{i=1}^{N} \left(1 - \frac{u_{ij}}{u_\infty}\right) \Delta y \tag{B.8}$$

where 'i' indicates data points in the wall-normal direction across the boundary layer, and Δy is the uniform spacing of data samples in the wall-normal direction. Expanding and simplifying,

$$\begin{aligned} \delta_j^\star &\approx \frac{\Delta y}{2u_\infty}\Big\{\big[\big(u_\infty - u_{1j}\big) + \big(u_\infty - u_{2j}\big)\big] + \big[\big(u_\infty - u_{2j}\big) + \big(u_\infty - u_{3j}\big)\big] + \dots \qquad \text{(B.9)} \\ &\quad + \big[\big(u_\infty - u_{N-2,j}\big) + \big(u_\infty - u_{N-1,j}\big)\big] + \big[\big(u_\infty - u_{N-1,j}\big) + \big(u_\infty - u_{Nj}\big)\big]\Big\} \\ &\approx \frac{\Delta y}{2u_\infty}\Big\{2(N-1)u_\infty - u_{1j} - 2u_{2j} - 2u_{3j} - \dots - 2u_{N-1,j} - u_{Nj}\Big\} \qquad \text{(B.10)} \end{aligned}$$

Substituting this expression into Equation B.7,

$$\epsilon_{\delta_j^\star} = \left[\left(\frac{\Delta y \epsilon_{u_{1j}}}{2u_\infty}\right)^2 + \left(\frac{\Delta y \epsilon_{u_{2j}}}{u_\infty}\right)^2 + \dots + \left(\frac{\Delta y \epsilon_{u_{N-1,j}}}{u_\infty}\right)^2 + \left(\frac{\Delta y \epsilon_{u_{Nj}}}{2u_\infty}\right)^2\right]^{\frac{1}{2}} \tag{B.11}$$

or more concisely,

$$\epsilon_{\delta_j^\star} = \frac{\Delta y}{2u_\infty}\left[\epsilon_{u_{1j}}^2 + \epsilon_{u_{Nj}}^2 + 4\sum_{i=2}^{N-1} \epsilon_{u_{ij}}^2\right]^{\frac{1}{2}} \tag{B.12}$$

Similarly for ϵ_{θ_j} we find the expression,

$$\epsilon_{\theta_j} = \frac{\Delta y}{2u_\infty^2}\left[\big(u_\infty - 2u_{1j}\big)^2 \epsilon_{u_{1j}}^2 + \big(u_\infty - 2u_{Nj}\big)^2 \epsilon_{u_{Nj}}^2 + 4\sum_{i=2}^{N-1} \big(u_\infty - 2u_{ij}\big)^2 \epsilon_{u_{ij}}^2\right]^{\frac{1}{2}} \tag{B.13}$$

where $\epsilon_{u_{ij}}$ varies across the boundary layer, depending on the local root mean square of the velocity fluctuation. Equation B.12 and B.13 are used in conjunction with Equation B.5 to produce an estimate of the local uncertainty in the shape factor, ϵ_{H_j}. The spanwise average $\overline{H}$ is evaluated as a simple arithmetic mean of M spanwise instances H_j, and thus the error $\epsilon_{\overline{H}}$ compounds in quadrature as

$$\epsilon_{\overline{H}} = \frac{1}{M}\left[\sum_{j=1}^{M} \epsilon_{H_j}^2\right]^{\frac{1}{2}} \tag{B.14}$$

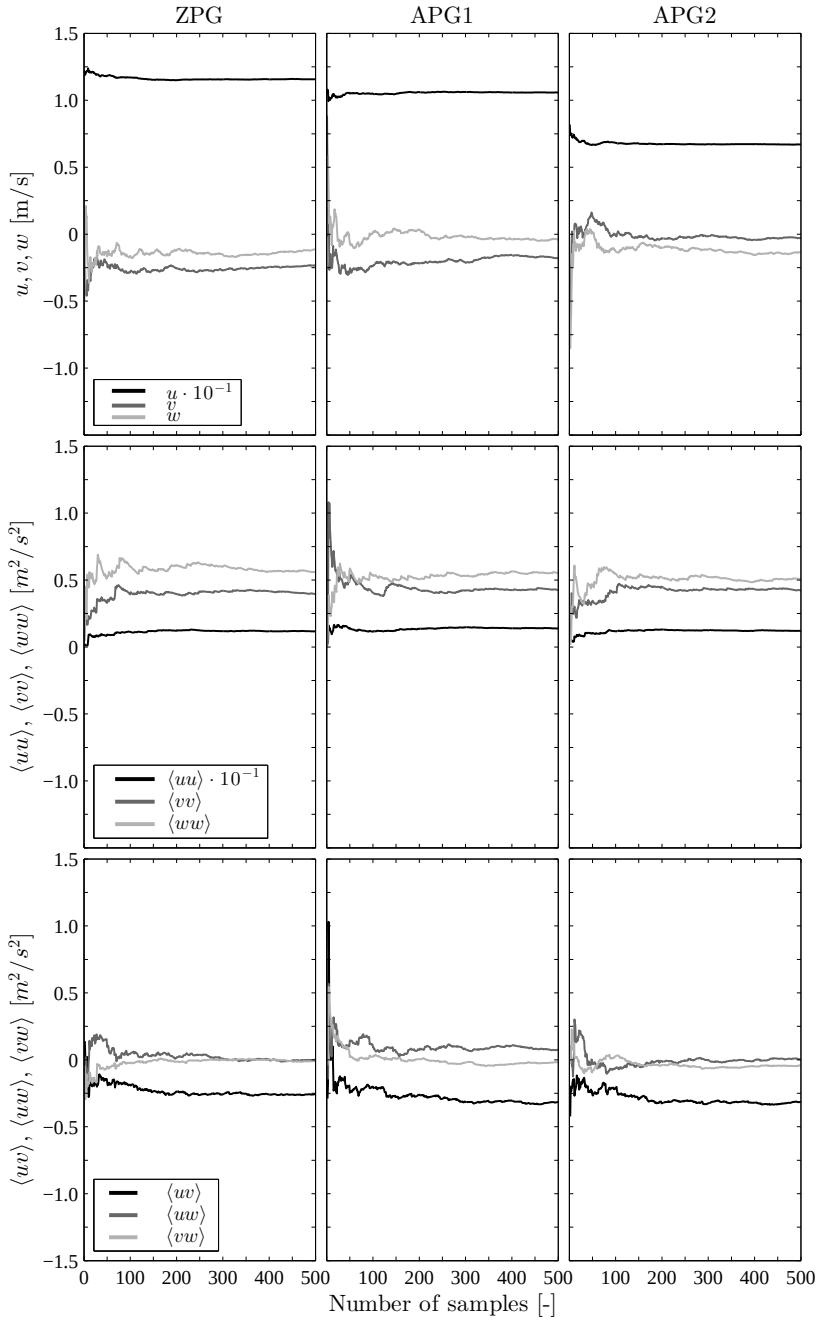

Figure B.3: Flow convergence for the baseflow in three different pressure gradients. Sampling point at $x_{VG} = 0, y/h = 1, z/D = 0$.

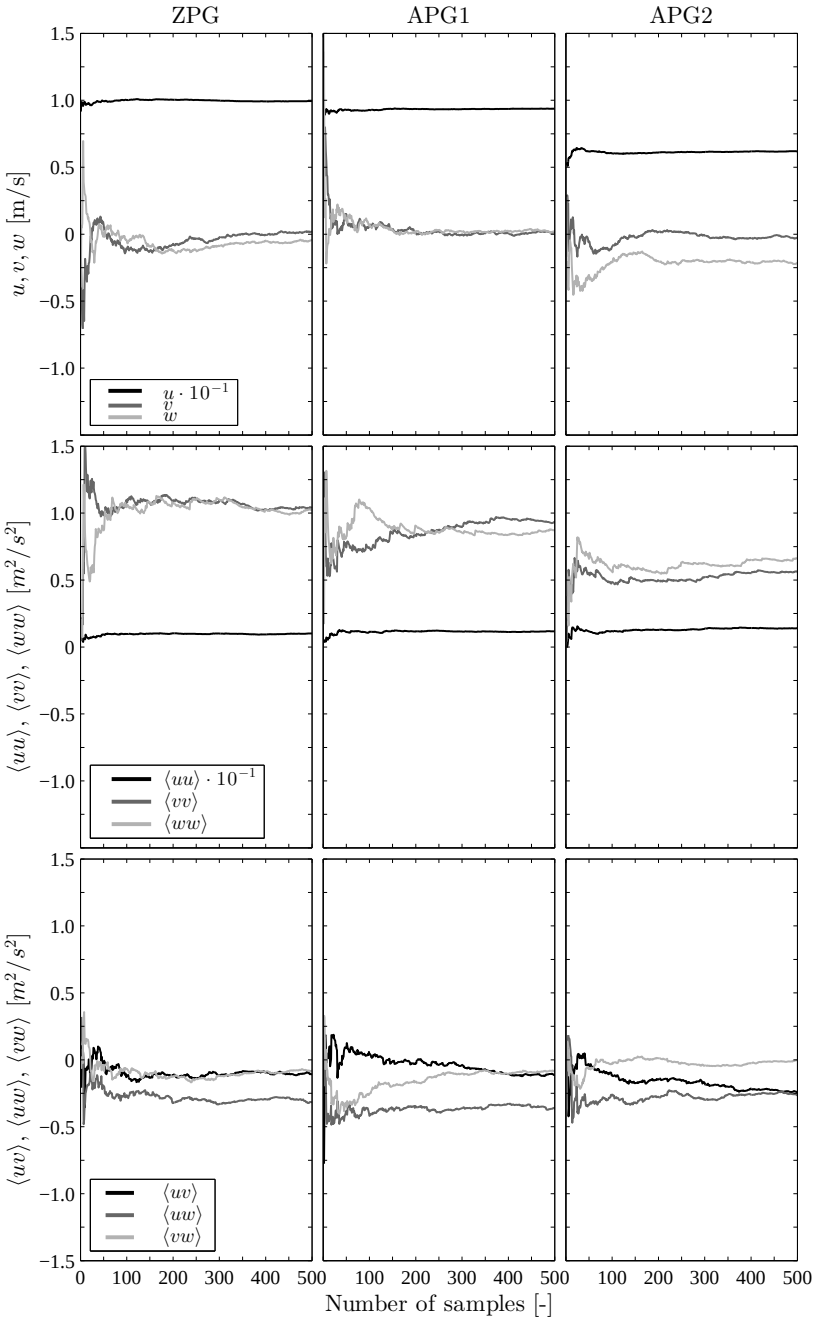

Figure B.4: Flow convergence for the controlled case in three different pressure gradients. Sampling point in the vicinity of the mean vortex centre at $x_{VG} = 25$: $y/h = 1.3, z/D = -0.3$.

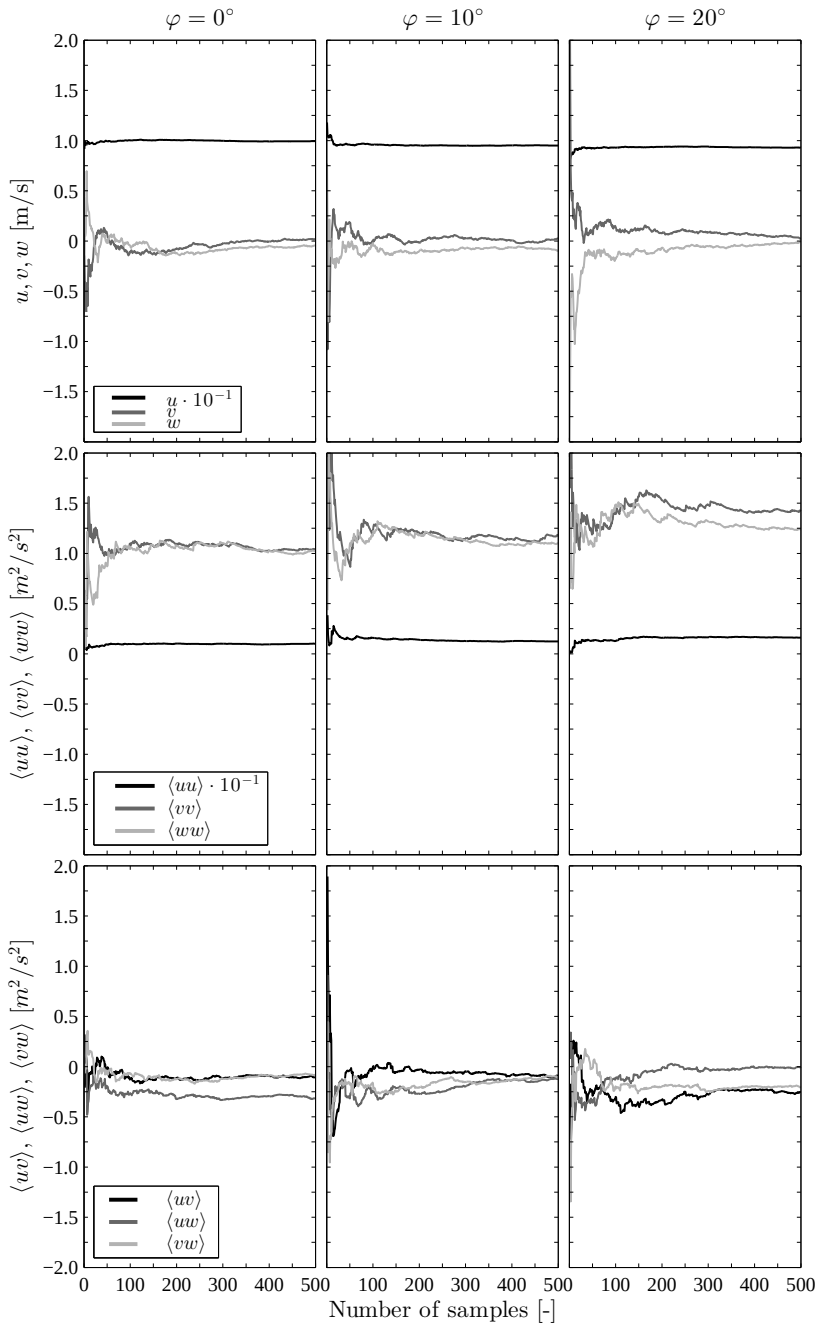

Figure B.5: Flow convergence for the controlled case for three different skew angles. Sampling point in the vicinity of the mean vortex centre at $x_{VG} = 25$; $\varphi = 0°$: $y/h = 1.3, z/D = -0.3$, $\varphi = 10°$: $y/h = 1.4, z/D = -0.5$, $\varphi = 10°$: $y/h = 1.6, z/D = -0.6$.

C

LTT Experiments

C.1. Low Turbulence Tunnel Schematic

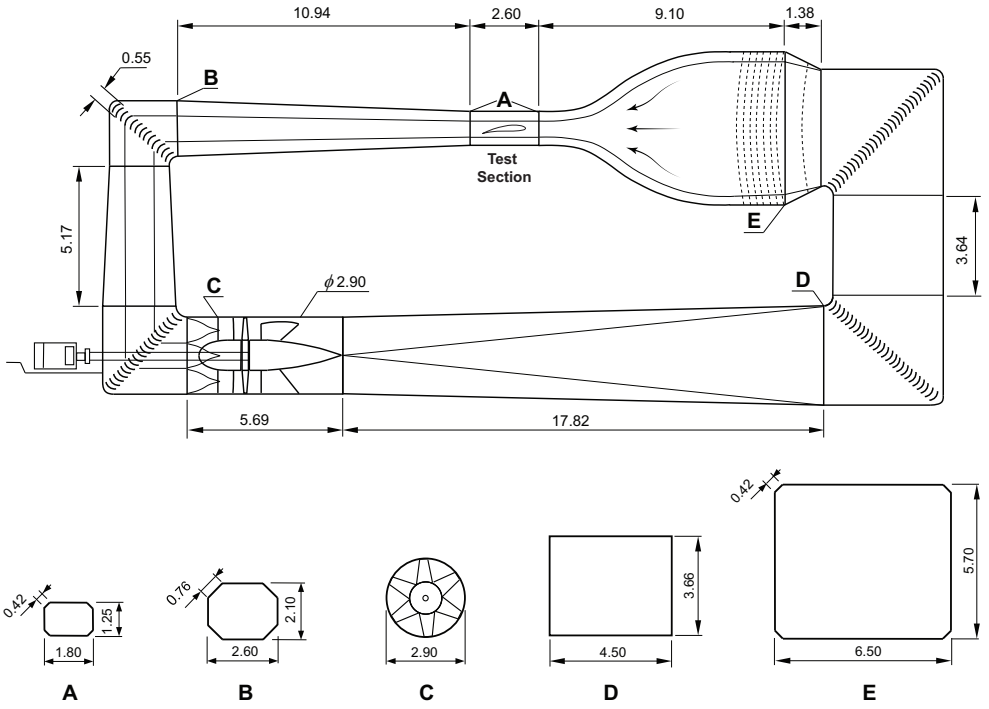

Figure C.1: Schematic of the Low Turbulence Tunnel (LTT).

C.2. Error analysis

Two-dimensional wind tunnel wing testing has a long history rooted in the aerospace field. Testing guidelines and wind tunnel corrections are therefore well established. However, different facilities implement these in slightly different ways. This perhaps explains the lack of a general framework for assessing uncertainty in such testing campaigns. This section proposes such a framework and assesses the uncertainties in a comprehensive fashion. Some indicative uncertainty estimates are finally given to complement the experimental results presented in Chapter 5.

Errors in such tests result from:

1. **Discretisation errors,** ϵ_N. Load coefficients (lift, drag and moments) are integral loads from the pressure and shear stress loads on the airfoil. A finite number of locations along the chord carry orifices for sampling the pressure and thus, an additional error manifests in the integral load calculations. This error is a function of the number of pressure orifices, as well as the computational integration scheme. A similar error is present in the total drag calculation from the wake rake pressure probes.

2. **Sensor accuracy,** ϵ_δ. Pressure signals are fed through electronic scanners which have a limited, albeit high, signal resolution. This is specified by the manufacturer and depends on the pressure rating of the scanner.

3. **Statistical sampling errors,** ϵ_S. For steady measurements, a given pressure signal is sampled at a specified rate for a certain amount of time, giving a finite sample size which is taken to be representative of the population. The finite size of this sample contributes a statistical error to ensemble averaged measurements.

4. **Miscellaneous**. Other error sources are difficult to quantify and can only be managed through good practice. For instance, the calculation of the total drag assumes a certain wake cut-off length aft of the airfoil. At low angles of attack, the exact location of this cut-off may influence the drag by a few counts. At high angles of attack or when separation starts encroaching the airfoil, three-dimensional effects comes into play and may skew pressure readings, especially if for instance orifices are arranged in staggered formation.

C.2.1. Convergence analysis

Due to the limited number of data points, a sampling error will be associated with the pressure measurements. Figure C.2 shows lift and drag monitors as a function of the sample size.

C.2.2. Discretisation error

Airfoil model pressure measurements require the surface static pressure to be sampled at finite points. A large number of orifices is desirable to obtain the best

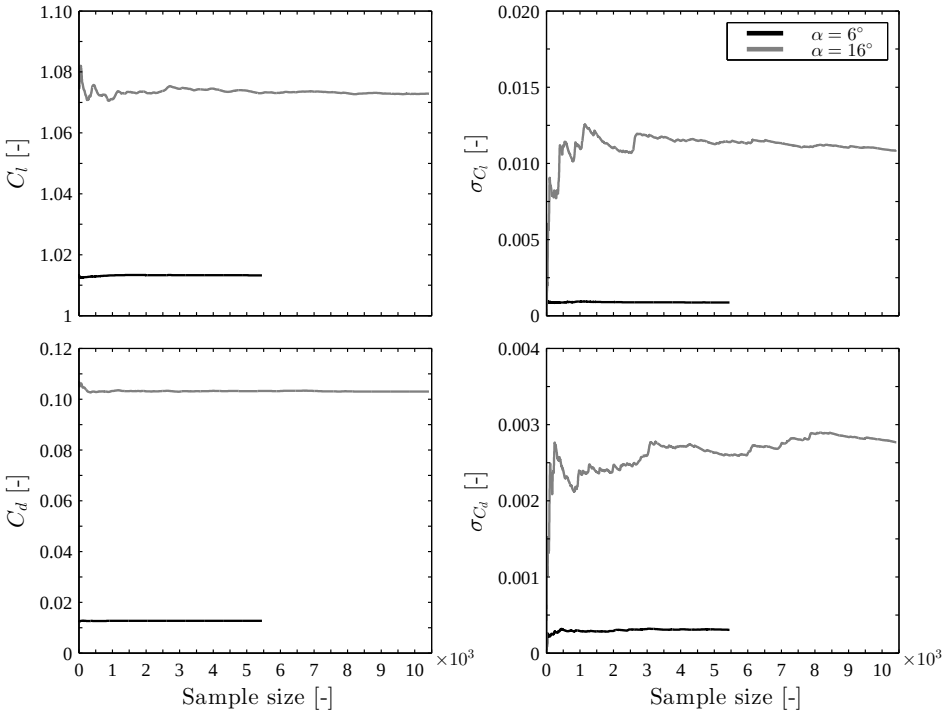

Figure C.2: Effect of sample size on (uncorrected) average lift and drag coefficients and their standard deviation. Analysis is shown for an attached and separated angle of attack ($\alpha = 6°$ and $16°$) for the clean, uncontrolled airfoil.

estimate of the true pressure distribution. However, space limitations for pressure tubes, model costs, available pressure scanners, and surface finish all limit the practical number of orifices possible. Therefore, the global loads are often deduced from first-order integral approximations using the discrete pressure distribution, such as the trapezium-rule. This approximation naturally introduces a spatial discretisation error, which cannot be assessed without knowing the true value of the measured quantity. To circumvent this and approach the problem in a generalised manner, we consider Joukowski airfoils whose profiles are parametrically defined in terms of thickness and camber, and more importantly, whose lift can be calculated in closed mathematical form. This inviscid model does not account for flow separation but provides nonetheless a useful assessment of errors inherent to discrete pressure sampling.

The Joukowski transformation maps a circle from the z-plane to an airfoil-like geometry in the ζ-plane. Although this class of airfoils have some atypical features such as a cusped trailing edge and a overly bulbous nose, the theoretical analysis

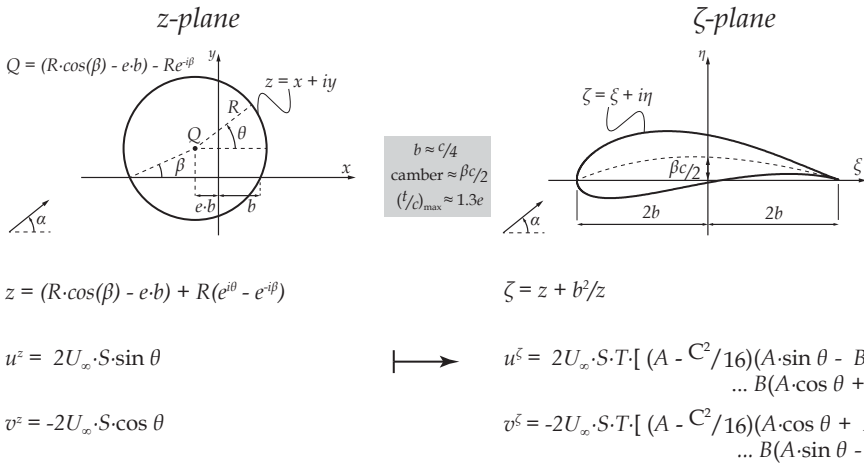

Figure C.3: Conformal mapping using a Joukowski transformation.

provides closed form solutions for the flow field, useful for this part of the error analysis. The principal transformation and resulting relations are depicted in Figure C.3. These relations are based on the forms given by Katz and Plotkin (2001) and have been modified to account for camber, valid for $\{e << 1 \,|\, e \in \mathbb{R}_{\geq 0}\}$. The following substitutions have been defined

$$S = \sin(\alpha+\beta) - \sin(\alpha-\theta) \tag{C.1}$$
$$k = -e\cdot b + R\cos\theta \tag{C.2}$$
$$A = k^2 - R^2[\sin\beta + \sin\theta]^2 \tag{C.3}$$
$$B = 2Rk[\sin\beta + \sin\theta] \tag{C.4}$$
$$T = \left[(A - \tfrac{C^2}{16})^2 + B^2\right]^{-1} \tag{C.5}$$

Simplifying the camber $\beta = 0°$ in these relations returns the expression for a symmetric airfoil as given in Katz and Plotkin (2001).[1]

Finally, the analytical form of the lift coefficient is given as

$$C_{L,exact} = 8\pi\frac{R}{c}sin(\alpha+\beta) \tag{C.6}$$

Assessing the effect of discretisation is then a simple matter of analytically evaluating the pressure along the Joukowski airfoil at discrete locations using Bernoulli's theorem,

[1] Note that A in the term $(A - C^2/16)$ (appearing here in the nominator) is erroneously squared in the reference text.

$$C_p = 1 - \frac{u^2 + v^2}{U_\infty^2} \tag{C.7}$$

The trapezium rule was used to estimate the integrals because of its robustness, wide-spread use and independence from the actual data point distribution (Titchener et al., 2015). The global error is then defined as

$$\epsilon = \frac{C_{L,num} - C_{L,exact}}{C_{L,exact}} \times 100\% \tag{C.8}$$

and is generally presented as a function of the sampling density N.

Due to the closed form solutions afforded by a Joukowski mapping, the error sensitivity to a number of parameters may be easily investigated, such as airfoil camber, thickness and angle of attack. The method of data point sampling may also be assessed, i.e. uniform/non-uniform spatial pressure sampling. The chordwise pressure orifice distribution x/c_{po} of the DU97-W-300 model is plotted in Figure C.4 for reference. Pressure orifices are clustered towards the airfoil leading edge to capture the considerable pressure gradients induced by the high nose curvature. This is a common practice in the instrumentation of 2D wing models. An analytic *cosine* distribution g describes the orifice positions relatively well. Therefore, non-uniformity in the ensuing analysis is simply prescribed using the mapping:

$$g : (X/c) \rightarrow 1 - \cos(X/c) \tag{C.9}$$

where $X/c = x/c \cdot \pi/2$ for $0 < x/c < 1$.

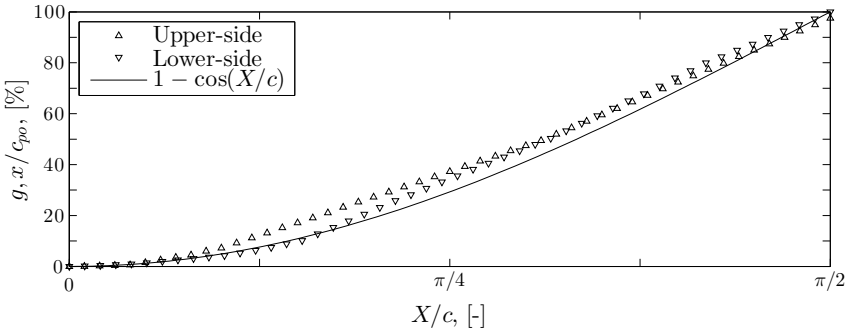

Figure C.4: Pressure orifice distribution on the DU97-W-300 model. Upper ($y/c_{po} > 0$) and lower side ($y/c_{po} < 0$) ports are distinguished with symbols and compared with an analytical *cosine* distribution function for modelling purposes (solid line).

The error sensitivities are shown in Figure C.5. The error for the uniform distribution is relatively insensitive to thickness, camber, as well as angle of attack, with $N_{0.1} \approx 80$ for all cases ($N_{0.1}$ refers to the number of points required to achieve

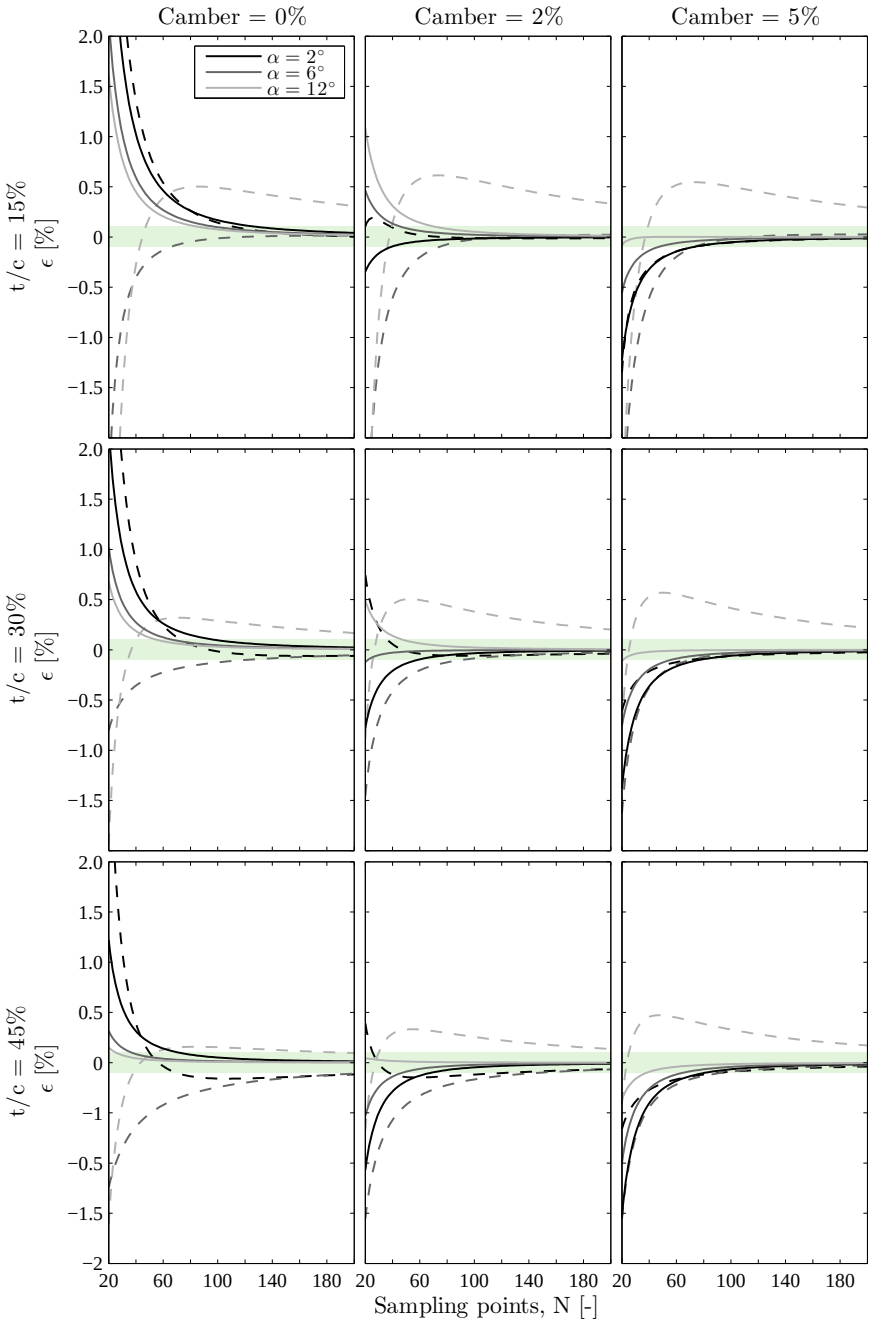

Figure C.5: Spatial sampling error as a function of airfoil thickness (rows), camber (columns), angle of attack (see color legend) and sampling method: uniform (- -) and non-uniform (–). The shaded region signifies the $\epsilon_{0.1}$ band.

a minimum error of 0.1%). Once the pressure is sampled non-uniformly, a given accuracy is generally achieved with fewer points. Practically, this implies that fewer pressure orifices would be required. Also evident is that for given N, the error is smaller at higher angles of attack of cambered airfoils. This occurs because the suction peak is drawn further forward where the spatial sampling is finer. Increasing thickness and camber require more points to achieve a given accuracy.

For the DU97-W-300 model, the thickness is 30% with approximately 2% camber. With its 102 pressure orifices distributed as shown in Figure C.5, we can expect a discretisation error $\epsilon_N < 0.05\%$.

C.2.3. Sensor/Sampling error

With the aid of Figure C.6, the principal airfoil loads can be written as

$$C_l = C_n \cos\alpha - C_t \sin\alpha \tag{C.10}$$

$$C_d = C_n \sin\alpha + C_t \cos\alpha \tag{C.11}$$

For pressure measurements, it is convenient to redefine the lift vector in terms of the drag component,

$$C_l = \frac{C_n}{\cos\alpha} - C_d \tan\alpha \tag{C.12}$$

Additionally, the drag evaluated through Equation C.11 considering only pressure forces, neglects shear forces. Thus, at low angles of attack, the drag is calculated from the model momentum loss evaluated with the wake rake:

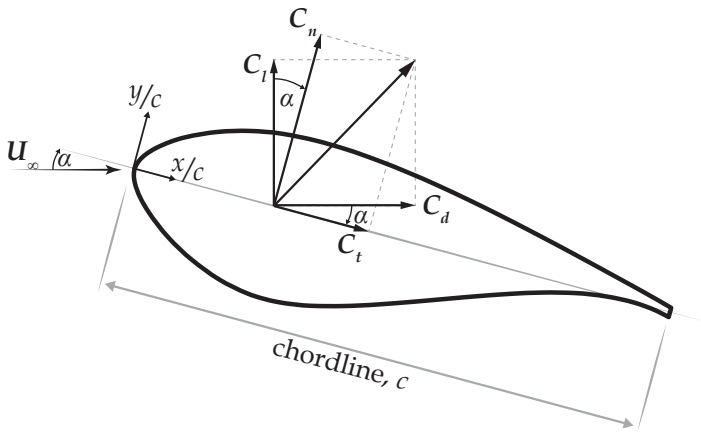

Figure C.6: Airfoil coordinate system and load conventions.

$$C_d = \int 2\left(\frac{U}{U_\infty} - \frac{U^2}{U_\infty^2}\right) d\left(\frac{y}{c}\right) \tag{C.13}$$

Within the airfoil reference frame $(x/c, y/c)$ as in Figure C.6, the normal and tangential pressure loads are determined as (Anderson, 2005):

$$C_n = \int C_{p,l}\, d\,(x/c) - \int C_{p,u}\, d\,(x/c) \tag{C.14}$$

$$C_t = \int C_{p,u} \frac{dy_u}{dx}\, d\,(x/c) - \int C_{p,l} \frac{dy_l}{dx}\, d\,(x/c) \tag{C.15}$$

The lift and drag are evidently compound quantities. To estimate their uncertainty, these must be decomposed in terms of the most basic measurement unit. In this case, this is the pressure signal measured on the airfoil model or in the wake. What follows is an assessment of the error propagation in all physical or derived quantities:

1. Pressure Signal, p

   The raw pressure signal resolution depends on the specific sensor type and range. The Initium Electronic pressure scanners were rated for ±10 and ±5 PSI ($\epsilon_r = 0.05\%$) and ±1 and ±0.36 PSI ($\epsilon_r = 0.1\%$).

   In conjunction with the limited sample size, errors combine to give

   $$\epsilon_p = \left[\left(\frac{1.96\sigma}{\sqrt{M}}\right)^2 + \epsilon_r^2\right]^{1/2} \tag{C.16}$$

   at a 95% confidence level; M is the sample size of the measured pressure signal and σ represents its standard deviation. A large sample size or finer measurement resolution clearly reduce the measurement uncertainty. We will next see how this basic error quantity propagates through derived quantities.

2. Pressure Coefficient, C_p

   $$C_p = \frac{p_i - p_\infty}{q_\infty} = \frac{p_i - p_\infty}{p_{T,\infty} - p_\infty} \tag{C.17}$$

   where subscript 'T' indicates total pressure. The error on the pressure coefficient is then,

   $$\epsilon_{C_p} = \left[\left(\frac{\partial C_p}{\partial p_i}\epsilon_{p_i}\right)^2 + \left(\frac{\partial C_p}{\partial p_\infty}\epsilon_{p_\infty}\right)^2 + \left(\frac{\partial C_p}{\partial p_{T,\infty}}\epsilon_{p_{T,\infty}}\right)^2\right]^{1/2} \tag{C.18}$$

   with $\dfrac{\partial C_p}{\partial p_i} = \dfrac{1}{(p_{T,\infty} - p_\infty)}$, $\dfrac{\partial C_p}{\partial p_\infty} = \dfrac{p_i - p_{T,\infty}}{(p_{T,\infty} - p_\infty)^2}$ and $\dfrac{\partial C_p}{\partial p_{T,\infty}} = \dfrac{p_i - p_\infty}{(p_{T,\infty} - p_\infty)^2}$.

   The error is shown for the uncontrolled (clean) case in Figure C.7, carrying an upper bound of 1%.

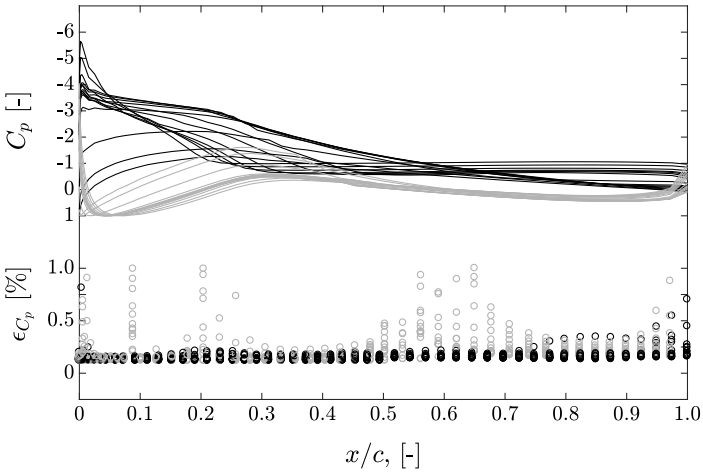

Figure C.7: Relative error distribution for the pressure coefficient: upper surface (black) and lower surface (grey). Case: uncontrolled ($\alpha = 0° - 24°$).

3. Normal Force Coefficient, C_n

   Again applying the Trapezium rule to evaluate the normal force,

$$C_n \approx \left[\frac{1}{2}C^0_{p,l}\Delta(x_l/c)^1 + \sum_{i=1}^{N_l-1}\left(C^i_{p,l}\Delta(X_l/c)^i\right) + \frac{1}{2}C^{N_l}_{p,l}\Delta(x_l/c)^{N_l}\right] - \left[\frac{1}{2}C^0_{p,u}\Delta(x_u/c)^1 + \sum_{i=1}^{N_u-1}\left(C^i_{p,u}\Delta(X_u/c)^i\right) + \frac{1}{2}C^{N_u}_{p,u}\Delta(x_u/c)^{N_u}\right] \tag{C.19}$$

   where $\Delta(X/c)^i = \dfrac{\Delta(x/c)^i + \Delta(x/c)^{i+1}}{2}$.

   It follows that the error is

$$\epsilon_{C_n} \approx \left[\left(\frac{1}{2}\Delta(x_l/c)^1\epsilon^0_{C_{p,l}}\right)^2 + \sum_{i=1}^{N_l-1}\left(\Delta(X_l/c)^i\epsilon^i_{C_{p,l}}\right)^2 + \left(\frac{1}{2}\Delta(x_l/c)^{N_l}\epsilon^{N_l}_{C_{p,l}}\right)^2 + \ldots \ldots\left(\frac{1}{2}\Delta(x_u/c)^1\epsilon^0_{C_{p,u}}\right)^2 + \sum_{i=1}^{N_u-1}\left(\Delta(X_u/c)^i\epsilon^i_{C_{p,u}}\right)^2 + \left(\frac{1}{2}\Delta(x_u/c)^{N_u}\epsilon^{N_u}_{C_{p,u}}\right)^2\right]^{1/2} \tag{C.20}$$

4. Tangential Force Coefficient, C_t

   The Tangential force is approximated by

$$C_t \approx \left[\frac{1}{2}C_{p,u}^0 \frac{dy_u}{dx}^0 \Delta(x_u/c)^1 + \sum_{i=1}^{N_u-1}\left(C_{p,u}^i \frac{dy_u}{dx}^i \Delta(X_u/c)^i\right) + \frac{1}{2}C_{p,u}^{N_u} \frac{dy_u}{dx}^{N_u} \Delta(x_u/c)^{N_u}\right] - \ldots$$
$$\left[\frac{1}{2}C_{p,l}^0 \frac{dy_l}{dx}^0 \Delta(x_l/c)^1 + \sum_{i=1}^{N_l-1}\left(C_{p,l}^i \frac{dy_l}{dx}^i \Delta(X_l/c)^i\right) + \frac{1}{2}C_{p,l}^{N_l} \frac{dy_l}{dx}^{N_l} \Delta(x_l/c)^{N_l}\right] - \ldots$$
$$C_{p,TE} \cdot h_{TE}/c \tag{C.21}$$

where the last term represents the additional contribution from a blunt trailing edge with thickness h_{TE}/c, if the pressure there is available. This results in an error of

$$\epsilon_{C_t} \approx \left[\left(\frac{1}{2}\frac{dy_u}{dx}^0 \Delta(x_u/c)^1 \epsilon_{C_{p,u}}^0\right)^2 + \sum_{i=1}^{N_u-1}\left(\frac{dy_u}{dx}^i \Delta(X_u/c)^i \epsilon_{C_{p,u}}^i\right)^2 + \left(\frac{1}{2}\frac{dy_u}{dx}^{N_u} \Delta(x_u/c)^{N_u} \epsilon_{C_{p,u}}^{N_u}\right)^2 + \ldots\right.$$
$$\ldots\left(\frac{1}{2}\frac{dy_l}{dx}^0 \Delta(x_l/c)^1 \epsilon_{C_{p,l}}^0\right)^2 + \sum_{i=1}^{N_l-1}\left(\frac{dy_l}{dx}^i \Delta(X_l/c)^i \epsilon_{C_{p,l}}^i\right)^2 + \left(\frac{1}{2}\frac{dy_l}{dx}^{N_l} \Delta(x_l/c)^{N_l} \epsilon_{C_{p,l}}^{N_l}\right)^2 + \ldots$$
$$\left.\ldots\left(h_{TE}/c\,\epsilon_{C_{p,TE}}\right)^2\right]^{1/2} \tag{C.22}$$

5. Drag Coefficient, C_d

Evaluating the drag from the airfoil loads using Equation C.11 yields

$$\epsilon_{C_d} = \left[\left(\frac{\partial C_d}{\partial \alpha}\epsilon_\alpha\right)^2 + \left(\frac{\partial C_d}{\partial C_n}\epsilon_{C_n}\right)^2 + \left(\frac{\partial C_d}{\partial C_t}\epsilon_{C_t}\right)^2\right]^{1/2} \tag{C.23}$$

with $\frac{\partial C_d}{\partial \alpha} = C_n \cos\alpha - C_t \sin\alpha$, $\frac{\partial C_d}{\partial C_n} = \sin\alpha$ and $\frac{\partial C_d}{\partial C_t} = \cos\alpha$.

When evaluated via the wake rake, the drag is again summed using the Trapezium rule along the direction of measurement. Using the nomenclature indicated in Figure C.8,

$$C_d \approx \frac{1}{2}\Delta(z/c)^1 C_d^0 + \sum_{i=1}^{N-1}\left(\Delta(Z/c)^i C_d^i\right) + \frac{1}{2}\Delta(z/c)^N C_d^N \tag{C.24}$$

where $\Delta(Z/c)^i = \frac{\Delta(z/c)^i + \Delta(z/c)^{i+1}}{2}$ and for convenience,

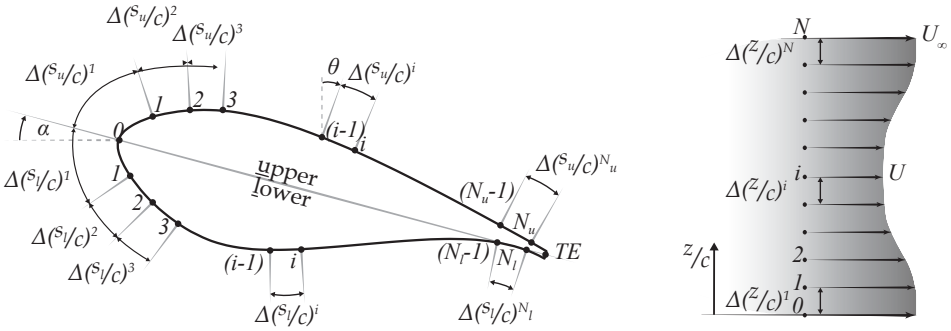

Figure C.8: Airfoil surface pressure distribution, wake discretisation and nomenclature.

$$C_d^i = 2\left(\frac{U}{U_\infty} - \frac{U^2}{U_\infty^2}\right) \tag{C.25}$$

$$= 2\left[\left(\frac{p_{T,wr}^i - p_{wr}^i}{p_{T,\infty} - p_\infty}\right)^{1/2} - \frac{p_{T,wr}^i - p_{wr}^i}{p_{T,\infty} - p_\infty}\right] \tag{C.26}$$

The errors in C_d and C_d^i are

$$\epsilon_{C_d} = \left[\left(\frac{1}{2}\Delta(z/c)^1 \epsilon_{C_d}^0\right)^2 + \sum_{i=1}^{N-1}\left(\Delta(Z/c)^i \epsilon_{C_d}^i\right)^2 + \left(\frac{1}{2}\Delta(z/c)^N \epsilon_{C_d}^N\right)^2\right]^{1/2} \tag{C.27}$$

$$\epsilon_{C_d^i} = \left[\left(\frac{\partial C_d^i}{\partial p_{T,wr}^i}\epsilon_{p_{T,wr}^i}\right)^2 + \left(\frac{\partial C_d^i}{\partial p_{wr}^i}\epsilon_{p_{wr}^i}\right)^2 + \left(\frac{\partial C_d^i}{\partial p_{T,\infty}}\epsilon_{p_{T,\infty}}\right)^2 + \left(\frac{\partial C_d^i}{\partial p_\infty}\epsilon_{p_\infty}\right)^2\right]^{1/2} \tag{C.28}$$

with

$$\frac{\partial C_d^i}{\partial p_{T,wr}^i} = 2\left[\frac{1}{2}\left(p_{T,wr}^i - p_{wr}^i\right)^{-\frac{1}{2}}\left(p_{T,\infty} - p_\infty^i\right)^{-\frac{1}{2}} - \left(p_{T,\infty} - p_\infty\right)^{-1}\right] \tag{C.29}$$

$$\frac{\partial C_d^i}{\partial p_{wr}^i} = 2\left[-\frac{1}{2}\left(p_{T,wr}^i - p_{wr}^i\right)^{-\frac{1}{2}}\left(p_{T,\infty} - p_\infty^i\right)^{-\frac{1}{2}} + \left(p_{T,\infty} - p_\infty\right)^{-1}\right] \tag{C.30}$$

$$\frac{\partial C_d^i}{\partial p_{T,\infty}} = 2\left[-\frac{1}{2}\left(p_{T,wr}^i - p_{wr}^i\right)^{\frac{1}{2}}\left(p_{T,\infty} - p_\infty^i\right)^{-\frac{3}{2}} + \left(p_{T,wr}^i - p_{wr}^i\right)\left(p_{T,\infty} - p_\infty\right)^{-2}\right] \tag{C.31}$$

$$\frac{\partial C_d^i}{\partial p_\infty} = 2\left[\frac{1}{2}\left(p_{T,wr}^i - p_{wr}^i\right)^{\frac{1}{2}}\left(p_{T,\infty} - p_\infty^i\right)^{-\frac{3}{2}} - \left(p_{T,wr}^i - p_{wr}^i\right)\left(p_{T,\infty} - p_\infty\right)^{-2}\right] \tag{C.32}$$

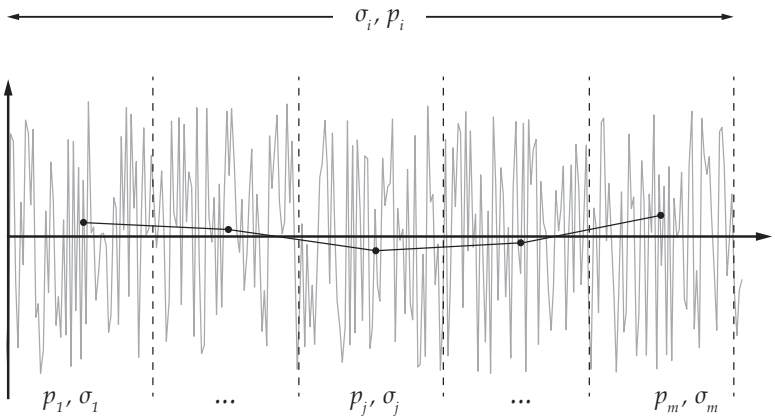

Figure C.9: Illustrating the relation between the sample and sub-sample statistics for a 1-second period with 5 sub-samples (5Hz). Each sub-sample mean p_j is represented by a filled symbol, which is associated with a certain σ_j.

6. Lift Coefficient, C_l

$$\epsilon_{C_l} = \left[\left(\frac{\partial C_l}{\partial \alpha} \epsilon_\alpha \right)^2 + \left(\frac{\partial C_l}{\partial C_n} \epsilon_{C_n} \right)^2 + \left(\frac{\partial C_l}{\partial C_d} \epsilon_{C_d} \right)^2 \right]^{1/2} \tag{C.33}$$

$$\text{with } \frac{\partial C_l}{\partial \alpha} = \frac{1}{\cos^2 \alpha} (C_n \sin \alpha - C_d), \frac{\partial C_l}{\partial C_n} = \frac{1}{\cos \alpha} \text{ and } \frac{\partial C_l}{\partial C_d} = -\tan \alpha.$$

Note on partitioned (sub-sampled) variable statistics

The pressure sensors used in LTT experiments are typically sampled at a frequency of approximately 337Hz. For efficient data transfer, the data acquisition system bundles this high frequency data on the fly into sub-samples with an associated mean p_j and standard deviation σ_j, at an effective rate of approximately 5Hz (see illustration C.9). Most data was collected in this way. This means that to deduce the global sample statistics (p_i, σ_i) at every operating point, we need to further process the sub-sample statistics to provide a correct estimate for ϵ_p.

Let s be the number of sub-samples, m the size of the sub-samples and M the global number of samples ($m = M/s$). Sub-samples are all of similar size. The global mean is simply equal to the mean of the sub-sample means, i.e.

$$p_i = \frac{1}{s} \sum_{j=1}^{s} \left(p_j \right) \tag{C.34}$$

Using the sub-sample statistics, it can be shown that the global standard deviation is

$$\sigma_i^2 = \frac{m-1}{M-1}\left[\frac{m(s-1)}{m-1}\sigma_{p_j}^2 + \sum_{j=1}^{s}\sigma_j^2\right] \tag{C.35}$$

where σ_{p_j} is the standard deviation of the sub-sample means.

Using p_j and σ_j as provided by the data acquisition system, Equation C.34 and Equation C.35 can be used in conjunction with Equation C.16 to estimate ϵ_p for each operating point on a polar.

C.2.4. Global error

The combination of sensor, sampling and discretisation errors yields overall errors on lift and drag as shown in Figure C.10. The lift error ϵ_{C_l} is below 0.1% whilst the drag carries a maximum 2% error.

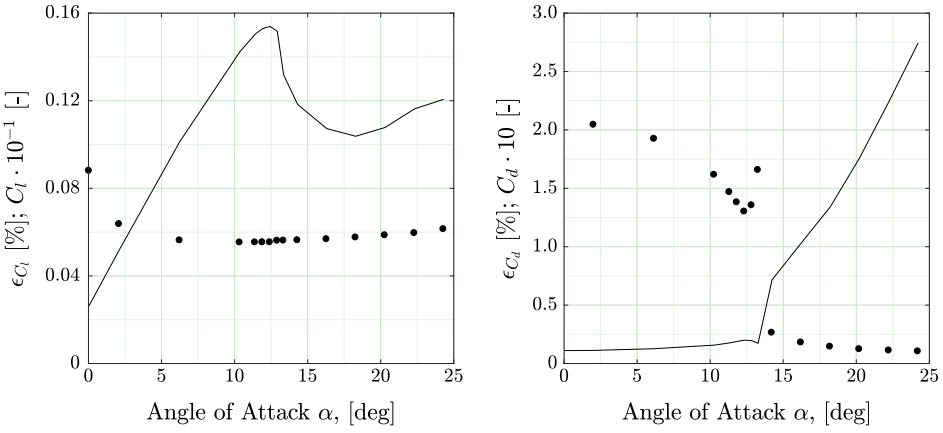

Figure C.10: Lift and drag polars (solid lines) and their respective relative errors (symbols). Note scaling of force coefficients for plotting purposes. Case: clean, uncontrolled airfoil.

C.3. Measurement Polars

Lift and drag polars are presented for all investigated sensitivities in this section. In all plots, the drag is shown with a pre-multiplier of 10^2 to elucidate comparisons. Many of the figures contain inserts detailing parts of the trends; the axes of these inserts correspond to the axes of the parent figure; all cases are clean unless otherwise stated.

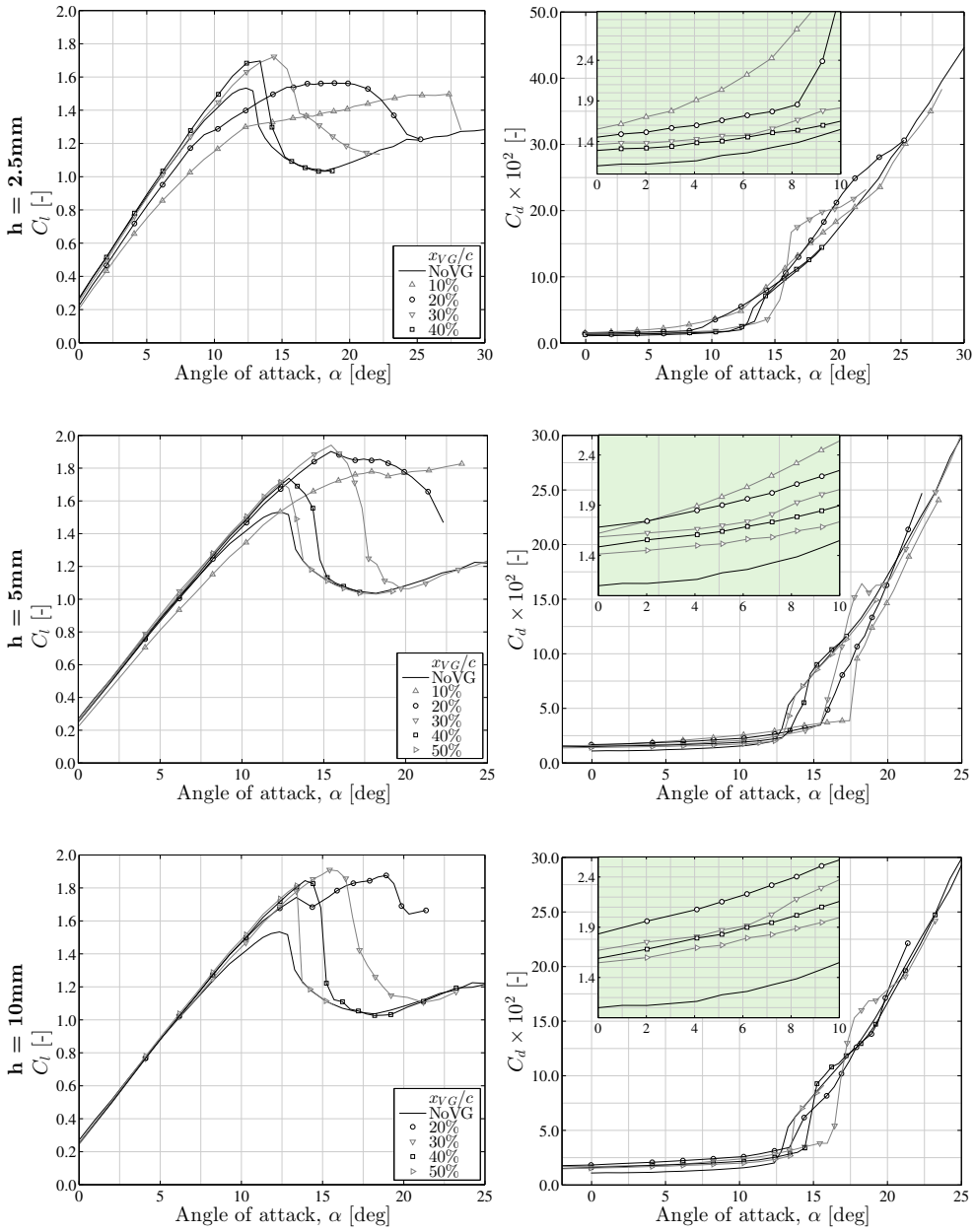

Figure C.11: Sensitivity to the VG vane height and array chordwise placement. Graphs are grouped into rows according to the VG height (top-bottom): $h = 2.5$, 5.0 and 10 mm.

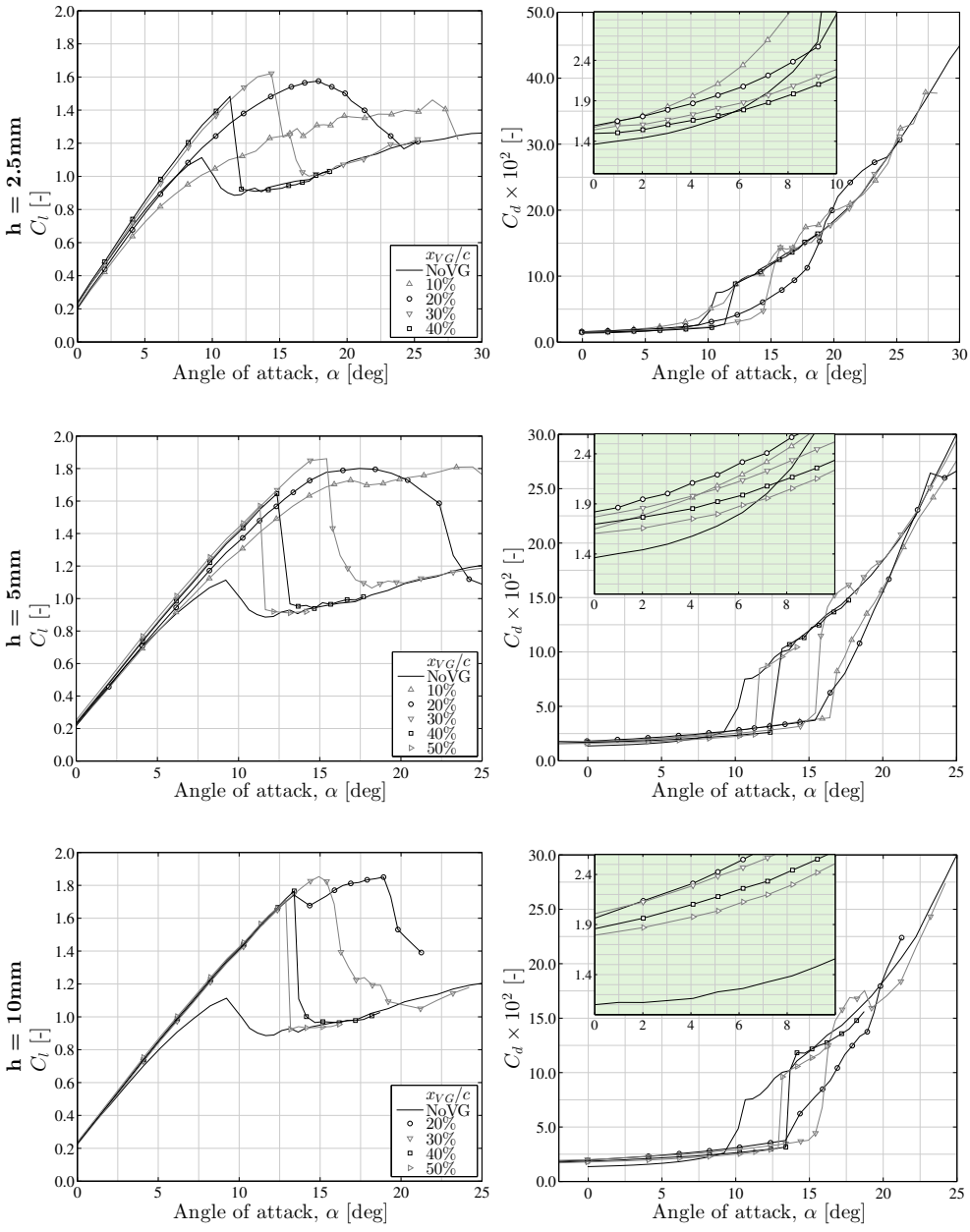

Figure C.12: Same as Figure C.11 for the rough condition.

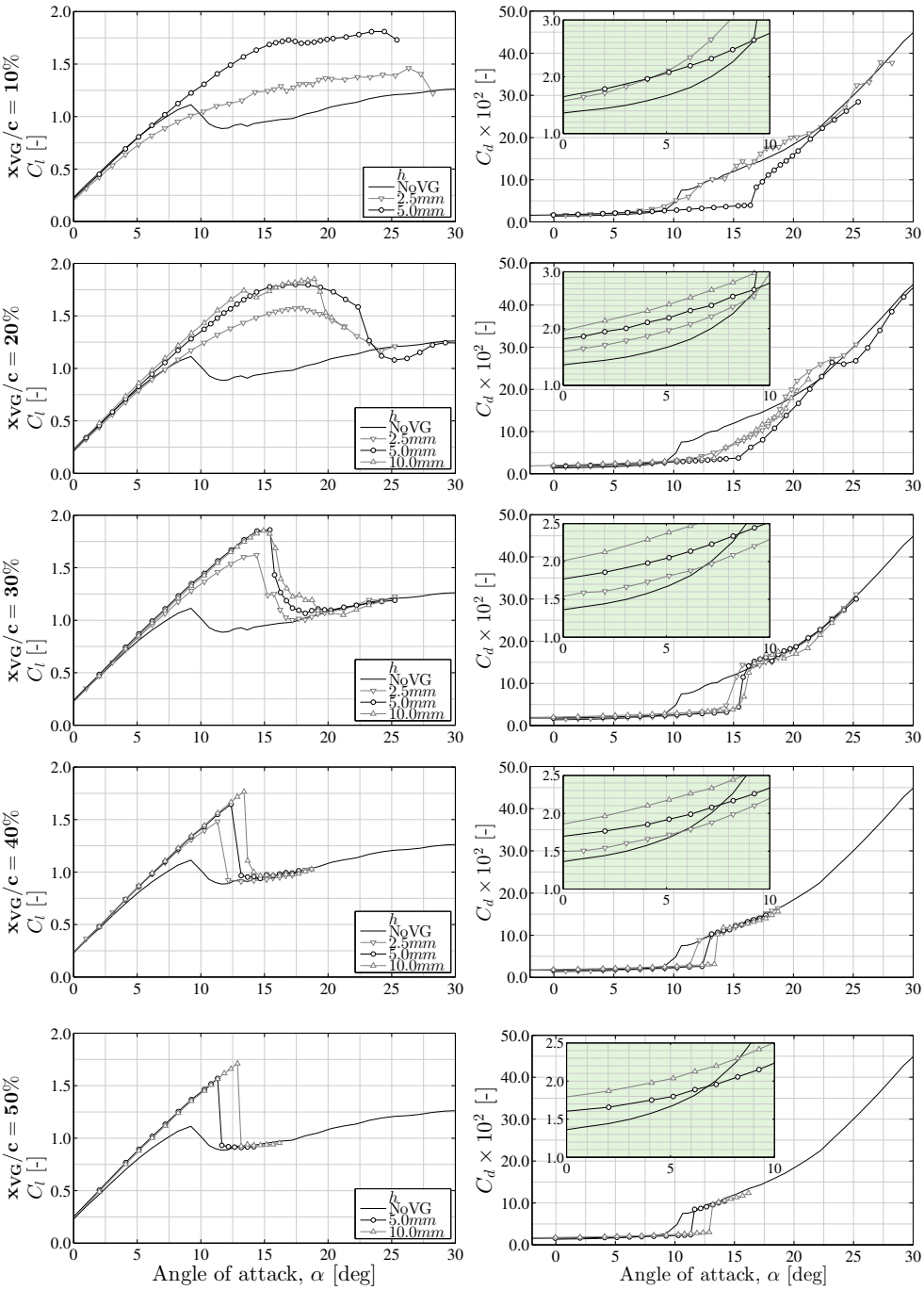

Figure C.13: Same as Figure 5.16 for the rough condition.

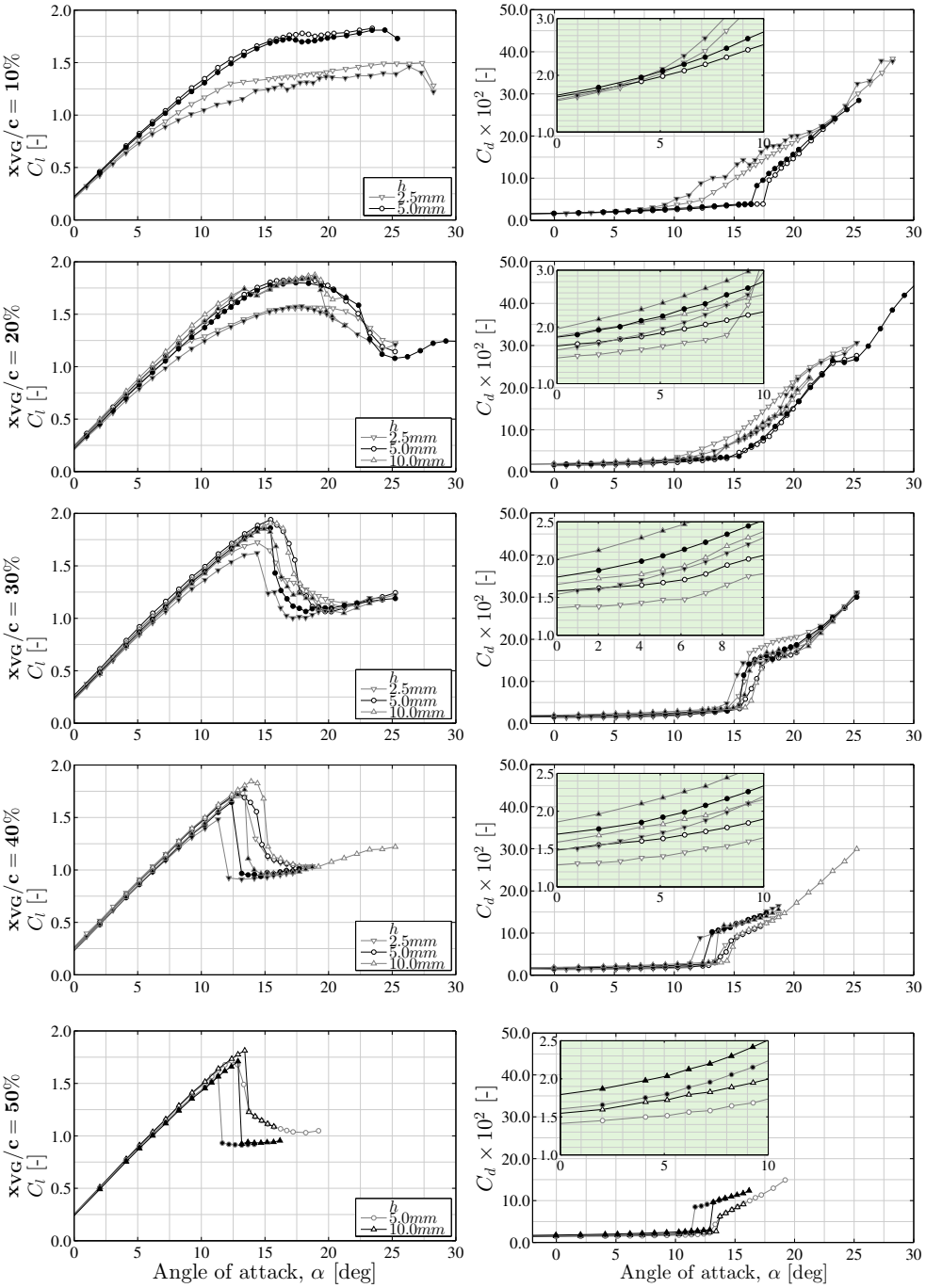

Figure C.14: Same as Figure 5.16, comparing the clean and rough condition. Filled white and black symbols indicate clean and rough conditions respectively.

D

Engineering model calibration database

Details of the datasets used for calibrating the engineering model (as presented in Chapter 6) as shown in this appendix.

No.	Airfoil model		VG configuration								Flow properties	
	Airfoil	Chord length [m]	Shape	Rotation	height [mm]	length [mm]	Internal distance [mm]	External distance [mm]	Inflow angle [deg]	Position [x/c]	Reynolds number [-]	Transiton
LTT01	DU97-W-300	0.65	Delta	CtR.	5	15	17.5	35	15	0.1	2.0×10^6	Free
LTT02	DU97-W-300	0.65	Delta	CtR.	5	15	17.5	35	15	0.2	2.0×10^6	Free
LTT03	DU97-W-300	0.65	Delta	CtR.	5	15	17.5	35	15	0.3	2.0×10^6	Free
LTT04	DU97-W-300	0.65	Delta	CtR.	5	15	17.5	35	15	0.4	2.0×10^6	Free
LTT05	DU97-W-300	0.65	Delta	CtR.	5	15	17.5	35	15	0.5	2.0×10^6	Free
LTT06	DU97-W-300	0.65	Delta	CtR.	10	30	35	70	15	0.2	2.0×10^6	Free
LTT07	DU97-W-300	0.65	Delta	CtR.	10	30	35	70	15	0.3	2.0×10^6	Free
LTT08	DU97-W-300	0.65	Delta	CtR.	10	30	35	70	15	0.4	2.0×10^6	Free
LTT09	DU97-W-300	0.65	Delta	CtR.	10	30	35	70	15	0.5	2.0×10^6	Free
LTT10	DU97-W-300	0.65	Delta	CtR.	5	15	17.5	35	15	0.2	1.0×10^6	Free
LTT11	DU97-W-300	0.65	Delta	CtR.	5	15	17.5	35	15	0.4	1.0×10^6	Free
LTT12	DU97-W-300	0.65	Delta	CtR.	10	30	35	70	15	0.2	1.0×10^6	Free
LTT13	DU97-W-300	0.65	Delta	CtR.	10	30	35	70	15	0.4	1.0×10^6	Free
LTT14	DU97-W-300	0.65	Delta	CtR.	5	15	17.5	35	15	0.2	3.0×10^6	Free
LTT15	DU97-W-300	0.65	Delta	CtR.	5	15	17.5	50	15	0.2	2.0×10^6	Free
LTT16	DU97-W-300	0.65	Delta	CtR.	5	15	17.5	35	12	0.2	2.0×10^6	Free
LTT17	DU97-W-300	0.65	Delta	CtR.	5	15	17.5	35	18	0.2	2.0×10^6	Free
LTT18	DU97-W-300	0.65	Delta	CtR.	5	15	17.5	35	15	0.1	2.0×10^6	Forced
LTT19	DU97-W-300	0.65	Delta	CtR.	5	15	17.5	35	15	0.2	2.0×10^6	Forced
LTT20	DU97-W-300	0.65	Delta	CtR.	5	15	17.5	35	15	0.3	2.0×10^6	Forced
LTT21	DU97-W-300	0.65	Delta	CtR.	5	15	17.5	35	15	0.4	2.0×10^6	Forced
LTT22	DU97-W-300	0.65	Delta	CtR.	5	15	17.5	35	15	0.5	2.0×10^6	Forced
LTT23	DU97-W-300	0.65	Delta	CtR.	10	30	35	70	15	0.2	2.0×10^6	Forced
LTT24	DU97-W-300	0.65	Delta	CtR.	10	30	35	70	15	0.3	2.0×10^6	Forced
LTT25	DU97-W-300	0.65	Delta	CtR.	10	30	35	70	15	0.4	2.0×10^6	Forced
LTT26	DU97-W-300	0.65	Delta	CtR.	10	30	35	70	15	0.5	2.0×10^6	Forced

No.	Airfoil model		VG configuration								Flow properties	
	Airfoil	Chord length [m]	Shape	Rotation	height [mm]	length [mm]	Internal distance [mm]	External distance [mm]	Inflow angle [deg]	Position [x/c]	Reynolds number [-]	Transiton
AVA01	DU331	6.06	Delta	CtR.	10	30	20	50	20	0.25	1.6×10^7	Forced
AVA02	DU331	6.06	Delta	CtR.	12	36	24	60	20	0.25	1.6×10^7	Forced
AVA03	DU331	6.06	Delta	CtR.	15	45	30	75	20	0.25	1.6×10^7	Forced
AVA04	DU331	6.06	Delta	CtR.	18	54	36	90	20	0.25	1.6×10^7	Forced
AVA05	DU331	6.06	Delta	CtR.	30	90	60	150	20	0.25	1.6×10^7	Forced
AVA06	DU331	6.06	Delta	CtR.	36	108	72	180	20	0.25	1.6×10^7	Forced
AVA07	DU331	6.06	Delta	CtR.	60	180	120	300	20	0.25	1.6×10^7	Forced
AVA08	DU331	6.06	Delta	CtR.	15	45	30	75	20	0.3	1.6×10^7	Forced
AVA09	DU331	6.06	Delta	CtR.	18	54	36	90	20	0.3	1.6×10^7	Forced
AVA10	DU331	6.06	Delta	CtR.	30	90	60	150	20	0.3	1.6×10^7	Forced
AVA11	DU331	6.06	Delta	CtR.	36	108	72	180	20	0.3	1.6×10^7	Forced
AVA12	DU331	6.06	Delta	CtR.	60	180	120	300	20	0.3	1.6×10^7	Forced
AVA13	DU331	6.06	Delta	CtR.	15	45	30	75	20	0.4	1.6×10^7	Forced
AVA14	DU331	6.06	Delta	CtR.	18	54	36	90	20	0.4	1.6×10^7	Forced
AVA15	DU331	6.06	Delta	CtR.	30	90	60	150	20	0.4	1.6×10^7	Forced
AVA16	DU331	6.06	Delta	CtR.	36	108	72	180	20	0.4	1.6×10^7	Forced
AVA17	DU331	6.06	Delta	CtR.	60	180	120	300	20	0.4	1.6×10^7	Forced
AVA18	DU331	6.06	Delta	CtR.	90	270	180	450	20	0.4	1.6×10^7	Forced
AVA19	FFAW3333	5.84	Delta	CtR.	10	30	20	50	20	0.25	1.4×10^7	Forced
AVA20	FFAW3333	5.84	Delta	CtR.	12	36	24	60	20	0.25	1.4×10^7	Forced
AVA21	FFAW3333	5.84	Delta	CtR.	15	45	30	75	20	0.25	1.4×10^7	Forced
AVA22	FFAW3333	5.84	Delta	CtR.	18	54	36	90	20	0.25	1.4×10^7	Forced
AVA23	FFAW3333	5.84	Delta	CtR.	30	90	60	150	20	0.25	1.4×10^7	Forced
AVA24	FFAW3333	5.84	Delta	CtR.	36	108	72	180	20	0.25	1.4×10^7	Forced
AVA25	FFAW3333	5.84	Delta	CtR.	60	180	120	300	20	0.25	1.4×10^7	Forced
AVA26	FFAW3333	5.84	Delta	CtR.	15	45	30	75	20	0.3	1.4×10^7	Forced
AVA27	FFAW3333	5.84	Delta	CtR.	18	54	36	90	20	0.3	1.4×10^7	Forced
AVA28	FFAW3333	5.84	Delta	CtR.	30	90	60	150	20	0.3	1.4×10^7	Forced
AVA29	FFAW3333	5.84	Delta	CtR.	36	108	72	180	20	0.3	1.4×10^7	Forced
AVA30	FFAW3333	5.84	Delta	CtR.	60	180	120	300	20	0.3	1.4×10^7	Forced
AVA31	FFAW3333	5.84	Delta	CtR.	15	45	30	75	20	0.4	1.4×10^7	Forced
AVA32	FFAW3333	5.84	Delta	CtR.	18	54	36	90	20	0.4	1.4×10^7	Forced
AVA33	FFAW3333	5.84	Delta	CtR.	30	90	60	150	20	0.4	1.4×10^7	Forced
AVA34	FFAW3333	5.84	Delta	CtR.	36	108	72	180	20	0.4	1.4×10^7	Forced
AVA35	FFAW3333	5.84	Delta	CtR.	60	180	120	300	20	0.4	1.4×10^7	Forced
AVA36	FFAW3333	5.84	Delta	CtR.	90	270	180	450	20	0.4	1.4×10^7	Forced
AVA37	FFAW3333	5.84	Delta	CtR.	10	30	20	50	15	0.4	1.4×10^7	Forced
AVA38	FFAW3333	5.84	Delta	CtR.	10	20	20	50	20	0.4	1.4×10^7	Forced
AVA39	FFAW3333	5.84	Delta	CtR.	10	30	15	50	20	0.4	1.4×10^7	Forced
AVA40	FFAW3333	5.84	Delta	CtR.	10	30	20	45	20	0.4	1.4×10^7	Forced
AVA41	FFAW3333	5.84	Delta	CtR.	10	30	20	55	20	0.4	1.4×10^7	Forced
AVA42	FFAW3333	5.84	Delta	CtR.	10	30	25	50	20	0.4	1.4×10^7	Forced
AVA43	FFAW3333	5.84	Delta	CtR.	10	30	20	50	25	0.4	1.4×10^7	Forced
AVA44	DU331	6.06	Delta	CtR.	10	30	20	50	15	0.4	1.6×10^7	Forced
AVA45	DU331	6.06	Delta	CtR.	10	20	20	50	20	0.4	1.6×10^7	Forced
AVA46	DU331	6.06	Delta	CtR.	10	30	15	50	20	0.4	1.6×10^7	Forced
AVA47	DU331	6.06	Delta	CtR.	10	30	20	45	20	0.4	1.6×10^7	Forced
AVA48	DU331	6.06	Delta	CtR.	10	30	20	55	20	0.4	1.6×10^7	Forced
AVA49	DU331	6.06	Delta	CtR.	10	30	25	50	20	0.4	1.6×10^7	Forced
AVA50	DU331	6.06	Delta	CtR.	10	30	20	50	25	0.4	1.6×10^7	Forced
TUD01	DU91W2250	0.6	Delta	CtR.	5	17	10	35	16.4	0.2	2.0×10^6	Free
TUD02	DU91W2250	0.6	Delta	CtR.	5	17	10	35	16.4	0.3	2.0×10^6	Free
TUD03	DU93W210	0.6	Delta	CtR.	5	17	10	35	16.4	0.2	1.0×10^6	Free
TUD04	DU93W210	0.6	Delta	CtR.	5	17	10	35	16.4	0.4	1.0×10^6	Free
TUD05	DU93W210	0.6	Delta	CtR.	5	17	10	35	16.4	0.6	1.0×10^6	Free
TUD06	DU97-W-300	0.6	Delta	CtR.	5	17	10	35	16.4	0.2	2.0×10^6	Free
TUD07	DU97-W-300	0.6	Delta	CtR.	5	17	10	35	16.4	0.4	2.0×10^6	Free
NTU01	NTUA18	0.6	Delta	CtR.	6	18	22.2	70.2	20	0.2	8.7×10^5	Forced
NTU02	NTUA18	0.6	Delta	CtR.	6	18	22.2	70.2	20	0.3	8.7×10^5	Forced

References

Acum, W. E. A., Garner, H. C., Maskell, E. C., and Rogers, E. W. E. Subsonic wind tunnel wall corrections. Technical Report AGARD-AG-109, Advisory Group for Aerospace Research and Development (North Atlantic Treaty Organisation), 1966.

Allen, H. J. and Vincenti, W. G. Wall interference in a two-dimensional flow wind tunnel with consideration of the effect of compressibility. Technical Report 782, NACA, Ames Aeronautical Lab, 1944.

Anderson, J. D. *Fundamentals of Aerodynamics*, chapter 1, pages 19–26. McGraw-HIll, 5th edition, 2005.

Angele, K. and Grewe, F. Instantaneous Behavior of Streamwise Vortices for Turbulent Boundary Layer Separation Control. *Journal of Fluids Engineering*, 129: 226–235, 2007.

Angele, K. and Muhammad-Klingmann, B. The effect of streamwise vortices on the turbulence structure of a separating boundary layer. *European Journal of Mechanics - B/Fluids*, 24(5):539–554, 2005.

Antoniou, I., Petersen, S. M., Øye, S., and Westergaard, C. The ELKRAFT 1MW Wind Turbine: Results from the Test Program. In *European Union Wind Energy Conference*, pages 251–255, 1996.

Aparicio, M., Martín, R., Muñoz, A., and González, A. AVATAR Deliverable 3.3: Results of a parametric study of flow devices, guidelines for design, April. Technical report, 2016.

Aref, H. Point vortex dynamics: A classical mathematics playground. *Journal of Mathematical Physics*, 48(6), 2007.

Ashill, P. R., Fulker, J. L., and Hackett, K. C. Research at DERA on Sub Boundary Layer Vortex Generators (SBVGs). *39th Aerospace Sciences Meeting and Exhibit*, (January):12, 2001.

Ashill, P. R., Fulker, J. L., and Hackett, K. C. A review of recent developments in flow control. *The Aeronautical Journal*, 109(1095):205–232, 2005.

AVATAR. AVATAR Project Site. http://www.eera-avatar.eu/. (accessed: 10-02-2016).

Babinsky, H., Li, Y., and Pitt Ford, C. W. Microramp Control of Supersonic Oblique Shock-Wave/Boundary-Layer Interactions. *AIAA Journal*, 47(3):668–675, 2009.

Bak, C., Skrzypiński, W., Gaunaa, M., Villanueva, H., Brønnum, N. F., and Kruse, E. K. Full scale wind turbine test of vortex generators mounted on the entire blade. *Journal of Physics: Conference Series*, 753:022001, 2016.

Baker, G. R., Barker, S. J., Bofah, K. K., and Saffman, P. G. Laser anemometer measurements of trailing vortices in water. *Journal of Fluid Mechanics*, 65(2): 325–336, 1974.

Baldacchino, D., Ferreira, C., Ragni, D., and van Bussel, G. J. W. Point vortex modelling of the wake dynamics behind asymmetric vortex generator arrays. *Journal of Physics: Conference Series*, 753(2), 2016a.

Baldacchino, D., Manolesos, M., Ferreira, C., González Salcedo, Á., Aparicio, M., Chaviaropoulos, T., Diakakis, K., Florentie, L., Ramos García, N., Papadakis, G., Sorensen, N. N., Timmer, N., Troldborg, N., Voutsinas, S. G., and van Zuijlen, A. Experimental benchmark and code validation for airfoils equipped with passive vortex generators. *Journal of Physics: Conference Series*, 753(2), 2016b.

Baldacchino, D., Ferreira, C., Tavernier, D. D., Timmer, W., and van Bussel, G. J. W. Experimental parameter study for passive vortex generators on a 30% thick airfoil. *Wind Energy*, 21(9):745–765, 2018.

Bannister, K. Landing kestrel. http://www.pixoto.com/images-photography/animals/birds/landing-kestrel--42814578, 2012. (accessed: 12-05-2019).

Basu, S. *Dynamics of vortices in complex wakes: modeling, analysis, and experiments*. PhD thesis, Virginia Polytechnic Institute and State University, 2014.

Basu, S. and Stremler, M. A. On the motion of two point vortex pairs with glide-reflective symmetry in a periodic strip. *Physics of Fluids*, 27(10), 2015.

Bender, E. E., Anderson, B. H., and Yagle, P. J. Vortex Generator Modelling for Navier-Stokes Codes. In *3rd Joint ASME/JSME Fluids Engineering Conference, San Francisco, CA.*, March 1999.

Beresh, S. J., Hen, J. F., and Spillers, R. W. Formation of a Fin Trailing Vortex in Undisturbed and Interacting Flows. *Engineering Sciences*, (June):1–13, 2009.

Beresh, S. J., Henfling, J. F., and Spillers, R. W. Meander of a fin trailing vortex and the origin of its turbulence. *Experiments in Fluids*, 49:599–611, 2010.

Beresh, S. J., Hen, J. F., and Spillers, R. W. Turbulence of a Fin Trailing Vortex in Subsonic Compressible Flow. *AIAA Journal*, 50(11), 2012.

Bradshaw, P. Turbulent Secondary Flows. *Annual Review of Fluid Mechanics*, 19(1): 53–74, jan 1987.

Bushnell, D. M. Body-turbulence interaction. In *17th Fluid Dynamics, Plasma Dynamics, and Lasers Conference, AIAA-84-1527, Snowmass, CO, U.S.A.*, 1984.

Cathalifaud, P., Godard, G., Braud, C., and Stanislas, M. The flow structure behind vortex generators embedded in a decelerating turbulent boundary layer. *Journal of Turbulence*, 10(February 2014):N42, jan 2009.

Choudhry, A., Arjomandi, M., and Kelso, R. Methods to control dynamic stall for wind turbine applications. *Renewable Energy*, 86:26–37, 2016.

Chow, J. S., Zilliac, G. G., and Bradshaw, P. Mean and Turbulence Measurements in the Near Field of a Wingtip Vortex. *AIAA Journal*, 35(10):1561–1567, 1997.

Churchfield, M. J. and Blaisdell, G. A. Reynolds Stress Relaxation Turbulence Modelling Applied to a Wingtip Vortex Flow. *AIAA Journal*, 51(11):2643–2655, 2013.

De Tavernier, D., Baldacchino, D., and Ferreira, C. An integral boundary layer engineering model for vortex generators implemented in xfoil. *Wind Energy*, 21 (10):906–921, 2018.

Dee, F. S. and Nicholas, O. P. Flight Measurement of Wing Tip Vortex Motion near the Ground. Technical report, CP 1065, British Aeronautical Research Council, London, England., 1968.

Devenport, W. J., Rife, M. C., Liapis, S. I., and Follin, G. J. The Structure and Development of a Wing-Tip Vortex. *Journal of Fluid Mechanics*, 312:67–106, 1996.

Drela, M. XFOIL: An analysis and design system for low Reynolds number airfoils. In Mueller, T. J., editor, *Low Reynolds number aerodynamics*, volume 54, pages 1–12. Notre Dame, Springer-Verlag, June 1989.

Drela, M. and Giles, M. B. Viscous-inviscid analysis of transonic & low reynolds number airfoils. *AIAA Journal*, 25:1347–1355, 1987.

Drela, M., Giles, M., and Thompkins, W. Newton solution of coupled euler and boundary layer equations. *Presented at the Third Symposium on Numerical and Physical Aspects of Aerodynamic Flows*, January 1985.

Drela, M. *Flight vehicle aerodynamics*. The MIT Press, 2014. Chapter 4.

Edstrand, A. M., Davis, T. B., Schmid, P. J., Taira, K., and Cattafesta, L. N. On the mechanism of trailing vortex wandering. *Journal of Fluid Mechanics*, 801, 2016.

Elsinga, G. E., Poelma, C., Schröder, A., Geisler, R., Scarano, F., and Westerweel, J. Tracking of vortices in a turbulent boundary layer. *Journal of Fluid Mechanics*, 697:273–295, 2012.

Escudier, M. Vortex breakdown: Observations and explanations. *Progress in Aerospace Sciences*, 25(2):189–229, jan 1988.

España, G., Aubrun, S., Loyer, S., and Devinant, P. Spatial study of the wake meandering using modelled wind turbines in a wind tunnel. *Wind Energy*, 2011.

Fernández-Gámiz, U., Zamorano, G., and Zulueta, E. Computational study of the vortex path variation with the vg height. *Journal of Physics: Conference Series*, 524 (1):012024, 2014.

Ferreira, C., Salcedo, A. G., Baldacchino, D., and Aparicio, M. Development of aerodynamic codes for modelling of flow devices on aerofoils and rotors. AVATAR Task 3.2 February, 2015.

Fish, F. E. and Lauder, G. V. Passive and Active Flow Control By Swimming Fishes and Mammals. *Annual Review of Fluid Mechanics*, 38(1):193–224, 2006.

Florentie, L., Van Zuijlen, A. H., and Bijl, H. Towards a multi-fidelity approach for cfd simulations of vortex generator arrays. In *11th World Congress on Computational Mechanics, WCCM 2014, 5th European Conference on Computational Mechanics, ECCM 2014 and 6th European Conference on Computational Fluid Dynamics, ECFD 2014*, pages 7187–7198, 2014.

Florentie, L., J., H. S., and van Zuijlen, A. H. Adjoint-based optimization of a source-term representation of vortex generators. *Computers & Fluids*, 162:139 – 151, 2018.

Fouatih, O. M., Medale, M., Imine, O., and Imine, B. Design optimization of the aerodynamic passive flow control on NACA 4415 airfoil using vortex generators. *European Journal of Mechanics - B/Fluids*, 56:82–96, 2016.

Fraunhofer-IWES. Wind monitor. http://www.windmonitor.de/windmonitor_en/index.html, 2017. (accessed: 01-12-2017).

Gad-el Hak, M. and Bushnell, D. M. Separation Control: Review. *Journal of Fluids Engineering*, 113(1):5, 1991.

Gao, L., Zhang, H., Liu, Y., and Han, S. Effects of vortex generators on a blunt trailing-edge airfoil for wind turbines. *Renewable Energy*, 76:303–311, 2015.

Gardarin, B., Jacquin, L., and Geffroy, P. Flow Separation Control With Vortex Generators. *4th Flow Control Conference*, (June):1–17, 2008.

Garrel, A. V. Integral boundary layer methods for wind turbine aerodynamics. Technical Report ECN-C–04-004, December 2003.

Gentile, V., Schrijer, F. F. J., van Oudheusden, B. W., and Scarano, F. Low-frequency behavior of the turbulent axisymmetric near-wake. *Physics of Fluids*, 28(6):065102, 2016.

Godard, G. and Stanislas, M. Control of a decelerating boundary layer. Part 1: Optimization of passive vortex generators. *Aerospace Science and Technology*, 10 (3):181–191, 2006.

Gould, D. G. The use of vortex generators to delay boundary layer separation: theoretical discussion supported by tests on a CF-100 aircraft. Technical Report LR-183, National Aeronautical Establishment (Canada), December, 1956.

Griffin, D. A. Investigation of Vortex Generators for Augmentation of Wind Turbine Power Performance. Technical Report NREL/SR-440-21399, NREL, December, 1996.

Gyatt, G. W. and Lissaman, P. B. S. Development and testing of tip devices for horizontal axis wind turbines. Technical Report NASA-CR-174991, May, 1985.

Haans, W., van Kuik, G., and van Bussel, G. J. W. The Inverse Vortex Wake Model: A Measurement Analysis Tool. *Journal of Solar Energy Engineering*, 130(January): 031009, 2008.

Hansen, M. O. L., Velte, C. M., Øye, S., Hansen, R., Sørensen, N. N., Madsen, J., and Mikkelsen, R. Aerodynamically shaped vortex generators. *Wind Energy*, 19(3): 563–567, 2016.

Harris, D. M. and Williamson, C. H. K. Instability of secondary vortices generated by a vortex pair in ground effect. *Journal of Fluid Mechanics*, 700:148–186, 2012.

Harris, D. M., Miller, V. A., and Williamson, C. H. K. A short wave instability caused by the approach of a vortex pair to a ground plane. *Physics of Fluids*, 22(2010): 2–3, 2010.

Harvey, J. K. and Perry, F. J. Flowfield produced by trailing vortices in the vicinity of the ground. *AIAA Journal*, 9(August):1659–1660, 1971.

Herráez, I., Akay, B., van Bussel, G. J. W., Peinke, J., and Stoevesandt, B. Detailed analysis of the blade root flow of a horizontal axis wind turbine. *Wind Energy Science*, 2016:1–33, 2016.

Heyes, A. L., Jones, R. F., and Smith, D. A. R. Wandering of wing-tip vortices. *12th International Symposium on Application of laser techniques to fluid mechanics, Lisbon, Portugal, July 2004*, 2004.

Hoerner, F. and Borst, H. V. *Fluid-Dynamic Lift: Practical Information on Aerodynamic and Hydrodynamic Lift*, chapter XVIII: Characteristics of Delta Wings. LA Hoerner, Brick Town, NJ, 1985.

Holden, H. and Babinsky, H. Effect of Microvortex Generators On Seperated Normal Shock/ Boundary Layer Interactions. *Journal of Aircraft*, 44(1):170–174, 2007.

International Energy Agency. World Energy Outlook 2016. Technical report, 2017.

International Renewable Energy Agency. Innovation Outlook Offshore Wind. Technical report, 2016.

Jacquin, L., Fabre, D., Sipp, D., Theofilis, V., and Vollmers, H. Instability and unsteadiness of aircraft wake vortices. *Aerospace Science and Technology*, 7(8):577 – 593, 2003.

Jasak, H. *Error Analysis and Estimation for the Finite Volume Method with Applications to Fluid Flows*. PhD thesis, Imperial College, University of London, 1996.

Jaworski, J. Silent flights: How owls could help make wind turbines and planes quieter. http://phys.org/news/2015-06-silent-flights\-owls-turbines-planes.html, 2015. (accessed: 12-05-2019).

Jensen, L. E., Knudsen, H. T., and Madsen, J. Mounting of vortex generator devices via mounting plate., October 2012. US Patent App. 13/364,467.

Jensen, P. H., Chaviaropoulos, T., and Natarajan, A. LCOE reduction for the next generation offshore wind turbines - Outcomes from the INNWIND.EU Project. Technical report, 2017.

Jeong, J. and Hussain, F. On the identification of a vortex. *Journal of Fluid Mechanics*, 285, 1995.

Jirasek, A. Vortex-generator model and its application to flow control. *Journal of Aircraft*, 42:1486–1491, 2005.

Jones, J. P. The Calculation of the Paths of Vortices from a System of Vortex Generators, and a Comparison with Experiment. Technical report, A.R.C., 1955.

Katz, J. and Plotkin, A. *Low-Speed Aerodynamics*, chapter 6, pages 138–141. Cambridge Aerospace Series (No. 13). Cambridge University Press, Second edition, 2001.

Kendall, A. and Koochesfahani, M. A method for estimating wall friction in turbulent wall-bounded flows. *Experiments in Fluids*, 44(5):773–780, 2008.

Kerho, M. and Kramer, B. Enhanced Airfoil Design Incorporating Boundary Layer Mixing Devices. 2003.

Kindler, K., Mulleners, K., van der Wall, B. G., Richard, H., and Raffel, M. Aperiodicity in the Near Field of Full-Scale Rotor Blade Tip Vortices. *Experiments in Fluids*, 50(6):1601–1610, 2011.

Lee, S. I., Kim, J., Park, H., Jabłoński, P. G., and Choi, H. The Function of the Alula in Avian Flight. *Scientific Reports*, 5(d):9914, 2015.

Lengani, D., Simoni, D., Ubaldi, M., Zunino, P., and Bertini, F. Turbulent boundary layer separation control and loss evaluation of low profile vortex generators. *Experimental Thermal and Fluid Science*, 35(8):1505–1513, 2011.

Leonard, B. P. A stable and accurate convective modelling procedure based on quadratic upstream interpolation. *Computer methods in applied mechanics and engineering*, 19:59–98, 1979.

Lin, J. C. Review of research on low-profile vortex generators to control boundary-layer separation. 38(4-5):389–420, 2002.

Liu, J., Piomelli, U., and Spalart, P. R. Interaction between a spatially growing turbulent boundary layer and embedded streamwise vortices. *Journal of Fluid Mechanics*, 326(-1):151, 1996.

Locke, C. Humpback whales solve a big problem for wind turbines. https://www.wired.com/2015/11/whales-wind-turbines, 2015. (accessed: 12-05-2019).

Lögdberg, O., Fransson, J. H. M., and Alfredsson, P. H. Streamwise evolution of longitudinal vortices in a turbulent boundary layer. *Journal of Fluid Mechanics*, 623:27, 2009.

Lögdberg, O., Angele, K., and Alfredsson, P. H. On the robustness of separation control by streamwise vortices. *European Journal of Mechanics - B/Fluids*, 29(1): 9–17, 2010.

Mack, L. M. Transition and laminar instability. Technical report, Jet Propulsion Laboratory, 1977.

Mai, H., Dietz, G., Geißler, W., Richter, K., Bosbach, J., Richard, H., and de Groot, K. Dynamic Stall Control by Leading Edge Vortex Generators. *Journal of the American Helicopter Society*, 53(1):26, 2008.

Manolesos, M. and Prospathopoulos, J. CFD & experimental database of flow devices. AVATAR Task 3.1, February, 2015.

Manolesos, M. and Voutsinas, S. G. Experimental investigation of the flow past passive vortex generators on an airfoil experiencing three-dimensional separation. *Journal of Wind Engineering and Industrial Aerodynamics*, 142:130–148, 2015.

Manolesos, M., Papadakis, G., and Voutsinas, S. G. Assessment of the cfd capabilities to predict aerodynamic flows in presence of vg arrays. *Journal of Physics: Conference Series*, 524(1):012029, 2014.

Manolesos, M., Papadakis, G., and Voutsinas, S. G. On the Application of the Bay Model for Vortex Generator Flows. In *Proceedings of ASME Turbo Expo, GT2018*, June 11-15, Oslo, Norway 2018.

Mehta, R. D. and Bradshaw, P. Longitudinal vortices imbedded in turbulent boundary layers Part 2. Vortex pair with 'common flow' upwards. *Journal of Fluid Mechanics*, 188:529–546, 1988.

Menter, F. R. Zonal two equation k-ω turbulence models for aerodynamic flows. In *AIAA 23rd Fluid Dynamics, Plasmadynamics, and Lasers Conference, 93-2906*, 1993.

Micallef, D., Ferreira, C., Sant, T., and van Bussel, G. J. W. An investigation of radial velocities for a horizontal axis wind turbine in axial and yawed flows. *Wind Energy*, 17(April 2013):657–669, 2014.

Michelsen, J. Basis3D-platform for development of multiblock PDE solvers. Tech. Rep. AFM 92-05, TU Denmark, 1992.

Michelsen, J. A. Block structured multigrid solution of 2D & 3D elliptic PDE's. Tech. Rep. AFM 94-06, TU Denmark, 1994.

Michelsen, J. A. Forskning i aeroelasticitet EFP-2001, chapter Beregning af laminar-turbulent omslag i 2D og 3D, page 73. Technical Report Risø-R1349(DA), 2002.

Miller, G. D. and Williamson, C. H. K. Free Flight of a Delta Wing. *Physics of Fluids*, 7(9):S9–S9, 1995.

Mueller-Vahl, H., Pechlivanoglou, G., Nayeri, C. N., and Paschereit, C. O. Vortex generators for wind turbine blades: a combined wind tunnel and wind turbine parametric study. In *Proceedings of ASME Turbo Expo, GT2012*, June 11-15, Copenhagen, Denmark 2012.

Nikolaou, I. G., Politis, E. S., and Chaviaropoulos, P. K. Modelling the Flow Around Airfoils Equipped with Vortex Generators Using a Modified 2D Navier-Stokes Solver. *Journal of Solar Energy Engineering*, 127(2):223, 2005.

Oerlemans, S. Wind turbine noise: primary noise sources. Technical Report NLR-TP-2011-066, NLR, 2011.

Okulov, V. L. On the stability of multiple helical vortices. *Journal of Fluid Mechanics*, 521:319–342, dec 2004.

Okulov, V. L. and Sorensen, J. N. Instability of a vortex wake behind wind turbines. *Doklady Physics*, 49(12):772–777, dec 2004.

Papadakis, G. and Voutsinas, S. G. In view of accelerating CFD simulations through coupling with vortex particle approximations. *Journal of Physics: Conference Series*, (Torque2014), 2014.

Pauley, W. R. and Eaton, J. K. Experimental Study of the Development of Longitudinal Vortex Pairs Embedded in a Turbulent Boundary Layer. *AIAA*, 26(7):816–823, 1988.

Pearcey, H. H. Shock induced separation and its prevention by design and boundary layer control. In Lachmann, G. V., editor, *Boundary layer and flow control*. 1961.

Pereira, R., de Oliveira, G., Timmer, W. A., and Quaeghebeur, E. Probabilistic design of airfoils for horizontal axis wind turbines. *Journal of Physics: Conference Series*, 1037:022042, June 2018.

Peterson, S. D. and Plesniak, M. W. Surface shear stress measurements around multiple jets in crossflow using the fringe imaging skin friction technique. *Experiments in Fluids*, 37(4):497–503, 2004.

Power Curve. http://www.powercurve.dk/, 2017. (accessed: 11-12-2017).

Pozrikidis, C. *Fluid Dynamics: Theory, Computation & numerical simulations*, pages 639–641. Springer, 2009.

Quackenbush, T. R., Danilov, P. V., and Whitehouse, G. R. Flow Driven Oscillating Vortex Generators for Control of Boundary Layer Separation. *40th Fluid Dynamics Conference and Exhibit*, (July):1–15, 2010.

Ramos-García, N., Sørensen, J. N., and Shen, W. Z. A strong viscous-inviscid interaction model for rotating airfoils. *Wind Energy*, 17:1957–1984, 2014.

Saffman, P. *Vortex Dynamics*, pages 130–133. Cambridge, 1992.

Sanders, M. P. J. *The Boundary layer over a flat plate*. Bachelor thesis, University of Twente, July 2014.

Sarpkaya, T. and Henderson Jr., D. O. Free Surface Scars and Striations Due to Trailing Vortices Generated by a Submerged Lifting Surface. *23th AIAA Aerospace Sciences Meeting Reno , NV*, (January), 1985.

Sarradj, E., Fritzsche, C., and Geyer, T. Silent Owl Flight: Bird Flyover Noise Measurements. *AIAA Journal*, 49(4):769–779, 2011.

Scarano, F., Benocci, C., and Riethmuller, M. L. Pattern recognition analysis of the turbulent flow past a backward facing step. *Physics of Fluids*, 11(12):3808, 1999.

Schreck, S. J. Rotationally Augmented Flow Structures and Time Varying Loads on Turbine Blades Preprint. *45th AIAA Aerospace Sciences Meeting and Exhibition, Wind Energy Symposium*, (January):1–13, 2007.

Schubauer, G. B. and Spangenberg, W. G. Forced mixing in boundary layers. *Journal of Fluid Mechanics*, 8:10–32, 1960.

Schülein, E. Optical method for skin-Friction measurements on fast-Rotating blades. *Experiments in Fluids*, 55(2):1–10, 2014.

Shabaka, I. M. M. A., Mehta, R. D., and Bradshaw, P. Longitudinal vortices imbedded in turbulent boundary layers. Part 1. Single Vortex. *Journal of Fluid Mechanics*, 155:37–57, 1985.

Shah, P. N., Atsavapranee, P., Hsu, T. Y., Wei, T., and McHUGH, J. Turbulent transport in the core of a trailing half-delta-wing vortex. *Journal of Fluid Mechanics*, 387:151–175, 1999.

Shahinfar, S., Sattarzadeh, S. S., Fransson, J. H. M., and Talamelli, A. Revival of Classical Vortex Generators Now for Transition Delay. *Physical Review Letters*, 109(7), 2012.

Siemens Wind Power. SCOE – Society's costs of electricity: How society should find its optimal energy mix. Technical report, 2014.

Sieros, G. Redesign of the AVATAR Reference Wind Turbine rotor. Technical report, 2017.

Skrzypiński, W., Gaunaa, M., and Bak, C. The Effect of Mounting Vortex Generators on the DTU 10MW Reference Wind Turbine Blade. *Journal of Physics: Conference Series*, 524:012034, 2014.

Smart-Blade. Performance improvement for wind turbines. http://smart-blade.com/products-services/vortex-generators.html, 2017. (accessed: 11-12-2017).

Smirnoff, D. The scales of shark skin may influence attachment of fouling microorganisms via shape and surface topography. https://asknature.org/strategy/skin-prevents-biofouling/#.WBNQO7Wfnyw, 2018. (accessed: 12-05-2019).

Smith, F. T. Theoretical prediction and design for vortex generators in turbulent boundary layers. *Journal of Fluid Mechanics*, 270:91–131, 1994.

Sørensen, N. N. *General purpose flow solver applied to flow over hills,*. PhD thesis, Risø-R-827-(EN), Denmark., 1995.

Sørensen, N. N., Zahle, F., Bak, C., and Vronsky, T. Prediction of the Effect of Vortex Generators on Airfoil Performance. *Journal of Physics: Conference Series*, 524(1): 012019, 2014.

Spalart, P. R. and Shur, M. On the sensitization of turbulece models to rotation and curvature. *Aerospace Science and Technology*, 5:297–302, 1997.

Spalart, P. R. and Venkatakrishnan, V. On the role and challenges of cfd in the aerospace industry. *The Aeronautical Journal*, 120:209–232, 1 2016.

Spalart, P. R., Shur, M. L., Strelets, M. K., and Travin, A. K. Direct Simulation and RANS Modelling of a Vortex Generator Flow. *Flow, Turbulence and Combustion*, 2015.

Stillfried, F. V., Wallin, S., and Johansson, A. V. Evaluation of a Vortex Generator Model in Adverse Pressure Gradient Boundary Layers. *AIAA Journal*, 49(5): 982–993, 2011.

Stremler, M. A., Salmanzadeh, A., Basu, S., and Williamson, C. H. K. A mathematical model of 2P and 2C vortex wakes. *Journal of Fluids and Structures*, 27(5-6):774–783, 2011.

Sullivan, T. and Regan, F. The characterization, replication and testing of dermal denticles of Scyliorhinus canicula for physical mechanisms of biofouling prevention. *Bioinspir . Biomim . Bioinsp . Biomim*, 6(6):46001–46001, 2011.

Sullivan, T. L. Effect of Vortex Generators on the Power Conversion Performance and Structural Dynamic Loads of the Mod-2 Wind Turbine. Technical report, 1984.

Swafford, T. W. Analytical Approximation of Two-Dimensional Separated Turbulent Boundary-Layer Velocity Profiles. *AIAA Journal*, 21(6):923–926, 1983.

Tanner, L. H. and Blows, L. G. A study of the motion of oil films on surfaces in air flow, with application to the measurement of skin friction. *Journal of Physics E: Scientific Instruments*, 9(3):194–202, 2001.

Taylor, H. D. The elimination of diffuser separation by vortex generators. Technical Report No. R-4012-3, United Aircraft Corporation, June, 1947.

Timmer, W. A. and van Rooij, R. P. J. O. M. Wind Tunnel Results for a 25% Thick Wind Turbine Blade Airfoil. In *European Community Wind Energy Conference*, pages 416–419, March 1993.

Timmer, W. A. and van Rooij, R. P. J. O. M. Summary of the Delft University Wind Turbine Dedicated Airfoils. *Journal of Solar Energy Engineering*, 125:488–496, 2003.

Titchener, N., Colliss, S., and Babinsky, H. On the calculation of boundary-layer parameters from discrete data. *Exp. Fluids*, 56(56(8)):159, 2015.

Törnblom, O. and Johansson, A. V. A reynolds stress closure description of separation control with vortex generators in a plane asymmetric diffuser. *AIP Physics of Fluids*, 19(11), November 2007.

van Ingen, J. L. A suggested semi-empirical method for the calculation of the boundary layer transition region. Technical Report VTH-74, Delft University of Technology, Dept. of Aerospace Engineering, The Netherlands, 1956.

van Rooij, R. P. J. O. M. Modification of the boundary layer calculation in RFOIL for improved airfoil stall prediction. Technical Report IW-96087R, TU Delft, The Netherlands, 1996.

van Rooij, R. P. J. O. M. and Timmer, W. A. Roughness sensitivity considerations for thick rotor blade airfoils. *Journal of Solar Energy Engineering*, 125:468–478, 2003.

Velte, C. M. Vortex Generator Flow Model Based on Self-Similarity. *AIAA Journal*, 51(2):526–529, 2013.

Velte, C. M., Hansen, M. O. L., and Okulov, V. L. Helical structure of longitudinal vortices embedded in turbulent wall-bounded flow. *Journal of Fluid Mechanics*, 619:167, dec 2008.

Velte, C. M., Okulov, V. L., and Hansen, M. O. L. Alteration of helical vortex core without change in flow topology. *Physics of Fluids*, 23:1–4, 2011.

Velte, C. M., Hansen, M. O. L., and Okulov, V. L. Multiple vortex structures in the wake of a rectangular winglet in ground effect. *Experimental Thermal and Fluid Science*, 72:31–39, 2016.

Vey, S., Lang, H. M., Nayeri, C. N., Paschereit, C. O., and Pechlivanoglou, G. Extracting quantitative data from tuft flow visualizations on utility scale wind turbines. *Journal of Physics: Conference Series*, 524(1):12011, 2014.

von Stillfried, F., Wallin, S., and Johansson, A. V. Vortex-Generator Models for Zero- and Adverse-Pressure-Gradient Flows. *AIAA Journal*, 50:855–866, apr 2012.

Wendt, B. J. Parametric Study of Vortices Shed from Airfoil Vortex Generators. *AIAA Journal*, 42(11):2185–2195, 2004.

Wendt, B. J., Greber, I., and Hingst, W. R. Structure and development of streamwise vortex arrays embedded in a turbulent boundary layer. *AIAA Journal*, 31(2):2–9, 1993.

Wendt, B. and Reichert, B. The modelling of symmetric airfoil vortex generators. *American Institute of Aeronautics and Astronautics*, January 1996. 34th Aerospace Sciences Meeting and Exhibit.

Wentz, W. H., Jr. Effectiveness of Spoilers on the GA(W)-1 Airfoil With a High-Performance Fowler Flap. Technical Report NASA-CR-2538, May, 1975.

Westphal, R. V. and Mehta, R. D. Interaction of an oscillating vortex with a turbulent boundary layer. *Experiments in Fluids*, 7:405–411, 1989.

Westphal, R. V., Eaton, J. K., and Pauley, W. R. Interaction Between a Vortex and a Turbulent Boundary Layer in a Streamwise Pressure Gradient. In Durst, F and Launder, B E and Lumley, J L and Schmidt, F W and Whitelaw, J M, editor, *Turbulent Shear Flows 5*, pages 266–277. Springer, 1987.

White, F. M. *Viscous Fluid Flow*. McGraw Hill, third edition, 2006.

Xuzhao, H. and Gursul, I. A Simple Model of Asymmetric Wakes for Periodically Oscillating Airfoils. *54th AIAA Aerospace Sciences Meeting*, (January):1–26, 2016.

Yu, X., Zhang, Z., and Liu, B. The evolution of the flow topologies of 3D separations in the stator passage of an axial compressor stage. *Experimental Thermal and Fluid Science*, 44:301–311, 2013.

Zhang, L., Yang, K., Xu, J., and Zhang, M. Modeling of delta-wing type vortex generators. *Science China Technological Sciences*, 54(2):277–285, feb 2011.

List of Publications

Peer-reviewed Journals and Conference Series

- De Tavernier, D., Baldacchino, D. and Ferreira, C. An integral boundary layer engineering model for vortex generators implemented in Xfoil. *Wind Energy*, 21(10), 906-921, 2018.

- Baldacchino, D., Ferreira, C., De Tavernier, D., Timmer, W. A. and van Bussel, G.J.W. Experimental parameter study for passive vortex generators on a 30% thick airfoil. *Wind Energy*, 21(9), 745-765, 2018.

- Baldacchino, D., Manolesos, M., Ferreira, C., Salcedo, Á. G., Aparicio, M., Chaviaropoulos, T., Diakakis, K., Florentie, L., García, N. R., Papadakis, G., Sørensen, N. N., Timmer, W. A., Troldborg, N., Voutsinas, S. and van Zuijlen, A. Experimental benchmark and code validation for airfoils equipped with passive vortex generators. *Journal of Physics: Conference Series*, 753(2), 2016.

- Baldachino, D., Ferreira, C., Ragni, D. and van Bussel, G.J.W. Point vortex modelling of the wake dynamics behind asymmetric vortex generator arrays. *Journal of Physics: Conference Series*, 753(2), 2016.

Conferences and Posters

- Baldachino, D., Ragni, D., Ferreira, C. and van Bussel, G.J.W. Dynamics of asymmetric embedded streamwise vortices. *IUTAM, Dynamics and topology of vorticity and vortices*, Marseille, France, June 2017.

- Baldachino, D., Ragni, D., Ferreira, C. and van Bussel, G.J.W. Experimental investigation of asymmetric steamwise vortices in a turbulent boundary layer. *34th Wind Energy Symposium, AIAA SciTech*, (AIAA 2016-1259), San Diego (CA), USA, January 2016.

- Baldachino, D., Ragni, D., Ferreira, C. and van Bussel, G.J.W. Towards integral boundary layer modelling of vane-type vortex generators. *45th AIAA Fluid Dynamics Conference, AIAA Aviation*, (AIAA 2015-3345), Dallas (TX), USA, June 2015.

- Baldachino, D., Ferreira, C., Ragni, D., and van Bussel, G.J.W. An integral boundary layer method for modelling the effects of vortex generators. *11th EAWE PhD Seminar on Wind Energy*, Stuttgart, Germany, 23-25 September, 2015.

- Baldachino, D., Ferreira, C. and van Bussel, G.J.W. Vortex generator induced flow: an integral boundary layer perspective. *10th EAWE PhD Seminar on Wind Energy*, Orleans, France, 28-31 October, 2014.

Other publications and project reports

- Yu, W., Ferreira, C., van Kuik, G. and Baldacchino, D. Verifying the Blade Element Momentum Method in unsteady, radially varied, axisymmetric loading using a vortex ring model. *Wind Energy*, 20(2), 269-288, 2017.
- Salcedo, Á. G., Baldacchino, D., Caboni, M., Kidambi, A., Manolesos, M. and Troldborg, N. Aerodynamic flow control: final report. *AVATAR Deliverable*, Work Package 3, December 2016.
- Ferreira, C., Salcedo, Á.G., Baldacchino, D., Aparicio, M., Gómez, S., Munduate, X., García, N.R., Sørensen, J.N., Jost, E., Knecht, S., Lutz, T., Chassapogiannis, P., Diakakis, K., Papadakis, G., Voutsinas, S., Prospathopoulos, J., Gillebaart, T. and van Zuijlen, A. Results of the AVATAR project for the validation of 2D aerodynamic models with experimental data of the DU95W180 airfoil with unsteady flap. *Journal of Physics: Conference Series*, 753(2), 2016.
- Sørensen, N.N., Méndez, B., Muñoz, A., Sieros, G., Jost, E., Lutz, T., Papadakis, G., Voutsinas, S., Barakos, G.N., Colonia, S., Baldacchino, D., Baptista, C. and Ferreira, C. CFD code comparison for 2D airfoil flows. *Journal of Physics: Conference Series*, 753(8), 2016.
- Ferreira, C., Salcedo, Á.G., Baldacchino, D., Aparicio, M. (Eds.). Development of aerodynamic codes for modelling of flow devices on airfoils and rotors. *AVATAR Deliverable*, Work Package 3 - Task 3.2, November 2015.
- van Heemst, J. W., Baldacchino, D., Mehta, D. and van Bussel, G.J.W. Coupling of a free wake vortex ring near-wake model with the Jensen and Larsen far-wake deficit models. *Journal of Physics: Conference Series*, 625(1), 2015.
- Baldacchino, D. and van Bussel, G.J.W. Wind turbine wake stability investigations using a vortex ring modelling approach. *Journal of Physics: Conference Series*, 555(1), 2014.

Datasets and models

Boundary layer PIV data

- Baldacchino, D., 2017, "Evolution and dynamics of embedded streamwise vortices in decelerating turbulent boundary layers", TU Delft, DataverseNL. https://hdl.handle.net/10411/097JVP

Airfoil measurement data

- Baldacchino, D. (Daniel) (2017) Experimental parameter study for passive vortex generators on a 30% thick airfoil, TU Delft, Dataset. https://doi.org/10.4121/uuid:e2a3fa3c-dc19-4cad-9375-3124cf95f9c5

XFOILVG

- De Tavernier, D., Baldacchino, D., and Ferreira, C. An integral boundary layer engineering model for vortex generators implemented in xfoil. Wind Energy, 21 (10):906–921, 2018
  https://github.com/ddetavernier/XFOILVG

All auxiliary measurement and computational data used in the benchmark (Chapter 3) and model creation (Chapter 6), are publicly accessible at:
http://windbench.net/avatar.

Curriculum Vitæ

Born on the 23rd of July 1988 in Malta.

2004-2006	St. Aloysius' College Sixth Form Mathematics and Physics
2006-2010	Bachelor of Engineering *Thesis* The aerodynamics of wind turbines in shear flow University of Malta, Malta
2008-2009	ERASMUS Exchange Programme Strathclyde University, Glasgow, Scotland
2010-2012	Master in Sustainable Energy Technology *Thesis* Horizontal Axis Wind Turbine wake stability investigations Delft University of Technology, The Netherlands
2012-2013	Flow and thermal consultant Analysis and simulation for high-tech and energy applications Segula Technologies, Eindhoven, The Netherlands
2013-2018	PhD Researcher *Thesis* Vortex generators for flow separation control Delft University of Technology, The Netherlands
2014-2015	Mechanical Engineer Electrification of rural Africa with pico-hydro power Engineers Without Borders, The Netherlands
2018-	R&D Engineer Mobile Hydraulics Hyva Holding, Alphen aan den Rijn, The Netherlands